SLAC-R-821
BABAR-THESIS-04/123

Rare B Meson Decays With Omega Mesons

Lei Zhang

Stanford Linear Accelerator Center
Stanford University
Stanford, CA 94309

SLAC-Report-821

Prepared for the Department of Energy
under contract number DE-AC02-76SF00515

Printed in the United States of America. Available from the National Technical Information Service, U.S. Department of Commerce, 5285 Port Royal Road, Springfield, VA 22161.

Rare B Meson Decays with ω Mesons

by

Lei Zhang

B.E., University of Science and Technology of China, 1996

M.S., Institute of High Energy Physics, Beijing, 1999

A thesis submitted to the

Faculty of the Graduate School of the

University of Colorado in partial fulfillment

of the requirements for the degree of

Doctor of Philosophy

Department of Physics

2004

This thesis entitled:
Rare B Meson Decays with ω Mesons
written by Lei Zhang
has been approved for the Department of Physics

_____

William T. Ford

_____

Prof. Thomas A. DeGrand

Date _____

The final copy of this thesis has been examined by the signatories, and we find that both the content and the form meet acceptable presentation standards of scholarly work in the above mentioned discipline.

Zhang, Lei (Ph.D., Physics)

Rare B Meson Decays with ω Mesons

Thesis directed by Prof. William T. Ford

Rare charmless hadronic B decays are particularly interesting because of their importance in understanding the *CP* violation, which is essential to explain the matter-antimatter asymmetry in our universe, and of their roles in testing the "effective" theory of B physics. The study has been done with the *BABAR* experiment, which is mainly designed for the study of *CP* violation in the decays of neutral B mesons, and secondarily for rare processes that become accessible with the high luminosity of the PEP-II B Factory.

In a sample of 89 million produced $B\overline{B}$ pairs on the *BABAR* experiment, we observed the decays $B^0 \to \omega K^0$ and $B^+ \to \omega\rho^+$ for the first time, made more precise measurements for $B^+ \to \omega h^+$ and reported tighter upper limits for $B \to \omega K^*$ and $B^0 \to \omega\rho^0$. The branching fractions measured are $\mathcal{B}(B^+ \to \omega\pi^+) = (5.5 \pm 0.9 \pm 0.5) \times 10^{-6}$, $\mathcal{B}(B^+ \to \omega K^+) = (4.8 \pm 0.8 \pm 0.4) \times 10^{-6}$, $\mathcal{B}(B^0 \to \omega K^0) = (5.9^{+1.6}_{-1.3} \pm 0.5) \times 10^{-6}$, $\mathcal{B}(B^0 \to \omega K^{*0}) = (3.4^{+1.8}_{-1.6} \pm 0.4) \times 10^{-6}$ ($< 6.0 \times 10^{-6}$), $\mathcal{B}(B^+ \to \omega K^{*+}) = (3.5^{+2.5}_{-2.0} \pm 0.7) \times 10^{-6}$ ($< 7.4 \times 10^{-6}$), $\mathcal{B}(B^0 \to \omega\rho^0) = (0.6^{+1.3}_{-1.1} \pm 0.4) \times 10^{-6}$ ($< 3.3 \times 10^{-6}$), and $\mathcal{B}(B^+ \to \omega\rho^+) = (12.6^{+3.7}_{-3.3} \pm 1.6) \times 10^{-6}$. We also measure time-integrated charge asymmetries $\mathcal{A}_{ch}(B^+ \to \omega\pi^+) = 0.03 \pm 0.16 \pm 0.01$, $\mathcal{A}_{ch}(B^+ \to \omega K^+) = -0.09 \pm 0.17 \pm 0.01$, and $\mathcal{A}_{ch}(B^+ \to \omega\rho^+) = 0.05 \pm 0.26 \pm 0.02$. For $B^+ \to \omega\rho^+$ we also measure the longitudinal polarization fraction $f_L(B^+ \to \omega\rho^+) = 0.88^{+0.12}_{-0.15} \pm 0.03$.

To my wife Yi Sun and my daughter Cindy.

Acknowledgements

I am very fortunate that lots of people have helped me so much that without them I could not possibly come this far in my academic study and get this research work done. It would take quite a few pages to name all of them, and I might not be able to express my deepest appreciation to them all explicitly. Nevertheless, I owe a great deal to the people who have supported me during various times.

First of all, I must gratefully acknowledge my advisor, Bill Ford, who has accepted me as Ph.D. student and given me the opportunity to undertake my research as part of the *BABAR* Collaboration. His enthusiasm, encouragement and endless support were always what I could rely on when things looked pessimistic. It has been a great pleasure to work him and it is hard for me to imagine that one could have a better advisor than Bill. I would also like to thank Jim Smith for his helpful advice and guidance during all the stages of this project. Discussions with him were so fruitful that I could end up with nothing otherwise when the analysis went stalled many times. Whenever it looked the hardest time to me, Jim and Bill were there to help.

It is a tremendous task requiring team effort for anyone to accomplish any achievement in this field, and I would like to thank Jean Roy for his early work on ωh^+ analysis; Mirna van Hoek for her great analysis tools, `Q2BUser` and `Q2BFit`; Paul Bloom for his insightful discussions and initial setup on ωK^* and $\omega\rho$ analysis; Fred Blanc for his invaluable help in different stages of the analysis. Thanks also to Phil, Corry, Keith, Fabian, Ian, Josh, Ishani, and all other Colorado group members who have made it such

a wonderful team to work with.

I am also very grateful to all the *BABAR* collaboration members who have made this work possible and all the PEP-II staff who have provided us with excellent luminosity and machine conditions. I want to thank Conveners and members from Quasi-Two-Body Charmless Analysis Working Group and many other AWGs of *BABAR*, for their unending support and beneficial discussions throughout the whole work and my special thanks go to Jim Olsen, Bill Ford, Adrian Bevan, Jim Smith, Erich Varnes, Luca Cavoto. I also thank Wouter Verkerke and David Kirkby for their wonderful contributions of `RooFit` packages, John Back for his helpful discussion on `RooDircPdf`, Alex Olivas for his help on digi-embedding studies, Andrei Gritsan and LLuisa Maria Mir for their valuable discussions on VV analysis, Shahram Rahatlou for his excellent research and thesis. Other colleagues who help me a lot and to whom I owe a lot are: Ming Chao, Jinlong Zhang, Wei Yang, Aidong Chen, Gerhard Raven, Nick Danielson, and many more. Thanks should also go to my analysis review committee members, Bob Cahn, Massimo Carpinelli, Sasha Telnov, Carlo Dallapiccola, Teela Marie Pulliam, Haibo Li, the institutional reviewers and the PubBoard members for their timely reviews, comments and final approvals. I want to thank Haibo again for being my best friend and mentor for so many years.

I have spent one year at SLAC, which turned out to be a very happy experience, and I could not leave without saying thanks to Vera Lüth, the leader of Group C which hosted me. I also need to thank the administrative and technical staff at SLAC, in particular Anna Pacheco, Nuria Ayala, Charlotte Hee, who have saved me lots of time and provided me with the best services. Life at SLAC was even more wonderful with all my friends around the Bay Area and I had lots of fun with many of them, including: Jiquan Guo (Stanford), Changjun Ma (SBC), Haiming Xu (Philips), Shunjiang Xu (SUN), Wei Zhao (Stanford), Rita Chen (SUN). My thanks to all of them and their families.

Throughout years of study at University of Colorado at Boulder, I have constantly received enlightenment and inspiration from many faculty members from the Department of Physics and other departments and I express my gratitude to all of them and particularly to Walter Wyss, Neil Ashby, Jim Shepard, Tom DeGrand, Uriel Nauenberg, Hal Gabow, Roger King, Kenneth Anderson. I would like to thank Susan Thompson, Kathy Oliver, Joe Hurst, Mary Dang and all the staff for their excellent work. Either on campus, or around Boulder and Denver Metro area, lots of friends from many different backgrounds make everyday part of excitements. I especially thank Madam Zhen Xia for treating my daughter like her own granddaughter; Changying Li's family for being our best friend and neighbor for almost four years.

In spite of my best efforts, this work can not be done on time without generous support from my committee, Bill Ford, Jim Smith, John Cumalat, Tom DeGrand, and Yung-Cheng Lee, to whom I owe a very special debt.

My acknowledgements would not be nearly complete without mentioning my family and relatives nearby or far apart. I must thank my parents for their timeless faith in me and constant support to me; and I should also thank my two sisters, who, during all the years I have been away from my parents, have showed the traditional merits of being company to my parents and making them happier. I am extremely grateful to my mother-in-law for her liberal help by taking care of my daughter many times. Lastly, and most important, I want to thank my wonderful wife. She gave up her job in Beijing, her hometown, where she never left before, to come with me for my study. She gave me perpetual love, support and encouragement that helped to bring this project to its successful completion.

Contents

Chapter

Tables

Table

Figures

Figure

Chapter 1

Theory

1.1 Introduction

People's desire to understand the structure of matter is never ending, and it is now well known that matter is built from molecules and atoms which in turn are made from nucleons and electrons. These subatomic particles are called elementary particles which are not necessarily truly elementary. Particle physics deals with such elementary particles and the interactions of these particles. The discovery of the electron by J. J. Thomson in 1897 [1] marked the first discovery of the elementary particles, and in the next 50 years many new particles were discovered, mainly from cosmic rays.

Particle physics came into a new era after the development of high energy accelerators and detectors, which provided intense and controlled beams and precise measurements of particles produced by collision. Modern experiments on particle physics are a challenge both to technology and human collaboration. In Chapter 2 we will describe one such particle physics experiment where this work has been done.

This chapter serves as a short review of our current knowledge in particle physics most relevant to this work; for a general introduction to the subject of particle physics, see for example Ref. 9. A very important concept in physics is symmetries and conservation laws. Symmetry properties or invariance principles under transformations are connected with conservation laws. For example, invariance of a system under spatial translations corresponds to conservation of momentum, and invariance under time

translations corresponds to conservation of energy.

Three discrete transformations, charge conjugation C, parity (spatial reflection) P, and time reversal T, are of particular interest in particle physics. While the laws of classical mechanics and electrodynamics are invariant under these discrete transformations, experimental evidence showed violations of these operations in weak interactions. P violation was first suggested by T. D. Lee and C. N. Yang [2] in 1956 and observed by C. Wu *et al.* [3] the next year. C violation was indicated by the measurement of neutrino helicity, which is left-handed for neutrinos and right-handed for antineutrinos, by M. Goldhaber *et al.* [4] in 1958. The transformations of C, P and CP on neutrino or antineutrino are shown in Figure 1.1. It was believed that the weak interactions were invariant under the CP operation until CP violation was discovered in 1964 by J. Christenson, J. Cronin, V. Fitch and R. Turlay from K_L^0 decays [5].

CP violation, which is an expected consequence of the so-called Standard Model with three quark generations, are necessary to explain the matter-antimatter asymmetry in our universe as the Sakharov criteria [6] show that three conditions are required to have matter-antimatter asymmetry:

- baryon number violation interactions exist;
- it must be in a non-equilibrium situation;
- CP and C must be violated.

The study of B meson decays is particularly interesting because CP violating effects are expected to be maximized for processes involving particles with a b quark (B mesons), which is about 3 orders of magnitude more massive than those with s quarks (Kaons).

In Chapter 3 we will discuss the analysis techniques used in this work and Chapter 4 presents the results for a number of B meson decays with ω mesons, and finally we discuss the results in Chapter 5. Charge conjugate decays are implied throughout this dissertation (for example, B^+ means $B^\pm$, etc.).

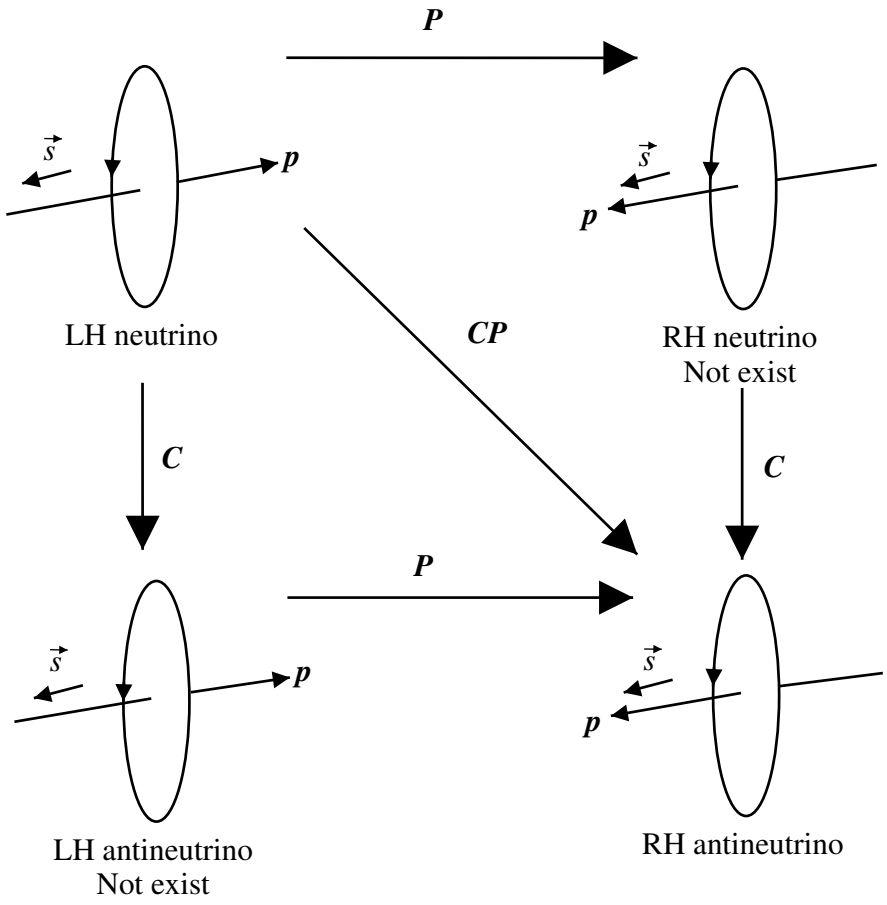

Figure 1.1: Schematic plots of operations C, P, and CP on neutrinos and antineutrinos. Right-handed neutrinos and left-handed antineutrinos do not exist in nature.

1.2 Fundamental Fermions and Interactions

The theoretical basis of most particle physics experiments is the Standard Model of particles and their interactions. In this model, the constituents of all matter are fundamental spin $\frac{1}{2}$ particles, or fermions: six quarks and six leptons, which are grouped into three generations (see Table 1.1), and the interactions between these fermions are described in terms of the exchange of gauge bosons (particles of integral spin). There are four types of interaction or field: strong, electromagnetic (EM), weak, and gravitational interactions as shown in Table 1.2.

The language of particle physics is quantum theory as is true for microscopic

Table 1.1: The fundamental fermions with spin=$1/2\hbar$. Three generations of two quarks and leptons are presented with charge and mass.

Quark	Q ($\|e\|$)	Mass (GeV/c^2)	Lepton	Q ($\|e\|$)	Mass (MeV/c^2)
u	$+\frac{2}{3}$	$1 \sim 5\,\mathrm{MeV}/c^2$	e	-1	0.511
d	$-\frac{1}{3}$	$3 \sim 9\,\mathrm{MeV}/c^2$	ν_e	0	$< 3\,\mathrm{eV}/c^2$
c	$+\frac{2}{3}$	$1.15 \sim 1.35$	μ	-1	105.7
s	$-\frac{1}{3}$	$0.075 \sim 0.17$	ν_μ	0	< 0.19
t	$+\frac{2}{3}$	$\simeq 174.3$	τ	-1	1777
b	$-\frac{1}{3}$	$4.0 \sim 4.4$	ν_τ	0	< 18.2

Table 1.2: The four fundamental interactions are tabulated with the boson mediators, spin, parity, mass, interaction range and coupling constant. ($Mc^2 = 1\,\mathrm{GeV}$)

		Electroweak		
	Gravitational	EM	Weak	Strong
Gauge boson	graviton	photon	$W^\pm$, Z^0	gluon
J^P	2^+	1^-	$1^-, 1^+$	1^-
Mass (GeV/c^2)	0	0	$80.4, 91.2$	0
Range (m)	∞	∞	10^{-18}	10^{-15}
Source	mass	electric charge	weak charge	color charge
Coupling constant	$\frac{G_N M^2}{4\pi\hbar c} =$ 5×10^{-40}	$\alpha = \frac{e^2}{4\pi\hbar c} =$ $\frac{1}{137}$	$\frac{G(Mc^2)^2}{(\hbar c)^3} =$ 1.17×10^{-5}	α_S ≤ 1

world in general. Particles can be classified into two types according to their spin: half-integral spin particles, or fermions, which obey Fermi-Dirac statistics, and integral spin particles, or bosons, which obey Bose-Einstein statistics. The spin-statistics theorem states that the wavefunction is symmetric under exchange of identical bosons, while the wavefunction is antisymmetric under exchange of identical fermions. One important implication of the theorem is the Pauli principle [7] that two or more identical fermions cannot occupy the same quantum state. For each particle there is an antiparticle with

the same mass and lifetime but with opposite charge, and fermions and antifermions can only be created or destroyed in pairs.

The leptons carry integral charge, $-|e|$, and the neutral leptons are called neutrinos. Leptons are grouped into pairs, electron e and electron neutrino ν_e, muon μ and muon neutrino ν_μ, tau τ and tau neutrino ν_τ. The quarks carry fractional charge, $+\frac{2}{3}|e|$ or $-\frac{1}{3}|e|$. The type of quark is called the flavor of quark and is donated by a letter for each 'flavor': u for 'up', d for 'down', s for 'strange', c for 'charmed', b for 'bottom' and t for 'top'. Just like leptons, the quarks are grouped into three generations: u and d, s and c, b and t. Leptons can exist as free particles, but quarks are confined in hadrons and single quarks as free particles have not been observed.

The interactions between particles are described in quantum field theory through the exchange of particular bosons associated with the interactions. As is shown in Table 1.2, gravitational interactions are the weakest force among all the fundamental interactions and have negligible effect on current experiments of particle physics. It is a long-range interaction mediated by exchange of spin 2 boson, the graviton, which must have no mass.

Electromagnetic interactions are mediated by photon (γ) exchange between charged particles as described in quantum electrodynamics (QED). The coupling constant of electromagnetic interactions, $\alpha \sim \frac{1}{137}$, specifies the strength of the interaction. The photon has no mass so the electromagnetic interactions are long-range interactions.

Weak interactions take place between all quarks and leptons, mediated by the massive $W^\pm$ and Z^0 bosons, which couple to fermions with g and g', respectively. At low momentum transfer, $q^2 \ll M_W^2$, the weak coupling mediated by $W^\pm$ can be written as

$$\frac{G}{\sqrt{2}} = \frac{g^2}{8M_W^2} = \frac{e^2}{8\sin^2\theta_W M_W^2}\,, \tag{1.1}$$

where θ_W is the weak mixing angle with $\sin^2\theta_W \simeq 0.22$, and $M_W = 80.4\,\mathrm{GeV}/c^2$ is

the mass of W boson. $G/\sqrt{2}$ is about $10^{-3}\alpha$, so the weak interactions are drowned by strong and electromagnetic interactions unless these interactions are forbidden by some conservation laws. Since the mediators of weak interactions also have mass, the interactions have very short range.

The weak and electromagnetic interactions can be unified through the electroweak theory proposed by Glashow, Weinberg and Salam [8], and we will discuss the electroweak interactions at length in section 1.5 for the importance of the theory to this work.

Strong interactions take place between quarks, and the interquark force is mediated by a massless boson, the gluon. In the theory of strong interactions, quantum chromodynamics (QCD), the source of interactions is six types of 'color charge'. A quark carries one of the three basic colors (red r, blue b, and green g) and antiquark carries anticolors ($\bar{r}$, $\bar{b}$, and $\bar{g}$). Gluons carry one color and one anti-color and form an octet of active states: $r\bar{b}, r\bar{g}, b\bar{g}, b\bar{r}, g\bar{r}, g\bar{b}, \frac{1}{\sqrt{2}}(r\bar{r} - b\bar{b}), \frac{1}{\sqrt{6}}(r\bar{r} + b\bar{b} - 2g\bar{g})$. The QCD potential has the form of

$$V = -\frac{4}{3}\frac{\alpha_S}{r} + kr\,. \tag{1.2}$$

At high q^2 (or small distance), where the first term dominates, single-gluon exchange is a good approximation, while at low q^2 (or large distance), where the second term dominates, the force increases indefinitely resulting in the color confinement of quarks and gluons inside hadrons. Thus there only exist color singlet bound states of quarks and antiquarks. The colorless quark combinations with lowest energy are the qqq states (baryons, for example, proton and neutron) and $q\bar{q}$ (mesons, for example, kaon, pion).

1.3 Static Quark Model of Hadrons

Though a dynamic structure of hadrons, as in the theory of QCD, and observed by experiments including lepton-nucleon scattering, is a collection of valence quarks,

Table 1.3: Light pseudoscalar mesons and vector mesons. The lowest meson states are given with quark contents and mass of mesons. The physical meson states, η and η', are linear combinations of η_8 and η_0; ω and ϕ are mixtures of ω_8 and ω_0 (see the text for discussion).

Quark Comb	$\mathbf{P}(0^-)$	Mass (MeV/c^2)	$\mathbf{V}(1^-)$	Mass (MeV/c^2)	Γ (MeV/c^2)
$u\overline{d}$	π^+	140	ρ^+	769	150
$d\overline{u}$	π^-		ρ^-		
$\frac{1}{\sqrt{2}}(d\overline{d}-u\overline{u})$	π^0	135	ρ^0		
$u\overline{s}$	K^+	494	K^{*+}	892	50.8
$d\overline{s}$	K^0	498	K^{*0}	896	50.7
$\overline{u}s$	K^-	494	K^{*-}	892	50.8
$\overline{d}s$	$\overline{K}^0$	498	$\overline{K}^{*0}$	896	50.7
$\frac{1}{\sqrt{6}}(d\overline{d}+u\overline{u}-2s\overline{s})$	η_8	547 (η)	ω_8	783 (ω)	8.4
$\frac{1}{\sqrt{3}}(d\overline{d}+u\overline{u}+s\overline{s})$	η_0	958 (η')	ω_0	1019 (ϕ)	4.5

quark-antiquark pairs, and gluons, it is a good approximation to consider the valence quarks only in the classification of hadrons. As is shown before, only colorless states can exist. The two lowest qqq baryon states are uud (proton p) and udd (neutron n) which are the constituents of nuclei. We will focus on $q\overline{q}$ meson states because they are more relevant to this work.

Mesons are the bound states of a quark and an antiquark. If we consider only three quark flavors, u, d, and s, we have SU(3) octet and singlet states. We also have spin triplet states of $J = 1$ (vector mesons), and spin singlet states of $J = 0$ (pseudoscalar mesons) given the $\frac{1}{2}\hbar$ spin of quarks. Most of these light mesons are the decay products of modes studied in this work, and we list them in Table 1.3.

The actual states observed in nature, η, η', ω, and ϕ, are octet-singlet mixtures. We discuss this matter for vector mesons in more detail because ω mesons are the

subject of this work. We can write the mixing as:

$$\phi = \omega_0 \sin\theta - \omega_8 \cos\theta \,,$$
$$\omega = \omega_8 \sin\theta + \omega_0 \cos\theta \,, \tag{1.3}$$

where ϕ, ω denote the physical vector mesons, and ω_0, ω_8, defined as

$$\omega_0 = \frac{1}{\sqrt{3}}(d\overline{d} + u\overline{u} + s\overline{s}) \,,$$
$$\omega_8 = \frac{1}{\sqrt{6}}(d\overline{d} + u\overline{u} - 2s\overline{s}) \,, \tag{1.4}$$

are the singlet and octet states, respectively. For the 'ideal mixing', $\sin\theta = 1/\sqrt{3}$, $\theta \simeq 35°$, (1.3) becomes

$$\phi = \frac{1}{\sqrt{3}}(\omega_0 - \sqrt{2}\omega_8) \,,$$
$$\omega = \frac{1}{\sqrt{3}}(\omega_8 + \sqrt{2}\omega_0) \,, \tag{1.5}$$

and with (1.4) we have

$$\phi = s\bar{s} \,,$$
$$\omega = \frac{1}{\sqrt{2}}(u\bar{u} + d\bar{d}) \,, \tag{1.6}$$

which means ϕ is composed of s quarks and ω of u and d. The fact that ϕ decays dominantly to $K\overline{K}$ while phase-space factors favor 3π decay, gives support to the $s\overline{s}$ composition of ϕ. Eq. (1.6) also suggests larger mass for ϕ and similar masses for ω and ρ, which is true as in Table 1.3, and the calculation of mixing angle based on mass formulas gives $\theta \simeq 40°$, which is very close to the ideal case.

Mesons with heavier quarks are listed in Table 1.4. The first observed charmonium state is J/ψ $(c\bar{c})$; one c quark and a light quark form D mesons (pseudoscalars) and D^* mesons (vectors). The first observed bound state of much heavier b quarks is Υ $(b\bar{b})$; one b quark and a light quark form B mesons (pseudoscalars) and B^* mesons (vectors).

Table 1.4: Heavy mesons with c, b quarks.

Quark Comb	Pseudoscalar ($J^P = 0^-$)	Vector ($J^P = 1^-$)
$c\bar{d}$, $\bar{c}d$, $c\bar{u}$, $\bar{c}u$	D^+, D^-, D^0, $\bar{D}^0$	D^{*+}, D^{*-}, D^{*0}, $\bar{D}^{*0}$
$c\bar{s}$, $\bar{c}s$	D_s^+, D_s^-	D_s^{*+}, $\bar{D}_s^{*-}$
$c\bar{c}$	η_c	J/ψ
$\bar{b}u$, $b\bar{u}$, $\bar{b}d$, $b\bar{d}$	B^+, B^-, B^0, $\bar{B}^0$	B^{*+}, B^{*-}, B^{*0}, $\bar{B}^{*0}$
$\bar{b}s$, $b\bar{s}$	B_s^0, $\bar{B}_s^0$	B_s^{*0}, $\bar{B}_s^{*0}$
$b\bar{b}$	η_b	Υ

The t quark is so massive with $M_t \simeq 174\,\mathrm{GeV}/c^2$ that no bound state can be formed before it decays to a b quark and a real W boson.

For heavy quark $Q\overline{Q}$ states, such as $b\bar{b}$ (Υ), the first term of (1.2) dominates at small r, and the momentum transfer q is much less than the quark mass, so they have similar energy levels as positronium, and then can be classified similarly by their principal (radial) quantum number n, together with the orbital angular momentum L, and the total spin S.

The vector $\Upsilon(4S)$ resonance is very important because it is just above the $B\overline{B}$ production threshold and decays into $B\overline{B}$ pairs, so the B Factory of SLAC is operating on the $\Upsilon(4S)$ resonance in order to produce large number of $B\overline{B}$ events. We will have detailed discussion on B physics and B Factory in section 1.6 and 2.2, respectively.

1.4 Decay of Resonance

Mesons are often referred to as resonances because they are usually short-lived bound states with finite width. In the rest frame of a particle of mass M, the rate of decay into n bodies is given by [12]

$$d\Gamma = \frac{(2\pi)^4}{2M}|\mathcal{M}|^2 d\Phi_n(P;\, p_1, \ldots, p_n)\,, \tag{1.7}$$

where $\mathcal{M}$ is the Lorentz-invariant matrix element between initial and final states, and $d\Phi_n$ is an element of n-body phase space given by

$$d\Phi_n(P;\ p_1,\ldots,p_n) = \delta^4(P - \sum_{i=1}^{n} p_i) \prod_{i=1}^{n} \frac{d^3p_i}{(2\pi)^3 2E_i}\,. \tag{1.8}$$

We are particularly interested in 2-body decays because they are the decay modes studied in this work and are relatively simple. The rate of two-body decay can be written as

$$d\Gamma = \frac{1}{32\pi^2}|\mathcal{M}|^2 \frac{|\mathbf{p}|}{M^2} d\Omega\,, \tag{1.9}$$

where $\mathbf{p}$ is the momentum of one of the final particles. There is no angular dependence for $P \to P_1P_2$ (P for spinless pseudoscalar meson) decays so the width of the decay is

$$\Gamma = \frac{|\mathbf{p}|}{8\pi M^2}|\mathcal{M}|^2\,, \tag{1.10}$$

by integrating over the full solid angle.

Decays involving particles with spin have complicated angular distributions. We can generally express the angular dependence for decays $P \to X_1X_2$, where X could be P (pseudoscalar), V (vector), etc., both X_1 and X_2 decaying into spinless particles, in terms of the spherical functions [10, 13]

$$\frac{d^3\Gamma}{d\cos\theta_1 d\cos\theta_2 d\phi} \propto |\sum_{|m|\le J_1,J_2} A_m \times Y_{J_1,m}(\theta_1,\phi_1) \times Y_{J_2,-m}(\theta_2,\phi_2)|^2\,, \tag{1.11}$$

where θ_1 and θ_2 are the helicity angles defined by the direction of the two-body X_i decay axis in the X_i rest frame (or by the normal to the three-body decay plane in the X_i rest frame) relative to the X_i momentum, $\phi = \phi_1 - \phi_2$ the azimuthal angle between the two decay planes (for the case with both X_1 and X_2 decaying into two particles; see Figure 1.2 for the definition of ϕ with $X_1 \to P_1P_2P_3$); A_m is the decay amplitude, and J_i is the angular momentum quantum number for X_i.

For $P \to P_1V_2$ decays, $J_1 = 0$ and $J_2 = 1$, then

$$\begin{aligned} d\Gamma &\propto |A_0 \times Y_{1,0}(\theta_2,\phi)|^2 d\cos\theta_2 d\phi \\ &\propto \cos^2\theta_2 d\cos\theta_2\,, \end{aligned} \tag{1.12}$$

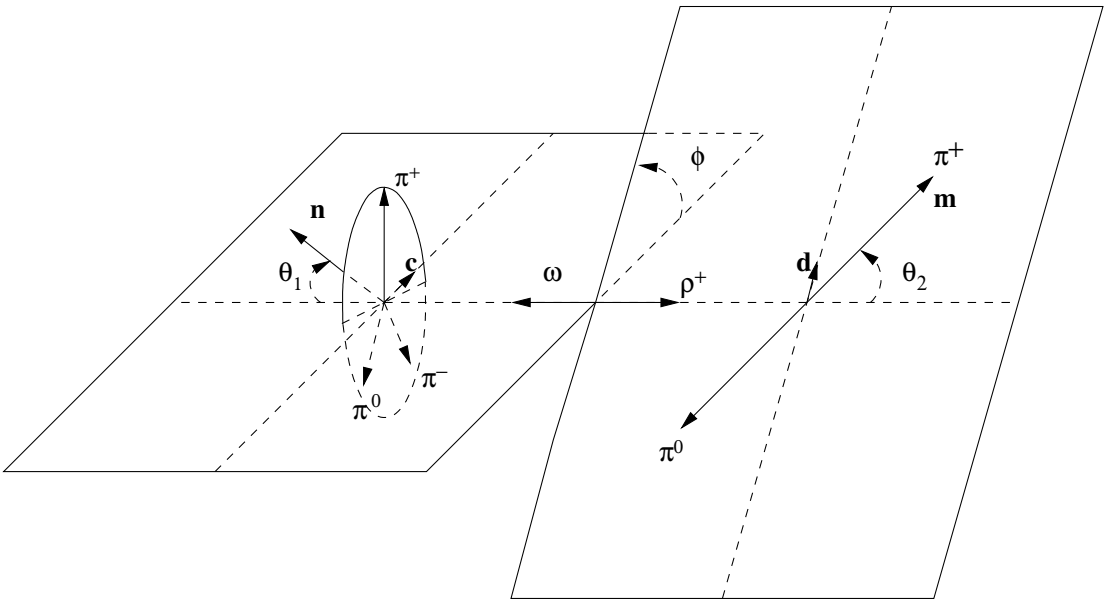

Figure 1.2: Helicity frame for $B^+ \to \omega\rho^+$. $\mathbf{n}$ is the normal to the ω decay plane (the ellipse) which is the plane of the 3π's in the ω rest frame; $\mathbf{m}$ is the flight direction of π^+ from ρ^+, measured in the ρ^+ rest frame; θ_1 is defined as the angle between $\mathbf{n}$ and the flight direction of ω (helicity axis), measured in the ω rest frame; θ_2 is defined as the angle between $\mathbf{m}$ and the direction of ρ in the ρ rest frame; $\mathbf{c}(\mathbf{d})$ is the unit vector along the projection of $\mathbf{n}$ ($\mathbf{m}$) orthogonal to the direction of ω (ρ^+); the azimuthal angle ϕ is defined as the angle between $\mathbf{c}$ and $\mathbf{d}$.

which means the helicity cosine $\mathcal{H} \equiv \cos\theta_H$ of the vector meson has a quadratic distribution.

In $P \to V_1V_2$ modes, $J_1 = 1$ and $J_2 = 1$, there are three amplitudes $A_\lambda, (\lambda = 0, \pm 1)$; then

$$\begin{aligned}\frac{1}{\Gamma}\frac{d^3\Gamma}{d\cos\theta_1 d\cos\theta_2 d\phi} &= \frac{9}{16\pi}\frac{1}{|A_0|^2+|A_{+1}|^2+|A_{-1}|^2} \\ \times\Bigg\{&\frac{1}{2}\sin^2\theta_1\sin^2\theta_2\left(|A_{+1}|^2+|A_{-1}|^2\right)+2\cos^2\theta_1\cos^2\theta_2|A_0|^2 \\ &+\sin^2\theta_1\sin^2\theta_2\left[\cos 2\phi\,\Re\mathrm{e}(A_{+1}A_{-1}^*)-\sin 2\phi\,\Im\mathrm{m}(A_{+1}A_{-1}^*)\right] \\ -\frac{1}{2}&\sin 2\theta_1\sin 2\theta_2\left[\cos\phi\,\Re\mathrm{e}(A_{+1}A_0^*+A_{-1}A_0^*)-\sin\phi\,\Im\mathrm{m}(A_{+1}A_0^*-A_{-1}A_0^*)\right]\Bigg\},\end{aligned} \tag{1.13}$$

where we may integrate over the azimuthal angles (assuming azimuthal uniformity of

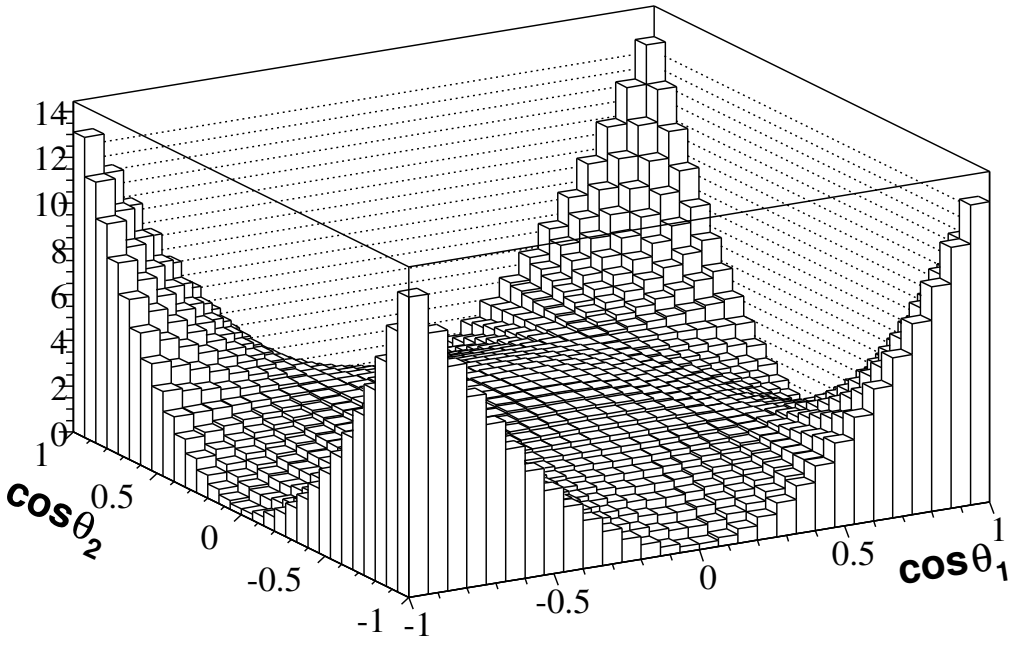

Figure 1.3: Distribution of the cosines of the helicity angles ($\cos\theta_1$ and $\cos\theta_2$) in $P \to VV$ decays with polarization $f_L = 0.5$.

the detector acceptance),

$$\frac{1}{\Gamma}\frac{d^2\Gamma}{d\cos\theta_1 d\cos\theta_2} = \frac{9}{4}\left\{\frac{1}{4}(1-f_L)\sin^2\theta_1\sin^2\theta_2 + f_L\cos^2\theta_1\cos^2\theta_2\right\}, \tag{1.14}$$

where f_L is the longitudinal polarization ratio defined by

$$f_L = \frac{\Gamma_L}{\Gamma} = \frac{|A_0|^2}{|A_0|^2 + |A_{+1}|^2 + |A_{-1}|^2}. \tag{1.15}$$

In Figure 1.3 we show correlated $\cos\theta_1$ and $\cos\theta_2$ distribution with $f_L = 0.5$.

We summarize in Table 1.5 the angular distributions of different types of two-body decays of pseudoscalar mesons relevant to this work. We can see that the PP and PV modes have specific distributions while the angular distribution of the final state for VV modes is *a priori* unknown. It is a combination of s-, p-, and d- wave contributions. Full angular analysis requires very high statistics while the typical branching fraction

Table 1.5: The longitudinal and transverse components of pseudoscalar two-body decays with PP, PV, and VV final states.

decay type	longitudinal	transverse
$P \to PP$	1	—
$P \to PV$	$\cos^2\theta_2$	—
$P \to VV$	$f_L \cos^2\theta_1 \cos^2\theta_2$	$(1-f_L) \times 0.25 \times \sin^2\theta_1 \sin^2\theta_2$

for the modes studied here is of order $10^{-6} \sim 10^{-5}$. Nevertheless, with the available data sample it is still possible to measure the longitudinal polarization fraction f_L which has its own importance. It is important to the measurement of the branching fraction because the detection efficiency is different between longitudinal and transverse decays. Some theoretical calculations predict rather large f_L [11], so it is interesting to check the prediction in experiment.

As we have demonstrated in this section, decay information gives us insight into the underlying interactions. The measurement of branching fractions and other quantities of different decays help us to understand the properties of fundamental physics laws. We present in Table 1.6 major decays of mesons listed in Table 1.3 with resonance mass, width, lifetime, branching fractions and branching fraction errors as measured in experiment [12]. The spectrum of decay modes with mesons in Table 1.4 are more complicated, involving many final states which can be grouped as semileptonic, charmed, charmless, etc., but there are usually no single dominant submodes. We want to point out that $M_{\Upsilon(4S)} = 10.58\,\text{GeV} \gtrsim 2M_B = 5.279\,\text{GeV}$, and the branching fraction of $\Upsilon(4S) \to B\overline{B}$ is greater than 96% with equal B^+B^- and $B^0\overline{B}^0$ production.

Table 1.6: Light meson decay information are given with mass, width (Γ), lifetime (τ), dominant decay modes, their branching fractions (Γ_i/Γ), and the branching fraction errors.

Meson	Mass (MeV)	Γ (MeV)	$c\tau$ (m)	Decay	Γ_i/Γ (%)	Error (%)
π^+	139.6		7.80	$\mu^+\nu_\mu$	99.99	4×10^{-5}
π^0	135.0		2.5×10^{-8}	2γ	98.80	0.03
K^+	493.7		3.71	$\mu^+\nu_\mu$	63.43	0.27
				$\pi^+\pi^0$	21.13	0.66
K^0_S	497.7		0.0268	$\pi^+\pi^-$	68.95	0.20
				$\pi^0\pi^0$	31.05	0.45
K^0_L	497.7		15.51	$\pi^+e^-\bar{\nu_e}$	38.81	0.70
				$\pi^+\mu^-\bar{\nu_\mu}$	27.19	0.92
				$3\pi^0$	21.05	1.09
				$\pi^+\pi^-\pi^0$	12.59	1.51
				$\pi^+\pi^-$	0.209	1.20
η	547.8	1.29×10^{-3}		2γ	39.43	0.66
				$3\pi^0$	32.51	0.89
				$\pi^+\pi^-\pi^0$	22.6	1.77
η'	957.8	0.202		$\pi^+\pi^-\eta$	44.3	3.39
				$\rho^0(\pi^+\pi^-)\gamma$	29.5	3.39
				$\pi^0\pi^0\eta$	20.9	5.74
ρ	775.8	150.3		$\pi\pi$	100	
K^{*+}	891.66	50.8		$K^0\pi^+$	66.67	
				$K^+\pi^0$	33.33	
K^{*0}	896.1	50.7		$K^+\pi^-$	66.67	
				$K^0\pi^0$	33.33	
ω	782.59	8.49		$\pi^+\pi^-\pi^0$	89.1	0.79
ϕ	1019.46	4.26		K^+K^-	49.1	1.2
				$K^0_LK^0_S$	34.0	1.5

1.5 Electroweak Interactions and *CP* Violation

The Standard Model is a gauge theory based on the $\mathrm{SU}(3)_C \times \mathrm{SU}(2)_L \times \mathrm{U}(1)_Y$ symmetry group, with three fermion generations, and *CP* violations arise from a single phase in the quark mixing matrix [14].

The electromagnetic and weak interactions can be unified into a single electroweak interaction through the $\mathrm{SU}(2)_L \times \mathrm{U}(1)_Y$ group: an $\mathrm{SU}(2)_L$ group of 'weak isospin' I and a $\mathrm{U}(1)_Y$ group of 'weak hypercharge' Y. Three of the four massless mediating bosons, $\mathbf{W}_\mu = W_\mu^{(1)}, W_\mu^{(2)}, W_\mu^{(3)}$, are the components of an $I = 1$ isovector triplet, while the fourth, B_μ, is an isosinglet. The minimal model also includes a single complex Higgs scalar doublet $\phi \equiv \begin{pmatrix} \phi^+ \\ \phi^0 \end{pmatrix}$, and with the so-called 'spontaneous symmetry breaking' process, due to the non-zero expectation value of the Higgs scalar field in the vacuum, $\langle \phi \rangle = v \neq 0$, three bosons, W_μ^+, W_μ^- and Z_μ^0, acquire mass, and one, A_μ (the photon), remains massless.

Each quark generation consists of three multiples,

$$Q_L^I = \begin{pmatrix} u_L^I \\ d_L^I \end{pmatrix} = (3,2)_{+1/6}\,, \quad u_R^I = (3,1)_{+2/3}\,, \quad d_R^I = (3,1)_{-1/3}\,, \tag{1.16}$$

where $(3,2)_{+1/6}$ denotes a triplet of $\mathrm{SU}(3)_C$, doublet of $\mathrm{SU}(2)_L$ with hypercharge $Y = Q - I_3 = +1/6$, similarly for the other representations, u_L^I (u_R^I) and d_L^I (d_R^I) denote the left-handed (right-handed) components of the up-type and down-type of quarks. The interactions of quarks with the $\mathrm{SU}(2)_L$ gauge bosons are described by

$$\mathcal{L}_W = -\frac{1}{2} g \overline{Q_{Li}^I} \gamma^\mu \tau^a \mathbf{1}_{ij} Q_{Lj}^I W_\mu^a\,, \tag{1.17}$$

where g is the weak coupling constant, γ^μ operates in Lorentz space, τ^a operates in $\mathrm{SU}(2)_L$ space, and $\mathbf{1}$ is the unit matrix operating in generation (flavor) space. This unit matrix is written explicitly to make the transformation to mass eigenbasis clearer. The Lagrangian of quarks interacting with the Higgs fields can be written as

$$\mathcal{L}_Y = -G_{ij} \overline{Q_{Li}^I} \phi d_{Rj}^I - F_{ij} \overline{Q_{Li}^I} \tilde{\phi} u_{Rj}^I + \mathrm{h.c.}\,, \tag{1.18}$$

where G and F are general complex 3×3 matrices. Their complex nature is the source of CP violation in the Standard Model. We can expand the Higgs scalar field near its vacuum state

$$\phi_0 = \frac{1}{\sqrt{2}} \begin{pmatrix} 0 \\ v \end{pmatrix}, \tag{1.19}$$

so we have

$$\phi = \begin{pmatrix} \phi^+(x) \\ \phi^0(x) \end{pmatrix} \rightarrow \frac{1}{\sqrt{2}} \begin{pmatrix} 0 \\ v + H^0 \end{pmatrix}, \tag{1.20}$$

and the symmetry of the scalar field is broken, with which the two components of the quark doublet become distinguishable, as are the three members of the W^μ triplet. The charged current interaction in (1.17) then can be written as

$$\mathcal{L}_{CC} = -\sqrt{\frac{1}{2}} g \overline{u^I_{Li}} \gamma^\mu \mathbf{1}_{ij} d^I_{Lj} W^+_\mu + \text{h.c.}\,. \tag{1.21}$$

The expansion also endows quarks with mass terms when substituted in (1.18):

$$\mathcal{L}_M = -\sqrt{\frac{1}{2}} v G_{ij} \overline{d^I_{Li}} d^I_{Rj} - \sqrt{\frac{1}{2}} v F_{ij} \overline{u^I_{Li}} u^I_{Rj} + \text{h.c.}\,, \tag{1.22}$$

with the mass matrices being

$$M_d = Gv/\sqrt{2}, \quad M_u = Fv/\sqrt{2}\,. \tag{1.23}$$

In general, the quark weak interaction eigenstates in (1.16) are different from the mass eigenstates, so the mass matrices in (1.23) are usually not diagonal. We can diagonalize the mass matrices by introducing four unitary matrices such that

$$V_{dL} M_d V^\dagger_{dR} = M_d^{\text{diag}}, \quad V_{uL} M_u V^\dagger_{uR} = M_u^{\text{diag}}, \tag{1.24}$$

where M_q^{diag} are diagonal and real, while V_{qL} and V_{qR} are complex. In the mass eigenbasis, the charged current interactions (1.21) becomes

$$\mathcal{L}_{CC} = -\sqrt{\frac{1}{2}} g \overline{u_{Li}} \gamma^\mu \overline{V}_{ij} d_{Lj} W^+_\mu + \text{h.c.}\,. \tag{1.25}$$

where u and d without superscript I (stands for weak Interaction) denote the mass eigenstates of quarks, and the matrix $\overline{V} = V_{uL} V^\dagger_{dL}$ is the unitary mixing matrix for three quark generations.

In general, there are nine parameters for the mixing matrix: three real angles and six complex phases, however the number of phases in $\overline{V}$ can be reduced by a transformation

$$\overline{V} \implies V = P_u \overline{V} P_d^* \,, \tag{1.26}$$

where P_u and P_d are diagonal phase matrices. The five phase differences among the elements of P_u and P_d can be chosen so that the transformation (1.26) eliminates five of the six independent phases from $\overline{V}$. Thus matrix V has one irreducible complex phase and three real angles. The mixing matrix V is called the Cabibbo-Kobayashi-Maskawa (CKM) matrix [15]

$$V_{CKM} \equiv \begin{pmatrix} V_{ud} & V_{us} & V_{ub} \\ V_{cd} & V_{cs} & V_{cb} \\ V_{td} & V_{ts} & V_{tb} \end{pmatrix} , \tag{1.27}$$

where each element $V_{q_i q_j}$ represents the amplitude of flavor-changing weak interactions between quarks q_i and q_j, and the phase is called the Kobayashi-Maskawa phase, δ_{KM}.

Three generations of quarks are necessary for the presence of the complex phase, and therefore *CP* violation in the Standard Model. With two generations of quarks, the Standard Model Lagrangian with a single Higgs field would remove all the complex phases and the 2×2 mixing matrix V is left with only one real parameter which is the Cabibbo angle.

The fact that there is only one *CP* violating phase in the Standard Model implies that all *CP* violating effects are very closely related. Therefore different physical processes can be used to probe the same source of *CP* violation, and the redundancy provides strict tests of the model.

1.5.1 The CKM Matrix

As we have seen, the weak interaction eigenstates of quarks are different from the quark mass eigenstates. The quark mixing can be described by V_{CKM} matrix

$$\begin{pmatrix} d' \\ s' \\ b' \end{pmatrix} = \begin{pmatrix} V_{ud} & V_{us} & V_{ub} \\ V_{cd} & V_{cs} & V_{cb} \\ V_{td} & V_{ts} & V_{tb} \end{pmatrix} \begin{pmatrix} d \\ s \\ b \end{pmatrix} , \tag{1.28}$$

where $\begin{pmatrix} u \\ d' \end{pmatrix}$, $\begin{pmatrix} c \\ s' \end{pmatrix}$, and $\begin{pmatrix} t \\ b' \end{pmatrix}$ form the three-generation quark doublets of weak interactions. The 90% confidence limits of the magnitude of the elements of the CKM matrix are summarized as [12]

$$|V_{CKM}| \equiv \begin{pmatrix} 0.9739 \sim 0.9751 & 0.221 \sim 0.227 & 0.0029 \sim 0.0045 \\ 0.221 \sim 0.227 & 0.9730 \sim 0.9744 & 0.039 \sim 0.044 \\ 0.0048 \sim 0.014 & 0.037 \sim 0.043 & 0.9990 \sim 0.9992 \end{pmatrix} , \tag{1.29}$$

using eight tree-level constraints, determined from weak decays of the relevant quarks, or, in some cases, from deep inelastic neutrino scattering, together with unitarity.

The unitarity of the CKM matrix ($VV^\dagger = 1$) implies three real constraints $\sum_{q_2} |V_{q_1 q_2}|^2 = 1$ and six complex constraints $\sum_{q_2} |V_{q_2 q_1} V_{q_2 q_3}|^2 = 0$, three of which are very useful in understanding the Standard Model predictions for *CP* violation

$$V_{ud}V_{us}^* + V_{cd}V_{cs}^* + V_{td}V_{ts}^* = 0 \,, \tag{1.30}$$

$$V_{us}V_{ub}^* + V_{cs}V_{cb}^* + V_{ts}V_{tb}^* = 0 \,, \tag{1.31}$$

$$V_{ud}V_{ub}^* + V_{cd}V_{cb}^* + V_{td}V_{tb}^* = 0 \,, \tag{1.32}$$

as are shown in Figure 1.4.

The unitarity of the CKM matrix can be explicitly exhibited in the 'standard' parameterization [16] in terms of three rotation angles $\theta_{12}, \theta_{23}, \theta_{13}$ and a complex phase

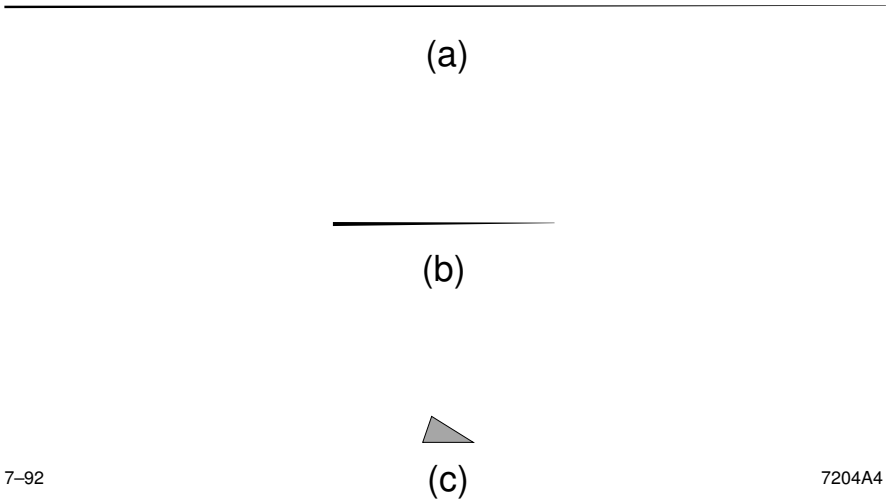

Figure 1.4: The unitarity triangles defined by (1.30) in (a), (1.31) in (b), and (1.32) in (c). All the three triangles are equal in area and the same scale has been used for all triangles. The lengths of the sides of the triangles are proportional to the mixing coupling strength and can be measured from corresponding decays, while the angles of the triangles measure the magnitude of the *CP* violating effects in the decays of K, B_s, and B_d mesons, respectively. The first two triangles almost collapse into a line, so the *CP* violation is small in the leading K and B_s decays, while the third triangle, related to B decays, is quite open, which suggests large *CP* asymmetries in B decays.

$\delta \equiv \delta_{\rm KM}$

$$V = \begin{pmatrix} c_{12}c_{13} & s_{12}c_{13} & s_{13}e^{-i\delta} \\ -s_{12}c_{23} - c_{12}s_{23}s_{13}e^{i\delta} & c_{12}c_{23} - s_{12}s_{23}s_{13}e^{i\delta} & s_{23}c_{13} \\ s_{12}s_{23} - c_{12}c_{23}s_{13}e^{i\delta} & -c_{12}s_{23} - s_{12}c_{23}s_{13}e^{i\delta} & c_{23}c_{13} \end{pmatrix}, \tag{1.33}$$

with $c_{ij} \equiv \cos\theta_{ij}$, $s_{ij} \equiv \sin\theta_{ij}$, and indices $i, j = 1, 2, 3$ corresponding to the three quark generations. In this parameterization, the angles θ_{ij} are related to the amount of 'mixing' between two generations i and j. For example θ_{12} corresponds to the Cabibbo angle [15]. From (1.29) we notice $|V_{ub}|$ is very simple, which implies $c_{13} \sim 1$, and the matrix becomes

$$V = \begin{pmatrix} c_{12} & s_{12} & s_{13}e^{-i\delta} \\ -s_{12}c_{23} & c_{12}c_{23} & s_{23} \\ s_{12}s_{23} - c_{12}c_{23}s_{13}e^{i\delta} & -c_{12}s_{23} & c_{23} \end{pmatrix}, \tag{1.34}$$

where it is clear that the dominant phase terms are V_{ub} and V_{td}. It is convenient to parameterize the CKM matrix in terms of four Wolfenstein parameters (A, λ, ρ, η) [17]

$$V = \begin{pmatrix} 1 - \frac{\lambda^2}{2} & \lambda & A\lambda^3(\rho - i\eta) \\ -\lambda & 1 - \frac{\lambda^2}{2} & A\lambda^2 \\ A\lambda^3(1 - \rho - i\eta) & -A\lambda^2 & 1 \end{pmatrix} + \mathcal{O}(\lambda^4)\,, \tag{1.35}$$

with $\lambda \equiv \sin\theta_C \simeq |V_{us}| \simeq 0.22$, $A \simeq 0.82$, and η represents the CP violating phase of the CKM matrix. The parameters of the standard parameterization (1.33) can be related to the Wolfenstein parameters in (1.35) by

$$s_{12} \equiv \lambda,\ s_{23} \equiv A\lambda^2,\ s_{13}e^{-i\delta} \equiv A\lambda^3(\rho - i\eta)\,. \tag{1.36}$$

and we have

$$V_{us} = \lambda,\ V_{cb} = A\lambda^2,\ V_{ub} = A\lambda^3(\rho - i\eta)\,, \tag{1.37}$$

so we can write

$$V_{td} = A\lambda^3(1 - \bar{\rho} - i\bar{\eta})\,, \tag{1.38}$$

$$\Im\mathrm{m}V_{cd} = -A^2\lambda^5\eta\,, \quad \Im\mathrm{m}V_{ts} = -A\lambda^4\eta\,, \tag{1.39}$$

with

$$\bar{\rho} = \rho(1 - \lambda^2/2)\,, \quad \bar{\eta} = \eta(1 - \lambda^2/2)\,. \tag{1.40}$$

We can rescale the Unitarity Triangle (1.32) by dividing all the three sides by $V_{cd}V_{cb}^*$, such that two vertices of the rescaled Unitarity Triangle are fixed at (0,0) and (1,0), while the third vertex is $(\bar{\rho}, \bar{\eta})$ in the Wolfenstein parameterizations (see Figure 1.5). The lengths of the two complex sides are

$$R_b \equiv \sqrt{\bar{\rho}^2 + \bar{\eta}^2} = \frac{1 - \lambda^2/2}{\lambda}\left|\frac{V_{ub}}{|V_{cb}|}\right|\,, \quad R_t \equiv \sqrt{(1 - \bar{\rho})^2 + \bar{\eta}^2} = \frac{1}{\lambda}\left|\frac{V_{td}}{V_{cb}}\right|\,, \tag{1.41}$$

and the three angles are

$$\alpha \equiv \arg\left[-\frac{V_{td}V_{tb}^*}{V_{ud}V_{ub}^*}\right]\,, \quad \beta \equiv \arg\left[-\frac{V_{cd}V_{cb}^*}{V_{td}V_{tb}^*}\right]\,, \quad \gamma \equiv \arg\left[-\frac{V_{ud}V_{ub}^*}{V_{cd}V_{cb}^*}\right] \equiv \pi - \alpha - \beta\,, \tag{1.42}$$

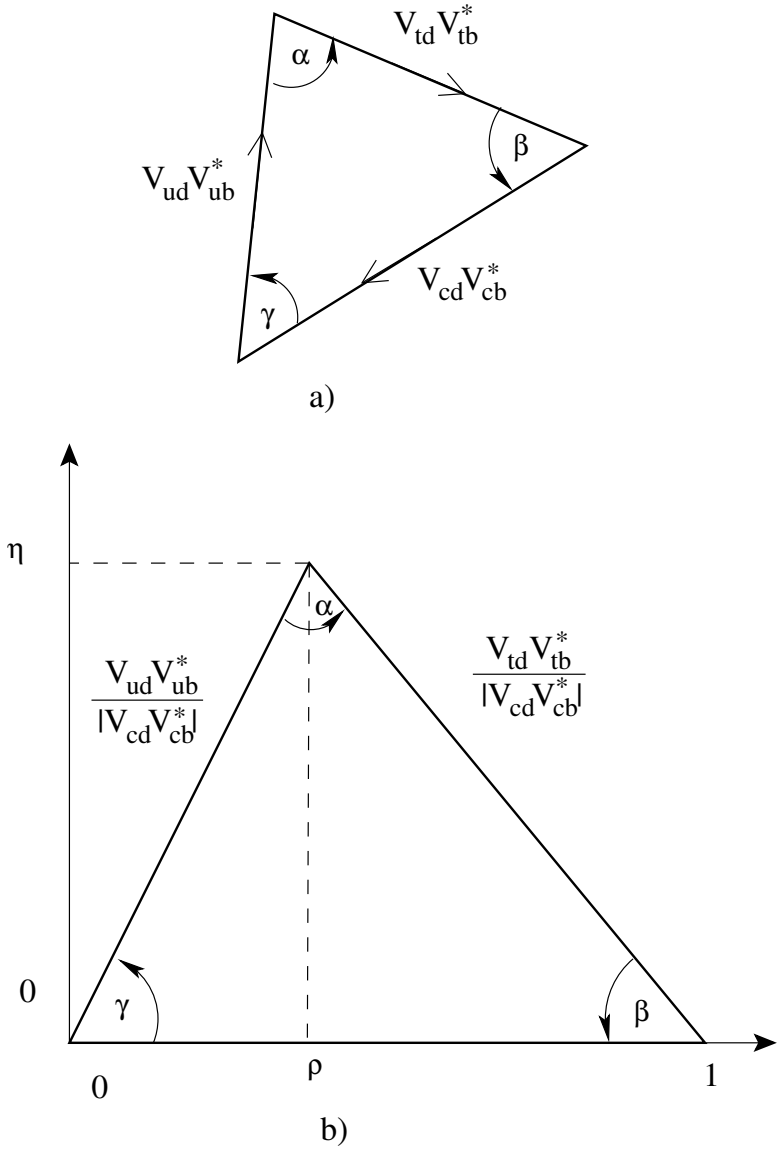

Figure 1.5: a) The Unitarity Triangle (1.32). b) The rescaled Unitarity Triangle with all sides divided by $V_{cd}V_{cb}^*$.

which can be expressed in terms of $\bar{\rho}$ and $\bar{\eta}$

$$\sin 2\alpha = \frac{2\overline{\eta}[\overline{\eta}^2 + \overline{\rho}(\overline{\rho}-1)]}{[\overline{\eta}^2 + (1-\overline{\rho})^2][\overline{\eta}^2 + \overline{\rho}^2]}\,, \quad \sin 2\beta = \frac{2\overline{\eta}(1-\overline{\rho})}{\overline{\eta}^2 + (1-\overline{\rho})^2}\,. \tag{1.43}$$

The sides and angles of the triangle are physical quantities and can be measured by CP violating processes in various B decays.

1.5.2 *CP* Violation in *B* Decays

Three possible *CP* violation effects in the B decays are classified as

(1) "direct" *CP* violation in decay,

(2) "indirect" *CP* violation in mixing,*

(3) *CP* violation in the interference between decays with and without mixing.

Direct *CP* violation in decay occurs when the amplitude for a decay and its *CP* conjugate process have different magnitudes, which could happen in both charged and neutral decays; indirect *CP* violation in mixing occurs when the two neutral mass eigenstates are not *CP* eigenstates; *CP* violation in the interference between mixing and decay occurs when the amplitude for a decay and its *CP* conjugate process have different phases, which happens to decays with final states common to B^0 and $\overline{B}^0$.

1.5.2.1 *CP* Violation in Decay

Direct *CP* violation is defined as the asymmetry of b and $\bar{b}$ decay rates

$$\mathcal{A}_{CP} = \frac{\Gamma(B \to f) - \Gamma(\overline{B} \to \bar{f})}{\Gamma(B \to f) + \Gamma(\overline{B} \to \bar{f})}\,, \tag{1.44}$$

which is measurable for charged B decays because it is the only process that can give *CP* violating effects for charged decays, and then it is also called charge asymmetry,

$$\mathcal{A}_{ch} = \frac{\Gamma(B^- \to \bar{f}) - \Gamma(B^+ \to f)}{\Gamma(B^- \to \bar{f}) + \Gamma(B^+ \to f)}\,, \tag{1.45}$$

Though direct *CP* violation can also occur for neutral B decays, it competes with the other two types of *CP* violating effects. For any final state f, each contribution to the total decay amplitude A_f has three parts: its magnitude A_i, its weak-phase term $e^{i\phi_i}$, and its strong-phase term $e^{i\delta_i}$. The weak phases occur only in the CKM matrix

* See Sec. 1.5.2.2 for the meaning of mixing here

and have opposite signs for A_f and $\overline{A}_{\overline{f}}$, while the strong phases do not violate CP and appear with the same signs for both A_f and $\overline{A}_{\overline{f}}$. So the total amplitude $A(B \to f)$ and $\overline{A}(\overline{B} \to \bar{f})$ are:

$$A_f = \sum_i A_i e^{i(\delta_i+\phi_i)}\,, \quad \overline{A}_{\overline{f}} = \sum_i A_i e^{i(\delta_i-\phi_i)}\,, \tag{1.46}$$

where we omit the overall phase difference between A_f and $\overline{A}_{\overline{f}}$. Then the convention-independent quantity is

$$\left|\frac{\overline{A}_{\overline{f}}}{A_f}\right| = \left|\frac{\sum_i A_i e^{i(\delta_i-\phi_i)}}{\sum_i A_i e^{i(\delta_i+\phi_i)}}\right|. \tag{1.47}$$

When CP is conserved, the weak phases ϕ_i are all equal, and thus $|\overline{A}_{\overline{f}}/A_f| = 1$; then

$$\left|\frac{\overline{A}_{\overline{f}}}{A_f}\right| \neq 1 \quad \Longrightarrow \quad CP \text{ violation.} \tag{1.48}$$

The difference between the magnitudes $|A|$ and $|\overline{A}|$ can be written as

$$|A|^2 - |\overline{A}|^2 = -2\sum_{i,j} A_i A_j \sin(\phi_i - \phi_j)\sin(\delta_i - \delta_j)\,, \tag{1.49}$$

and we can see the CP violating effects arise from the interference among different phase terms of the contributions to the total amplitude. $\mathcal{A}_{CP}$ (1.44) can be expressed in terms of the decay amplitude

$$\mathcal{A}_{CP} = \frac{1 - |\overline{A}/A|^2}{1 + |\overline{A}/A|^2}\,. \tag{1.50}$$

The only direct CP violation effect observed was in the K system [18, 19] before the advent of PEP-II and KEKB.[†] Substantial direct CP violation in B decays can arise from the interference of penguin (P) and tree (T) diagrams (see Sec. 1.6) [25]. In the limit of $T \ll P$, we have:

$$\mathcal{A}_{CP} \simeq 2\left|\frac{T}{P}\right| \sin\Delta\phi \, \sin\Delta\delta\,, \tag{1.51}$$

so sizable effects of ~ 0.1 could be expected if $\Delta\phi$ and $\Delta\delta$ are not too small. However, calculation of such asymmetries is complicated by the presence of magnitude and

[†] The direct CP violation evidence in B decays is from $B^0 \to K^+\pi^-$ by *BABAR* [20, 21], and from $B^0 \to \pi^+\pi^-$ by Belle [22].

strong phases involving long distance strong interactions and cannot be done from first principles. The calculations generally contain two parts: First, the operator product expansion and QCD perturbation theory are used to write any underlying quark process as a sum of local quark operators with well-determined coefficients; second, the matrix elements of the operators between the initial and final hadron states must be calculated. We will discuss these theoretical approaches further in section 1.6 because of their importance in understanding the rare B decays. Calculations based on effective theory and factorization predict asymmetries in rare B meson decays of about $\pm 10\%$ [26]. These expectations could be enhanced by larger phases due to FSI, for example, or due to new physics beyond the Standard Model.

1.5.2.2 *CP* Violation in Mixing

In the neutral B system, the Hamiltonian eigenstates with definite mass and lifetime are not the flavor eigenstates, namely, $B^0 = \bar{b}d$ and $\overline{B}^0 = b\bar{d}$. The flavor eigenstates have definite quark content and are useful to understand particle production and decay. Once B^0 or $\overline{B}^0$ mesons are produced, they are mixing together through a box diagram with two W exchange (Figure 1.6). This process is usually called B^0– $\overline{B}^0$ oscillation and was first observed by the ARGUS [23] and UA1 [24] collaborations.

The Hamiltonian H describing the neutral B meson system can be written as

$$H = M - \frac{i}{2}\Gamma\,, \tag{1.52}$$

where M and Γ are 2×2 Hermitian matrices

$$\begin{pmatrix} H_{11} & H_{12} \\ H_{21} & H_{22} \end{pmatrix} = \begin{pmatrix} M & M_{12} \\ M_{12}^* & M \end{pmatrix} - \frac{i}{2}\begin{pmatrix} \Gamma & \Gamma_{12} \\ \Gamma_{12}^* & \Gamma \end{pmatrix}\,, \tag{1.53}$$

where $H_{11} = H_{22}$. The off-diagonal terms, M_{12} and Γ_{12} are due to second order B^0–$\overline{B}^0$ transition via on-shell intermediate states, and are particularly important in the discussion of *CP* violation. The Schrödinger equation of a linear combination of the

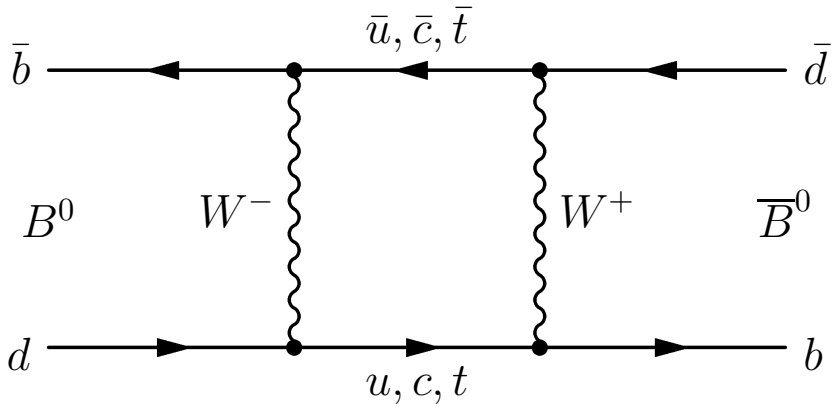

Figure 1.6: Feynman diagram describing B^0 – $\overline{B}^0$ mixing.

neutral B flavor eigenstates,

$$a|B^0\rangle + b|\overline{B}^0\rangle\,, \tag{1.54}$$

can then be written as

$$i\frac{d}{dt}\begin{pmatrix} a \\ b \end{pmatrix} = H\begin{pmatrix} a \\ b \end{pmatrix} = (M - \frac{i}{2}\Gamma)\begin{pmatrix} a \\ b \end{pmatrix}. \tag{1.55}$$

The two mass eigenstates, B_L (for light B) and B_H (for heavy B) can be expressed as

$$|B_L\rangle = p|B^0\rangle + q|\overline{B}^0\rangle\,, \tag{1.56}$$

$$|B_H\rangle = p|B^0\rangle - q|\overline{B}^0\rangle\,, \tag{1.57}$$

where the complex coefficients p and q satisfy

$$|q|^2 + |p|^2 = 1\,, \tag{1.58}$$

and we can then express B^0 and $\overline{B}^0$ in terms of B_L and B_H

$$|B^0\rangle = \frac{1}{2p}(|B_L\rangle + |B_H\rangle)\,, \tag{1.59}$$

$$|\overline{B}^0\rangle = \frac{1}{2q}(|B_L\rangle - |B_H\rangle)\,. \tag{1.60}$$

The mass and width of the light (heavy) B are M_L (M_H) and Γ_L (Γ_H), respectively, so

the two mass eigenstates evolve in time as

$$|B_L(t)\rangle = e^{-iM_L t} e^{-\Gamma_L t} |B_L(t=0)\rangle \,, \tag{1.61}$$

$$|B_H(t)\rangle = e^{-iM_H t} e^{-\Gamma_H t} |B_H(t=0)\rangle \,, \tag{1.62}$$

and we define the mass difference Δm_d and width difference $\Delta\Gamma$ as

$$\Delta m_d \equiv M_H - M_L \,, \quad \Delta\Gamma \equiv \Gamma_H - \Gamma_L \,, \tag{1.63}$$

then we get by solving the Schrödinger equation of the system (1.55)

$$(\Delta m_d)^2 - \frac{1}{4}(\Delta\Gamma)^2 = 4(|M_{12}|^2 - \frac{1}{4}|\Gamma_{12}|^2) \,, \tag{1.64}$$

$$\Delta m_d \Delta\Gamma = 4\, \Re\mathrm{e}(M_{12}\Gamma_{12}^*), \tag{1.65}$$

$$\frac{q}{p} = -\frac{\Delta m_d - \frac{i}{2}\Delta\Gamma}{2(M_{12} - \frac{i}{2}\Gamma_{12})} = -\frac{2(M_{12}^* - \frac{i}{2}\Gamma_{12}^*)}{\Delta m_d - \frac{i}{2}\Delta\Gamma} \,, \tag{1.66}$$

The magnitude of (1.66) is independent of phase conventions and is physically meaningful

$$\left|\frac{q}{p}\right|^2 = \left|\frac{M_{12}^* - \frac{i}{2}\Gamma_{12}^*}{M_{12} - \frac{i}{2}\Gamma_{12}}\right| . \tag{1.67}$$

When *CP* is conserved, the mass eigenstates are *CP* eigenstates, and the relative phase between M_{12} and Γ_{12} vanishes, which gives $|q/p| = 1$, and then (1.67) implies

$$\left|\frac{q}{p}\right| \neq 1 \quad \Longrightarrow \quad CP \text{ violation.} \tag{1.68}$$

This type of *CP* violation is called *CP* violation in mixing and is often referred to as "indirect" *CP* violation. It has been observed in the neutral K system through semileptonic decays. For neutral B system, the indirect *CP* violating effect could be measured through time-dependent asymmetries in semileptonic decays,

$$a_{\mathrm{sl}} = \frac{\Gamma(\overline{B}^0(t) \to l^+\mu X) - \Gamma(B^0(t) \to l^-\mu X)}{\Gamma(\overline{B}^0(t) \to l^+\mu X) + \Gamma(B^0(t) \to l^-\mu X)} \,, \tag{1.69}$$

which can be expressed in terms of $|q/p|$,

$$a_{\mathrm{sl}} = \frac{1 - |q/p|^4}{1 + |q/p|^4} \,. \tag{1.70}$$

The expected CP violation in mixing of neutral B decays is small, $\mathcal{O}(10^{-}2)$, since q/p is close to unity, and it is also difficult to relate such asymmetries to the CKM parameters because of theoretical uncertainties in the calculation of Γ_{12} and M_{12}.

1.5.2.3 *CP* Violation in the Interference between Mixing and Decay

The third type of CP violation occurs for neutral B decays into final CP eigenstates, f_{CP} [27–29], which are accessible for both B^0 and $\overline{B}^0$, and CP violation is from the interference of the two amplitudes $B^0 \to f_{CP}$ and $B^0 \to \overline{B}^0 \to f_{CP}$ (see Figure 1.7). The time-dependent asymmetry may be observed by comparing decays into final CP eigenstates of a time-evolving neutral B state that begins as B^0 to those of the state that begins as a $\overline{B}^0$ [30]:

$$\mathcal{A}_{CP}(t) = \frac{\Gamma(B^0(t) \to f_{CP}) - \Gamma(\overline{B}^0(t) \to f_{CP})}{\Gamma(B^0(t) \to f_{CP}) + \Gamma(\overline{B}^0(t) \to f_{CP})} \,. \tag{1.71}$$

As (1.47) for CP violation in decay, and (1.67) for CP violation in mixing, the convention independent quantity here is defined by

$$\lambda = \frac{q}{p}\frac{\overline{A}_f}{A_f} \,, \tag{1.72}$$

which has physical significance associated with this type of CP violation. The equations

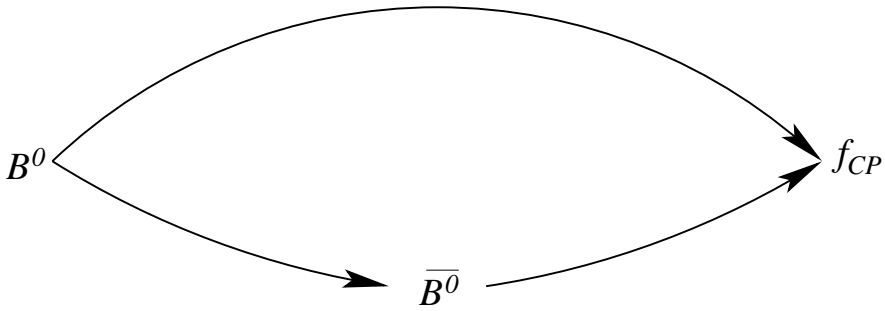

Figure 1.7: CP violation in the interference between decays with and without mixing. B^0 meson can directly decay into CP eigenstate f_{CP}, or first becomes $\overline{B}^0$ which then decays into f_{CP}. The same thing happens to $\overline{B}^0$.

(1.64), (1.65), and (1.66) can be simplified into

$$\Delta m_d = 2|M_{12}|\,, \quad \Delta\Gamma = 2\,\Re\mathrm{e}(M_{12}\Gamma_{12}^*)/|M_{12}|\,, \tag{1.73}$$

$$q/p = -|M_{12}|/M_{12}\,, \tag{1.74}$$

considering that $\Delta\Gamma \ll \Gamma$ [31]

$$\Delta\Gamma/\Gamma = \mathcal{O}(10^{-2})\,, \tag{1.75}$$

and Δm_d has been measured [12],

$$x_d \equiv \Delta m_d/\Gamma = 0.771 \pm 0.012\,, \tag{1.76}$$

and we can get

$$\Delta\Gamma \ll \Delta m_d\,. \tag{1.77}$$

We are interested in the time evolution of neutral B state, $|B^0_{\rm phys}\rangle$, which is pure B^0 when created at time $t = 0$, and similarly for $|\overline{B}^0_{\rm phys}\rangle$, pure $\overline{B}^0$ at $t = 0$. From (1.59) and (1.60) we get

$$|B^0_{\rm phys}(t)\rangle = g_+(t)|B^0\rangle + (q/p)g_-(t)|\overline{B}^0\rangle\,, \tag{1.78}$$

$$|\overline{B}^0_{\rm phys}(t)\rangle = (p/q)g_-(t)|B^0\rangle + g_+(t)|\overline{B}^0\rangle\,, \tag{1.79}$$

where

$$g_+(t) = e^{-iMt}e^{-\Gamma t/2}\cos(\Delta m_d\, t/2)\,, \tag{1.80}$$

$$g_-(t) = e^{-iMt}e^{-\Gamma t/2} i\sin(\Delta m_d\, t/2)\,, \tag{1.81}$$

and $M = \frac{1}{2}(M_H + M_L)$.

In the *BABAR* experiment, $B^0\overline{B}^0$ pairs from $\Upsilon(4S)$ are produced in a coherent $L = 1$ state, which means that while each of the two particles evolves in time as described above, there is exactly one B^0 and one $\overline{B}^0$ present, at any given time, before one of them decays. Being such, we can 'tag' the flavor of B decaying into final CP eigenstate, f_{CP},

using the other B, $B_{\rm tag}$, which decays into a tagging mode, that is a mode identifying its b-flavor, at time $t_{\rm tag}$, then we know at time $t_{\rm tag}$, the flavor of the B to f_{CP} is opposite to $B_{\rm tag}$. The time-dependent rate for tagging $\overline{B}^0$ to decay at $t = t_{\rm tag}$ and B^0 to decay to f_{CP} at $t = t_{f_{CP}}$ is given by

$$R(t_{\rm tag}, t_{f_{CP}}) = Ce^{-\Gamma(t_{\rm tag}+t_{f_{CP}})}|\overline{A}_{\rm tag}|^2|A_{f_{CP}}|^2\{1+|\lambda_{f_{CP}}|^2$$
$$+\cos[\Delta m_d(t_{f_{CP}}-t_{\rm tag})](1-|\lambda_{f_{CP}}|^2) - 2\sin[\Delta m_d(t_{f_{CP}}-t_{\rm tag})]\,\Im{\rm m}(\lambda_{f_{CP}})\}\,, \qquad (1.82)$$

where C is an overall normalization factor, $\overline{A}_{\rm tag}$ is the amplitude for $\overline{B}^0$ to decay to tagging mode, $A_{f_{CP}}$ is the amplitude for B^0 to decay to f_{CP}, and

$$\lambda_{f_{CP}} \equiv \frac{q}{p}\frac{\overline{A}_{f_{CP}}}{A_{f_{CP}}} = \eta_{f_{CP}}\frac{q}{p}\frac{\overline{A}_{\bar{f}_{CP}}}{A_{f_{CP}}}\,, \qquad (1.83)$$

where $\eta_{f_{CP}}$ is the CP eigenvalue of the state f_{CP} and

$$\overline{A}_{f_{CP}} = \eta_{f_{CP}}\overline{A}_{\bar{f}_{CP}}\,. \qquad (1.84)$$

A similar equation to (1.82), with reversed signs for both cosine and sine terms, applies for the case where B^0 is the tagging B identifying the second B as $\overline{B}^0$ at time $t_{\rm tag}$. Then the time-dependent CP asymmetry (1.71) is

$$\mathcal{A}_{CP}(t) = \frac{1-|\lambda_{f_{CP}}|^2}{1+|\lambda_{f_{CP}}|^2}\cos\Delta m_d t - \frac{2\,\Im{\rm m}\lambda_{f_{CP}}}{1+|\lambda_{f_{CP}}|^2}\sin\Delta m_d t\,, \qquad (1.85)$$

where $t = t_{f_{CP}} - t_{\rm tag}$.

If CP is conserved, $|q/p| = 1$, $|\overline{A}_{\bar{f}_{CP}}/A_{f_{CP}}| = 1$, and furthermore, $\lambda_{f_{CP}} = \pm 1$, so, as we can see from (1.85)

$$\lambda_{f_{CP}} \neq \pm 1 \quad \Longrightarrow \quad CP \text{ violation.} \qquad (1.86)$$

Any CP violation from (1.48) or (1.68), leads to (1.86), even if there is no CP violation from the first two types, i.e., $|q/p| = 1$ and $|\overline{A}/A| = 1$, it is still possible to have CP violating effect, if

$$|\lambda_{f_{CP}}| = 1, \quad \Im{\rm m}\lambda_{f_{CP}} \neq 0\,. \qquad (1.87)$$

In such case, (1.85) can be reduced to

$$\mathcal{A}_{CP}(t) = -\,\Im\mathrm{m}\lambda_{f_{CP}}\sin(\Delta m_d t)\,. \tag{1.88}$$

We can define

$$A_f = Ae^{i(\phi_W+\delta)}\,, \tag{1.89}$$

$$\overline{A}_f = \eta_{f_{CP}}Ae^{i(-\phi_W+\delta)}\,, \tag{1.90}$$

$$q/p = e^{-2i\phi_M}\,, \tag{1.91}$$

and then

$$\lambda_{f_{CP}} = \eta_{f_{CP}}e^{-2i(\phi_W-\phi_M)},, \tag{1.92}$$

where we can further write (1.88) as

$$\mathcal{A}_{CP}(t) = \eta_{f_{CP}}\sin(2\phi_W - 2\phi_M)\sin(\Delta m_d t)\,. \tag{1.93}$$

Measurements of $\mathcal{A}_{CP}(t)$ from these 'clean' modes allow us to extract the angles of Unitarity Triangle. For example, in decay $B^0 \to \psi K^0_S$, $2\phi_W - 2\phi_M = 2\beta$, allows to measure $\sin 2\beta$; in decay $B^0 \to \pi^+\pi^-$, $2\phi_W - 2\phi_M = 2\alpha$, allows to measure $\sin 2\alpha$, though the "penguin pollution" (see Sec 1.6 below) makes the measurement more challenging. The richness of B decays provides many ways to determine the Unitarity Triangle parameters and the consistency of the results offers an important test of the Standard Model.

1.6 Hadronic B Decays

1.6.1 Decay Diagrams

The flavor-changing weak decays of b quark are mediated by $W^\pm$ boson as in the Lagrangian (1.25) describing the charged current interactions. Though there is no flavor-changing neutral current in the Standard Model, an 'effective' neutral current, introduced by loop, or "penguin" [32], transition, can have contributions to most decay channels [25]. The penguins are classified according to the roles of the quark in the loop,

because diagrams with different intermediate quarks may have both different strong phases and weak phases. The gluonic and electroweak penguins have the same phase structure. However, the electroweak penguins are usually suppressed of an order of 10^{-1} relative to the corresponding gluonic penguins because of smaller coupling constants [33], though they can be enhanced by a factor of M_t^2/M_Z^2 in certain cases. We show in Figure 1.8 the quark diagrams for tree, penguin and electroweak penguin contributions. The decay amplitude $A(q\bar{q}q')$ for $b \to q\bar{q}q'$ can be written as [10]

$$A(q\bar{q}q') = V_{tb}V_{tq'}^* P_{q'}^t + V_{cb}V_{cq'}^*(T_{c\bar{c}q'}\delta_{qc} + P_{q'}^c) + V_{ub}V_{uq'}^*(T_{u\bar{u}q'}\delta_{qu} + P_{q'}^u)\,, \tag{1.94}$$

where P and T denote contributions from tree-level and penguin diagrams, excluding the CKM elements.

The quark-level amplitude, however, can not be used directly to calculate the amplitude of B hadronic decays because of strong interactions between quarks in final states. They are still useful to classify the types of decays. We are particularly focusing on rare charmless hadronic B decays of $B \to h_1 h_2$, where h_1 and h_2 are light pseudoscalar (vector) mesons in the flavor U(3) nonet as in Table 1.3. These decays involve the tree diagrams and/or penguin diagrams, with both gluonic and electroweak penguin contributions [34]. The rare B decays with $|\Delta S| = 1$ involve a K or K^* meson in the final state and have Cabibbo suppressed tree-level $b \to u\bar{u}s$ and dominant gluonic penguin $b \to sg^*$ contributions, while decays with $|\Delta S| = 0$ are expected to have dominant contributions from Cabibbo favored tree-level $b \to u\bar{u}d$ diagram, and the penguin process $b \to dg^*$ is suppressed by V_{td}.

We show in Figure 1.9 the Feynman diagrams [35, 36]: (a) external tree – T, (b) internal tree – C, (c) internal penguin – P, (d) external penguin – P^C, (e) electroweak external penguin – P_{EW}, and (f) electroweak internal penguin – P_{EW}^C. In addition to the CKM suppression or CKM enhancement of different contributions, there are other rules to suppress a particular final state which is formed by the decay product of b

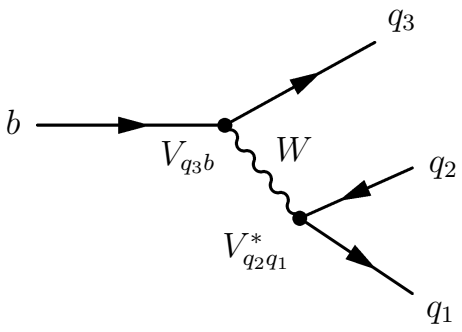

(a) Tree diagram

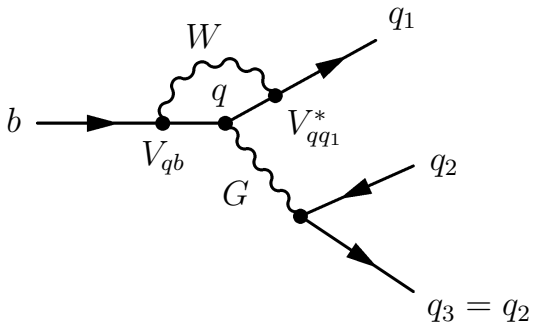

(b) QCD penguin diagram

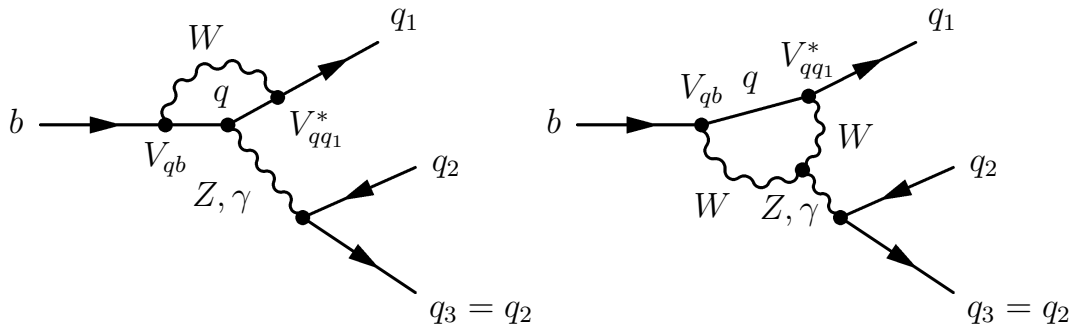

(c) EW penguin diagram

Figure 1.8: Quark diagrams describing b decays

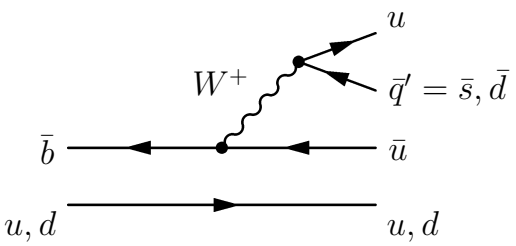

(a) External tree – T

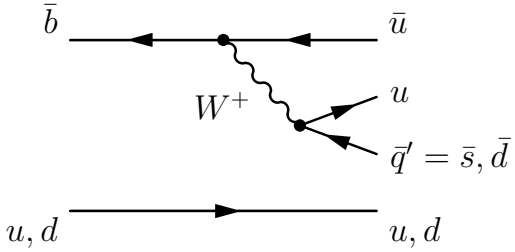

(b) Internal tree – C

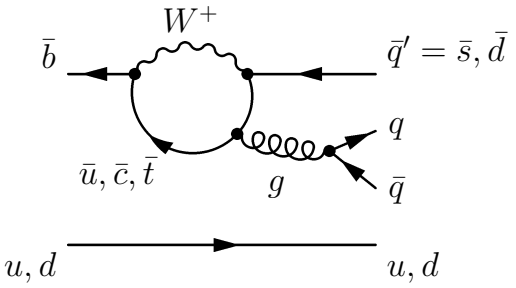

(c) Internal penguin – P

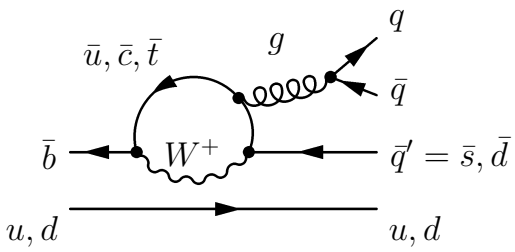

(d) External penguin – P^C

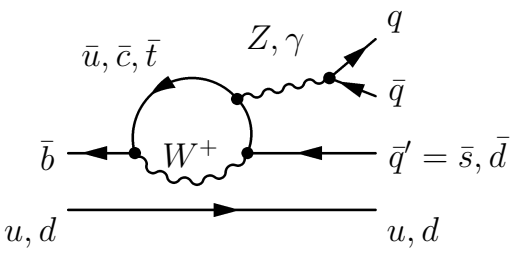

(e) EW external penguin – P_{EW}

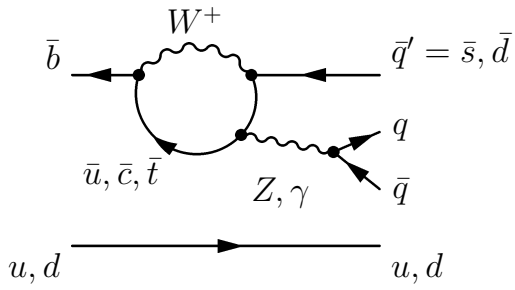

(f) EW internal penguin – P^C_{EW}

Figure 1.9: Feynman diagrams describing rare B decays; $q' = s, d$ for $|\Delta S| = 1, 0$, respectively, and $q = u, d, s$.

quark and the spectator quark in B meson. Specifically, transition in Figure 1.9(d) is color-suppressed because from the quark-antiquark pair from a color octet gluon it is hard to form a colorless meson, while the quark-antiquark pair from W or Z^0 is colorless, so it is enhanced for this pair to form a meson and it is suppressed for each of

them to form a meson with other quarks. Thus, diagrams in Figure 1.9(b) and 1.9(f) are color suppressed. As stated before, electroweak penguins are suppressed because of small coupling constants relative to gluonic penguins. Other sources of suppression may include delicate cancellations due to competition among different diagrams [34].

Particularly as the subject of this work, we will study decays $B \to h_1 h_2$, where h_1 is a vector meson, ω, and h_2 is another light meson, pseudoscalar (K^+, π^+, or K_S^0) or vector (K^{*+}, K^{*0}, ρ^+, or ρ^0). Because these charmless B decays involve couplings with small CKM mixing matrix elements, several amplitudes potentially contribute with similar strengths, as indicated in Figure 1.10. The B^+ modes receive contributions from external tree, color-suppressed tree, and penguin amplitudes, with the penguin strongly favored by CKM couplings for $B^+ \to \omega K^+$, $B^+ \to \omega K^{*+}$, and the external tree favored for $B^+ \to \omega \pi^+$, $B^+ \to \omega \rho^+$. For the B^0 modes there are no external tree contributions, and again for $B^0 \to \omega K^0$, $B^0 \to \omega K^{*0}$ the penguin is CKM-favored. For $B^0 \to \omega \rho^0$ the color-suppressed trees cancel, leaving only a Cabibbo suppressed penguin, which gives rather small expected branching fraction.

1.6.2 Low-Energy Effective Hamiltonians

Direct QCD calculations of hadronic decays give very limited information because of non-perturbation of strong interaction at long distance. One of the most efficient tools to do quantitative analysis of B decays is based on the low-energy effective Hamiltonian [37], which is constructed using the operator product expansion (OPE) with transition matrix elements of the form

$$\langle f|\mathcal{H}_{eff}|i\rangle \propto \sum_k \langle f|Q_k(\mu)|i\rangle C_k(\mu)\,, \tag{1.95}$$

where μ denotes a renormalization scale, $\langle f|Q_k(\mu)|i\rangle$ are the nonperturbative hadronic matrix elements describing the long-distance contributions to the decay amplitude, $C_k(\mu)$ are the perturbatively calculable Wilson coefficient functions describing the short-

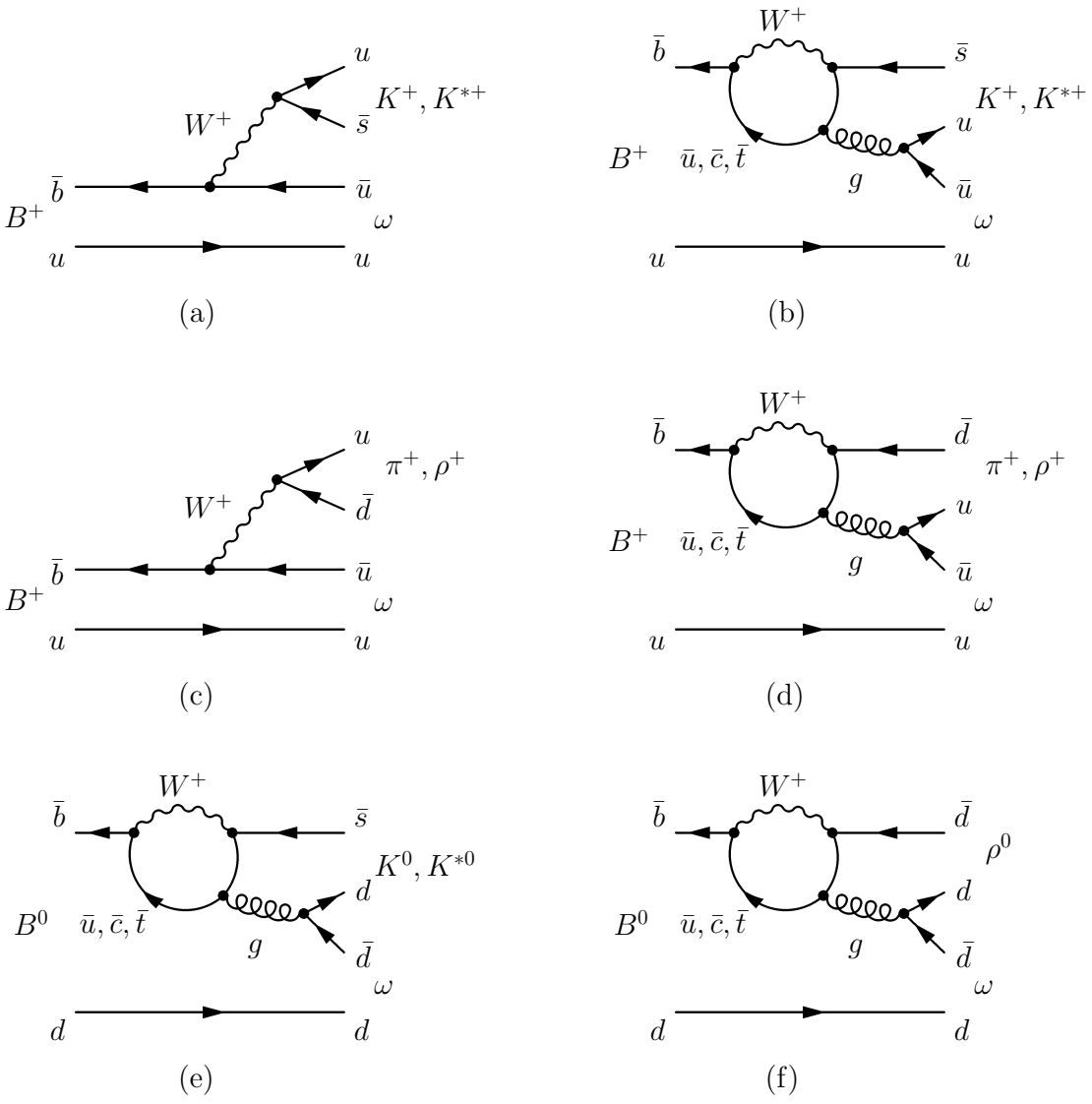

Figure 1.10: Feynman diagrams for decays $B \to \omega h_2$, where h_2 is another light meson, pseudoscalar (K^+, π^+, or K_s^0) or vector (K^{*+}, K^{*0}, ρ^+, or ρ^0).

distance contributions.

In the case where $|\Delta b| = 1$, $\Delta c = \Delta u = 0$, we can write the effective Hamiltonian as:

$$\mathcal{H}_{eff} = \frac{G_F}{\sqrt{2}} \left\{ V_{ub}V_{uq}^* \left[Q_1^q C_1(\mu) + Q_2^q C_2(\mu) \right] - V_{tb}V_{tq}^* \sum_{i=3}^{10} Q_i^q C_i(\mu) \right\} + \text{h.c.}\,, \tag{1.96}$$

where G_F is the Fermi constant, the renormalization scale μ is of $\mathcal{O}(m_b)$, q stands for d, s corresponding to $b \to d$ and $b \to s$ transitions, respectively, and Q_k^q are the Wilson operator product expansion [38], which can be classified into three categories:

(1) Current-current operators:

$$\begin{aligned} Q_1^q &= (\overline{u}_\alpha b_\alpha)_{V-A} (\overline{q}_\beta u_\beta)_{V-A} \\ Q_2^q &= (\overline{u}_\alpha b_\beta)_{V-A} (\overline{q}_\beta u_\alpha)_{V-A} \end{aligned} \tag{1.97}$$

(2) QCD penguin operators:

$$\begin{aligned} Q_3^q &= (\overline{q}_\alpha b_\alpha)_{V-A} \sum_{q'} (\overline{q}'_\beta q'_\beta)_{V-A} \\ Q_4^q &= (\overline{q}_\alpha b_\beta)_{V-A} \sum_{q'} (\overline{q}'_\beta q'_\alpha)_{V-A} \\ Q_5^q &= (\overline{q}_\alpha b_\alpha)_{V-A} \sum_{q'} (\overline{q}'_\beta q'_\beta)_{V+A} \\ Q_6^q &= (\overline{q}_\alpha b_\beta)_{V-A} \sum_{q'} (\overline{q}'_\beta q'_\alpha)_{V+A} \end{aligned} \tag{1.98}$$

(3) EW penguin operators:

$$\begin{aligned} Q_7^q &= \frac{3}{2} (\overline{q}_\alpha b_\alpha)_{V-A} \sum_{q'} e_{q'} (\overline{q}'_\beta q'_\beta)_{V+A} \\ Q_8^q &= \frac{3}{2} (\overline{q}_\alpha b_\beta)_{V-A} \sum_{q'} e_{q'} (\overline{q}'_\beta q'_\alpha)_{V+A} \\ Q_9^q &= \frac{3}{2} (\overline{q}_\alpha b_\alpha)_{V-A} \sum_{q'} e_{q'} (\overline{q}'_\beta q'_\beta)_{V-A} \\ Q_{10}^q &= \frac{3}{2} (\overline{q}_\alpha b_\beta)_{V-A} \sum_{q'} e_{q'} (\overline{q}'_\beta q'_\alpha)_{V-A} \end{aligned} \tag{1.99}$$

where $(\overline{q}_1 q_2)_{V\pm A} \equiv \overline{q}_1 \gamma_\mu (1 \pm \gamma_5) q_2$, α and β are SU(3) color indices, q' runs over the quark flavors to the scale $\mu = \mathcal{O}(m_b)$, i.e., $q' \in \{u, d, c, s, b\}$, and $e_{q'}$ is the electrical charge of q'.

Since the hadronic matrix elements $\langle h_1 h_2 | Q_k^q | B \rangle$ are too complicated to be calculated in lattice-QCD methods, the approach employed here is based on factorization [26, 34, 39–41], where with the factorization Ansatz, the matrix element can be factorized into the product of two factors $\langle h_1 | J_1 | B \rangle \langle h_2 | J_2 | 0 \rangle$, where J_1 and J_2 are current operators determined by form factors and decay constants, which are theoretically more tractable and can be calculated in well-defined theoretical frameworks, such as lattice-QCD [42], QCD sum rules [43], and potential model [44]. One can then make quantitative predictions, for example, to the decay rates of $B \to h_1 h_2$, in this framework, with guidance from experiments as the input parameters. The theoretical predictions have many uncertainties: CKM matrix elements, quark masses, form factors, etc., so they are usually given as ranges. We summarize predictions [45–50] and previous measurements [51–53] for modes studied here in Table 1.7.

The factorization procedure is justified by the phenomenon of color-transparency [54], that a pair of energetic quarks in a color-singlet state effectively decouples from soft gluons. For the decays $B \to h_1 h_2$, with $E_{h_1,h_2} \sim M_B/2$, the energy of the quarks leaving the interaction is large, so the (soft) final state interactions (FSI) due to gluon exchange are small and factorization is a good approximation.

Table 1.7: Theoretical predictions and previous measurements of branching fractions for the modes studied in this work. The theoretical predictions are from Ref. 45–50, and the previous measurements are from Ref. 51–53.

	Mode	model	CLEO	Belle
		$\mathcal{B}(\times 10^{-6})$		
$B \to PV$	$B^+ \to \omega\pi^+$	1 – 7	$11.3^{+3.3}_{-2.9} \pm 1.4$	$4.2^{+2.0}_{-1.8} \pm 0.5 < 8.1$
	$B^+ \to \omega K^+$	1 – 7	$3.2^{+2.4}_{-1.9} \pm 0.8 < 7.9$	$9.2^{+2.6}_{-2.3} \pm 1.0$
	$B^0 \to \omega K^0$	1 – 6	$10.0^{+5.4}_{-4.2} \pm 1.4 < 21$	—
$B \to VV$	$B^+ \to \omega\rho^+$	10 – 25	< 61	—
	$B^0 \to \omega\rho^0$	0.4 – 0.6	< 11	—
	$B^+ \to \omega K^{*+}$	0.4 – 15	< 87	—
	$B^0 \to \omega K^{*0}$	2 – 8	< 23	—

Chapter 2

The *BABAR* Experiment

2.1 Introduction

This chapter is a short overview of the PEP-II B Factory and the *BABAR* detector, where this work has been done. Section 2.2 summarizes the main characteristics of the PEP-II collider while a brief overview of the *BABAR* detector and its components is given in Section 2.3. A more detailed description of the PEP-II collider and the *BABAR* detector can be found in Ref. 55–57.

The primary goal in the design of the *BABAR* experiment is the study of *CP* violation in the decays of neutral B mesons. Other goals include a sensitive measurement of the CKM matrix, V_{ub}, rare B decays, other B-physics, the physics of charm and τ leptons, two-photon physics, etc. The PEP-II B Factory was designed to deliver the B mesons to the *BABAR* detector in order to achieve these goals.

2.2 The PEP-II B Factory

To measure the time-dependent *CP* asymmetry, one needs to measure the interval between the two B meson decays, $t = t_{f_{CP}} - t_{\text{tag}}$ (see Eq. 1.85 on page 29), as in most cases, the asymmetry cancels to zero when integrated from $t = 0$ to ∞. The problem is solved in the asymmetric design of the PEP-II storage rings with beams of unequal energy.

The PEP-II B Factory is an asymmetric e^+e^- collider operating at Stanford Linear Accelerator Center (SLAC). It has two separate rings. One is the e^- High

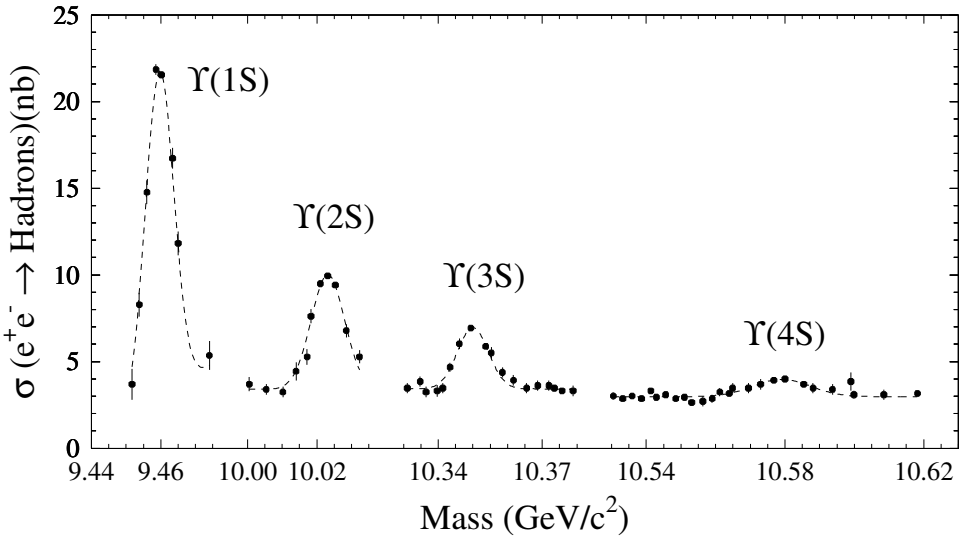

Figure 2.1: The e^+e^- hadronic cross-section at the Υ resonances. The mass of the $\Upsilon(4S)$ is just above the $B\overline{B}$ production threshold.

Energy Ring (HER) of $E_{e^-} = 9.0\,\text{GeV}$, the other is the e^+ Low Energy Ring (LER) of $E_{e^+} = 3.1\,\text{GeV}$, which results in the center-of-mass energy being at the $\Upsilon(4S)$ resonance, $10.580\,\text{GeV}$, with a boost of $\langle\beta\gamma\rangle = 0.56$ to the B mesons in the laboratory frame. Since the $B\overline{B}$ pairs are produced almost at rest in the center-of-mass frame, the boost is crucial in separating the B decay vertices in order to measure the relative decay time of the B mesons. The time interval Δt can then be written as

$$\Delta t \approx \frac{\Delta z}{\langle\beta\gamma\rangle c}\,, \tag{2.1}$$

where Δz is the separation between the two decay vertices. The boost results in an average $\Delta z \approx 250\,\mu\text{m}$, which can be measured with good precision.

The e^+e^- collider operating at the $\Upsilon(4S)$ resonance provides the best source of B mesons [58]. We show in Figure 2.1 the hadronic cross-section structure of e^+e^- at the Υ resonances. The $\Upsilon(4S)$ resonance decays almost exclusively into $B\overline{B}$ pairs with equal numbers of $B^0\overline{B}^0$ and B^+B^- pairs, which reduces the possibility of combinatorial backgrounds from any other decays of $\Upsilon(4S)$. Furthermore, B meson system from $\Upsilon(4S)$

Table 2.1: The production cross-sections of e^+e^- at $\sqrt{s} = 10.58\,\text{GeV}$. The cross-section is the effective cross-section including the detector acceptance effects.

$e^+e^- \to$	Cross-section (nb)
$b\bar{b}$	1.05
$c\bar{c}$	1.30
$s\bar{s}$	0.35
$u\bar{u}$	1.39
$d\bar{d}$	0.35
$\tau^+\tau^-$	0.94
$\mu^+\mu^-$	1.16
e^+e^-	~ 40

has several kinematic constraints, which can also help to suppress backgrounds. The total hadronic cross-section of e^+e^- collision at 10.58 GeV is about 3.8 nb while the cross-section of $e^+e^- \to \Upsilon(4S)$ is about 1.05 nb, which means a high signal-to-background ratio of $\sigma_{b\bar{b}}/\sigma_{\text{tot}} \simeq 0.28$ (see Table 2.1). Events of $e^+e^- \to q\bar{q}$ with $q = u, d, s, c$ are commonly referred to as continuum background, and are the major combinatorial background for the charmless (quasi-)two-body B decays studied in this work. In order to study this source of background, about 10% of the total data are taken at a center-of-mass energy 40 MeV below the $\Upsilon(4S)$ peak (off-peak, or off-resonance, data, while data taken on the $\Upsilon(4S)$ peak are called on-peak, or on-resonance, data), where no $B\overline{B}$ pairs can be produced. The QED processes $e^+e^- \to e^+e^-$ (Bhabha scattering), $\mu^+\mu^-$, $\tau^+\tau^-$ can be used to monitor the luminosity and calibrate detector, while the reaction $e^+e^- \to e^+e^-\gamma\gamma \to e^+e^-X$, where two virtual photons combine to give the final state X, is important to the study of final states with $C = +1$.

At the PEP-II B Factory, the electron and positron beams are produced from the SLAC Linac, a linear accelerator 3 km long, and are injected into the two separate rings, which are installed on top of each other in a 2.2 km tunnel (see Figure 2.2). The e^- and e^+ bunches collide head-on in a single Interaction Point (IP) and then are separated

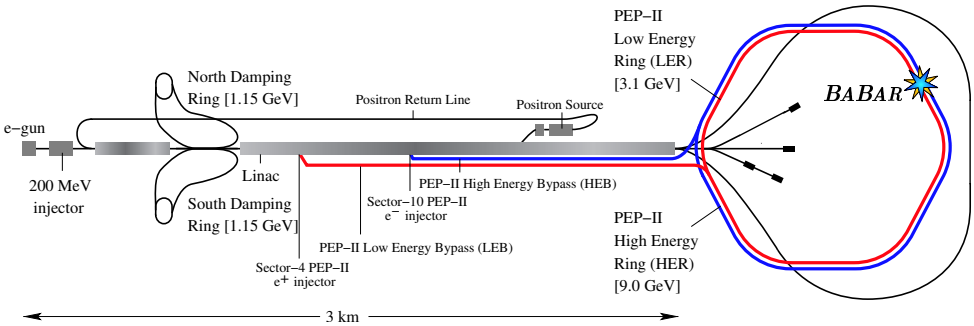

Figure 2.2: The Linac, PEP-II storage rings, and the location of the *BABAR* detector.

in the horizontal plane by permanent dipole magnets (B1), located at ± 21 cm on both sides of the IP, followed by a series of focusing quadrupoles, Q1-Q5 (see Figure 2.3). Q1 quadrupoles are permanent magnets placed ± 90 cm from the IP, and within the *BABAR* solenoid. Q2, Q4 and Q5 are standard iron magnets located outside of the solenoid. The interaction region is enclosed by a water cooled beam pipe of 27.9 mm outer radius. The beam pipe, the permanent magnets and the silicon vertex tracker are enclosed in a 4.5 m long support tube spanning the interaction region. The collision axis is offset from the z-axis of the *BABAR* detector by about 20 mrad in the horizontal plane in order to minimize the perturbation of the beams by the solenoid field [59].

The parameters of the PEP-II storage rings are presented in Table 2.2 [60]. PEP-II has surpassed its design goals both in terms of the instantaneous and the integrated daily luminosity. The present peak luminosity as of June 2004 is over three times the design and the best integrated luminosity per month is $16\,\mathrm{fb}^{-1}$ which is five times the design. The total integrated luminosity delivered by PEP-II and recorded on *BABAR* until May 2004 is shown in Figure 2.4.

The relative luminosity is monitored by PEP-II through the measurement of the radiative Bhabha scattering. The absolute luminosity is measured by *BABAR* offline, from other QED processes, primarily e^+e^- and $\mu^+\mu^-$ production. For a data sample of $1\,\mathrm{fb}^{-1}$, the statistical uncertainty is less than 1%, and the relative changes of luminosity

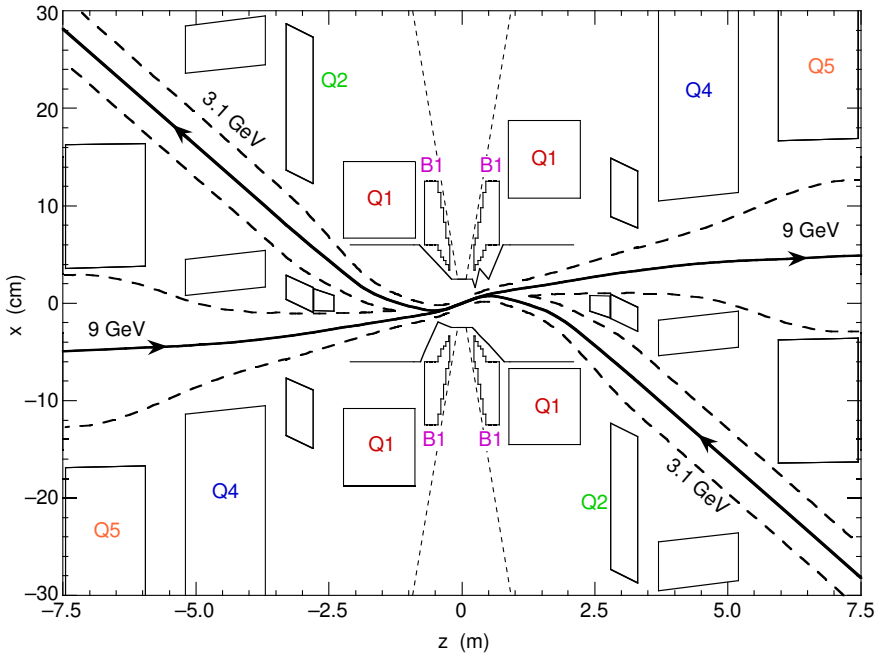

Figure 2.3: A Schematic view of the interaction region in the horizontal plane of the accelerator (z axis in m, x axis in cm). The separation dipoles B1 and focusing quadrupoles Q1-Q5 are also shown.

Table 2.2: The design and typical values of the PEP-II beam parameters as of June 2004. HER and LER refer to the high energy e^- and low energy e^+ ring, respectively. σ_{Lx}, σ_{Ly}, and σ_{Lz} are the horizontal, vertical, and longitudinal rms size of the luminous region.

Parameters	Design	Present
Energy HER/LER (GeV)	9.0/3.1	9.0/3.1
Current HER/LER (A)	0.75/2.15	1.55/2.45
# of bunches	1658	1588
σ_{Lx} (μm)	222	170
σ_{Ly} (μm)	6.7	7.2
σ_{Lz} (mm)	11	13
Lumin. ($10^{33}\,\mathrm{cm}^{-2}\mathrm{s}^{-1}$)	3	9.21
Int.Lumin. (fb^{-1}/mon.)	3.3	16.02
Tot.Int.Lumin. (fb^{-1})	100 (for CPV)	240

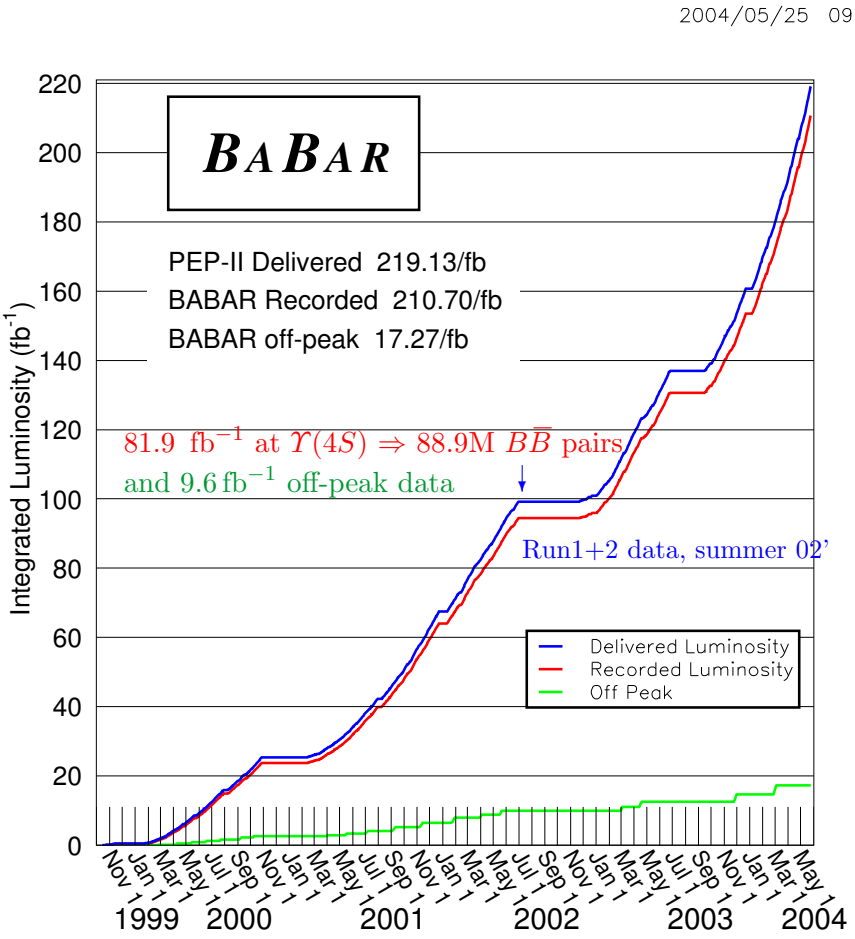

Figure 2.4: The integrated luminosity delivered by PEP-II B Factory and recorded by *BABAR* detector between October 1999 and May 2004. The arrow indicates the data sample used for this work.

is less than 0.5%. The absolute luminosity has an estimated systematic error of about 1.5% mainly due to Monte Carlo generator and detector simulation.

The beam energies are necessary input to calculate two important kinematic variables used to separate signal from combinatorial background (see Sec. 3.5.1 on page 118). The mean energies of the two beams are computed from the total magnetic bending strength and the average deviations of the accelerating frequencies from their central values during operation. While the systematic uncertainty in the calculation of the absolute beam energies is estimated to be 5–10 MeV, the relative energy setting for each beam is accurate and stable to about 1 MeV. The rms energy spreads of the LER and

HER beams are 2.3 MeV and 5.5 MeV, respectively. *BABAR* also monitors the ratio of $B\overline{B}$ events to lepton pairs and uses online fully reconstructed B events to ensure the data are recorded close to the peak of $\Upsilon(4S)$ resonance. An absolute error of 1.1 MeV to the c.m. energy is obtained for an integrated luminosity of $1\,\mathrm{fb}^{-1}$.

The parameters of the luminous region (see Table 2.2) are crucial for the time-dependent analyses and their values are monitored continuously both online and offline mainly using two-track events. The uncertainties in the average beam position are of the order of a few μm in the transverse plane and $100\,\mu$m along the collision axis. Run-by-run variations of the beam position are comparable to these measurement uncertainties, indicating the beams are stable over a period of a typical run.

The main sources of steady-state beam background are synchrotron radiation in the vicinity of the interaction region; interactions between the beam particles and the residual gas in either ring; and electromagnetic showers generated by beam-beam collisions, in the order of increasing importance. The beam backgrounds can cause high occupancy of the detector and may cause significant radiation damage to the detector over time. Various methods are needed to monitor the backgrounds and protect the detector against the radiation.

The layout of the interaction region and the synchrotron-radiation masks have been designed such that most of the radiation is channeled to a distant dump, and the residual background is relatively low without significant importance. The background from beam-gas scattering can be improved significantly with time of operation because of the scrubbing effects of the vacuum pipe by the synchrotron radiation. Nevertheless, beam-gas scattering remains the primary source of radiation damage in the SVT and dominant source of background in all sub-detectors, except for the DIRC. The background of electromagnetic showers generated by beam-beam collisions increases proportionally with the instantaneous luminosity and is the dominant background in the DIRC.

A system has been developed to monitor the instantaneous and integrated radiation doses, and to either abort the beams or to halt or limit the rate of injection, if conditions become critical, in order to protect the *BABAR* detector. In addition, DCH and IFR currents, DIRC and IFR counting rates, are also monitored; abnormally high rates signal critical conditions.

2.3 The *BABAR* Detector

The *BABAR* detector has been designed to operate optimally on the PEP-II B Factory in order to achieve its physics goals.

For a large and uniform acceptance to the production on an asymmetric collider, the *BABAR* detector needs to have a forward-backward asymmetric design along the direction of the beam. The center of the *BABAR* detector is shifted by 0.37 m from the IP, in the boost direction of the more energetic e^- beam, as is shown in Figure 2.5. Other asymmetric features include that the electromagnetic calorimeter only has a forward end-cap; the read-out electronics of the drift chamber are placed at the backward end of the detector.

The high luminosity needed for CP violation measurements and other rare B decay studies requires unusual beam optics with machine components being very close to the interaction region, and the *BABAR* detector needs to accommodate the machine elements without much impact on its performance.

The vertexing system should have excellent vertex resolution along the z-axis and in the transverse plane in order to measure the decay time distributions. Vertex resolution also stresses the importance of minimizing multiple scattering.

High reconstruction efficiency and good momentum resolution for charged particles, together with reconstruction of the neutral particles, are important to fully reconstruct the final states of B decay, and to separate signal events from background. The detector should be able to do tracking over a range of $\sim 60\,\mathrm{MeV} < p_T <\sim 4\,\mathrm{GeV}$,

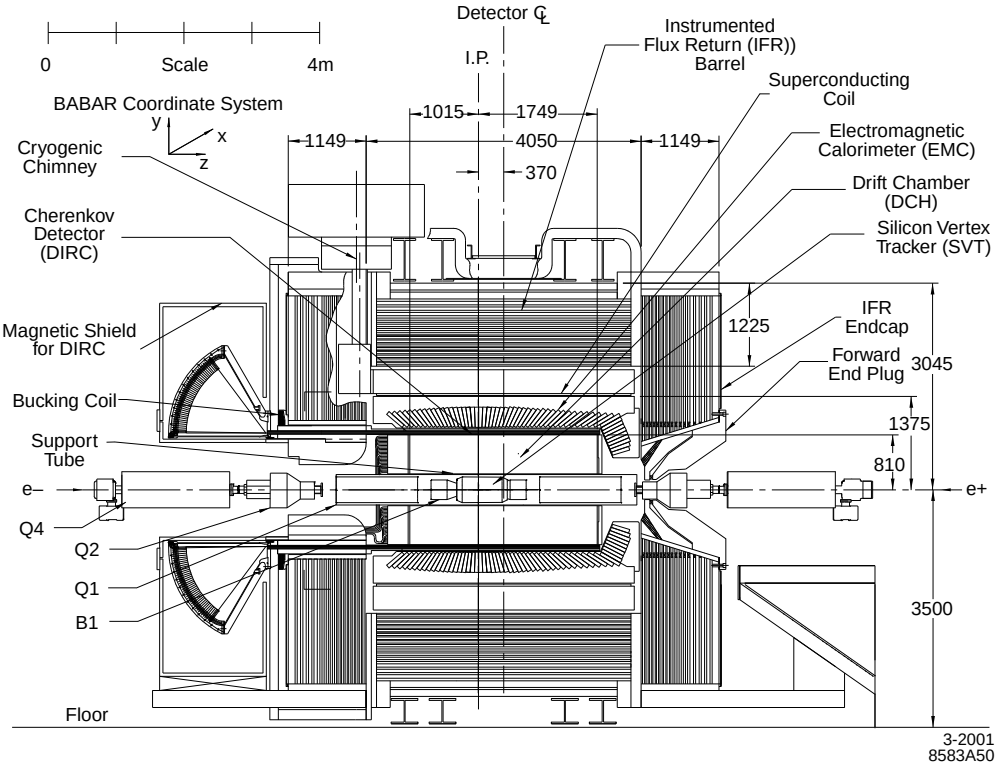

Figure 2.5: Longitudinal section of the *BABAR* detector. All dimensions are in mm.

and have good particle identification capability between e, μ, π, K and p over a wide kinematic range. The system also need to detect photons and π^0's over the wide energy range of $\sim 20\,\mathrm{MeV} < E <\sim 5\,\mathrm{GeV}$ and to have neutral hadron identification capability.

The layers of sub-detectors of *BABAR* are arrange concentrically around the IP as is shown in transverse cross-section of the detector in Figure 2.6. From innermost to outermost, the major subsystems of the detector include: a Silicon Vertex Tracker (SVT), a Drift Chamber (DCH), a Detector of Internally Reflected Čerenkov light (DIRC), a Caesium Iodide Electromagnetic Calorimeter (EMC), a superconducting coil, which provides a 1.5 T solenoidal magnetic field, and an Instrumented Flux Return (IFR).

The SVT is a five-layer system for the precise reconstruction of decay vertices and for tracking of low energy charged particles. The DCH is the main tracking system of the *BABAR* detector; together with SVT, it provides the momentum measurement

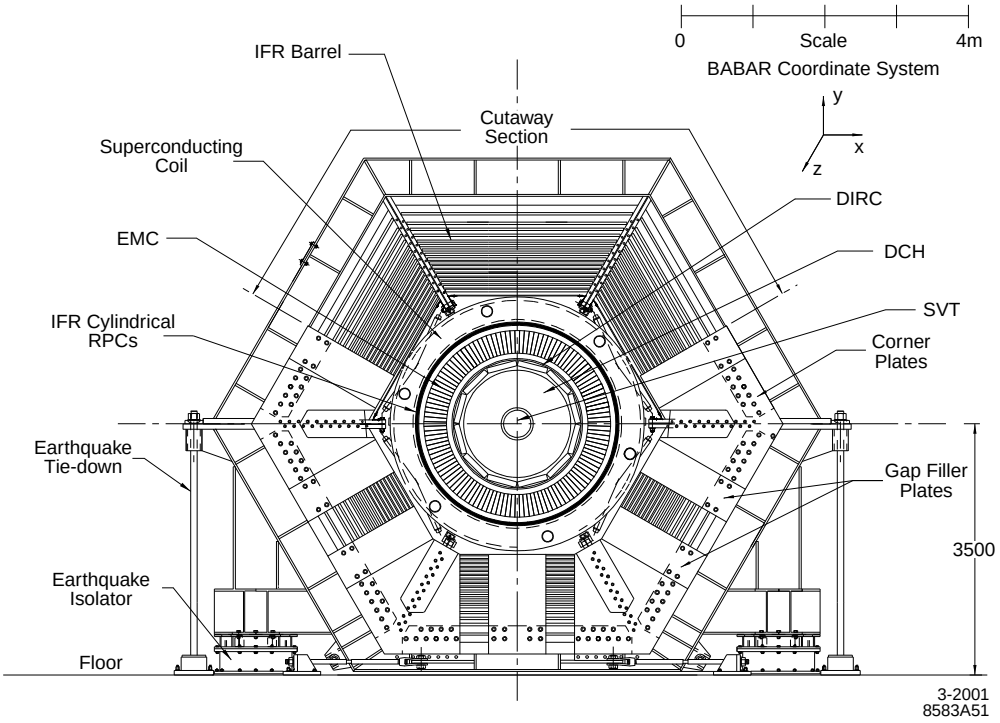

Figure 2.6: Forward end view of the *BABAR* detector. All dimensions are in mm.

for charge particles. It also provides particle identification information through $\mathrm{d}E/\mathrm{d}x$ measurements for tracks with transverse momenta less than 700 MeV/c. DIRC is designed and optimized for high momentum charged hadron particle identification, which is crucial for rare charmless hadronic B decays. It provides a separation of better than 4σ between kaons and pions for track momenta between 700 MeV/c and 3 GeV/c, and better than 2.5σ for track momenta up to 4.5 GeV/c. The EMC calorimeter has barrel and a forward end-cap. It provides measurements of photo energies, good electron identification down to about 0.5 GeV, and information of neutral hadrons. The IFR is the outermost sub-detector of *BABAR* and is designed to identify muons down to about 0.6 GeV and neutral hadrons such as K_L^0 mesons.

We summarize the coverage, segmentation, and performance of the subsystems in Table 2.3 [57] and will have more descriptions of each of them in the next several sections.

Table 2.3: Overview of the coverage, segmentation, and performance of the *BABAR* detector systems. The notation (C), (F), and (B) refers to the central barrel, forward and backward components of the system, respectively. The detector coverage in the laboratory frame is specified in terms of the polar angles θ_1 (forward) and θ_2 (backward). The number of readout channels is listed. Performance numbers are quoted for 1 GeV/c particles, except where noted. The performances for the SVT and DCH are quoted for a combined Kalman fit [61] (for the definition of the track parameters, see Sec. 2.3.2.)

System	θ_1 (θ_2)	No Channels	No. Layers	Segmentation	Performance
SVT	20.1° (−29.8°)	150K	5	50–100 μm r − ϕ 100–200 μm z	$\sigma_{d_0} = 55\,\mu$m $\sigma_{z_0} = 65\,\mu$m
DCH	17.2° (−27.4°)	7,104	40	6–8 mm drift distance	$\sigma_\phi = 1$ mrad $\sigma_{tan\lambda} = 0.001$ $\sigma_{p_T}/p_T = 0.47\%$ $\sigma(dE/dx) = 7.5\%$
DIRC	25.5° (−38.6°)	10,752	1	35 × 17 mm^2 ($r\Delta\phi \times \Delta r$) 144 bars	$\sigma_{\theta_c} = 2.5$ mrad per track
EMC(C)	27.1° (−39.2°)	2 × 5760	1	47 × 47 mm^2 5760 crystals	$\sigma_E/E = 3.0\%$ $\sigma_\phi = 3.9$ mrad
EMC(F)	15.8° (27.1°)	2 × 820	1	820 crystals	$\sigma_\theta = 3.9$ mrad
IFR(C)	47° (−57°)	22K+2K	19+2	20–38 mm	90% $\mu^\pm$ eff. 6–8% $\pi^\pm$ mis-id
IFR(F)	20° (47°)	14.5K	18	28–38 mm	(loose selection, 1.5–3.0 GeV/c)
IFR(B)	−57° (−26°)	14.5K	18	28–38 mm	

2.3.1 The Silicon Vertex Tracker (SVT)

The main task of SVT is to reconstruct the decay vertices of the two primary B mesons in order to determine the time between the two decays. It is therefore crucial for the measurement of time-dependent *CP* asymmetries. The minimal requirement for *CP* violation study to the measurement of the z separation between the two B vertices is with a precision of better than one half of the mean separation, $\sim 250\,\mu$m, which

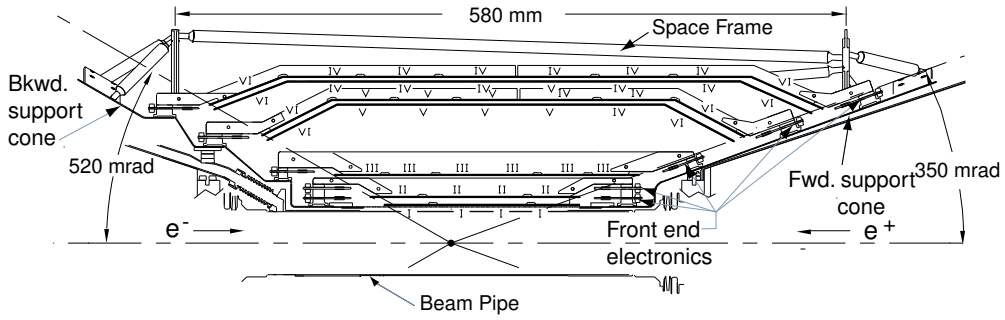

Figure 2.7: Schematic view of the longitudinal section of SVT. The roman numerals label the six different types of sensors.

corresponds to a single vertex precision of better than 80 μm. The required resolution in the x-y plane arises from the need to reconstruct τ and charm decays as well as B decays. In the decays like $B^0 \to D^+D^-$, separating the two D vertices is important. The typical distance between the the D's in the x-y plane for this type of decay is $\sim 275\,\mu$m, so resolution of order $\sim 100\,\mu$m in the plane is needed from SVT.

Charged particles with transverse momenta p_T lower than 100 MeV/c can not reach the drift chamber, so the SVT provides the complete tracking information for these particles. The SVT must provide standalone tracking for particles with $p_T < 120$ MeV/c, the minimum that can be measured reliably in the DCH alone. The SVT also provides the best measurement of track angles, which is crucial for the measurement of the Čerenkov angle for high momentum tracks.

As can be seen in Figure 2.7 and 2.8, the SVT consists of five concentric cylindrical layers of double-sided silicon sensors. The sensors are organized in 6, 6, 6, 16 and 18 modules respectively. The strips on the opposite sides of each sensor are oriented orthogonally to each other: the ϕ measuring strips (ϕ strips) on the outer sides run parallel to the beam and the z measuring strips (z strips) on the inner sides are oriented transversely to the beam axis. The modules of the inner three layers are straight while the outer two layers are arch shaped in the z-R plane (Figure 2.7) to minimize the

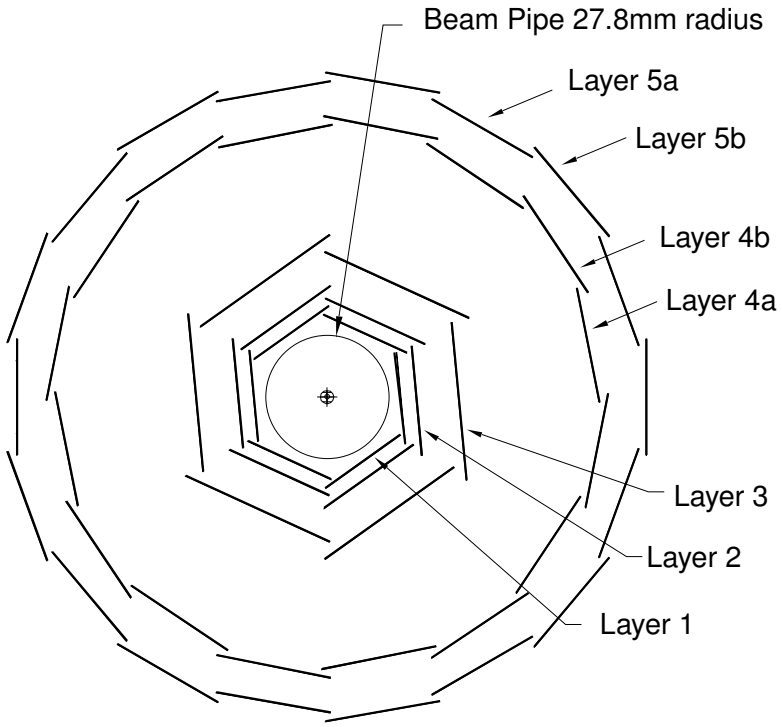

Figure 2.8: Schematic view of the transverse section of SVT.

amount of silicon needed to cover the same solid angle and to increase the crossing angle for particles near the edges of acceptance.

The modules of inner three layers are tilted in ϕ by 5° giving overlap between adjacent modules in order to provide full azimuthal coverage and to aid alignment. The outer modules cannot be tilted because of the arch geometry. To avoid gaps and to have a suitable overlap in the ϕ plane, layer 4 and 5 are divided into two sub-layers (4a, 4b, 5a, 5b) and placed at slightly different radii (Figure 2.8).

The SVT sensors use double-sided silicon strip detectors, AC coupled with polysilicon bias resistors [62]. They have p^+ strips on the p-side and n^+ strips on the opposite, n-side. They are fabricated on 300 μm thick high-resistivity (6–15 kΩ- cm) n-type substrates. Six types of detectors (I to VI, Figure 2.7) are needed, having different physical dimensions, number of strips and readout pitches. The smallest detectors are 43 $\times$ 42 mm^2 ($z \times \phi$), and the largest are 68 $\times$ 53 mm^2.

The *BABAR* silicon vertex tracker has 340 silicon detectors in total, covering an active area of $0.96\,\mathrm{m}^2$, and a total of 150,000 readout channels. The geometrical acceptance of SVT is 90% of the solid angle in the c.m. system, typically 86% are used in charged particle tracking.

Each of the modules is divided electrically into two half modules which are read out at each end. The ϕ strips in the same half module are electrically connected to form a single readout strip. The signals from the z strips are brought to the readout electronics using fanout circuits. To minimize the material in the acceptance region, the readout electronics are mounted entirely outside the active detector volume.

Signals from strips are amplified, shaped and compared with a threshold. The time interval during which they exceed the threshold is approximately logarithmically related to the charge induced on the strips. The length of this interval, called "time over threshold" (TOT), is digitally recorded and, in the case of level-1 trigger acknowledgment, is read by the data acquisition system.

The alignment of the SVT is performed in two steps. The first step consists of determining the relative positions of the 340 silicon sensors. Once this is accomplished, the next step is to align the SVT as a whole within the global coordinate system defined by the DCH. The SVT is calibrated for both types of alignment through tracks from $e^+e^- \to \mu^+\mu^-$ events and cosmic rays.

During the first run of the *BABAR* detector, an SVT hit reconstruction efficiency of 97% was obtained using $\mu^+\mu^-$ pair events. Figure 2.9 shows the SVT hit resolution for z and ϕ side hits as a function of track incident angle, for each of th five layers. The measured resolutions are in excellent agreement with expectations from Monte Carlo simulations.

The SVT can make up to ten $\mathrm{d}E/\mathrm{d}x$ measurements for each track, and a 2σ separation between the kaons and pions can be achieved with momentum up to $500\,\mathrm{MeV}/c$.

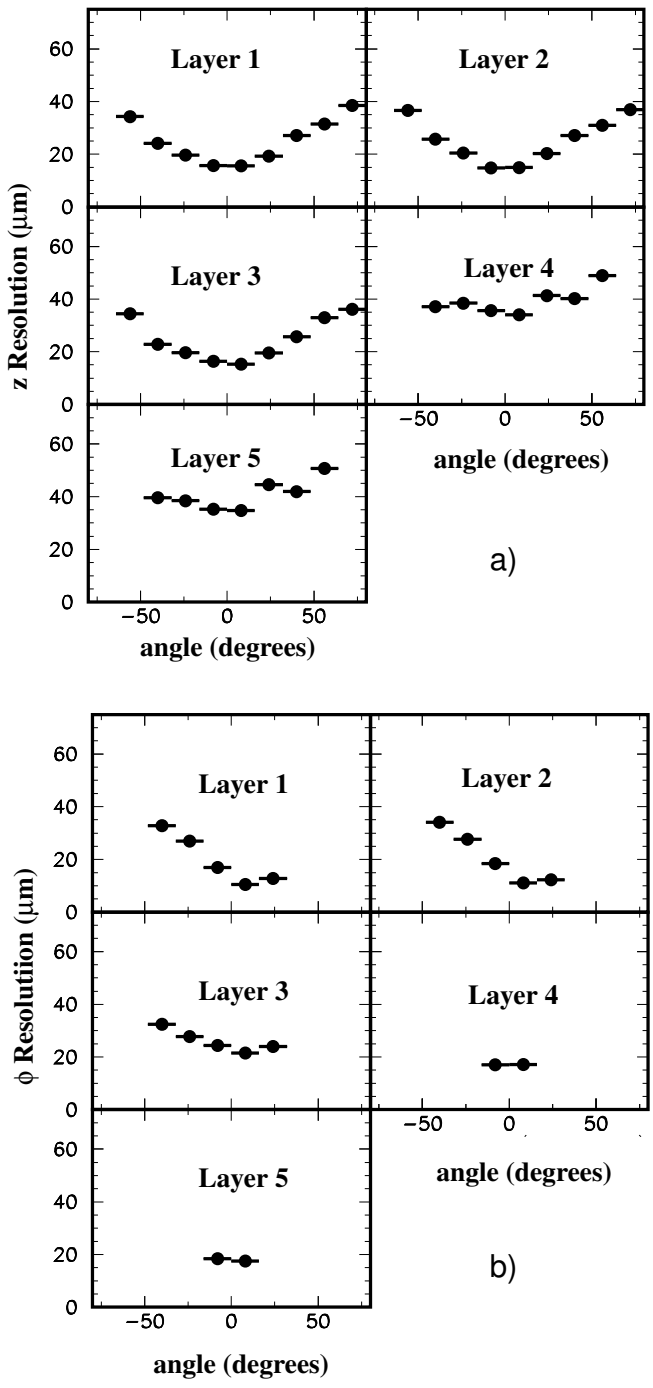

Figure 2.9: SVT hit resolution in the a) z and b) ϕ coordinate in microns, plotted as a function of track incident angle. The track incident angle in the ϕ coordinate is smaller for layers 4 and 5, corresponding to fewer points.

2.3.2 The Drift Chamber (DCH)

The DCH is the main tracking device of the *BABAR* detector. It needs to provide up to 40 measurements of space coordinate to ensure high reconstruction efficiency for tracks with $p_T > 100\,\mathrm{MeV}/c$. The reconstruction of decay vertices outside of SVT, for example the K^0_S decays, relies solely on the DCH, so the chamber should also be able to measure the longitudinal position of tracks, with a resolution of $\sim 1\,\mathrm{mm}$. Combined with SVT, the *BABAR* tracking system should provide excellent spatial and momentum resolution enabling the exclusive reconstruction of B and D meson decays. The DCH complements the measurements of the impact parameter and the directions of charged tracks provided by the SVT, and it is the key to extrapolation of charged tracks to the DIRC, EMC, and IFR.

The DCH also provides $\mathrm{d}E/\mathrm{d}x$ measurements for charged tracks to allow particle identification of tracks with low momentum where the DIRC is not effective. A resolution of about 7% is needed to allow π/K separation up to $700\,\mathrm{MeV}/c$. For tracks with $p > 1\,\mathrm{GeV}/c$, a resolution of $\sigma_{p_T} = 0.3\% \times p_T$ is expected. In addition, the DCH is designed to provide one of the principal triggers for the experiment.

The DCH is a 280 cm-long cylinder, with an inner radius of 23.6 cm and an outer radius of 80.9 cm as shown in Figure 2.10. It is offset by 37 cm from the IP to give greater coverage in the forward region. The design of the detector is also optimized to reduce the material in the forward end in front of the calorimeter endcap. The backward endplate is made of 24 mm thick aluminum while the forward endplate is 12 mm thick, and all the electronics is mounted on the backward endplate. The inner cylinder is made of 1 mm beryllium, corresponding to 0.28% radiation length (X_0). The outer cylinder consists of 2 layers of carbon fiber on a honeycomb core, corresponding to 1.5% X_0.

The DCH consists of 7104 drift cells, which are arranged in a total of 40 layers. The 40 layers are grouped into 10 superlayers with 4 layers each. The stereo angles of

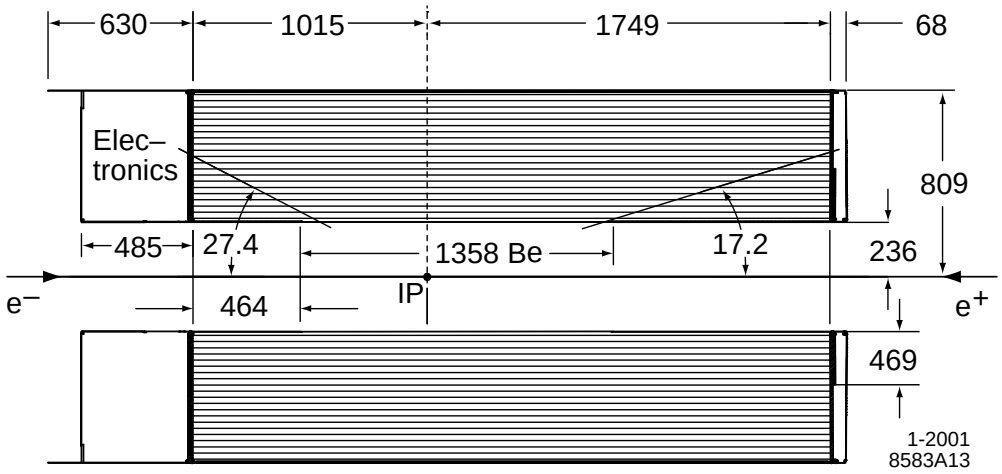

Figure 2.10: Longitudinal section of the DCH with principal dimensions in mm; The chamber center is offset by 370 mm from the IP.

the superlayers alternate between axial (A) and stereo (U, V) superlayers, in a pattern AUVAUVAUVA as shown on the left of Figure 2.11. The stereo angles vary between 45 mrad in the innermost stereo superlayers, to 76 mrad in the outermost stereo superlayers. The superlayer structure is beneficial to the fast local segment finding for the Level 1 trigger. The chamber is filled with a 4:1 mixture of helium:isobutane, which provides good spatial and $\mathrm{d}E/\mathrm{d}x$ resolution and reasonably short drift time, while the low mass gas mixture keeps multiple scattering to a minimum. The gas and the wires total 0.2% X_0 for tracks at normal incidence.

On the right of Figure 2.11 shows the design of the drift cells for the four innermost superlayers. The hexagonal drift cells are of small-cell design, with a typical size of $1.2\times1.8\,\mathrm{cm}^2$, to minimize the drift time. The sense wires are 20 μm gold-plated tungsten-rhenium, and the field wires are gold-plated aluminum with diameters of 120 μm and 80 μm. Nominal voltages of 1960V for the sense wires and 340V for the field-shaping wires at the boundaries of the superlayers are supplied by HV assemblies mounted on the feedthroughs of the rear endplate.

The DCH electronics is designed to provide a measurement of the drift time and

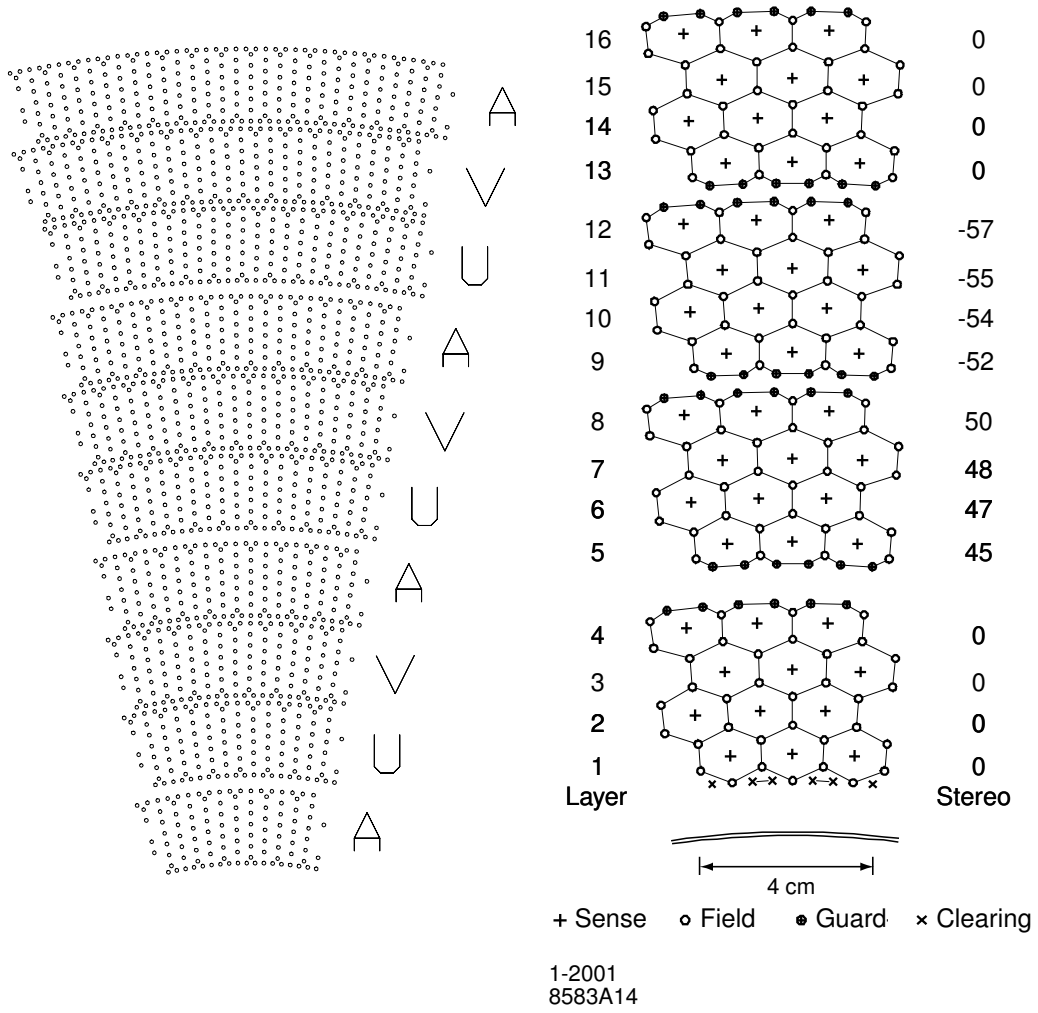

Figure 2.11: The DCH cell layout. 10 superlayers with 4 layers in each are shown on the left. On the right are the drift cells for the four innermost superlayers. Lines have been added between field wires in visualization of the cell boundaries. The numbers one the right side give the stereo angles (mrad) of sense wires in each layer. The 1 mm-thick beryllium inner wall is shown inside the first layer.

the integrated charge, as well as a single bit to the trigger system for every wire with a signal. The electronics used for amplification, digitization and trigger interface are housed outside of the detector fiducial volume within 48 aluminum boxes mounted on the rear endplate of the detector, on top of the HV Assembly. The amplifier IC receives the input signal from the sense wire and produces a discriminator output signal for the drift time measurement and a shaped analog signal for the $\mathrm{d}E/\mathrm{d}x$ measurement. The

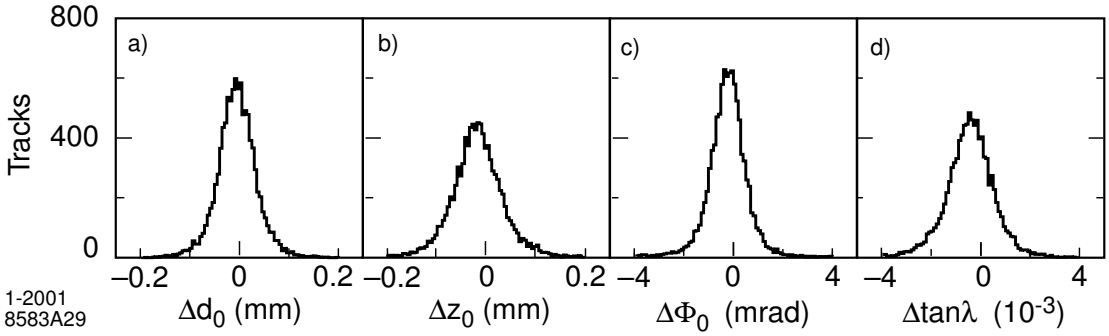

Figure 2.12: Measurements of the difference between the fitted track parameters of the two halves of cosmic ray muons, with $p_T > 3\,\mathrm{GeV}/c$, a) Δd_0, b) Δz_0, c) $\Delta\phi_0$, and d) $\Delta \tan\lambda$. The distributions are symmetric, and the non-Gaussian tails are small. The distributions in b) and d) show a clear offset due to the residual problems with the internal alignment of the SVT.

signals are sent to a customized digitizer IC having a 4-bit TDC for time measurement and a 6-bit 15 MHz FADC to measure the total deposited charge.

Charged tracks are defined by five parameters (d_0, ϕ_0 ω, z_0, $\tan\lambda$) which are measured at the point of closest approach to the z-axis, and their associated error matrix. d_0 and z_0 represent the distance of a track from the origin of the coordinate system in the x-y plane and along the z-axis; The angle ϕ_0 is the azimuth of the track; λ is the dip angle relative to the transverse plane; and $\omega = 1/p_T$ is its curvature. Figure 2.12 shows the resolutions of these parameters using cosmic rays recorded during normal data-taking, and based on the full width at half maximum of these distributions the resolutions for single tracks can be parameterized as

$$\begin{aligned} \sigma_{d_0} &= 23\,\mu\mathrm{m} \qquad \sigma_{\phi_0} = 0.43\,\mathrm{mrad} \\ \sigma_{z_0} &= 29\,\mu\mathrm{m} \quad \sigma_{\tan\lambda} = 0.53 \cdot 10^{-3}\,. \end{aligned} \tag{2.2}$$

The track reconstruction efficiencies as a function of p_T and polar angle are shown in Figure 2.13. We can see the efficiency falling off when $p_T < 250\,\mathrm{MeV}/c$. The overall tracking efficiency is $98 \pm 1\%$ for track above $200\,\mathrm{MeV}/c$ and polar angle $\theta > 500\,\mathrm{mrad}$ at the voltage of 1960V.

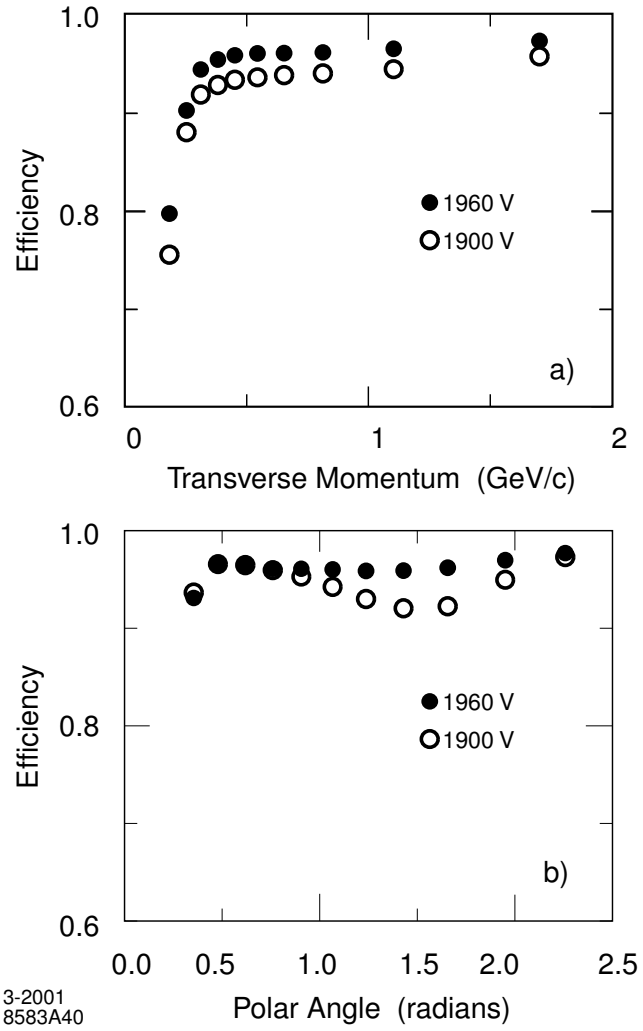

Figure 2.13: The track reconstruction efficiency in the DCH at 1900V and 1960V. The efficiency is measured in multi-hadron events, as a function of transverse momentum (top) and polar angle (bottom).

The DCH contributes primarily to the p_T measurement. The resolution of measured p_T, $\sigma p_T/p_T$, as a function of p_T is shown in Figure 2.14 and can be written as a linear function

$$\sigma p_T/p_T = (0.13 \pm 0.01)\% \cdot p_T + (0.45 \pm 0.03)\% \,. \tag{2.3}$$

The $\mathrm{d}E/\mathrm{d}x$ as a function of momentum is shown in Figure 2.15. Good K/π separation is achieved up to $600\,\mathrm{MeV}/c$.

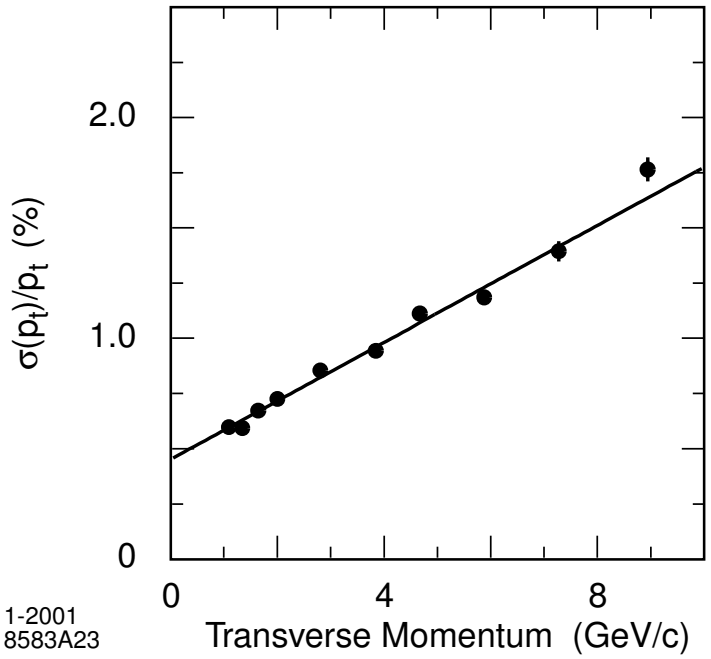

Figure 2.14: Resolution of the transverse momentum p_T as measured from cosmic ray muons that traverse both DCH and SVT.

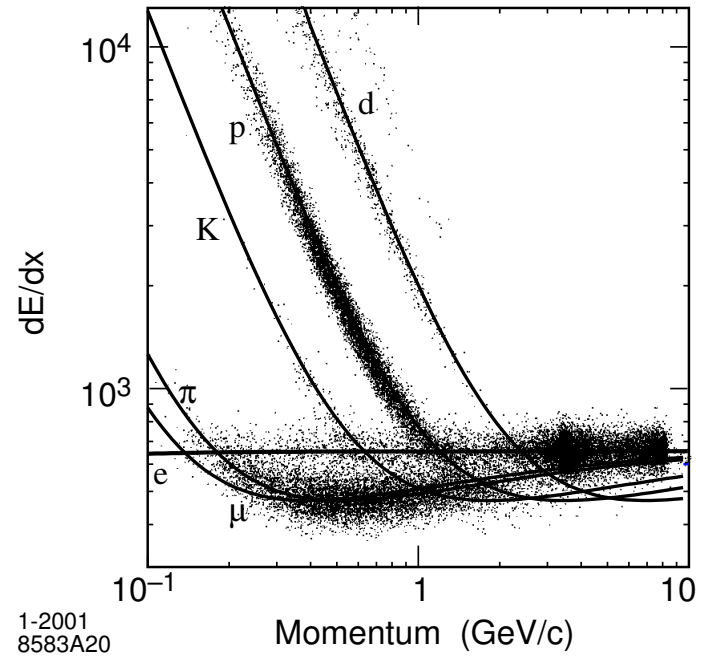

Figure 2.15: Corrected DCH $\mathrm{d}E/\mathrm{d}x$ measurement as a function of track momentum, for a sample of data obtained using beam background triggers. The Bethe-Bloch fits are derived from selected control samples from data.

2.3.3 DIRC

One important key to the study of *CP* violation is the ability to tag the flavor of one of the B meson via the cascade decay $b \to c \to s$ by identifying the final product kaons, which have a momentum up to about 2 GeV/c, with most of them below 1 GeV/c. In addition, pions and kaons from rare B decays, which are the subject of this work, must be well separated. The momenta of those tracks are between 1.7 and 4.2 GeV/c with a strong momentum-polar angle correlation because of the c.m. system boost.

The particle identification (PID) system of the *BABAR* detector is a new kind of ring-imaging Čerenkov detector, Detector of Internally Reflected Čerenkov light (the DIRC), which relies on the detection of Čerenkov photons trapped in the radiator due to total internal reflection [63]. It is expected to provide better than 4σ π/K separation for all tracks from B meson decays in the momentum range 0.7∼4.2 GeV/c.

The DIRC is based on the principle that the angles of light are maintained upon reflection from a flat surface. The overall design is shown in Figure 2.16, which illustrates the principles of light production, transport, and imaging. The DIRC radiator consists of 144 long, straight bars of fused synthetic silica (mean index of refraction $n = 1.473$) with rectangular section, arranged in a 12-sided polygonal barrel with each bar box containing 12 bars (see Figure 2.17). The bars are 1.7 cm thick, 3.5 cm wide and 4.9 m long. Each bar is assembled from four 1.225 m pieces that are glued end-to-end.

For particles with $\beta \approx 1$, some photons will always lie within the total internal reflection limit, and will be transported to either one or both ends of the bar. A mirror is placed at the forward end to reflect the photons towards the backward readout end. Each bar has a fused silica wedge glued to it at the readout end to reflect photons at large angles relative to the bar axis so as to reduce the size of the required detection surface and recover those photons that would otherwise be lost due to internal reflection at the fused silica/water interface. The twelve wedges in a bar box are glued to a

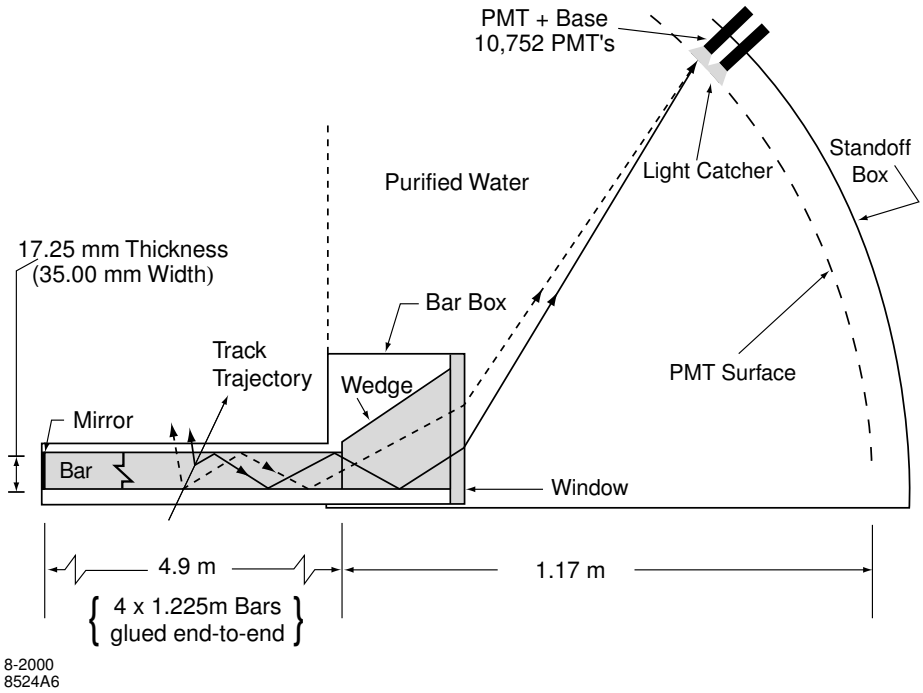

Figure 2.16: Schematics of the DIRC fused silica radiator bar, which transports the Čerenkov photons emitted within it, the optical wedge, which reflects the photon at large angle, a region of purified water as the expansion medium, and an array of imaging PMTs.

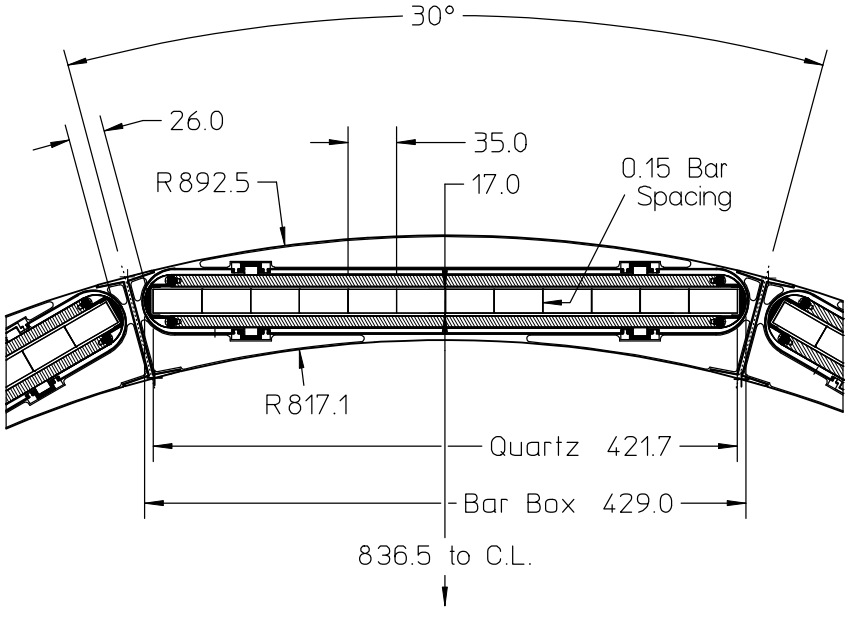

Figure 2.17: Transverse cross-section of a DIRC bar box embedded in the Central Support Tube (CST). All dimensions are in mm.

common 10 mm-thick fused silica window, which provides the interface and seal to the purified water in the expansion region, called the standoff box. Water is chosen as the expansion medium because it is inexpensive and has an average index of refraction (n≈1.346) reasonably close to that of fused silica. The standoff box is made of stainless steel, consisting of a cone, cylinder, and 12 sectors of PMTs, and it contains about 6,000 liters of purified water.

The photons are detected by an array of densely packed photo-multiplier tubes (PMTs), each surrounded by reflecting light catcher cones to capture light. The PMTs are placed at a distance of about 1.2 m from the bar end on the 12 PMT sectors at the rear of the standoff box. Each of the 12 PMT sectors contains 896 PMTs with 29 mm-diameter.

The DIRC occupies 80 mm of radial space and a total of about 17% radiation length. The radiator bars cover a solid angle corresponding to about 94% of the azimuth and 83% of the c.m. polar angle cosine.

The DIRC front-end electronics (FEE) is designed to measure the arrival time of each Čerenkov photon detected by the PMT array to an accuracy of 1.5 ns limited by the intrinsic transit time spread of the PMTs. The DIRC FEE is mounted on the outside of the standoff box. Each of the 168 Front-end Boards (DFBs) processes 64 PMT inputs and contain 8 custom analogue chips, 4 TDCs and one 8-bit FADC.

The Čerenkov angle information is reconstructed from the position and arrival time of the PMT signals. The timing measurements are used to suppress background hits and to separate photons from different tracks. Figure 2.18 shows the pattern of Čerenkov photon before and after the timing cut.

The emission angle and arrival time of the Čerenkov photons are transformed into the Čerenkov coordinate system, θ_c, the Čerenkov angle, ϕ_c, the azimuthal angle of a Čerenkov photon around the track direction, and δt, the difference between the measured and expected photon arrival time. An unbinned maximum likelihood method

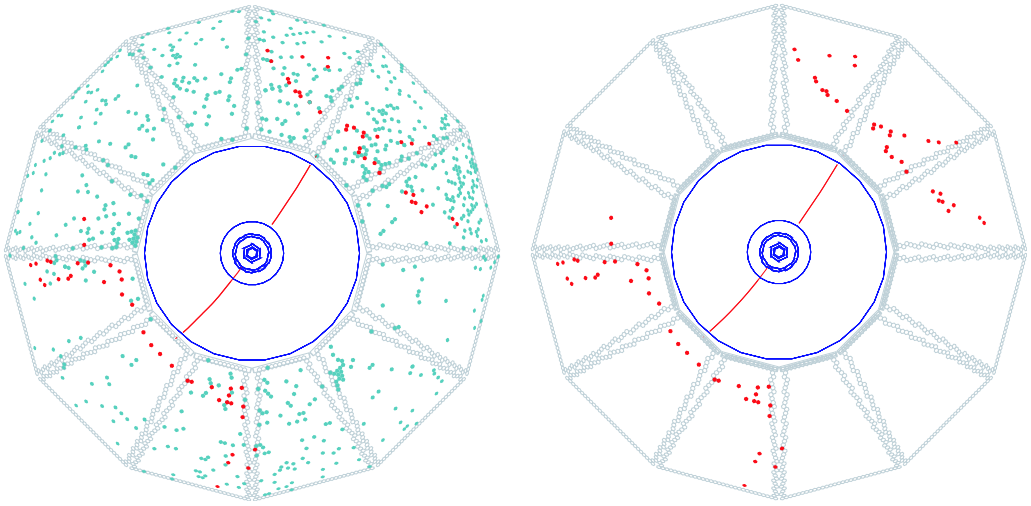

Figure 2.18: Display of DIRC PMT hit pattern for a di-muon event. On the left, all the PMT hits within ±300 ns trigger window are shown. On the right, only PMT hits within ±8 ns of the expected arrival time of the tracks are shown.

is used to assign for each track the likelihoods of being e, μ, π, K, and p. The likelihood is maximized for the right hypothesis.

Figure 2.19 shows that the expected K/π separation from the decay $B^0 \to \pi^{\pm}K^{\mp}$ is about 4.2σ at 3 GeV/c, and is better than 3σ except for the very high momentum. Figure 2.20 shows the distributions of the measured Čerenkov angle θ_c in a control sample of $D^0 \to K^-\pi^+$.

2.3.4 The Electromagnetic Calorimeter (EMC)

The EMC is designed to measure electromagnetic showers with high efficiency, and energy and angular resolution over an energy range from 20 MeV to 9 GeV. This allows the detection of photons from π^0 and η as well as from electromagnetic and radiative processes. By identifying electrons, the EMC plays an important role in the flavor tagging of neutral B mesons via semi-leptonic decays, as well as in the study of semi-leptonic and rare decays of B and D mesons, and τ leptons.

The upper bound of the energy range comes from the need to measure QED

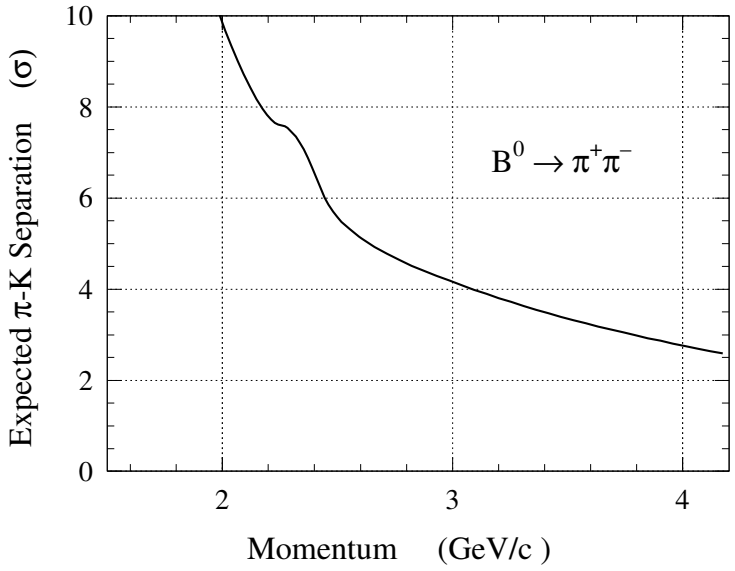

Figure 2.19: Expected K/π separation in $B^0 \to \pi^+\pi^-$ events as a function of track momentum inferred from the measured Čerenkov angle resolution and number of Čerenkov photons per track in di-muon events.

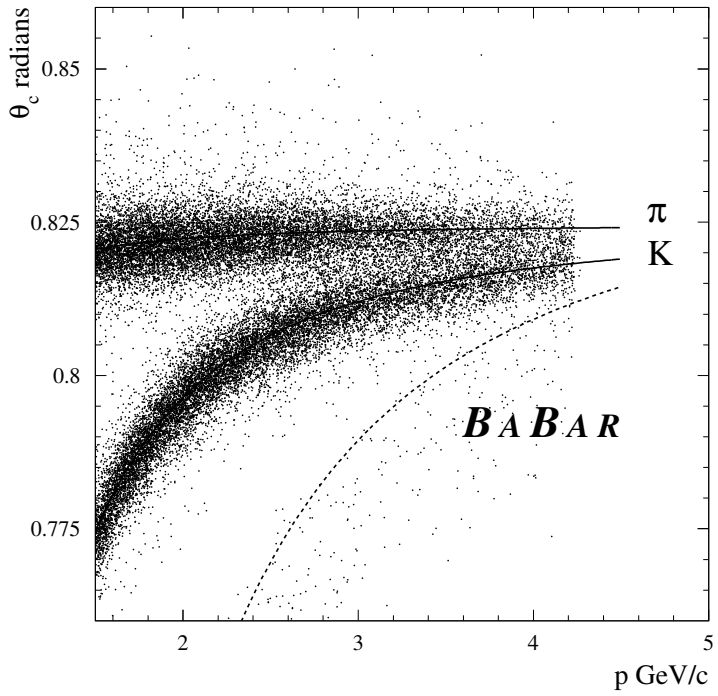

Figure 2.20: The distributions of the measured Čerenkov angle θ_c in a control sample of $D^0 \to K^-\pi^+$.

Table 2.4: Properties of CsI(Tl)

Parameter	Values
Radiation Length	1.85 cm
Molière Radius	3.8 cm
Density	4.53 g/ cm^3
Light Yield	50,000 γ/ MeV
Light Yield Temp. Coeff.	0.28%/°C
Peak Emission $\lambda_{\max}$	565 nm
Refractive Index ($\lambda_{\max}$)	1.80
Signal Decay Time	680 ns (64%)
	3.34 μs (36%)

processes, such as $e^+e^- \to e^+e^-(\gamma)$ and $e^+e^- \to \gamma\gamma$, for calibration and luminosity. The lower bound is set by the need for full reconstruction decays of B and D mesons containing multiple π^0s and η^0s. Rare decays of B meson with π^0s, such as the decay $B^0 \to \pi^0\pi^0$ requires an energy resolution of order 1–2%. Below 2 GeV, the π^0 mass resolution is mainly from the energy resolution, while at higher energies, the angular resolution becomes dominant, and it is required to be of the order of a few mrad.

The EMC has full coverage in azimuth and extends from 15.8° to 141.8° corresponding to 90% of the solid angle in the c.m. system (see Figure 2.21). The EMC is designed to be a total absorption calorimeter and is composed of a finely segmented array of thallium-doped caesium iodide (CsI(Tl)) crystals. The properties of CSI(Tl) are summarized in Table 2.4. The high light yield and small Molière radius allow for excellent energy and angular resolution. A total of 6,580 crystals are arranged in a cylindrical barrel and a conical forward endcap of the EMC. The barrel contains 5,760 crystals in 48 distinct rings with 120 identical crystals each, and the endcap holds 820 crystals in eight rings. The crystals have a tapered trapezoidal cross-section, with the length range from 29.6 cm ($16X_0$) in the backward to 32.4 cm ($17.5X_0$) in the forward direction to limit the effects of shower leakage from increasingly higher energy particles.

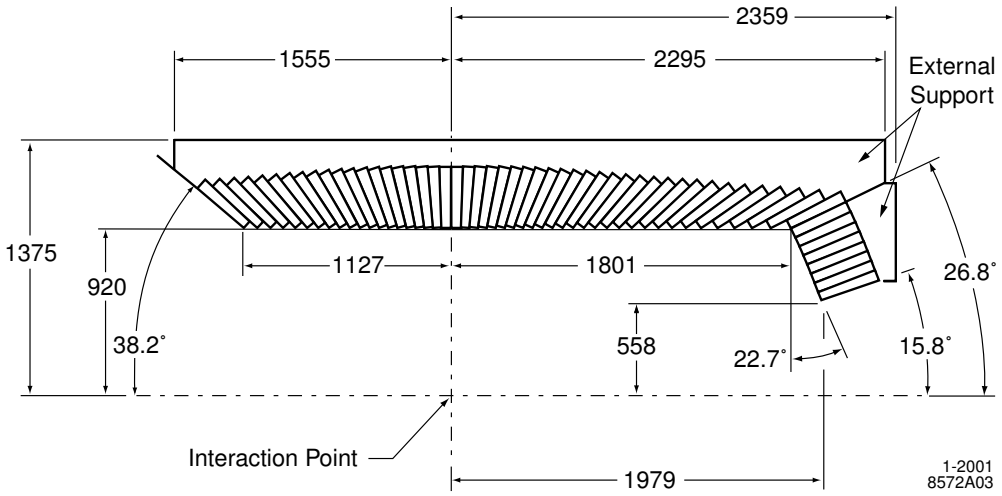

Figure 2.21: Longitudinal cross-section of the top half of EMC. All dimensions in mm.

The CsI(Tl) crystal serves as a total absorption scintillating material and also as light guide to collect light at the photodiodes mounted at the rear surface. Two silicon photodiodes are used to allow redundancy and averaged signal readout to reduce noise. The signal from each photodiode is initially amplified by the preamplifiers mounted close to the diode (see Figure 2.22).

The signals are carried out the crystal through shielded ribbon cable to the rest of the electronics which are housed outside the active detector volume. In the barrel the ribbon cables run along the θ direction to mini-crates housed on both ends of the barrel. The forward 24 rings of crystals are read out at the front face, while the backward 24 rings are read out at the backward face. In the forward endcap the mini-crates are mounted immediately adjacent to each section of crystals.

Each mini-crate houses 6 Analogue-to-Digital Boards (ADB), while endcap mini-crates have 4 ADBs with each ADB serving 12 crystals. Each ADB contains 3 Custom AutoRange Encoding (CARE) chips and ADC circuits. Each CARE chip serves 4 crystals and provides dynamic amplification of the signal. The output of each ADB then is passed to one Input-Output-Board (IOB) which serves the mini-crate, and then is

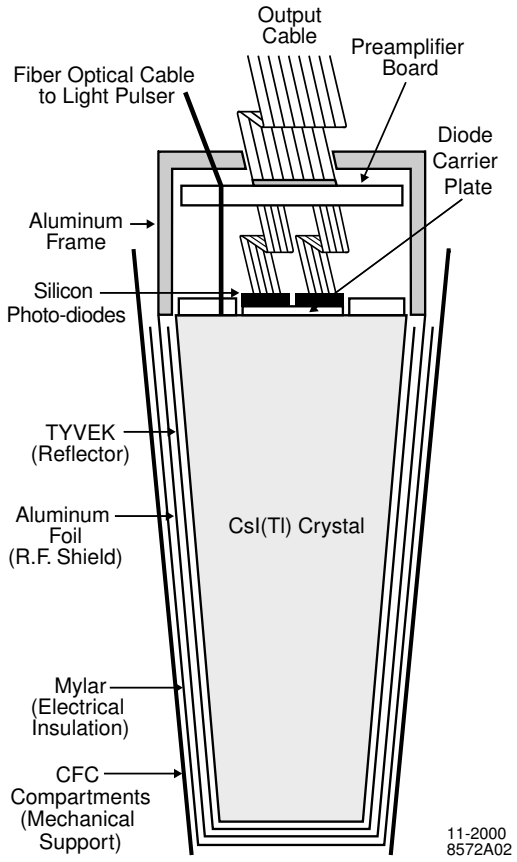

Figure 2.22: Schematics of a wrapped CsI(Tl) crystal and the front-end readout package mounted on the rear face.

sent through an optical fiber to the Readout Modules (ROMs) housed in the electronics house for further processing.

A periodical calibration procedure is needed for EMC to extract the energy of incident photon or electron and to monitor short- and long-term variations of its response.

A typical electromagnetic shower spreads over many adjacent crystals, forming a cluster of energy deposits. The individual crystals are grouped into clusters, which are identified and associated to a charged or a neutral particle by pattern recognition algorithms. Two kinds of clusters are reconstructed: single clusters with one energy maximum, and merged clusters with several local energy maxima (bumps). Correction

factors are applied to the cluster and bump energies to take account of energy lost through leakage and from particle showering before entering the calorimeter.

At low energy the energy resolution is measured directly with a radioactive source yielding $\sigma_E/E = 5.0 \pm 0.8\%$ at 6.13 MeV. At high energy, the resolution is derived from Bhabha scattering where the energy can be predicted by the polar angle of the $e^{\pm}$. The measured resolution is $\sigma_E/E = 1.90 \pm 0.07\%$ at 7.5 GeV. Figure 2.23 shows the energy resolution as a function of the shower energy. It is described empirically as a quadratic sum of two terms:

$$\frac{\sigma_E}{E} = \frac{(2.32 \pm 0.30)\%}{\sqrt[4]{E(\,\mathrm{GeV})}} \oplus (1.85 \pm 0.12)\% \,. \tag{2.4}$$

Figure 2.24 shows the angular resolution as a function of the shower energy. It can be empirically parameterized as a sum of two terms:

$$\sigma_\theta = \sigma_\phi = \left[\frac{(3.87 \pm 0.07)}{\sqrt{E(\,\mathrm{GeV})}} + (0.00 \pm 0.04) \right] \mathrm{mrad} \,. \tag{2.5}$$

Electrons are separated from charged hadrons primarily on the basis of the shower energy, lateral shower moments [64], and track momentum. The most important variable for the discrimination of hadrons is the ratio of the shower energy to the track momentum (E/p). The efficiency for electrons identification and the pion misidentification probability as a function of momentum and polar angle of the particle are shown in Figure 2.25. The efficiency in the momentum range $0.5 < p < 2\,\mathrm{GeV}/c$ is $\sim 88\%$, while the average misidentification probability is $\sim 0.15\%$.

2.3.5 The Instrumented Flux Return (IFR)

The instrumented flux return is the muon and neutral hadron (primarily K_L^0) detector of *BABAR*. Muons identification with high efficiency and good purity down to momentum below $1\,\mathrm{GeV}/c$ is important for tagging the flavor of neutral B mesons via semi-leptonic decays, for the reconstruction of vector mesons, like the J/ψ through

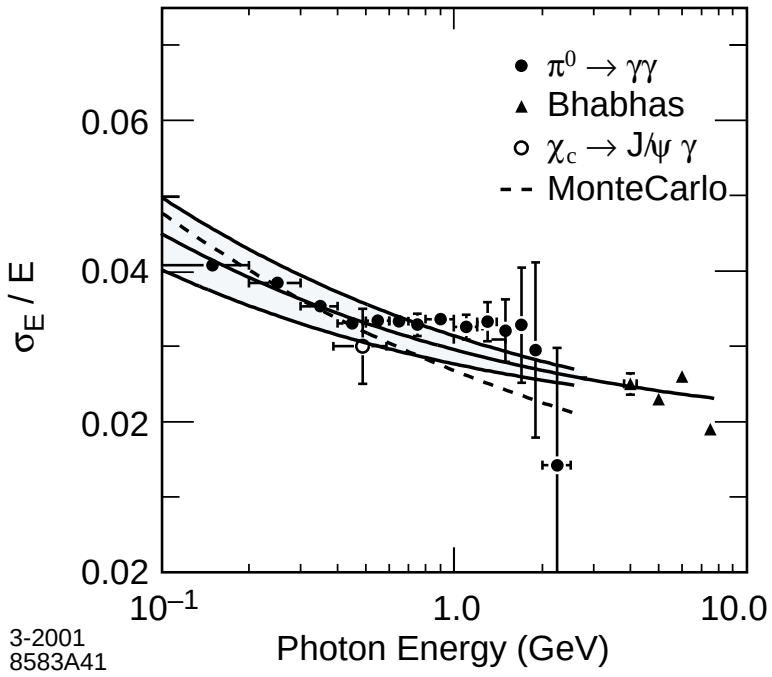

Figure 2.23: The EMC energy resolution as a function of the shower energy. It has been measured with photons from several processes. The solid curve is a fit to Eq. 2.4 and the shaded area denotes the rms error of the fit.

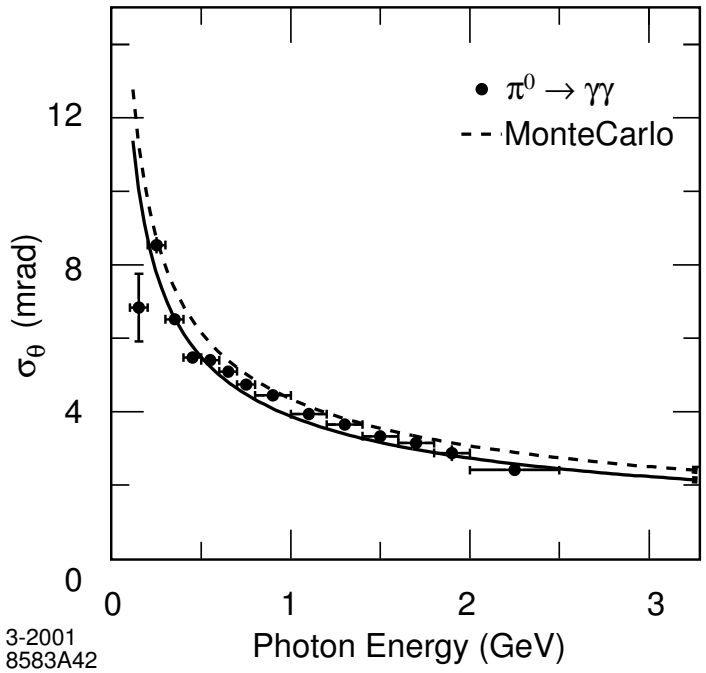

Figure 2.24: The EMC angular resolution as a function of the shower energy. It has been measured with photons from π^0 decays. The solid curve is a fit to Eq. 2.5.

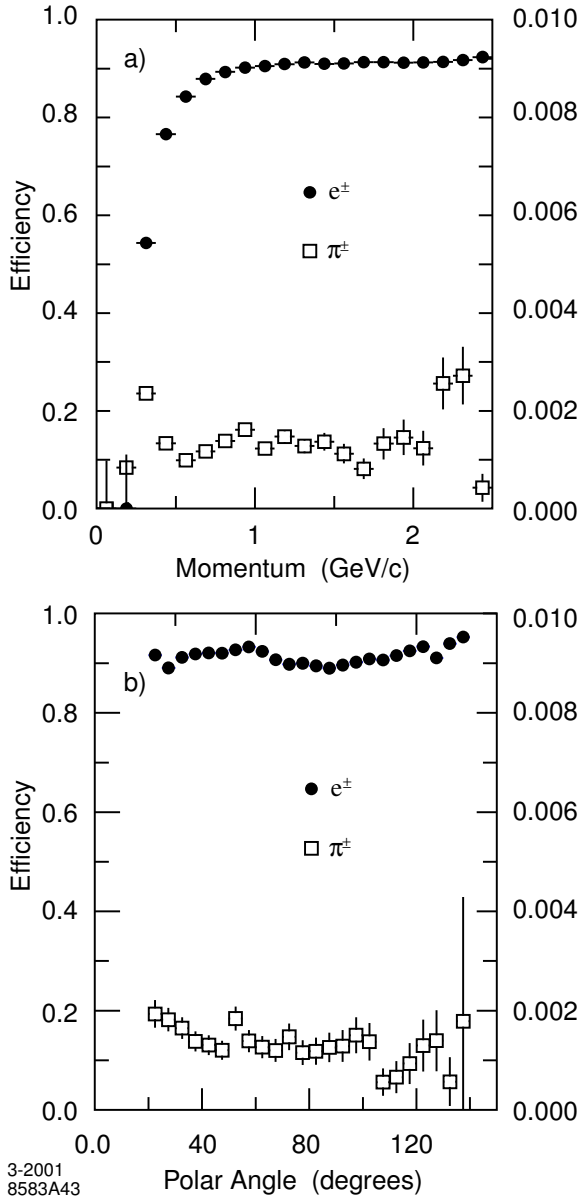

Figure 2.25: EMC electron efficiency and pion misidentification probability as a function a) the particle momentum and b) the polar angle, measured in the laboratory system. The electron efficiency is measured using radiative Bhabhas and $e^+e^- \to e^+e^-e^+e^-$ events. The pion misidentification probability is measured for selected charged pions from K^0_S decays and three-prong τ decays.

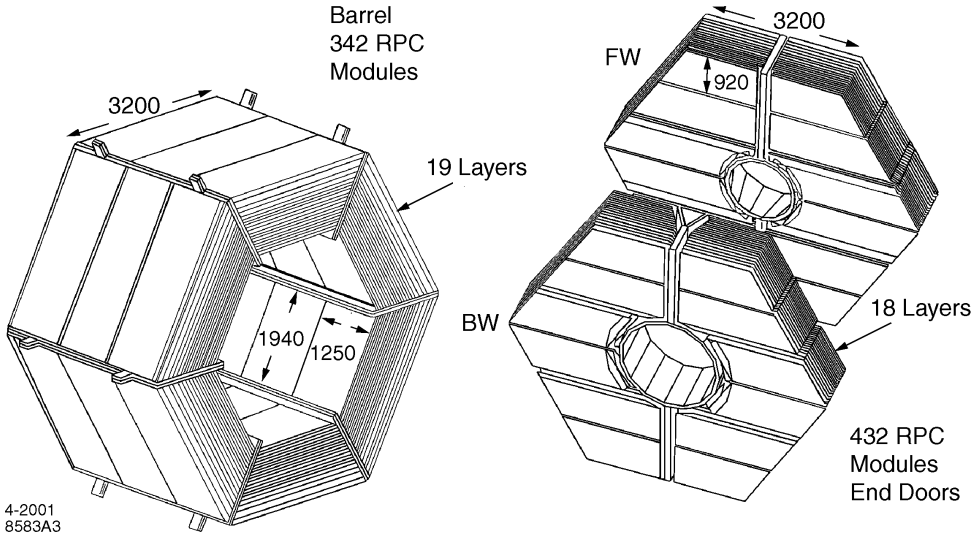

Figure 2.26: Overview of the IFR: Barrel sectors and forward (FW) and backward (BW) end doors; the shape of RPC modules and their dimensions are indicated. All dimensions are in mm.

$\mu^+\mu^-$, and for the study of semi-leptonic and rare decays involving leptons of B and D mesons and τ lepton. K_L^0 detection over a wide range of momenta and angles allows the study of exclusive B decays, in particular CP eigenstates, like $B^0 \to J/\psi\, K_L^0$. The IFR can also help in vetoing charm decays and improve the reconstruction of neutrinos. Due to the size and inaccessibility of the IFR, high reliability and extensive monitoring of the detector and associated electronics are required.

As shown in Figure 2.26, the IFR consists of a central part (Barrel), which is concentric to the z-axis with inner radius of 182 cm, outer radius of 304 cm, and two end doors (Forward and Backward End Caps), which extend the solid angle coverage down to 300 mrad in the forward direction and 400 mrad in the backward direction. Each of the end door sections is vertically divided into two halves that can be separated to allow access to the inner detector.

The IFR uses the steel flux return of the magnet as a muon filter and hadron absorber. The large iron structure is finely segmented into 18 plates, with thickness

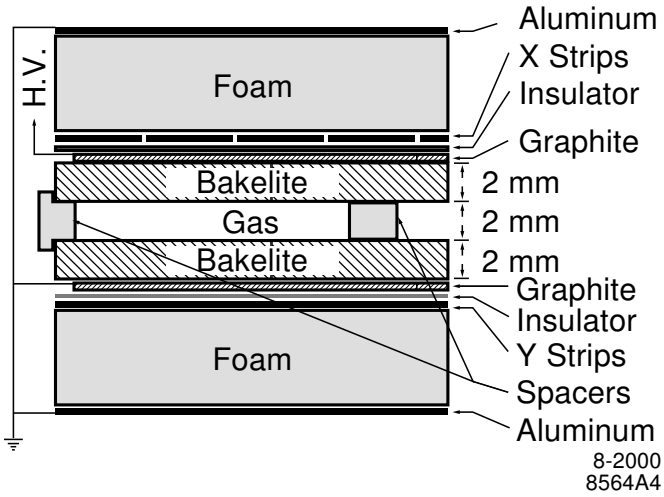

Figure 2.27: Cross section of a planar RPC showing the schematics of the high voltage (HV) connection.

increasing from 2 cm for the inner plates to 10 cm for the outermost plates, giving a total thickness of 65 cm in the Barrel and 60 cm in the End Caps. The gaps between the plates are 3.5 cm wide for the inner layers of the Barrel and 3.2 cm elsewhere, and instrumented with Resistive Plate Chambers (RPCs), in order to provide muon identification and neutral hadron detection. There are 19 RPC layers in the Barrel and 18 in each End Cap. In addition, two layers of cylindrical RPCs are installed between the EMC and the magnet cryostat to detect particles exiting the EMC.

A cross-section of an RPC is shown schematically in Figure 2.27. Two 2 mm thick sheets of bakelite (phenolic polymer) are separated by a 2 mm gap enclosed at the edge by a 7 mm wide frame. The gap is filled with a non-flammable gas mixture of 56.7% argon, 38.8% Freon134a, and 4.5% isobutane. The external surfaces of the bakelite are coated with graphite and connected to a high voltage ($\sim$ 8 kV) and ground. The RPCs are operated in limited streamer mode and the signals are read out capacitively on both sides of the gap by external electrodes.

The IFR detectors cover a total active area of about 2,000 m^2 and consist of 806

RPC modules, 57 in each of the six barrel sectors, 108 in each of the four half end doors, and 32 in the two cylindrical layers. More than 25 different shapes and sizes of the RPCs are needed. In the barrel sectors, the gaps between the steels plates extend 375 cm in the z direction and vary in width from 180 cm to 320 cm. Three modules are needed to cover the whole area as shown in Figure 2.26.

Each barrel module has 32 strips perpendicular to the beam axis to measure the z coordinate and 96 strips in the orthogonal direction extending over three modules to measure ϕ. Each of the four half end doors is divided into three sections. Each of these section is covered by two RPC modules that are joined to form a larger chamber with horizontal and vertical readout strips.

RPCs detect streamers from ionizing particles via capacitive readout strips. Data from strips are sent to Front End Card (FEC). Each FEC serves 16 input strips. Signals from the 3,300 FECs are transmitted to eight custom front end crates, from where the data are buffered and sent through an optical fiber to the DAQ system upon receiving a signal from the trigger system.

One-dimensional IFR clusters are formed as a group of adjacent hits in one of the two readout coordinates. The cluster position is defined as the centroid of the strips in the cluster. Two-dimensional clusters are formed by joining one-dimensional clusters (of the same readout coordinate) in different layers. In each sector, two-dimensional clusters in different coordinates are combined into three-dimensional clusters provided there are fewer than three layers missing in one of the two coordinates. The clusters are matched to tracks reconstructed in the DCH, and a number of variables are defined for each IFR cluster associated with a charged track to discriminate muons from charged hadrons. Those variables include n_λ, the total number of interaction lengths traversed from the IP to the last RPC layer with an associated cluster, Δn_λ, the difference between n_λ and the predicted penetration depth for a muon of the same momentum and angle, etc [65]. K_L^0's and other neutral hadrons are identified as clusters that are not associated with a

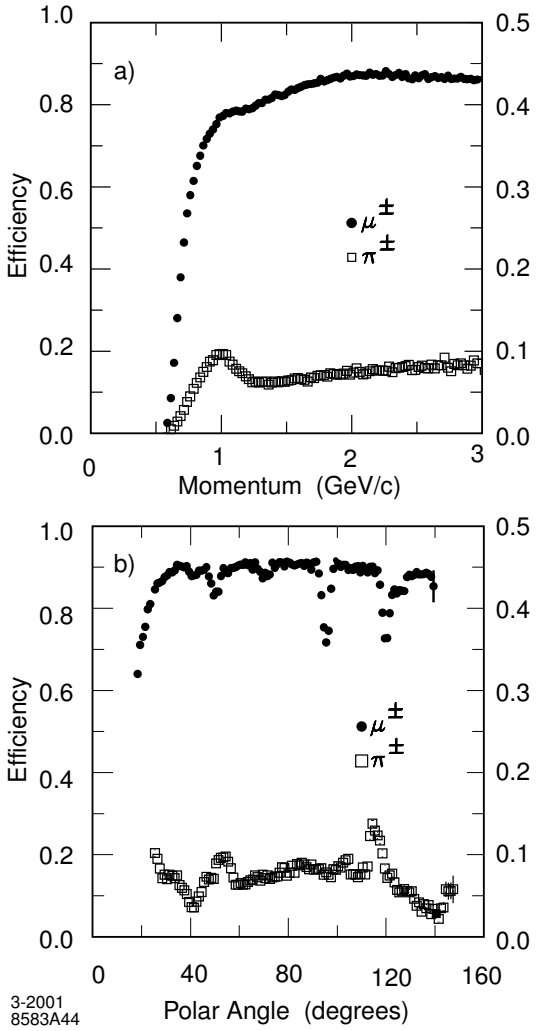

Figure 2.28: The Muon efficiency (left scale) and pion misidentification rates (right scale) of IFR as a function of a) track momentum, and b) polar angle, obtained with loose selection criteria.

charged track.

Figure 2.28 shows that the muon efficiency close to 90% has been achieved in the momentum range of $1.5 < p < 3.0\,\mathrm{GeV}/c$ and pion misidentification rate of about 6–8%. The K_L^0 detection efficiency increases roughly linearly with momentum, and it varies between 20–40% in the momentum range of 1–4 GeV/c.

Table 2.5: Event rates for the principal physics processes at 10.58 GeV for a luminosity of $3 \times 10^{33}\,\mathrm{cm}^{-2}\mathrm{s}^{-1}$. The e^+e^- cross-section refers to events with either the e^+, e^-, or both inside the EMC detection volume.

Event type	Cross section (nb)	Production rate (Hz)	L1 Trigger rate (Hz)
$b\bar{b}$	1.1	3.2	3.2
$q\bar{q}$	3.4	10.2	10.1
e^+e^-	$\sim$53	159	156
$\mu^+\mu^-$	1.2	3.5	3.1
$\tau^+\tau^-$	0.9	2.8	2.4

2.3.6 The Trigger System

The *BABAR* trigger system is required to select $B\overline{B}$ events and other events of interest with a high, stable, and well-understood efficiency of over 99% for all $B\overline{B}$ events and at least 95% for continuum events, while rejecting background events and keeping the total event rate low (below 120 Hz at design luminosity).

The rates of beam-induced background are typically about 20 kHz each for one or more tracks in the DCH with $p_T > 129\,\mathrm{MeV}/c$ or at least one EMC cluster with $E > 100\,\mathrm{MeV}$ at a luminosity of $3 \times 10^{33}\,\mathrm{cm}^{-2}\mathrm{s}^{-1}$, a few orders higher than the production rates of interested events as shown in Table 2.5.

The *BABAR* trigger system must be robust and flexible in order to function even under extreme background situations. It must also be able to operate in an environment with dead and noisy electronics channels, and it should contribute no more than 1% to dead time. The trigger system is implemented as a two-level hierarchy, the Level 1 (L1) which executes in hardware and Level 3 (L3) which executes in software after the event assembly. It is designed to accommodate up to ten times the initially projected PEP-II background rates at design luminosity and to degrade slowly for backgrounds above that level. Provision is made for an intermediate trigger (Level 2) should severe conditions require additional sophistication.

The Level 1 trigger consists of three hardware processors: a drift chamber trigger (DCT), for charged tracks in the DCH, an electromagnetic trigger (EMT), for showers in the EMC, and an instrumented flux return trigger (IFT), for tracks in IFR. Each of the three L1 trigger processors generates trigger primitives, summary data on the position and energy of particles, which are sent to the global trigger (GLT) every 134 ns. The GLT processes all trigger primitives and then delivers them to the Fast Control and Timing System (FCTS). If the trigger primitives satisfies trigger criteria, a L1 Accept is issued.

The DCT and EMT both satisfy all trigger requirements independently with high efficiency over 99% for $B\overline{B}$ events, and thereby provide a high degree of redundancy, which enables the measurement of trigger efficiency, and gives a combined efficiency of $\approx 99.9\%$ for selecting $B\overline{B}$ events.

During normal operation, the L1 triggers are produced within a fixed latency window of 11–12 μs after the e^+e^- collision, and the L1 is configured to have an overall trigger rate of about 1 kHz.

The L3 trigger system receives the output from L1, performs a second stage rate reduction for the main physics sources, and identifies and flags the special categories of events needed for luminosity determination, diagnostic, and calibration purposes. At design luminosity, the L3 physics event acceptance rate is about $\sim$100 Hz, while $\sim$30 Hz contain the other special event categories.

The L3 trigger is a software based system, complying with the same software conventions and standards used in all other *BABAR* software, thereby simplifying its design, testing, and maintenance. The L3 trigger system has full access to the complete event data, including the output of the L1 trigger, for making its event selection. To provide optimum flexibility under different run conditions, L3 is designed according to a general logic model that can be configured to support an unlimited variety of event selection mechanisms. Event classification in L3 is based on several key event parameters

such as L3 DCH tracks, constructed by L3 fast track finding and track fitting, L3 EMC clusters, formed by L3 EMC-based trigger using an optimized look-up-table technique.

The L3 system runs within the Online Event Processing (OEP) framework. Events passing L3 are recorded and passed to the Online Prompt Reconstruction (OPR) system for full reconstruction.

2.3.7 The Data Acquisition (DAQ) and Online Computing System

The *BABAR* online computing system consists of the DAQ system, detector and DAQ control and monitoring systems, data quality control and online calibration systems. The major subsystems include: Online Dataflow (ODF), which is responsible for communication with and control of the FEEs, and the acquisition of event data from them; Online Event Processing (OEP), which is responsible for processing of complete events, including L3 triggering, data quality monitoring, and final stages of calibrations; Logging Manager (LM), which is responsible for receiving events from OEP and writing them to disk as input to the Online Prompt Reconstruction (OPR) processing; Online Detector Control (ODC), which is responsible for the control and monitoring of environmental conditions of the detector systems; Online Run Control (ORC), which ties together all the other components, and is responsible for sequencing their operations, and providing a Graphical User Interface (GUI) for operator control.

The *BABAR* DAQ system was designed to support an L1 trigger rate of up to 2 kHz, with an average event size of ∼32 kB and an L3 output rate of up to 120 Hz. It must contribute no more than a time-averaged 3% dead time during normal DAQ.

The components of the *BABAR* DAQ system are shown schematically in Figure 2.29. All *BABAR* sub-detectors share a common electronics architecture. Raw analog signals from detectors are processed, digitized, and buffered in the FEEs. Upon the L1 Accept signal, under the control of ODF, raw data from the FEEs of each subdetector are passed via optical fibers to the VME based Readout Modules (ROMs) in

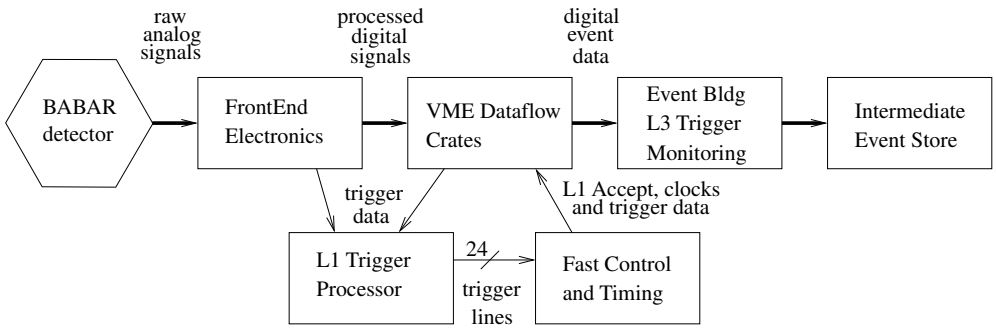

Figure 2.29: Schematic diagram of the *BABAR* DAQ system.

the Dataflow crates. The ROMs are based on single-board computers that run the VxWorks [66] realtime operating system and detector specific software. ODF builds the complete event data and then pass them from the ROMs to a farm of 32 Unix workstations, which run the OEP software including L3 filtering. Events passing the L3 trigger are sent to the LM, which combines all the events from 32 OEP nodes and write to a single file for each run. This file is then processed for full event reconstruction by the OPR, which selects physics events and collects monitoring data for quality control, and finally write the output into an object oriented event store.

The OPR also performs one important task of rolling calibrations, where calibration constants generated during event reconstruction for one run, are then used during the reconstruction of events in the next run by OPR. These constants are stored in a condition database for use when reading the processed events from the event store.

Chapter 3

Analysis Techniques

In this chapter, we will discuss major analysis techniques used for this work. First we have an overview of the *BABAR* software and analysis framework in Sec. 3.1. Sec. 3.2 lists the data samples used for this work, and then we will go through the criteria for particle reconstruction and identification, reconstruction of B daughters, and B candidate selection, in Sec. 3.3, 3.4, and 3.5, respectively. We summarize our main analysis method to extract final results, the Maximum Likelihood (ML) fit, and relevant topics in Sec. 3.6, and finally we will discuss systematic uncertainties of our analyses in Sec. 3.7.

A **blind** analysis technique [67] is used for all the modes studied in this work. This means we conceal the signal region of the data sample until the analysis has been optimized for best signal-to-background ratio, and all the problems have been fixed. A false signal could be enhanced if the selection criteria are made to do so intentionally. By not looking at the signal region, this blind procedure reduces the risk of any such bias introduced while tuning the analysis parameters. When the analysis has been finalized, we are ready for **unblinding** to get analysis results from the full data sample.

3.1 The *BABAR* Software and Analysis Tools

The *BABAR* software environment includes online and offline systems. The online system is responsible for real-time control of the detector, monitoring, calibration, and

data acquisition as summarized in Sec. 2.3.7 on page 77.

The offline system consists of tools for simulation, reconstruction, data quality control, physics analysis, etc. Both online and offline systems are based on Object-Oriented (OO) design and use C++ [68] as their primary programming language. Codes are divided into modules, each of which performs a particular task, such that they can be reused for many purposes and across the two systems.

The offline tools share the same OO architecture in the *BABAR* Application Framework [69], which is a flexible, general purpose structure to enforce certain well designed standards of code behavior, using the Tool Command Language, TCL [70], as the user interface. The Framework is implemented as a class library, which defines the form of all user classes and the interactions between these classes.

The building blocks in the *BABAR* Framework are objects called **modules**. All the module classes inherit from the class `AppModule` so they share the same interface and can interact to each other in a coherent way. Four types of module are defined: input modules and output modules to control the input and output of data, filter modules to terminate or redirect subsequent data processing, and processing modules to take data from an event, run specific algorithms, and finally put the resulting data back to the event for later use.

Several related modules form a Framework **sequence** to be executed in an ordered manner to provide a defined service to the Framework, such as the reconstruction of a sub-detector. A **path** is formed by sequences and individual modules to control the flow of execution in the Framework. The actual *BABAR* offline job is done with an **execution path**, which starts from an active input module, ends at an active output module, and consists of one or more paths. Each module, sequence, or path, can be enabled (default) or disabled. Only those enabled can be seen by the Framework and executed.

Monte Carlo Simulation

The *BABAR* Monte Carlo (MC) Simulation produces simulated data for the signal and background studies in the blind analysis stage, and for cross check after unblinding. Several stages are required to produce these simulated data:

(1) Generation of the physics event.

Several event generators are used in the MC simulation for different purposes. They are interfaced to the *BABAR* Framework through `GenFwkInt` (Generators-Framework Interface) package [71]. The most commonly used generators are `EvtGen` [72] for simulating exclusive physics processes in decays of B mesons, and `Jetset` [73] for other inclusive B decays, and generic continuum events.

(2) Particle transport and calculation of energy deposits in the detector.

The propagation of the generated particles through the *BABAR* detector is simulated by `BOGUS`, the *BABAR* Object-oriented Unified Simulation program [74], which is implemented via `GEANT4` [75], a toolkit for the simulation of the passage of particles through matter.

The first two stages are done in one executable called `BgsApp`. The program produces an output file in a data structure called **GHits**, which contains the (idealized) energy deposited by the particles passing through the detector, and the locations of the deposit.

(3) Overlaying of backgrounds and digitization of the energy deposits.

The idealized `GHits` data is then processed by a package called `SimApp`. This program overlays backgrounds with the `GHits` and produces signals which look as exactly as possible as the real data collected by the detector electronics.

The backgrounds overlaid are not simulated. They are actual detector event samples recorded with a random trigger.

(4) Reconstruction.

The raw data from simulation is reconstructed with a package called `Bear`, in the same way as the real data is reconstructed in OPR by a package called `Elf`. The Bear application (`BearApp`) runs the full reconstruction chain, invoking the reconstruction modules within the SVT, DCH, DIRC, EMC and IFR sub-systems. Each reconstruction module uses pattern recognition, fitting algorithms, etc. to produce a set of objects representing the reconstructed information, such as candidates of cluster, track, etc. The output is various candidate lists of clusters, tracks, which can be used in physics analyses.

MC data for this work are produced in this `BgsApp-SimApp-Bear` three-step procedure. A new scheme, called **MOOSE** (Monolithic Object-Oriented Simulation Executable) [76], which finishes all the stages in one step, is now available for Simulation Production (SP).

Beta Toolkit

`Beta` [77] is a toolkit for use with *BABAR* data to do physics analysis. It consists of multiple packages, including:

- `Beta`, basic package of the base classes, etc.
- `BetaTools` and `BetaCoreTools`, analysis level tools.
- `BetaUser`, sample package which can be used to build user-level analysis tools.

and many more.

In this level, there is usually no need to access raw data, rather, `Beta` provides lists of **candidate**, which is the `Beta` representation of particle that may have existed in the event in question. For example, charged tracks can be candidate pions, and neutral clusters can be candidate photons. The output of vertexing two candidates is a composite candidate for a particle which decays into those two candidates. The

vertexing is one of the **operators** `Beta` provides to combine one or more candidates to form new ones. Other operators include four-vector addition, geometric or kinematic fitting, etc.

`Beta` also defines higher level classes for physics analysis. Candidates can be filtered by **selectors** which apply some "cuts" to select appropriate hypotheses. Selectors include many different types from general PID selectors based on various algorithms, to composite selectors which build, for example, D and B mesons, and to specific selectors tailored for individual analyses. **Associators** can be used to link daughter and mother particles in decay trees, and to associate charged track candidates with neutral cluster candidates, etc., or to associate reconstructed candidates with their appropriate MC truth candidates for MC data.

Based on `Beta`, the `BetaTools` and `BetaCoreTools` packages [78] provide a diverse set of tools essential to many physics analyses. The `BetaCoreTools` package contains classes that calculate event shape variables (those associated with an event, or part of an event), utility functions for tasks like boosting a candidate and all its decay products, and simple vertexing (adding 4 momenta). The `BetaTools` package contains classes that provide MC truth association with reconstructed candidates, micro smearing/killing classes for efficiency corrections of MC data, and various candidate selectors and other useful tools not in the core package.

Users can build their own analysis tools on top of `Beta`, making use of the existing physics analysis tools, to add new features specific to their own needs. `BetaUser` package is provided as a template for such purpose. Analyses in this work are done on the `Beta` level using a package called `Q2BUser` [79], which provides a generic framework for the study of charmless-2-body decays. The event reconstruction, selection, and output has been standardized for all the decays of this type, and `tcl` configuration files specific to individual decay modes are used to control the package to use appropriate data, perform corresponding analysis, and produce desirable output for each of them.

CompositionTools

As mentioned before, `Beta` provides a whole collection of `operators` and `selectors` to reconstruct **composite** particles from existing candidates. `CompositionTools` [80], which consists of many such tools, is the package used to produce lists of composite candidates describing a given decay reaction.

The reconstruction of composite candidates in this package is performed in two separated and independent steps:

- Combinatorics.

  Possible combinations of candidates are determined according to the decay tree based on the charge and type of input candidates. A generic combinatoric engine is implemented.

- Selection.

  Several selection criteria are applied to those combinations, and those passing the selections are output into the final list of composite candidates corresponding to the decay tree. Several generic vertexing/kinematic fitters and vertexers have been implemented.

All the classes of `CompositionTools` inherit from `CompositeSelector`, which can take up to 5 lists of daughters, their mass hypotheses, and a set of selection criteria, reconstruct decay trees in the two steps with generic implementations, and finally store the composite candidates into an output list for later use. Based on `CompositeSelector`, other base composite candidate selector classes include: `CompTwoBodySelector`, a base class for selectors of particles decaying to two body, `CompV0Selector`, a base class for selectors of long-lived particles (K^0s, Λ, etc.), `CompB0Selector`/`CompBSelector`, base classes for selection of neutral and charged Bs.

It is beneficial to have the two-step design of reconstruction and the hierarchy of selectors. A new selector just needs to have the decay tree specified if other imple-

mentations of the selector are quite standard and, if more specific criteria are required, only those selection functions need to be overridden. It is convenient for selectors to have several levels of selection criteria for different purposes, and because of the architecture of the package, it is very easy to implement several similar selectors. Four levels of criteria are usually defined for selectors: `VeryLoose`, `Loose`, `Tight`, and `VeryTight` selectors.

In addition to the selector implementation standards and many base classes, the `CompositionTools` package provides a **factory** of numerous specific selectors already implemented and validated for many physics analyses.

The `Q2BUser` package makes use of the base selectors and selectors in the factory of `CompositionTools` to reconstruct full B decay trees for charmless (quasi-)two-body rare B decays with minimal efforts in the actual coding of the selectors and most of the control and configurations can be done in individual `tcl` files.

ROOT and RooFit

Higher level data analysis than `Beta` deals with physics variables which can be decoupled from the *BABAR* environments. Common platforms for this final stage of the whole analysis cycle are `PAW`, Physics Analysis Workstation [81], and `ROOT` [82]. PAW, written in Fortran, was a popular interactive analysis tool in the experimental particle physics community before `ROOT` was introduced in 1995.

`ROOT` is an object-oriented data analysis system written by the creators of PAW. The `ROOT` system provides a set of OO frameworks with all the functionality needed to handle and analyze large amounts of data in a very efficient way. Its programming language is C++, which is also the command language, and the scripting, or macro, language of the system because it has a builtin CINT [83] C++ interpreter which can run C++ codes interpretively. Its class library can be grouped into several categories: base classes, container classes, histogram classes, tree and ntuple classes, graphics classes,

etc., which provides a powerful set of tools capable to do sophisticated experimental particle physics analysis and beyond.

Analysis packages can also be built upon `ROOT` infrastructure. One widely used package in *BABAR* analysis is `RooFit` [84], a toolkit for data modeling based on `ROOT`. It provides a powerful extension to `ROOT` for data modeling, fitting, plotting, and data generating for various studies, which satisfies the needs of *BABAR* physics analysis. Users can build their own analysis package based on `RooFit` and `ROOT`.

Final analyses for this work are done with `Q2BFit` [85,86], a fitting package based on `RooFit` and `ROOT`, and working with `Q2BUser`, for the purpose of charmless rare B decay analysis. The `Q2BFit` package provides a general fitting environment for this type of analysis. In this package, the coding is minimal and the fitter is controlled through plain ASCII configuration files, which are understandable to the program through the `RooFit` interface. Several types of fitting procedures are defined to fulfill different stages of the final analysis, including distribution shape modeling, plotting, fitting validation, final branching fraction fitting, time-dependent fitting, etc. `Q2BFit`, together with other small scripts and programs, is the main tool to extract our final results.

The *BABAR* software packages have been developed and improved constantly. The Software Release Tools (SRT), based on Concurrent Version System (CVS) [87], are used to manage the release control. Stable versions of packages are given logical tags. A *BABAR* software release contains a consistent set of packages, one tagged version for each of them, together with the libraries and binaries created for various machine architectures. Users usually create their own `working` release by checking out a light-weighted collection of packages of particular releases and then tailor those packages for their analyses.

In addition to the software and tools mentioned above, *BABAR* also makes use of many other available software systems. These include the Experimental Physics and

Industrial Control System (EPICS) [88], which is the interface for detector control, the Java Analysis Studio (JAS) [89], a java [90] based application, which is used for *BABAR* online data quality monitoring, and World-Wide Web Interactive Remote Event Display (WIRED) [91], which is *BABAR*'s java based graphical tool for event display (see plots in Figure 3.15 on page 122 for display examples).

3.2 Data Sets

The data sample used for the analyses in this work is based on full Run1 (1999–2000) and Run2 (2001–Summer 2002) datasets with integrated luminosity of $9.6\,\mathrm{fb}^{-1}$ for off-peak data and $81.9\,\mathrm{fb}^{-1}$ for on-peak data (see Figure 2.4 on page 44) which corresponds to 88.9×10^6 produced $B\overline{B}$ pairs. These data have been processed or reprocessed with 10-series releases.

The *BABAR* reconstructed data are stored in several formats with different levels of detail: The "Raw" database which contains the Raw data out of the detector (e.g. details of individual "hits" on crystals in the EMC) for each subdetector, the "Reco" database which contains the processed Raw data as well as the Raw data, the new "Mini" database which is a reduced Reco for better efficiency, the "Micro" database which contains all the information needed for physics analysis, and the "Nano" database which contains tags for fast data access [92].

The *BABAR* data are grouped into different "skims" and "streams" to reduce the data sample for a given analysis. A skim usually refers to events selected for a particular channel, while several skims group together to form a stream. Among the many different physical databases used to store these streams in *BABAR*, the Kanga (Kind ANd Gentle Analysis) [93] databases are most convenient for individual physics analyses.

We use stream 12 (charmless stream) Kanga data and start from all events passing the `TagOmegaTwoBody_maxCmsPmaxCosT` tag bit for ω. For the $B^0 \to \omega K^0$ analysis, we also require that the `TagK_S0TwoBody_maxCmsPmaxCosT` is set for K^0_S.

Table 3.1: Summary of signal Monte Carlo samples used for different modes. Each polarization component for VV modes is listed.

mode	# Evt	mode	transverse	longitudinal
ωK^+	40K	$\omega K^{*+}_{K^0_S\pi^+}$	41K	41K
		$\omega K^{*+}_{K^+\pi^0}$	41K	39K
ωK^0	36K	$\omega K^{*0}_{K^+\pi^-}$	40K	40K
$\omega\pi^+$	43K	$\omega\rho^+$	41K	41K
		$\omega\rho^0$	36K	36K

For signal Monte Carlo studies we use SP4 (MC production with 10-series releases) exclusive signal Monte Carlo samples produced with 10-series releases. A summary of the signal Monte Carlo samples used by each analysis can be found in Table 3.1. We use these data to determine the selection efficiency for each mode and obtain signal distributions of observables.

We use the sideband region (see Sec. 3.5.1 on page 118) of on-peak data for continuum backgrounds studies, and different types of Monte Carlo samples for various background studies, including a sample of 17.2 million charmless $B\overline{B}$ SP4 MC events (corresponding to a sample of 345 million generic $B\overline{B}$ events) and 137 million B^+B^- (127 million $B^0\overline{B}^0$) SP4 MC events. We also use exclusive Monte Carlo samples for background studies if needed, and those samples are listed in Sec. 3.5.3.

The charmless $B\overline{B}$ MC data consist of a "cocktail" of charmless hadronic B decay modes. One of the B's in each event is forced to decay into charmless hadronic final states, while the other B decays freely. We use these data to study the backgrounds from other charmless hadronic B decays with similar kinematics to those modes studied here. Generic $B\overline{B}$ events, where B mesons decay inclusively, are used to study peaking $b \to c$ backgrounds.

Several "smearing/killing" procedures are applied to the MC data to correct for the efficiency differences between MC and data, including the Spring 2002 "neutral smearing" procedure [94] recommended by the Neutral Reconstruction AWG (Analysis

Working Group), a procedure based on the standard "PID Killing" [95], which forces the PID efficiencies in Monte Carlo to match those measured from data control samples and documented in the official PID efficiency tables.

We also use Charmed control samples which are topologically similar to our signal modes to study how well the Monte Carlo reproduces quantities directly related to our decay modes.

The Kanga data are processed by the `Q2BApp` of the `Q2BUser` package based on the `analysis-13` release. The list of non-default reconstruction packages used in this work can be found in Table 3.2. The output is Ntuples in `root` files. Each Ntuple has about 150 variables storing reconstructed physics information about events, B mesons, B decay daughters, and final decay particles.

Table 3.2: List of package versions later than those contained in `analysis-13` release for Ntuple production.

Package	Version
PARENT release	10.4.4-physics-1 (`analysis-13`)
workdir	V00-04-08
Q2BUser	V00-10-44
AbsBTagging	V00-02-01
BTaggingSequences	jb-050102
BTaggingTools	V00-02-01
BTaggingUser	V00-02-01
BTaggingUtils	V00-02-01
BetaCoreTools	mvh20052002
BetaMicro	V00-01-17-03
BetaMicroTruth	V00-00-06-01
BetaTools	V00-10-27-07
CompositionSequences	fdl030102
CompositionUtils	fdl030102

3.3 Particle Reconstruction and Identification

The reconstructed data for physics analysis are candidate lists of charged tracks, neutral particles as energy deposits in the EMC, etc. We use these candidates to reconstruct our final decay products, B daughter particles, B mesons, and event shape variables.

3.3.1 Charged Tracks

Several charged track lists are defined for analysis purposes, including:

- `ChargedTracks`:

  Candidates with non-zero charge and with pion mass hypothesis.

- `GoodTracksVeryLoose`: Subset of `ChargedTracks` with additional requirements:
  - $0 < p_T < 10\,\mathrm{GeV}/c$;
  - $\mathrm{DOCA}_{xy} < 1.5\,\mathrm{cm}$;*
  - $|\mathrm{DOCA}_z| < 10\,\mathrm{cm}$.
- `GoodTracksLoose`: Subset of `GoodTracksVeryLoose` with:
  - $p_T > 0.1\,\mathrm{GeV}/c$;
  - DCH Hits ≥ 12.
- `GoodTracksAccLoose`: Subset of `GoodTracksLoose` with:
  - $0.410 < \theta < 2.54\,\mathrm{rad}$.
- `GoodTracksTight`: Subset of `GoodTracksLoose` with additional cuts:
  - DCH Hits ≥ 20.
  - $\mathrm{DOCA}_{xy} < 1\,\mathrm{cm}$;
  - $|\mathrm{DOCA}_z| < 3\,\mathrm{cm}$.

* DOCA: Distance of closest approach of a track to the beam spot center

We use `ChargedTracks`, `GoodTracksVeryLoose`, and `GoodTracksLoose` charged track lists for our analyses.

3.3.2 Neutral Particles

Similar to charged tracks, the neutral particles reconstructed from the EMC are organized in several lists:

- `CalorNeutral`: Candidates which are single EMC bumps not matched with any track. Photon mass hypothesis assigned.
- `CalorClusterNeutral`: Candidates that are multi-bump neutral clusters or single bumps which are not part of a cluster which is matched with a track.
- `GoodNeutralLooseAcc`: Subset of `CalorNeutral` with additional requirements:
  - $E > 30\,\mathrm{MeV}$;
  - Lateral Moment ≤ 1.1;
  - $0.410 < \theta < 2.409$.
- `GoodPhotonLoose`: Subset of `CalorNeutral` with additional requirements:
  - $E > 30\,\mathrm{MeV}$;
  - Lateral Moment ≤ 0.8.
- `GoodPhotonDefault`: Subset of `GoodPhotonLoose` with:
  - $E_\gamma > 100\,\mathrm{MeV}$;

We use `GoodPhotonLoose` list for photons in our analyses.

3.3.3 Electron, Muon, and Proton Identification

Electrons, muons, or protons are not in the final states of B decays in our studies and we need to identify and reject these background tracks.

As we have discussed in Chapter 2, electrons are separated from charged hadrons primarily on the basis of the shower energy, lateral shower moments, and track momen-

Table 3.3: Electron identification selectors with selection criteria. The dE/dx is only from DCH and has a roughly Gaussian distribution with a peak at ~ 650 and $\sigma \sim 50$ for electron, LAT is lateral shower moments, A_{42} is the modulus of the Zernike moment of order (4,2) [96], DIRC cut is 3σ consistent with an electron hypothesis with the number of Čerenkov photons greater than 9.

Selector	dE/dx	E/p	LAT	A_{42}	DIRC cut	Trk-EMC match
`VeryLoose`	$-3\sigma, 7\sigma$	0.5, 5.0	$-10, 10$	$-10, 10$	—	—
`Loose`	$-3\sigma, 7\sigma$	0.65, 5.0	$-10, 10$	$-10, 10$	—	—
`Tight`	$-3\sigma, 7\sigma$	0.75, 5.0	0, 0.6	$-10, 10$	—	—
`VeryTight`	$-2.2\sigma, 4\sigma$	0.89, 1.2	0.1, 0.6	$-10, 0.11$	yes	yes

tum. Several selectors have been defined for electron PID (see Table 3.3) and we use the `VeryTight` one where the electron PID efficiency is about 88% and π misidentification rates are below 0.3%.

Muon identification depends almost entirely on the IFR, while the IFR muon identification system has very high π misidentification rates of about 6–8% (see Figure 2.28 on page 74), and combinatorial backgrounds from muon is not high. So we do not use muon veto for the purpose of higher selection efficiency.

Protons are identified using the `LH` proton selector which is a likelihood based selector. It calculates the likelihoods of the charged track being proton, π, or K (see Sec. 3.3.4) and compares the ratio of likelihoods to determine if the track is proton. The criteria are listed in Table 3.4, and we use the `VeryTight` criteria of the selector, which has a proton PID efficiency of about 30% and K, π misidentification rates less than $\sim 0.3\%$ [97].

3.3.4 Kaon Identification

Kaons are selected with information from three *BABAR* sub-detectors: dE/dx in SVT and DCH, the number of Čerenkov photons and the Čerenkov angle in the DIRC [98–100].

Table 3.4: Proton LH selectors with different criteria. $\mathcal{L}(\pi, K, p)$ are the likelihoods of being π, K, and p, respectively.

Types	$\mathcal{L}(p)/\mathcal{L}(K) >$	$\mathcal{L}(p)/\mathcal{L}(\pi) >$	electron veto	muon veto
`VeryLoose`	4/3	0.50	—	—
`Loose`	3.0	0.50	if $p > 0.75\,\mathrm{GeV}/c$	—
`Tight`	5.0	0.75	if $p > 0.75\,\mathrm{GeV}/c$	—
`VeryTight`	10.0	0.96	if $p > 0.75\,\mathrm{GeV}/c$	yes

The momenta of the kaons from K^* extend up to about $3.5\,\mathrm{GeV}/c$, with most of them below $1.5\,\mathrm{GeV}/c$. Kaons and pions directly from B mesons have momenta between 1.7 and $4.2\,\mathrm{GeV}/c$.

From the truncated-mean $\mathrm{d}E/\mathrm{d}x$ measurements a better than 2σ K/π separation is possible for particle momentum up to $0.7\,\mathrm{GeV}/c$ in the DCH and $0.6\,\mathrm{GeV}/c$ in the SVT. For momenta above $0.7\,\mathrm{GeV}/c$ the DCH provides about 2σ $\mathrm{d}E/\mathrm{d}x$ K/π separation (see Figure 2.15 on page 59). The DIRC provides K/π separation of $\sim 4\sigma$ or greater, for all tracks from B-meson decays, with momenta from the pion Čerenkov threshold, up to $3\,\mathrm{GeV}/c$.

The differences between the measured truncated-mean $\mathrm{d}E/\mathrm{d}x$ in the DCH and the expected mean for the pion, kaon, and proton hypotheses have Gaussian distributions with typical resolution of 7.5%. The difference between the measured 60% truncated-mean $\mathrm{d}E/\mathrm{d}x$ in the SVT and the expected $\mathrm{d}E/\mathrm{d}x$ can be described by an asymmetric Gaussian distribution with resolution of about 14%. In the DIRC, the expected number N_γ of Čerenkov photons has a Poisson distribution, and the difference between the measured average Čerenkov angle θ_c (see Figure 2.20 on page 64) and the expected angle θ_c^0, for a given hypothesis, has a Gaussian distribution. The likelihoods for π, K, and p hypotheses, $\mathcal{L}(\pi)$, $\mathcal{L}(K)$ and $\mathcal{L}(p)$, are calculated based on the those distributions.

The `PidKaonSMSSelector` is a likelihood-based selector for kaon selection. It makes use of information from SVT, DCH, or DIRC based on track momenta. It also

has several selection modes with different requirements.

- `NotAPion`: optimized with respect to kaon efficiency by rejecting pions
  momentum range [GeV/c]
  SVT : < 0.5
  DCH : < 0.6
  DIRC : > 0.6
  $\mathcal{L}$ cut : reject, if $r_\pi \mathcal{L}(\pi) > \mathcal{L}(K)$ & $r_\pi \mathcal{L}(\pi) > \mathcal{L}(p)$
  $p \leq 0.5\,\mathrm{GeV}/c$: $r_\pi = 0.1$
  $p > 0.5\,\mathrm{GeV}/c$: $r_\pi = 1.0$

- `Loose`:
  momentum range [GeV/c]
  SVT : $< 0.7, p > 1.5$
  DCH : $< 0.7, p > 1.5$
  DIRC : > 0.6
  $\mathcal{L}$ cut : $\mathcal{L}(K) > r_\pi \mathcal{L}(\pi)$ if no DIRC information
  : $\mathcal{L}(K) > r_\pi \mathcal{L}(\pi)$ & $\mathcal{L}(K) \geq r_p \mathcal{L}(p), r_p = 1$
  $p < 2.7\,\mathrm{GeV}/c$: $r_\pi = 1$
  $p > 2.7\,\mathrm{GeV}/c$: $r_\pi = 80$
  $0.5 < p < 0.7\,\mathrm{GeV}/c$: $r_\pi = 15$

- `Tight`:
  momentum range [GeV/c]
  SVT : < 0.7
  DCH : < 0.7
  DIRC : > 0.6
  $\mathcal{L}$ cut : $\mathcal{L}(K) > r_\pi \mathcal{L}(\pi)$ & $\mathcal{L}(K) > r_p \mathcal{L}(p), r_p = 1$
  $p < 2.7\,\mathrm{GeV}/c$: $r_\pi = 1$
  $p > 2.7\,\mathrm{GeV}/c$: $r_\pi = 80$
  $0.5 < p < 0.7\,\mathrm{GeV}/c$: $r_\pi = 15$

- `VeryTight`:
  momentum range [GeV/c]
  SVT : < 0.6
  DCH : < 0.6
  DIRC : > 0.6
  $\mathcal{L}$ cut : $\mathcal{L}(K) > r_\pi \mathcal{L}(\pi)$ & $\mathcal{L}(K) > r_p \mathcal{L}(p), r_p = 1$
  $p < 2.5\,\mathrm{GeV}/c$: $r_\pi = 3$
  $p > 2.5\,\mathrm{GeV}/c$: $r_\pi = 200$
  $0.4 < p < 0.7\,\mathrm{GeV}/c$: $r_\pi = 20$

We use the `VeryTight` kaon selector, which is optimized to keep the mis-identification rates below 2% up to momenta of 4 GeV/c, for particle identification of tracks from B-daughter resonances. (see Sec. 3.4).

3.3.5 π^0 Selection

Candidates for π^0 are reconstructed from two photons through $\pi^0 \to \gamma\gamma$ with branching fraction $\mathcal{B} \sim 98.80\%$. The `Pi0Selector` combines two photon candidates from `GoodPhotonLoose` list. Several π^0 selectors are defined [101] to create the following lists:

- `pi0VeryLoose`:
  photon list : `GoodPhotonLoose`
  E_γ : > 30 MeV
  LAT : < 0.8
  M_{π^0} : > 90 MeV/c^2
  M_{π^0} : < 165 MeV/c^2

- `pi0Loose`: same cuts as `pi0VeryLoose`, with more requirements:
  E_{π^0} : > 200 MeV
  M_{π^0} : > 100 MeV/c^2
  M_{π^0} : < 160 MeV/c^2

- `pi0LooseMass`: same cuts as `pi0Loose`, with additional requirements:
  π^0 mass constraint : yes
  Use primary vertex: yes

- `pi0DefaultMass`: subset of `pi0LooseMass`, with more requirements:
  M_{π^0} : > 115 MeV/c^2
  M_{π^0} : < 150 MeV/c^2

We show in Figure 3.1 the invariant mass, $M_{\gamma\gamma}$, distribution of π^0 candidates output by `pi0DefaultMass` for the π^0 in ω decays. The background is mainly from combinatorics. To further reduce the backgrounds, we require tighter cuts after Ntuple production:

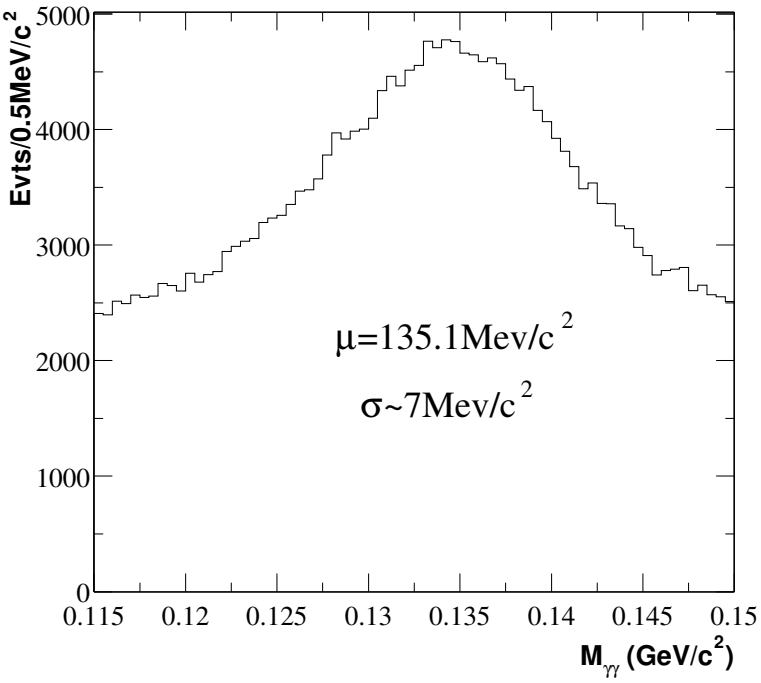

Figure 3.1: Invariant mass $M_{\gamma\gamma}$ for π^0 candidates with $E_{\pi^0} > 200\,\mathrm{MeV}$. The π^0's are from ω decays in on-peak data. (The plots shown in this chapter using full on-peak data are got after all the analyses have been done and serve as demonstrations only.)

- $120 < m^{\pi^0}_{\gamma\gamma} < 150$ MeV/c^2,
- $E_{\pi^0} > 250\,\mathrm{MeV}$,
- $E_\gamma > 50\,\mathrm{MeV}$.

3.3.6 K^0_S Selection

Neutral kaons are reconstructed through decays $K^0_S \to \pi^+\pi^-$ with a branching fraction of 68.95%. The `KsToPiPiSelector` combines two opposite charged tracks from `ChargedTracks` list to form K^0_S. The following K^0_S lists are created with different criteria [102, 103]:

- `KsLoose`:
  `ChargedTracks` : All opposite charged combinations
  $M_{\pi^+\pi^-}$(unfitted) : $[300, 700]\,\mathrm{MeV}/c^2$

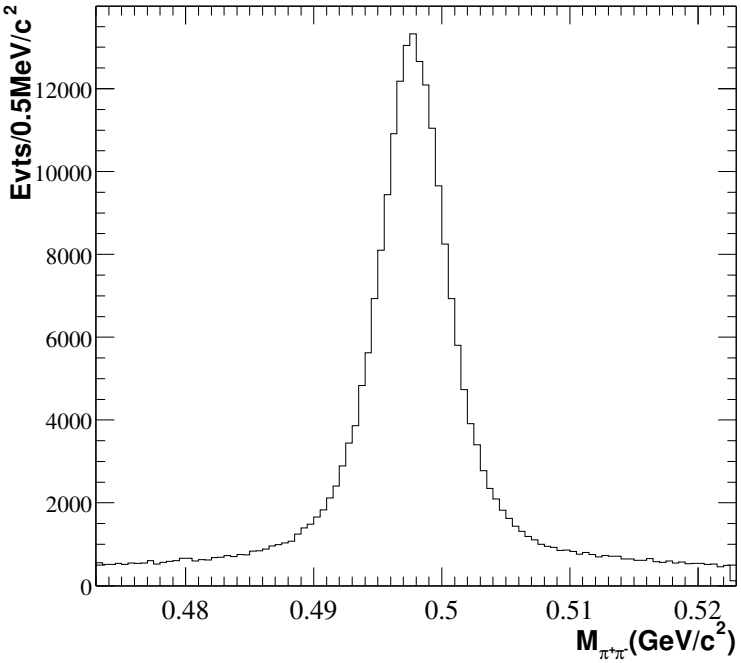

Figure 3.2: Invariant mass $M_{\pi^+\pi^-}$ for K^0_S candidates in `KsDefault` list. The K^0_S's are from on-peak data with $B^0 \to \omega K^0$ decay hypothesis.

- `KsDefault`: Subset of `KsLoose`, with fits on both position and momentum information [104], and:
  $M_{\pi^+\pi^-}$(fitted) : within $\pm 25\,\mathrm{MeV}/c^2$ PDG value

- `KsTight`: Subset of `KsDefault` with mass constraint.

- `KsVeryTight`: Subset of `KsDefault` with cuts:
  $M_{\pi^+\pi^-}$(fitted) : within $\pm 15\,\mathrm{MeV}/c^2$ PDG value

The invariant mass $M_{\pi^+\pi^-}$ distributions for candidates in the `KsDefault` list are shown in Figure 3.2, from where we can see very clean signals.

After the Ntuple production, we require additional cuts on K^0_S's:

- For non-prompt K^0_S: the lifetime significance ($\tau/\sigma_\tau > 3$);

- For prompt K_S^0:
  - Primary vertex is used in the `KsDefault` selector,
  - three-dimensional flight distance from the primary vertex $> 2\,\text{mm}$,
  - two-dimensional angle between flight and momentum vectors $< 40\,\text{mrad}$.

We also set tighter mass range of K_S^0 for both cases: $488 < M_{\pi\pi}^{K_S^0} < 508\,\text{MeV}/c^2$, but do not apply any further PID cuts to its $\pi^+\pi^-$ daughters.

3.4 *B* Daughter Selection

We will discuss the reconstruction and selection of B decay products in this section. The distributions of the invariant masses of B daughters and other physics quantities, which can be described by probability density functions (PDFs), are very important to distinguish signals from backgrounds, and we rely on their discriminating power to get final results.

3.4.1 ω Selection

The ω mesons are reconstructed from two charged tracks in `GoodTracksLoose` list and a π^0 in `pi0DefaultMass` list through the channel $\omega \to \pi^+\pi^-\pi^0$ with a branching fraction of 89.1%. After combining two charged tracks and one neutral track, the ω selector does kinematic and geometric fits to the candidates and also requires the invariant mass within a $[-50, 50]\,\text{MeV}/c^2$ range of the ω mass [12]. We make additional cuts after finishing the `Beta` job and require:

- $735 < m_{\pi\pi\pi}^{\omega} < 825$ MeV/c^2,
- Additional cuts on π^0 as in Sec. 3.3.5,
- Charge π's must NOT satisfy the `VeryTight` criteria of the electron `Micro` selector, or the `VeryTight` criteria of the proton `LH` selector (see Sec. 3.3.3),

Table 3.5: Scale factors, $f_{\rm scale}$, and shift parameters, $\mu_{\rm offset}$, applied to the $\omega_{3\pi}$ mass distributions to correct for differences between data and Monte Carlo.

Mode	Scale Factor	Shift (MeV/c^2)
$\omega\pi^+$	1.138 ± 0.041	1.5 ± 0.3
ωK^+	1.087 ± 0.067	1.0 ± 0.5
$\omega K^{*+}_{K^+\pi^0}$	0.942 ± 0.100	1.1 ± 0.6
$\omega K^{*+}_{K^0_S\pi^+}$	0.933 ± 0.080	0.8 ± 0.5
$\omega K^{*0}_{K^+\pi^-}$	1.149 ± 0.079	0.5 ± 0.4
$\omega\rho^+$	0.990 ± 0.053	1.3 ± 0.3
$\omega\rho^0$	0.984 ± 0.051	1.0 ± 0.3
average	1.05 ± 0.02	1.1 ± 0.1

- Charge π's must NOT satisfy the `Tight` criteria of the `SMS` kaon selector (see Sec. 3.3.4).

Shown in Figure 3.3 are the invariant mass distributions of ω for signal and continuum background. We fit the signal distributions with double-Gaussian, which has a mean of about 782 MeV/c^2, $\sigma_{\rm core} \sim 8.4$ MeV/c^2 for the core distribution, which is close to ω width [12], and $\sigma_{\rm tail} \sim 25$ MeV/c^2 for the tail distribution, which is mainly due to mis-reconstructed ω. In addition to combinatoric background, there is real ω in the continuum background, so we fit the continuum background distributions with the double-Gaussian of signal for real ω, with distribution parameters fixed, and a quadratic component for the combinatoric background.

The distribution parameters from fits to the signal MC can be slightly different from the true values for real data, so we define the core-Gaussian mean offset terms, $\mu_{\rm offset}$, and width scale factors, $f_{\rm scale}$, to allow for the differences between data and MC. In the final fitting, the core mean is set to $\mu_{MC} + \mu_{\rm offset}$ and the core width to $\sigma_{MC} \times f_{\rm scale}$.

We find adequate statistics for this purpose in the sideband sample to fit directly for these correction parameters. We tabulate them in Table 3.5 along with values

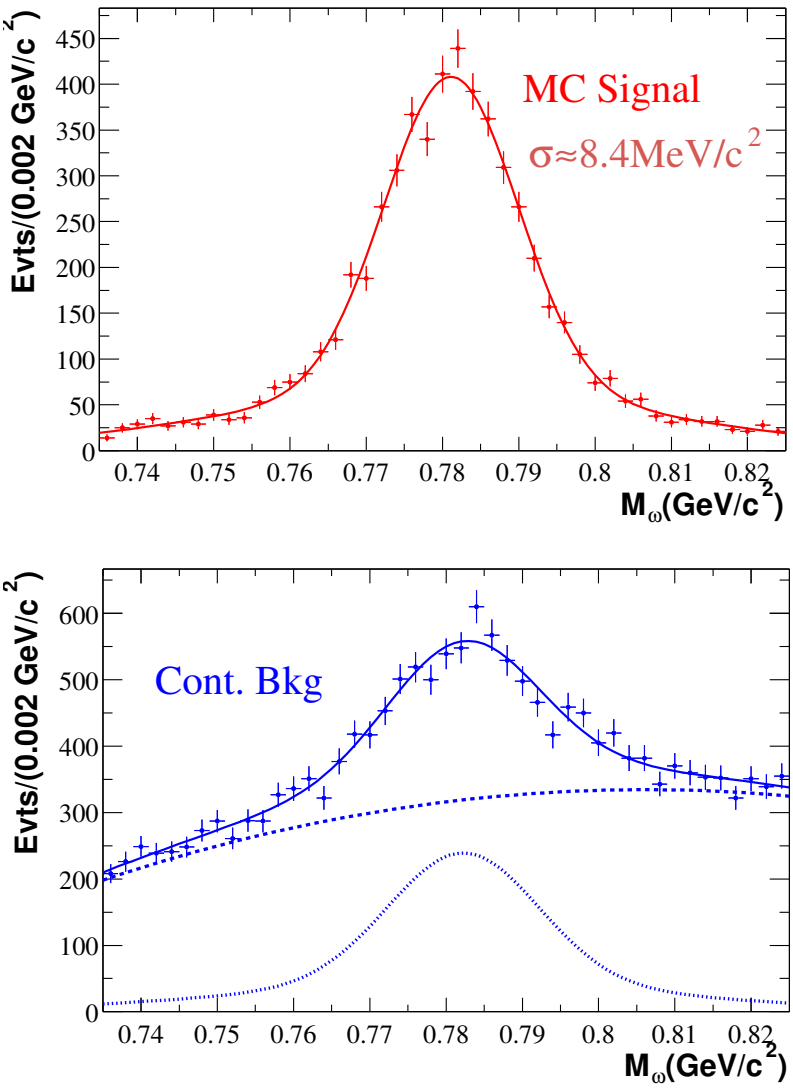

Figure 3.3: Distributions of invariant mass $M_{\pi^+\pi^-\pi^0}$ of ω candidates for signal (top) from signal MC data, and continuum background (bottom) from sideband data. The distribution shape for signal is double-Gaussian, with $\mu \sim 782\,\mathrm{MeV}/c^2$ and $\sigma_{\mathrm{core}} \sim 8.4\,\mathrm{MeV}/c^2$; the shape for continuum background is a quadratic component (dashed curve) overlaid with a real ω component (dotted curve).

averaged over the several fits [105,106]. These averages become fixed parameters in the final fits.

3.4.2 K/π Separation

As we have discussed in Sec. 2.3.3, and 3.3.4, the high momentum K/π tracks directly from B mesons are identified mainly through information from DIRC. When a high momentum charged track with $\beta = v/c$ passes the DIRC, Čerenkov photons are emitted to form a light cone in the particle flight direction with open angle θ_c, the Čerenkov angle, being $\cos^{-1}(1/n\beta)$, where $n = 1.473$ is the index of refraction of the DIRC quartz bar. The DIRC measures θ_c with an error of σ_{θ_c}, and for each particle identification hypothesis, there is an expected Čerenkov angle, ${\theta_c}^i$, where $i = K, \pi$. We define the DIRC pull S^i as:

$$S^i = \frac{\theta_c - {\theta_c}^i}{\sigma_{\theta_c}}, \quad i = K, \pi. \tag{3.1}$$

The pull S^i distributions for particle with correct hypotheses are normal Gaussian with $\mu = 0$, and $\sigma = 1$, while those for wrong hypotheses are shifted from zero, with wider widths, as shown in Figure 3.4.

We include the pull distributions in our final fits for modes with a bachelor track directly from B's and fit the modes with K/π together, so we make very loose cuts on the pulls after `Beta` jobs:

- $-3.5 < S^K < 24.5$,
- $-24.5 < S^\pi < 3.5$

and let the fitter resolve the ambiguity of K/π identification for the overlapped region between the two distributions. We also require the number of measured Čerenkov photons (DIRC PMT hits) for the bachelor track > 5 to ensure the quality of θ_c.

The DIRC pull calculation is done actually after `Beta` jobs and just before we make additional cuts, using information of θ_c, ${\theta_c}^{K/\pi}$, track momentum, charge, etc.,

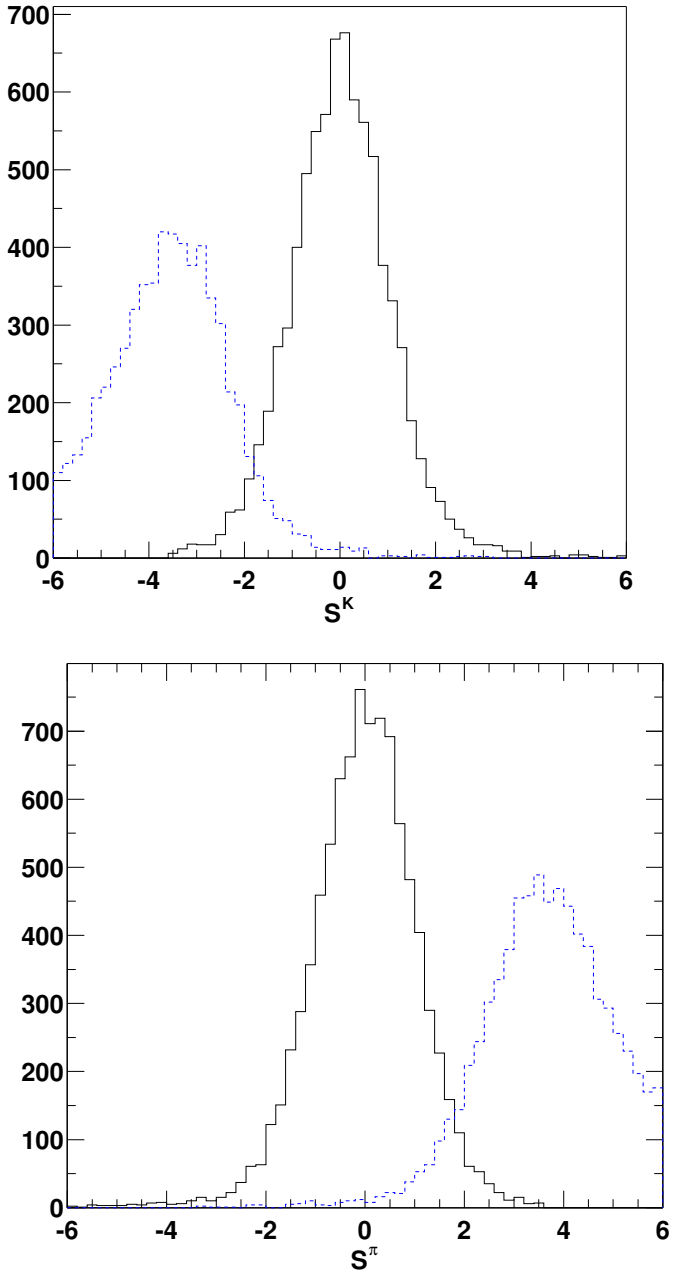

Figure 3.4: Distributions of DIRC pull S^i for K (top) and π (bottom), where the solid curves are for correct hypotheses, with normal Gaussian distributions, and the dashed curves are for incorrect hypotheses, with shifted means, and wider widths. The distributions are got from signal MC for ωK^+ (top) and $\omega\pi^+$ (bottom) with corrections (see text for explanation).

with a function called `DrcThetaFix` [107]. `DrcThetaFix` takes the θ_c "pull" $(\theta_c - {\theta_c}^{K/\pi})$ as input, and uses information about the charge of the track and its polar angle to bin the θ_c pulls so that each bin has optimized corrections to the θ_c pull distributions. In order to determine the DIRC pull, we add the offset $\mu^{(K,\pi)}_{(\mathrm{MC,Data})}$ and divide by the resolution $\sigma^{(K,\pi)}_{(\mathrm{MC,Data})}$ of each polar angle bin. The offsets and resolutions are tabulated in `DrcThetaFix` for both data and MC. The resulting pulls are shown in (3.2) and (3.3) for MC and data, respectively:

$$S^K_{\mathrm{MC}} = \frac{\left(\theta_{c,\mathrm{MC}} - {\theta_c}^K\right) + \mu^K_{\mathrm{MC}}}{\sigma^K_{\mathrm{MC}}} \qquad S^\pi_{\mathrm{MC}} = \frac{\left(\theta_{c,\mathrm{MC}} - {\theta_c}^\pi\right) + \mu^\pi_{\mathrm{MC}}}{\sigma^\pi_{\mathrm{MC}}} \tag{3.2}$$

$$S^K_{\mathrm{Data}} = \frac{\left(\theta_{c,\mathrm{Data}} - {\theta_c}^K\right) + \mu^K_{\mathrm{Data}}}{\sigma^K_{\mathrm{Data}}} \qquad S^\pi_{\mathrm{Data}} = \frac{\left(\theta_{c,\mathrm{Data}} - {\theta_c}^\pi\right) + \mu^\pi_{\mathrm{Data}}}{\sigma^\pi_{\mathrm{Data}}}\,. \tag{3.3}$$

Computing the pulls in this manner would be adequate if the MC properly represented the θ_c distribution in data. However, the MC θ_c distribution has better resolution, causing the MC K/π separation to be too good. As a result, we use information already known about the θ_c pulls to match the θ_c distribution in MC to that of data.

Because the MC and data θ_c distributions were independently calibrated [107] to give normal Gaussian pulls for the correct hypothesis, we know that for the same value of polar angle and charge, a unique pair of $\theta_{c,\mathrm{MC}}$ and $\theta_{c,\mathrm{Data}}$ values will give the same DIRC pull. We can thus equate $S^{(K,\pi)}_{\mathrm{MC}}$ and $S^{(K,\pi)}_{\mathrm{Data}}$ and solve for $\theta_{c,\mathrm{Data}}$. When doing this, we must be careful to use the data and MC pulls corresponding to the true species of the track in question; this is where we use the MC truth of the track. The corrected θ_c value for the MC, $\theta_{c,\mathrm{MCcorr}}$, as the result of solving for $\theta_{c,\mathrm{Data}}$ is shown in (3.4) for a true kaon, and (3.5) for a true pion.

$$\text{True MC Kaon:}\quad \theta_{c,\mathrm{MCcorr}} = {\theta_c}^K + \left[\left(S^K_{\mathrm{MC}}\,\sigma^K_{\mathrm{Data}}\right) - \mu^K_{\mathrm{Data}}\right]\ \text{“=”}\,\theta_{c,\mathrm{Data}} \tag{3.4}$$

$$\text{True MC Pion:}\quad \theta_{c,\mathrm{MCcorr}} = {\theta_c}^\pi + \left[\left(S^\pi_{\mathrm{MC}}\,\sigma^\pi_{\mathrm{Data}}\right) - \mu^\pi_{\mathrm{Data}}\right]\ \text{“=”}\,\theta_{c,\mathrm{Data}}\,. \tag{3.5}$$

We then use the corrected θ_c distribution as the input to the original `DrcThetaFix` code, but using the data offsets and resolutions to compute the corrected DIRC pull. In (3.6)

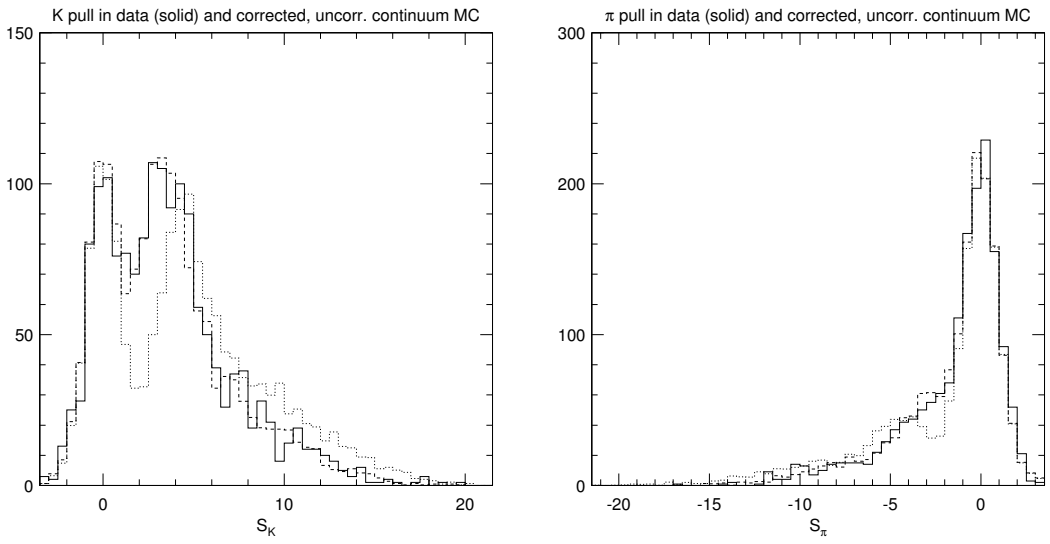

Figure 3.5: Kaon (left) and pion (right) pull distributions for off-peak data (solid line), corrected continuum MC (dashed line) and uncorrected continuum MC (dotted line). The distributions are for $B^+ \to \eta h^+$ ($h = K, \pi$) hypothesis.

and (3.7) we give the corrected kaon and pion pull calculation, respectively.

$$\text{Corr. MC Kaon Pull:} \quad S^K_{\text{MCcorr}} = \frac{\left(\theta_{c,\text{MCcorr}} - \theta_c{}^K\right) + \mu^K_{\text{Data}}}{\sigma^K_{\text{Data}}} \text{ “=” } S^K_{\text{Data}} \tag{3.6}$$

$$\text{Corr. MC Pion Pull:} \quad S^\pi_{\text{MCcorr}} = \frac{\left(\theta_{c,\text{MCcorr}} - \theta_c{}^\pi\right) + \mu^\pi_{\text{Data}}}{\sigma^\pi_{\text{Data}}} \text{ “=” } S^\pi_{\text{Data}}\,. \tag{3.7}$$

By construction, if we have a true pion and compute the pion pull, we end up with the normal Gaussian distribution by simply using the MC pull calculation (without correcting θ_c, as given in (3.2)). The difference comes, however, when we compute, for example, the pion pull for a true kaon. Now we use $\theta_{c,\text{MCcorr}}$, so that the resulting pull value for the true kaon under the pion hypothesis will have identical separation to that of real data.

We show in Figure 3.5 the comparison between uncorrected continuum MC (dotted line) and off-peak data (solid line). With the dashed line in this figure, we show the results of the correction on continuum MC, which illustrates that our pull correction returns DIRC pull distributions consistent with those observed in data [108].

As we can see from Figure 3.6, the pull values of a given track for different K/π hypotheses are highly correlated, so S^K and S^π can not be taken as independent variables and special treatments are needed to put those variables into our final fits. We will discuss this matter in more detail in Sec. 3.6.1.

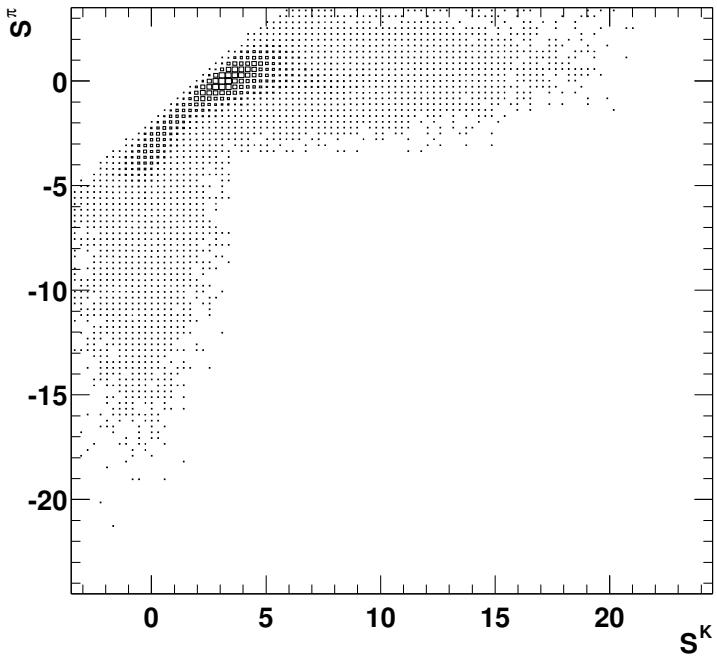

Figure 3.6: 2D distributions of DIRC pulls of K/π hypotheses, S^K (x-axis) vs. S^π (y-axis), for a given track. The correlation of the two pulls are clearly shown. The distributions are got from on-peak data for $B^+ \to \omega h^+$ decay hypothesis.

3.4.3 K^0_S Selection

We have discussed the reconstruction and selection of prompt K^0_S directly from B in Sec. 3.3.6. As we can see from Figure 3.2 on page 97, the K^0_S candidates in background (as is true for most of on-peak data) are dominantly real K^0_Ss, so fitting the mass distributions of K^0_S only deweight an already small combinatoric background.

Thus we only apply the cuts listed in Sec. 3.3.6 to K^0_S in the Ntuples and do not include K^0_S masses in our final fits.

3.4.4 K^* Selection

We reconstruct K^{*+} from two channels: $K^{*+} \to K^0_S\pi^+$ and $K^{*+} \to K^+\pi^0$, both with branching fractions of 33.3%, and K^{*0} from $K^{*0} \to K^+\pi^-$ with a branching fraction of 66.7%.

One charged track from `GoodTracksLoose` list of π hypothesis and one K^0_S from `KsDefault` list are combined to form K^{*+} candidates, or K^{*+} are selected from combinations of one charged track from `GoodTracksLoose` with K hypothesis and one π^0 from `pi0DefaultMass` list. Two opposite charged tracks from `GoodTracksLoose` are combined to form K^{*0} candidates. The selectors require the invariant masses of $K^+\pi^-$ and $K^0_S\pi^+$ to be within $[-100, 100]\,\mathrm{MeV}/c^2$ range of the known value [12] of the K^* mass, and $K^+\pi^0$ combinations within $[-150, 150]\,\mathrm{MeV}/c^2$ range. The selectors do vertex fits on the candidates using both kinematic and geometric information. Combinations with good fit quality are stored in candidate lists `KstarKsPiLoose`, `KstarKPi0Loose`, and `KstarKPiLoose`, for $K^{*+}_{K^0_S\pi^+}$, $K^{*+}_{K^+\pi^0}$, and $K^{*0}_{K^+\pi^-}$ candidates, respectively, for reconstruction of B mesons.

We make additional cuts on the K^* candidates after the `Beta` jobs have been finished:

- $755 < m^{K^*}_{K\pi} < 1035\ \ \mathrm{MeV}/c^2$,
- Additional π^0 cuts are made for modes with π^0 (see Sec. 3.3.5 on page 95), but without any cut on π^0 energy. To reject soft π^0s, we use decay angle cuts (see Sec. 3.4.6.2),
- K^0_S's lifetime significance $\tau/\sigma_\tau > 3$ for mode with K^0_S,
- Charged K's or π's must NOT satisfy the `VeryTight` criteria of the electron `Micro` selector, or the `VeryTight` criteria of the proton `LH` selector (see Sec. 3.3.3),

- Charged π's must NOT satisfy the `Tight` criteria of the `SMS` kaon selector (see Sec. 3.3.4),
- Charged K's MUST satisfy the `Tight` criteria of the `SMS` kaon selector.

We show in Figure 3.7 the invariant mass distributions of K^{*+} and K^{*0} for signal and continuum background. We fit the signal distributions with double-Gaussians, which have a mean of about $892\,\mathrm{MeV}/c^2$ for K^{*+}, $\sim 896\,\mathrm{MeV}/c^2$ for K^{*0}, and $\sigma_{\mathrm{core}} \sim 20\,\mathrm{MeV}/c^2$ for the core distribution, $\sigma_{\mathrm{tail}} \sim 50\,\mathrm{MeV}/c^2$ for the tail distribution. Like the case with ω, there are real K^*'s in continuum backgrounds, so we fit the continuum background distributions with the double-Gaussian of signal for real K^*, with distribution parameters fixed, and a quadratic component for the combinatoric background.

K^* mesons have much larger width than ω's, more combinatoric backgrounds are expected, and also because of the wider distributions, we find the difference of the mass PDF parameters between MC and real data is negligible within errors, so there are no corrections applied for K^* mass signal PDFs.

3.4.5 ρ Selection

The ρ mesons decay almost entirely into two pions. The ρ^+ is reconstructed through decays $\rho^+ \to \pi^+\pi^0$ and ρ^0 from $\rho^0 \to \pi^+\pi^-$.

One charged track from `GoodTracksLoose` list of π hypothesis and one π^0 from `pi0DefaultMass` list are combined to form ρ^+ candidates, and two opposite charged tracks with π hypotheses from `GoodTracksLoose` are combined to form ρ^0 candidates. The selectors require the invariant masses of ρ^+ candidates are within $\pm 320\,\mathrm{MeV}/c^2$ of the known value [12] of the ρ^+ mass, and $\pm 300\,\mathrm{MeV}/c^2$ for ρ^0 candidates. The ρ selectors do kinematic and geometric fits to the candidates, and those with good fit quality are stored in candidate lists `rhoCDefault` and `rho0Default` for ρ^+ and ρ^0 candidates, respectively, for later use to reconstruct B mesons.

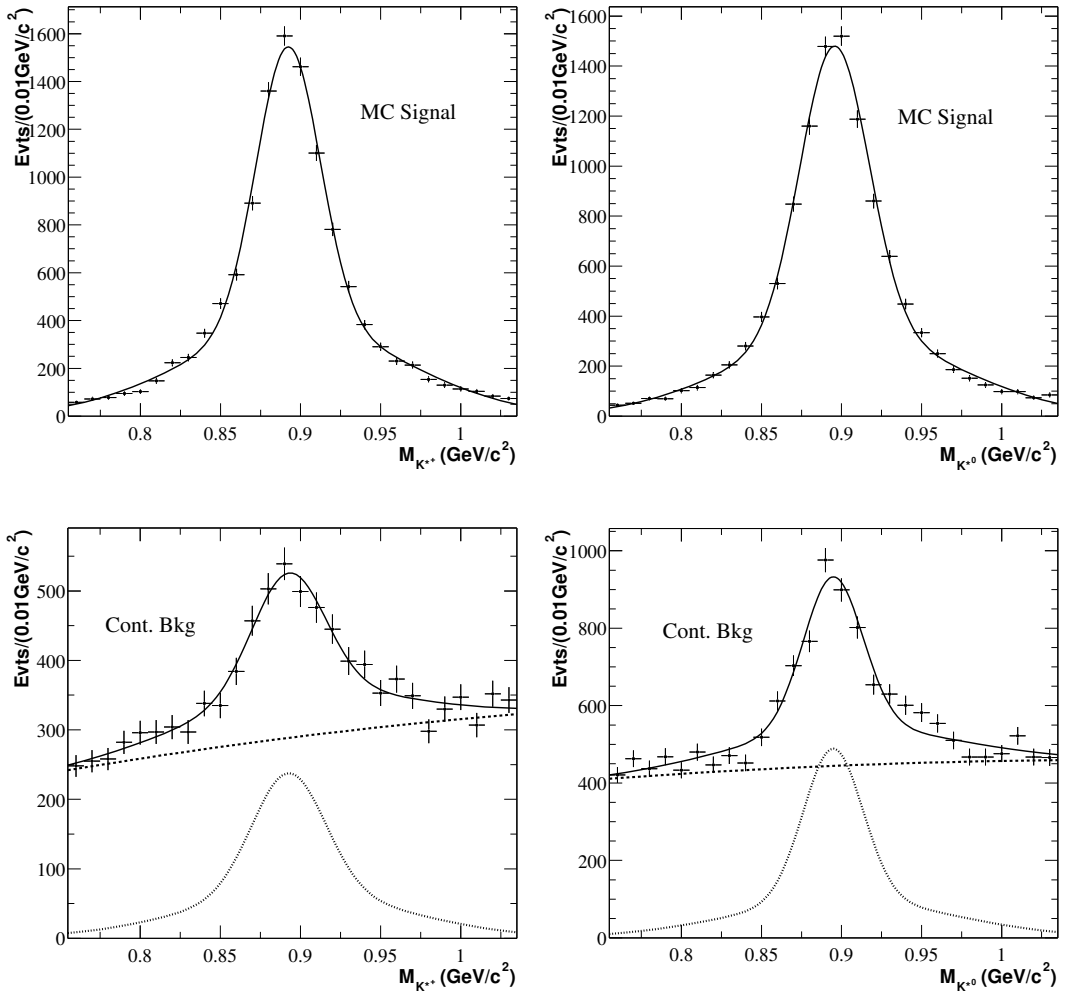

Figure 3.7: Distributions of invariant mass $M_{K\pi}$ of K^* candidates for signal (top) from signal MC data, and continuum background (bottom) from sideband data. The left side plots are for $K^{*+} \to K^0_S\pi^+$ and the right side plots are for $K^{*0} \to K^+\pi^-$. The distribution shape for signal is double-Gaussian, with $\mu \sim 892\,\mathrm{MeV}/c^2$ for K^{*+}, $\mu \sim 896\,\mathrm{MeV}/c^2$ for K^{*0}, and $\sigma \sim 50\,\mathrm{MeV}/c^2$; the shape for continuum background is a quadratic component (dashed curve) overlaid with a real K^* component (dotted curve).

We make additional cuts on the ρ masses after the Ntuple production:

- $470 < m^{\rho^+}_{\pi\pi} < 1070$ MeV/c^2,
- $510 < m^{\rho^0}_{\pi\pi} < 1060$ MeV/c^2, with tighter lower limit to reject K^0_S,
- Additional π^0 cuts for ρ^+ (see Sec. 3.3.5), but without cut on π^0 energy. We use helicity cuts to reject soft π^0s (see Sec. 3.4.6.2),
- Charge π's must NOT satisfy the `VeryTight` criteria of the electron `Micro` selector, or the `VeryTight` criteria of the proton `LH` selector (see Sec. 3.3.3),
- Charge π's must NOT satisfy the `Tight` criteria of the `SMS` kaon selector (see Sec. 3.3.4),

We show in Figure 3.8 the invariant mass distributions of ρ^+ and ρ^0 for signal and continuum background. We fit the signal distributions with double-Gaussians, which have a mean of about 766 MeV/c^2, and $\sigma_{\rm core} \sim 53$ MeV/c^2 for the core distribution, $\sigma_{\rm tail} \sim 170$ MeV/c^2 for the tail distribution. There are real ρ's in continuum backgrounds, so we fit the continuum background distributions with the double-Gaussian of signal for real ρ, and a quadratic component for the combinatoric background.

The ρ mesons have a Breit-Wigner width of about 150 MeV/c^2, which is much larger than ω's and K^*'s. We find the difference of the mass PDF parameters between MC and real data is negligible within errors, so there is no corrections applied for ρ mass signal PDFs.

3.4.6 Helicity Distributions

3.4.6.1 *PV* Modes

The cosine of ω helicity angle (defined as the angle between the normal to the ω decay plane and the flight direction of the ω relative to the B, measured in the ω rest

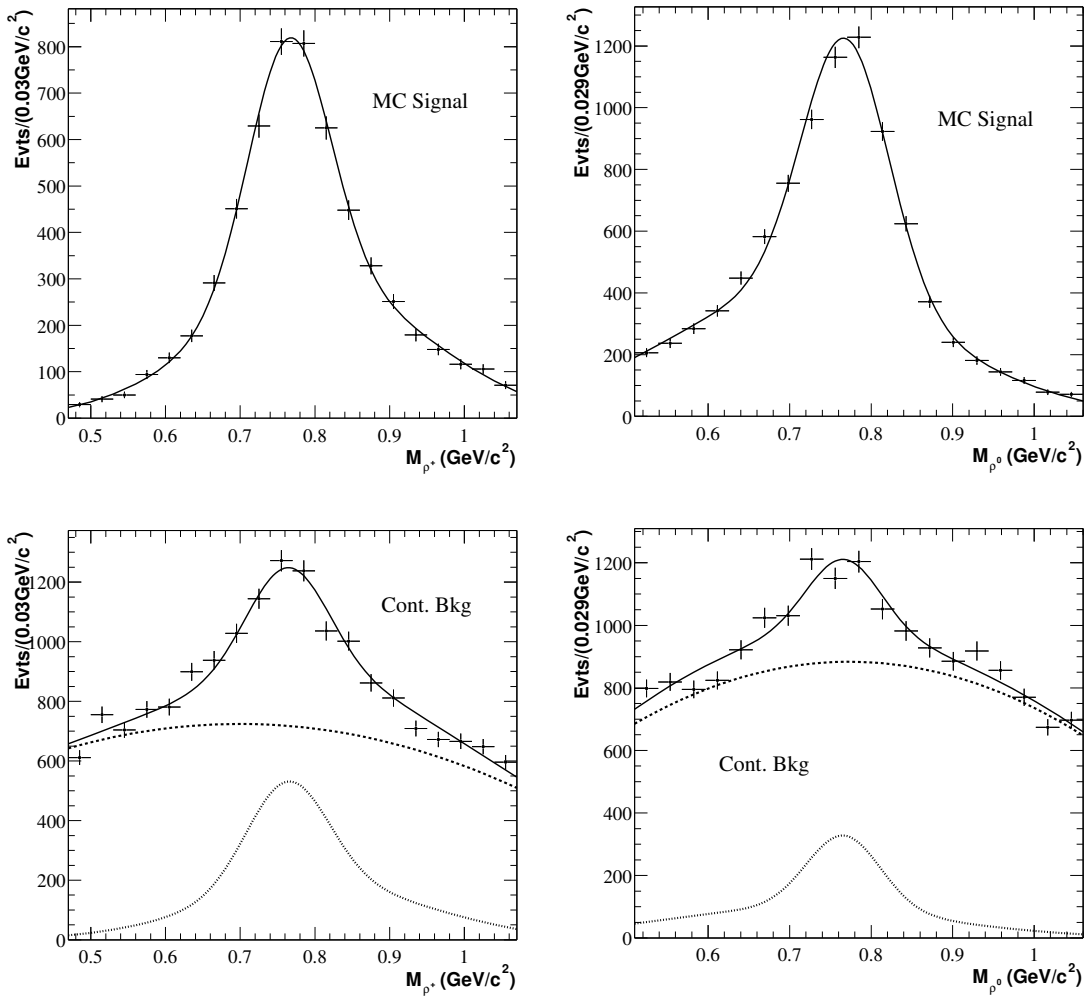

Figure 3.8: Distributions of invariant mass $M_{\pi\pi}$ of ρ candidates for signal (top) from signal MC data, and continuum background (bottom) from sideband data. The left side plots are for ρ^+ and the right side plots are for ρ^0. The distribution shape for signal is double-Gaussian, with $\mu \sim 766\,\mathrm{MeV}/c^2$ and $\sigma \sim 150\,\mathrm{MeV}/c^2$; the shape for continuum background is a quadratic component (dashed curve) overlaid with a real ρ component (dotted curve).

frame, see Figure 1.2 on page 11), $\mathcal{H} \equiv \cos\theta_H$, has quadratic signal distributions for $B \to PV$ modes (see Eq. 1.12 on page 10). We actually model the absolute value of $\mathcal{H}_\omega$ because the sign of $\cos\theta_H$ for ω has no physics significance.

We fit the signal $\mathcal{H}$ distribution with a second order polynomial. For backgrounds, we expect $\mathcal{H}$ would have a nearly flat distribution, corresponding to a sum of combinatoric resonance background and background of true resonances from generic production mechanisms. Thus we determine separate PDFs for combinatoric ω background (away from the ω mass peak) and background of true continuum ω's. The actual procedure to get the two-component $\mathcal{H}$ PDF for background is done with a fit of ω mass and $\mathcal{H}$ two-dimensional PDF for background to the on-peak sideband data with the ω mass distributions determined and fixed before the fit.

We show in Figure 3.9 the $\mathcal{H}$ signal distribution for the sum of $B^+ \to \omega K^+$ and $B^+ \to \omega\pi^+$ signal MC, which produces the expected quadratic distribution, and background distributions from on-peak sideband data. The total background distribution of $\mathcal{H}$ is nearly flat, and the two components are shown in the two lower plots. We fit the background distributions to higher order polynomials and require the PDF function for real ω's is even because we take the absolute value of cosine ω helicity angle. Though we can see the difference between the two background components, it is not dramatic (both nearly flat), and for some other PV modes, the difference is not very visible. We further check that with two component background helicity PDF in our final fit, or with one total background PDF, the fit results are consistent within errors.

We include helicity PDFs described here for signal and continuum background in our final fits for the PV modes studied: $B^+ \to \omega K^+$, $B^+ \to \omega\pi^+$, and $B^0 \to \omega K^0$.

3.4.6.2 *VV* Modes

We have five VV (sub-)modes: $B^+ \to \omega K^{*+}_{K^0_S\pi^+}$, $B^+ \to \omega K^{*+}_{K^+\pi^0}$, $B^0 \to \omega K^{*0}_{K^+\pi^-}$, $B^+ \to \omega\rho^+$, and $B^0 \to \omega\rho^0$. For K^*/ρ, we define here the helicity angle θ_H as the angle

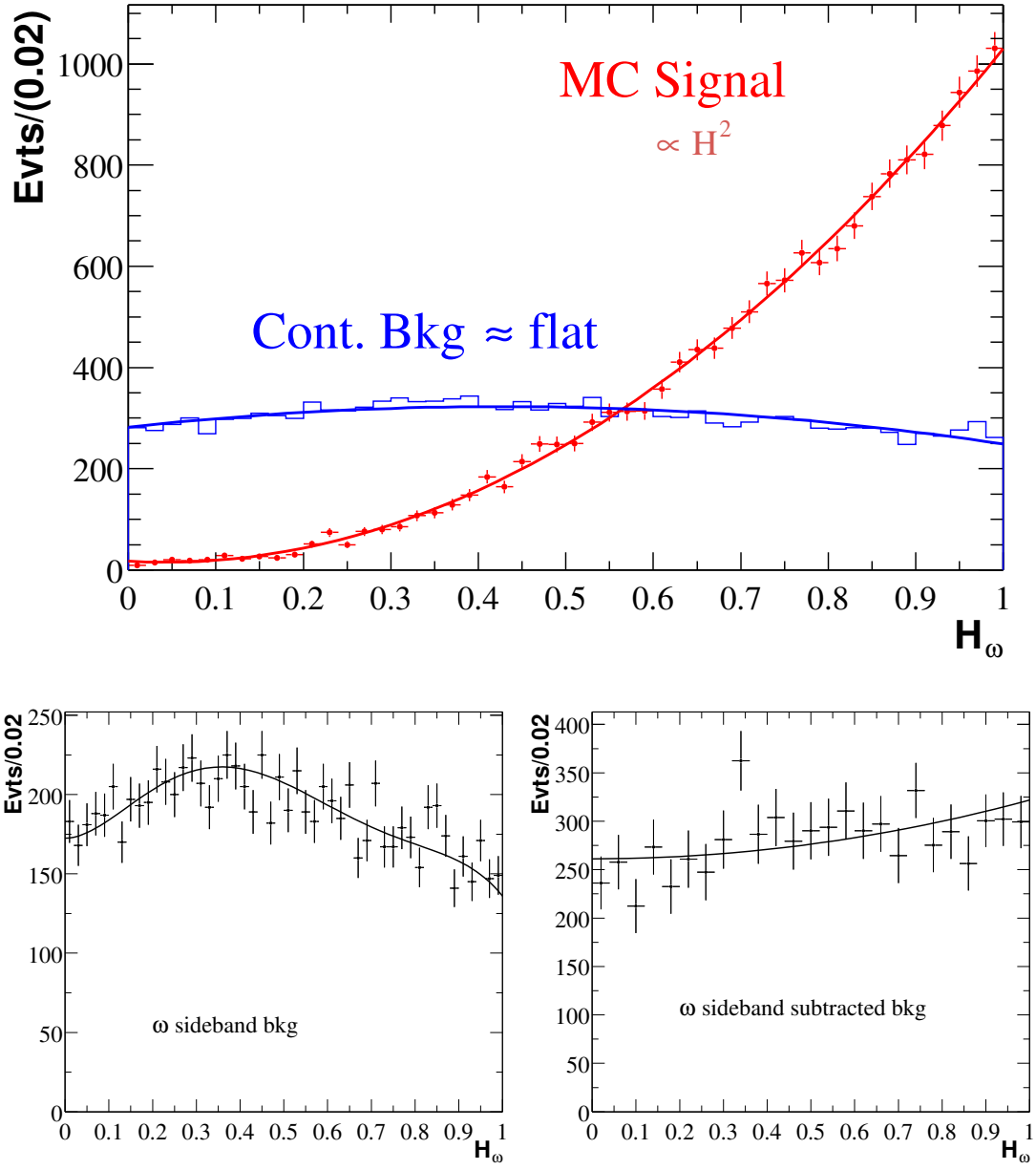

Figure 3.9: Distributions of cosine ω helicity angles for $B \to PV$ modes as in $B^+ \to \omega h^+$ decays. The top plots show the signal MC distributions fitted to a second order polynomial, and the total background distribution which is nearly flat. Two lower two plots show the two components of the background PDF. The left plot shows the distribution of ω mass sideband for pure combinatorial background; the right plot show the distribution of ω mass sideband subtracted background for real ω's.

between the direction of one of the K^*/ρ daughters and that of the parent B of K^*/ρ in the K^*/ρ rest frame. The daughter used is positively-charged (or only charged) track for the ρ case or the kaon for the K^* case.

The helicity distribution for $B \to VV$ modes is given by (1.14). However, we need to take the detector acceptance effects into account for final signal PDFs. Since the normalization for each component is computed internally by `RooFit`, the total helicity signal PDF can be written as:

$$\begin{aligned} \mathcal{P}_{\rm sig}^{\rm hel}(\theta_1, \theta_2, f_L) &= ((1 - F_L) \times \sin^2\theta_1 \times \sin^2\theta_2 + F_L \times \cos^2\theta_1 \times \cos^2\theta_2) \\ &\quad \times \mathcal{G}_1(\theta_1) \times \mathcal{G}_2(\theta_2)\,, \end{aligned} \tag{3.8}$$

where f_L is the longitudinal polarization fraction, and $\mathcal{G}_1(\theta_1)$ and $\mathcal{G}_2(\theta_2)$ are parameterizations of the detector acceptance effects for the two helicity angles. We assume the acceptance effects for the two vector mesons are independent so that the parameterizations can be written as product of a function of θ_1 and one of θ_2. The quantity F_L is the "effective" polarization fraction seen by the fitter after all the detection acceptance effects, and can be written as

$$F_L = \frac{f_L}{(1 - f_L)R_\epsilon + f_L}\,, \tag{3.9}$$

where R_ϵ is the ratio of transverse to longitudinal efficiency.

In the VV modes, we also take the absolute value of cosine helicity angle for ω as in the PV modes for the same reason that the sign of $\omega \cos\theta_H$ has no physics significance. We show in Figure 3.10 the ideal signal helicity distributions and the distributions with acceptance effects for the VV modes.

The acceptance effects are mainly due to the $p_T > 0.1\,\mathrm{GeV}/c$ and DCH Hits ≥ 12 cuts for `GoodTracksLoose` (see Sec. 3.3.1 on page 90). The "roll-off" effect can happen near $\mathcal{H}_{K^*/\rho}$ values of ± 1. In particular, for the decay of a K^* or ρ with a charged pion, the helicity distribution of the vector meson will show a characteristic roll-off

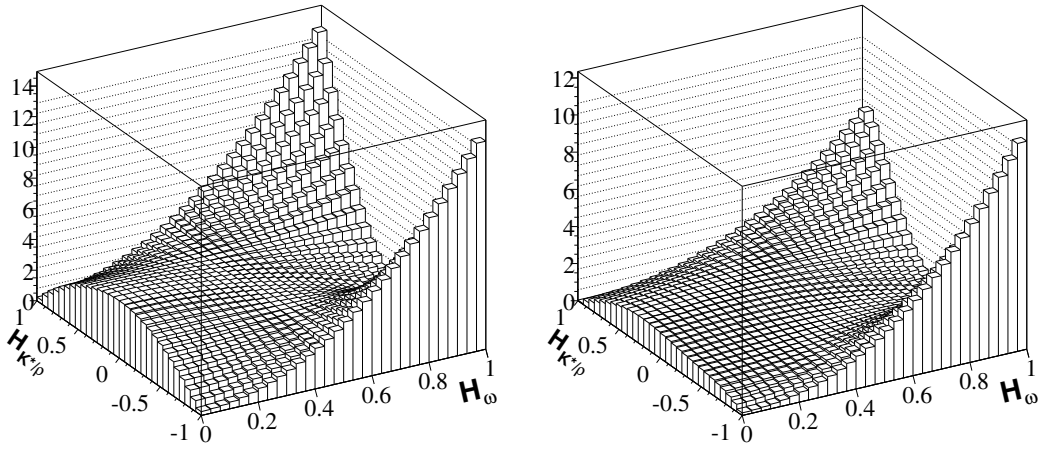

Figure 3.10: The 2D signal $\mathcal{H}$ distributions for $P \to VV$ decays with perfect acceptance (left) and real acceptance effects (right), with the polarization fraction f_L =0.5. The left plot is got using distribution (1.14); the right plot is got using (3.8) with parameters of $\mathcal{G}_1(\theta_1)$ and $\mathcal{G}_2(\theta_2)$ determined from fits to $B \to \omega\rho$ signal MC with f_L =0.5. For comparison purpose, the distributions are plotted over the full ranges of $\mathcal{H}$. Due to acceptance effects, we have to make cuts on $\mathcal{H}_{K^*/\rho}$, so the actual ranges of $\mathcal{H}$ for K^*/ρ in the final fits are narrower. See text for more detail.

in the region populated by low momentum pions because of the cuts on the pions by the selector (see Figure 3.11). This effect is also present for low momentum charged kaons but is negligible due to the shifted momentum fraction distribution of the strange quarks. Those stringent quality requirements to the `GoodTracksLoose` list, however, are necessary to reduce combinatorial background under the broad K^* and ρ resonances. The ω mesons can also have such soft pions, but the $\mathcal{H}$ angle is defined differently here as the angle between the ω flight direction and the normal to the ω decay plane (see Figure1.2 on page 11), so the soft pions dominate around $\mathcal{H}$ =0. For the $\mathcal{H}_\omega$ distribution of the longitudinal component, the effects are invisible because of the quadratic nature of the distribution, and for the transverse component, the effects are less severe because the decay plane is less sensitive to the soft pions, as we show also in Figure 3.11, the ω helicity distributions for longitudinal and transverse components.

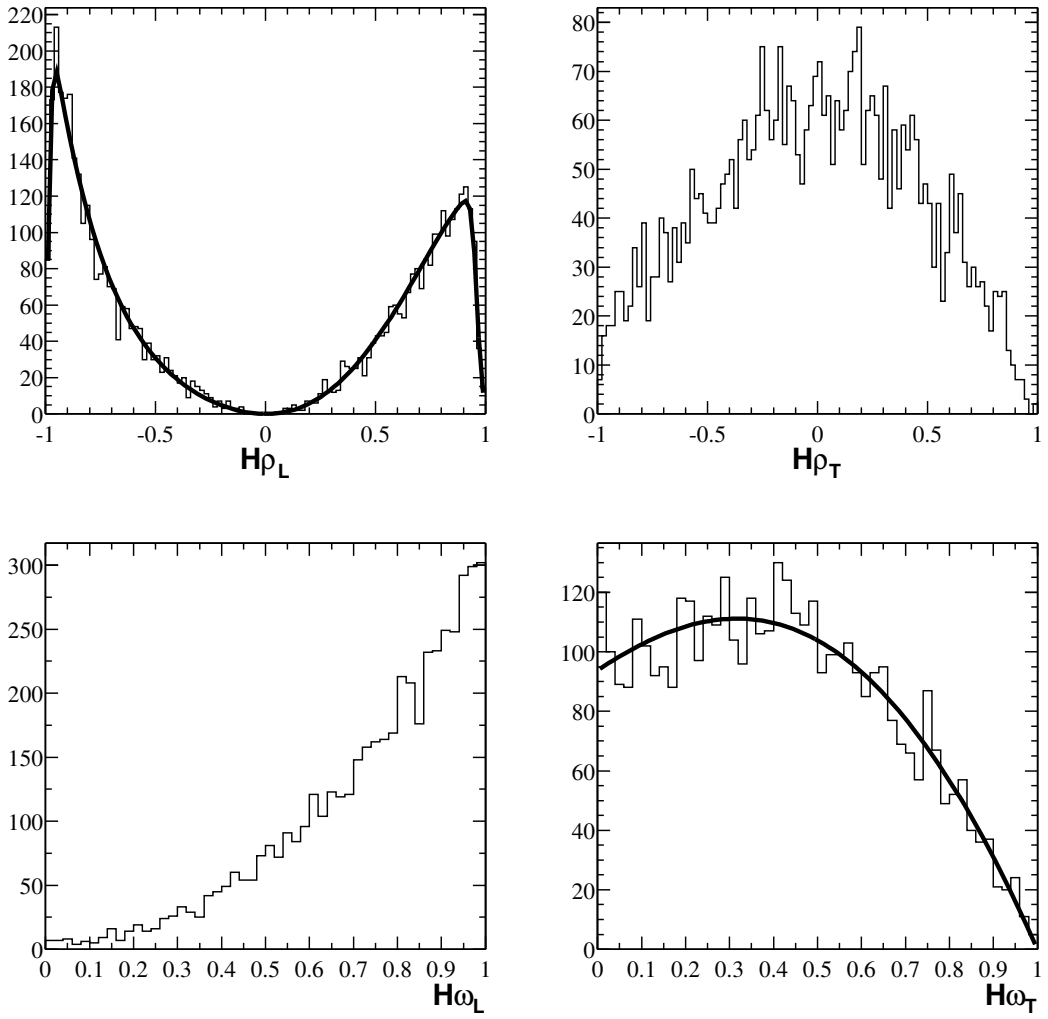

Figure 3.11: The roll-off effects of $\mathcal{H}$ distributions demonstrated by longitudinal and transverse signal MC data of $B \to \omega\rho$. Soft pions along the helicity axis are most likely to be ejected by the track selector, so the efficiency is very low close to $\mathcal{H} = \pm 1$ for K^*/ρ, causing the $\mathcal{H}$ roll-off, as is shown in the upper left plot of the $\mathcal{H}$ distributions for longitudinal signal MC, while the $\mathcal{H}$ distribution for transverse component is proportional to $\sin^2\theta_H$, which makes the effect invisible (upper right plot). On the other hand, the ω $\mathcal{H}$ is defined differently, so the soft pions are close to $\mathcal{H}$ =0, which is negligible for longitudinal component(lower left plot), and because the ω decay plane is less sensitive to soft pions, the roll-off effects for its transverse component are moderate (lower right plot).

The roll-off effects in the signal or background can be modeled by multiplying the primary PDF shape by an appropriate Fermi function, which can be written as

$$\mathcal{G}_F(\mathcal{H};\mu_{\rm thres},\sigma_{\rm slope}) = \frac{1}{1+e^{\pm(\mathcal{H}-\mu_{\rm thres})/\sigma_{\rm slope}}}\,, \tag{3.10}$$

where $\mu_{\rm thres}$ describes the position of the roll-off, $\sigma_{\rm slope}$ determines the sharpness of the roll-off, and depending on the direction of roll-off, there is '+' sign for the right-side roll-off and '−' sign for the left one.

Another source of acceptance effects is due to soft π^0s for modes decaying to π^0, $K^{*+}_{K^+\pi^0}$ and ρ^+. Soft π^0s are mainly background and we usually require energy cut to get rid of soft π^0s. For $K^{*+}_{K^+\pi^0}$ or ρ^+, the soft π^0s are concentrating at $\mathcal{H}=-1$ by definition. We could cut on π^0 energy, which has been done to π^0s from ω, but we prefer to cut directly on $\mathcal{H}$ so that we can directly get rid of the low acceptance range of $\mathcal{H}$ due to soft π^0 cuts. Requirement of $\mathcal{H}>-0.5$ is effectively to have π^0 energy cut of $>350\,$MeV. To be conservative, we require $\mathcal{H}>-0.6$ for these two modes.

It is inevitable either to model the acceptance effects, or to have cuts to remove those low acceptance ranges. We choose a combined method. We reject those ranges as much as possible to eliminate the uncertainty in modeling them, and also keep as much as possible not to have the selection efficiency too low.

We list the cuts we apply to the $\mathcal{H}$ in Table 3.6. We choose the $(\pm)0.85$ K^*/ρ helicity fiducial cut to remove as much as possible the region where the efficiency rolls off. The efficiency loss from this is $<10\%$ for longitudinal component which is more sensitive to this cut. For modes with π^0s, we need tighter cut, -0.6, to reject soft π^0s. Unlike some other VV modes, for example, $\rho\rho$, this cut will not lose as much efficiency because there is only one such π^0.

The residual acceptance effects are parameterized by $\mathcal{G}_1(\theta_1)$ and $\mathcal{G}_2(\theta_2)$ as high order polynomials (up to seventh order) and/or the "roll-off" functions. We fit the total PDF as in (3.8) to a cocktail of longitudinal and transverse signal MC data, the f_L and

Table 3.6: K^*/ρ $\mathcal{H}$ cuts applied to VV modes

mode	$\omega K^{*+}_{K^0_S\pi^+}$	$\omega K^{*+}_{K^+\pi^0}$	$\omega K^{*0}_{K^+\pi^-}$	$\omega\rho^+$	$\omega\rho^0$
$\cos\theta^{K^*/\rho}_{\rm hel}$	$[-0.85, 1]$	$[-0.6, 1]$	$[-0.85, 1]$	$[-0.6, 0.85]$	$[-0.85, 0.85]$

F_L of which we know. After the fit, we fix the acceptance function parameters and let f_L float in the final fit to get the longitudinal polarization fraction.

We expect $\mathcal{H}$ distribution for backgrounds is nearly flat as in the PV modes, and furthermore, the background distributions for the two vector mesons are independent of each other. We also determine separate $\mathcal{H}$ PDFs for combinatoric resonance background (away from the resonance mass peak) and background of true continuum resonances by fitting the combined PDFs of resonance mass and $\mathcal{H}$ to the on-peak sideband data. We fit the two background components with high order polynomials (up to fifth order). Shown in Figure 3.12 are background distributions of $B \to \omega K^*$ for VV modes.

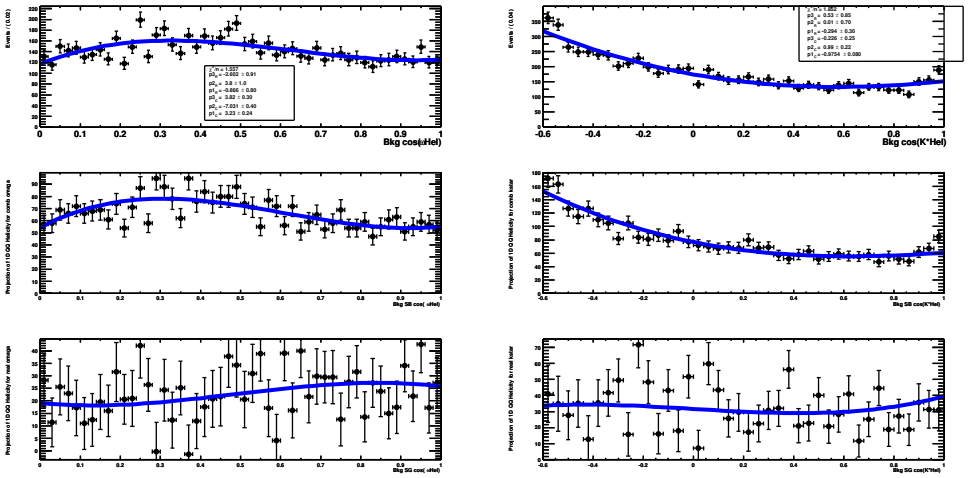

Figure 3.12: Background distributions of $\mathcal{H}$ for $B \to VV$ modes as in $B \to \omega K^*$ decays. The left-side plots are for ω and right-side plots for K^*. The top plots show the total background distributions which are nearly flat. The middle ones are the distributions for resonance sidebands which are pure combinatorial backgrounds. The bottom plots are for resonance mass sideband subtracted backgrounds. The distributions are from on-peak sideband data.

3.5 B Reconstruction

We fully reconstruct B mesons by combining an ω candidate with another light meson, K, π, K^*, or ρ candidate through decay chains:

$$
\begin{array}{ll}
B^+ \to \omega K^+, & B^+ \to \omega K^{*+}_{K^0_S\pi^+}, \\
 & B^+ \to \omega K^{*+}_{K^+\pi^0}, \\
B^0 \to \omega K^0, & B^0 \to \omega K^{*0}_{K^+\pi^-}, \\
B^+ \to \omega \pi^+, & B^+ \to \omega \rho^+_{\pi^+\pi^0}, \\
 & B^0 \to \omega \rho^0_{\pi^+\pi^-}.
\end{array}
$$

Each selector for these modes combines two B daughter candidates from appropriate lists. The invariant mass range is set very loose to $4.5 < M_B < 6.0$ GeV/c^2, and the selectors require beam energy cut $\Delta E < 400\,\mathrm{MeV}$ (see below for the definition of ΔE). Kinematic and geometric fits are applied to the decay trees, and finally the output form the B candidate lists.

In this section we describe distributions of variables characteristic of B meson decays, and their uses to suppress backgrounds and to get the final results.

3.5.1 ΔE and m_{ES}

B mesons are characterized kinematically by two invariant variables: energy difference ΔE, defined as

$$\Delta E = E^*_B - \frac{1}{2}\sqrt{s}\,, \tag{3.11}$$

where E^*_B is the energy of B candidate in the c.m. frame, and $\sqrt{s}$ is the c.m. energy, and beam-energy-substituted mass m_{ES}, defined as

$$m_{\mathrm{ES}} = \sqrt{(\frac{1}{2}s + \mathbf{p}_0 \cdot \mathbf{p}_B)^2/E_0^2 - p_B^2}\,, \tag{3.12}$$

where the subscripts $_0$ and $_B$ refer to the $\Upsilon(4S)$ and to the B candidate, respectively.

The distribution of ΔE for real B is expected to be centered at zero with a typical resolution of about 30 MeV to the analyses performed here, mainly due to errors of B

energy reconstruction [109], while that for continuum background is expected to be flat due to random combinations. We show in Figure 3.13 the distributions of ΔE for signal with peak at zero and continuum backgrounds with a rather flat distribution. The PDFs we use for signal are double-Gaussian and second order polynomial for continuum background.

The $m_{\rm ES}$ distribution for real B is expected to peak at its mass central value, $5.279\,{\rm GeV}/c^2$, with a width of about $3\,{\rm MeV}/c^2$, mainly due to the beam energy spread and quite independent of individual decay modes [109]. The distribution for continuum background is expected to spread over the whole mass range and not to have any peaking structure. Figure 3.14 shows such distributions. We model the signal PDF by double-Gaussian and the continuum background distributions can be described well by the ARGUS function [110]:

$$\mathcal{P}_{\rm argus}(m_{\rm ES}; E_{\rm beam}, \xi) = A\, x\sqrt{1-x^2}\ \exp^{\xi(1-x^2)}\,, \tag{3.13}$$

where $x = m_{\rm ES}/E_{\rm beam}$, ξ, the ARGUS exponent, controls the slope of the shape with a typical fitted value of about -23, and A is a normalization factor.

Our signal region is defined as an area of $5.27 < m_{\rm ES} < 5.29$ GeV/c^2 and $|\Delta E| < 100\,{\rm MeV}$. We use a much wider range for the purpose of continuum background study, so we require loose cuts on ΔE and $m_{\rm ES}$ to the Ntuples from `Beta` jobs:

$$|\Delta E| < 200\,{\rm MeV}, \qquad 5.20 < m_{\rm ES} < 5.29\ {\rm GeV}/c^2.$$

To study continuum background, we define grand sideband region (of $m_{\rm ES}$) as $m_{\rm ES} < 5.27\,{\rm GeV}/c^2$ and ΔE sideband region as $|\Delta E| > 100\,{\rm MeV}$.

Studies of $B \to D$ control samples [111,112] show that the MC data is a reasonable representation of the data with respect to the ΔE and $m_{\rm ES}$ distributions. Only very small corrections are needed. For ΔE, the width of the core distribution from MC is scaled by a factor of 1.05 in order to have appropriate width, and for $m_{\rm ES}$, we find that

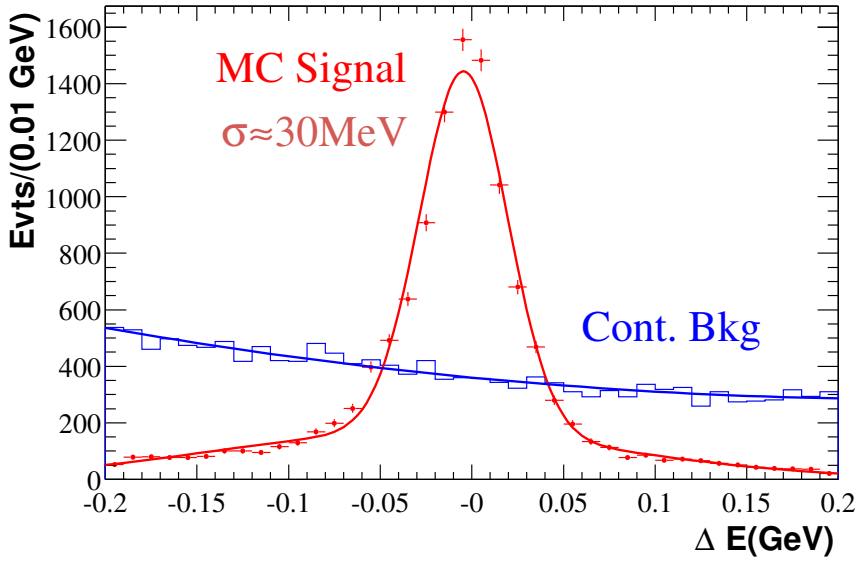

Figure 3.13: Signal ΔE distribution from MC data is centered at 0, with $\sigma \approx 30\,\mathrm{MeV}$, the continuum background distribution from sideband data is flat across the whole range. We fit the signal distribution with double-Gaussian, and fit the continuum background with second order polynomial.

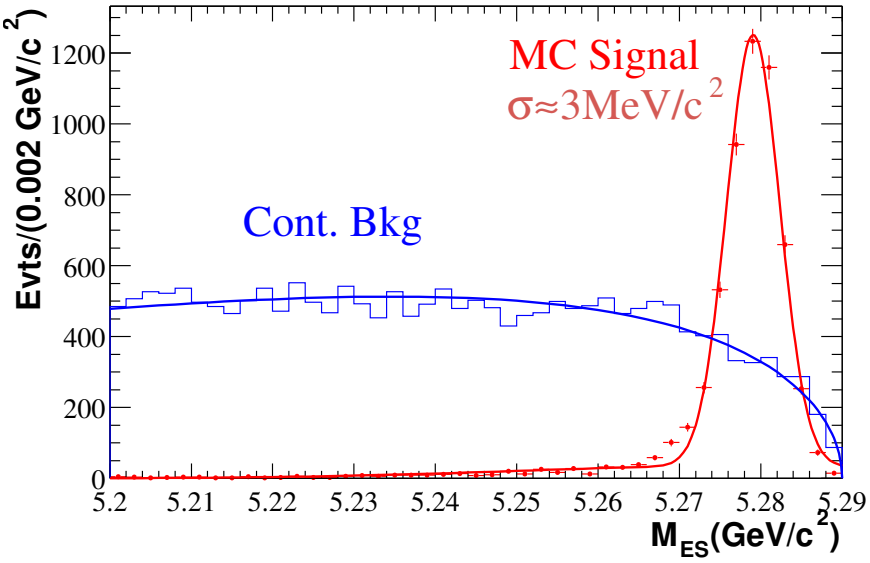

Figure 3.14: Signal m_{ES} distribution from MC data is peaked at $5.279\,\mathrm{GeV}/c^2$, with $\sigma \approx 3\,\mathrm{MeV}/c^2$, the continuum background from ΔE sideband are spread across the whole mass range smoothly with cut-off at the c.m. beam energy. We model signal PDF as double-Gaussian and continuum background as ARGUS function.

the mean value of the core distribution needs to be shifted by $0.7\,\mathrm{MeV}/c^2$ to match the data.

There are other choices of B kinematic variables for physics analyses but these two variables are well understood and more importantly, they are nearly uncorrelated, which is crucial to our methods, so we include them in our final fits.

3.5.2 Continuum Background Suppression

Our major backgrounds in the study of charmless rare B decays are continuum backgrounds from $e^+e^- \to q\overline{q}$ as we can see from Table 2.1 on page 41 that the cross-section of $q\overline{q}$ events is about three times that of $b\bar{b}$ events at the $\Upsilon(4S)$ resonance. Furthermore, typical branching fractions for the modes here are very small, of the order $10^{-6} \sim 10^{-5}$, so we need to reject those backgrounds with a factor at least to that magnitude.

Major continuum background can be discriminated from B events and thus rejected by the characteristic kinematics for different decay topologies. Since the energy of the $\Upsilon(4S)$ resonance is just above $B\overline{B}$ pair production threshold, B mesons are created almost at rest in the $\Upsilon(4S)$ frame, so the decay products of real $B\overline{B}$ event tend to be isotropic. However, $q\overline{q}$ pair is produced as two energetic back-to-back jets in the $\Upsilon(4S)$ frame, forming highly correlated two-jet structure with final decay products. We show in Figure 3.15 two typical events for real $B\overline{B}$ and background $q\overline{q}$, where we can see that the event shapes are dramatically different.

Discriminating variables are defined to identify and suppress the continuum background, utilizing the event shape difference between $q\overline{q}$ and $B\overline{B}$. The one we choose for preliminary event-shape selection on the Ntuples is the "thrust angle" θ_{T}, defined as the angle between the thrust axis of the B candidate decay products and the thrust axis of the rest of the event (ROE). The thrust axis, $\hat{T}$, is defined to be the direction which maximizes the sum of the longitudinal momenta of the particles in question, and

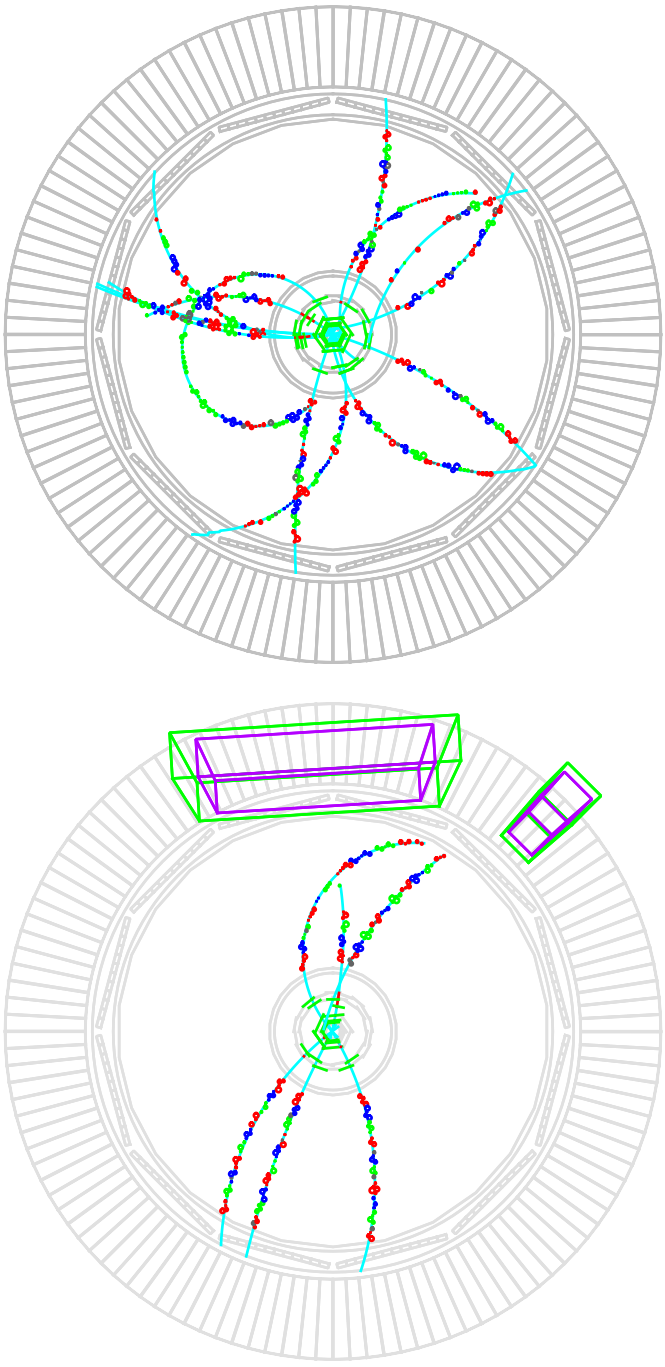

Figure 3.15: Typical $B\overline{B}$ event (up) with isotropical event shape, and typical $q\overline{q}$ continuum background with two-jet structure.

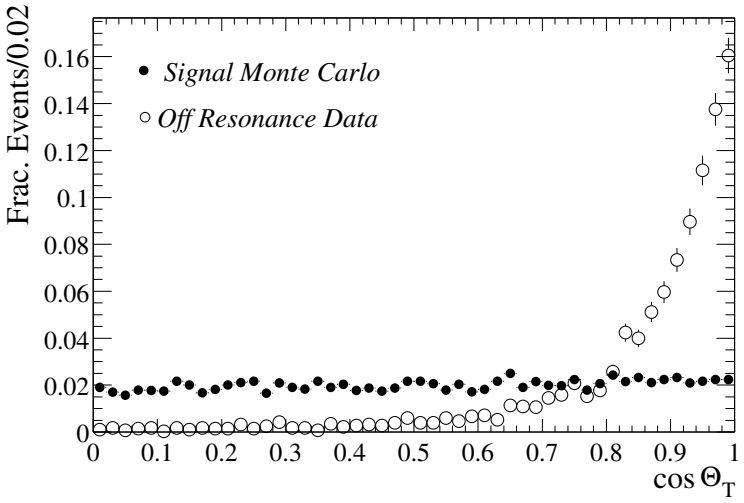

Figure 3.16: The cosine thrust angle $\cos\theta_{\rm T}$ distributions are nearly flat for $B\overline{B}$ signal (MC data) and peaking at +1 for $q\overline{q}$ background (off-peak data).

thrust, T, is the maximized sum related to this direction [113]

$$T = \frac{\sum_i |\hat{T}\cdot\vec{p_i}|}{\sum_i |\vec{p_i}|} \,. \tag{3.14}$$

For $B\overline{B}$ signal events, the distribution of $|\cos\theta_{\rm T}|$ is approximately flat, while it is strongly peaked at +1 for continuum background as is shown in Figure 3.16.

For preliminary selection, we require

$$N_{\rm trks} \geq N_{\rm tracks\ in\ decay\ mode} + 1$$

in order to be able to define thrust axis for the rest of the event. We evaluate the optimum cuts on $|\cos\theta_{\rm T}|$ such that the sensitivity of measurements (ratio of signal yield over its uncertainty) is maximized. We list the $\cos\theta_{\rm T}$ cuts applied in Table 3.7.

We simply cut on $\cos\theta_{\rm T}$ and do not include it in final fits because the signal distribution is flat and has not much discriminating power left. Instead, we construct a multivariate Fisher discriminant [114], $\mathcal{F}$, as the variable in the final fit to make use of event shape information. Traditionally, we use the CLEO Fisher [115], based on the "CLEO virtual calorimeter" (VCal), which determines the momentum flow into nine

Table 3.7: $\cos\theta_{\rm T}$ cuts applied to the modes to reject continuum backgrounds. The cuts for $B \to \omega\rho$ modes are much tighter because background is more severe and fit errors tend to be much larger if more events are selected.

mode	ωh^+	ωK^0	ωK^*	$\omega\rho$
$\lvert\cos\theta_{\rm T}\rvert \leq$	0.8	0.9	0.8	0.65

10°-wide cones sharing $\hat{T}$ of the B candidate as common axis. The sum of the momenta of all particles from the ROE emitted within each of the nine cones is used as input to the Fisher discriminant. As a generalization to those discrete cones in the CLEO Fisher, *BABAR* introduced momentum-weighted Legendre polynomials [116], L_j $(j = 0, 2, 6)$, defined by

$$L_j = \sum_i p_i \times |\cos\theta_i|^j \,, \tag{3.15}$$

where p_i is the momentum of (charged/neutral) tracks in the ROE, θ_i is the angle between the momentum and $\hat{T}$ of the B candidate. The advantages to use Legendre-based Fisher are that there is no need for binning and only few (instead of 9) such polynomials are necessary to describe the momentum distributions. We use four discriminating variables,

- $|\cos\theta_C|$, the unsigned cosine of the angle between the signal candidate $\hat{T}$ and the beam axis (z),
- $|\cos\theta_B| = |\cos(\vec{p}_B, \vec{z})|$, the unsigned cosine of the angle between the B candidate momentum and the beam axis (z),
- the Legendre polynomials L_0 and L_2,

to construct the new Fisher, $\mathcal{F}_{LGD}$ [86]:

$$\begin{aligned}\mathcal{F}_{LGD} = 0.367 \times (1.60287 \cdot |\cos\theta_C| + 1.89495 \cdot |\cos\theta_B| \\ + 0.224181 \cdot L_0 + 1.779 \cdot L_2) - 1.3 \,,\end{aligned} \tag{3.16}$$

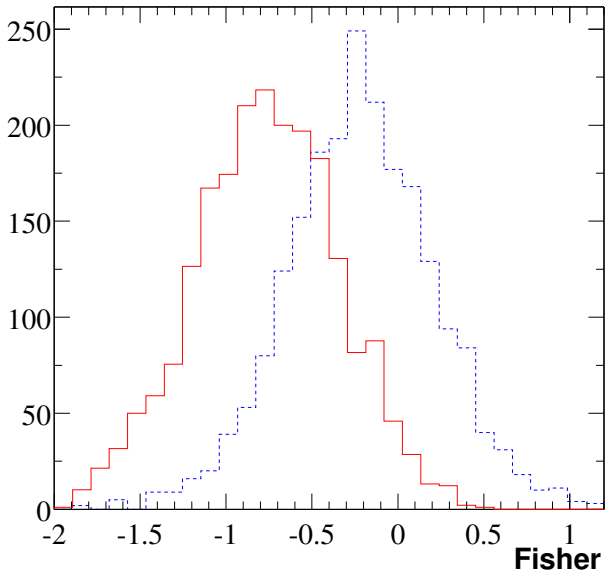

Figure 3.17: The Fisher discriminant $\mathcal{F}$ distributions for real signal from MC data (solid) and continuum background from on-peak sideband data (dashed) after $\cos\theta_{\rm T}$ cuts.

where the four coefficients inside the parenthesis are directly determined by the optimization program, the overall multiplicative ($0.367\times$) and additive (-1.3) coefficients are introduced to match the range of other Fisher discriminants, with no effect on the separation between signal and background. For modes with tagging information, we include the tagging categories in the $\mathcal{F}$ calculation [117]

$$\mathcal{F}_{LTC} = \mathcal{F}_{LGD} + 0.06225 \cdot \mathrm{MCat} - 3.57\,, \tag{3.17}$$

where MCat is a tagging category for all tagged events (MCat $= 50-58$). The Legendre-Tagging-Category Fisher (LTCFisher) is used to remove the correlation between Fisher and tagging category and to improve the CP measurements.

We show in Figure 3.17 the distributions of $\mathcal{F}$ for signal and continuum background. We fit both distributions to bifurcated Gaussian, i.e., a Gaussian with different widths on the left and right sides of its peak, and add a regular Gaussian to model tails

for backgrounds. The shape of Fisher is correlated with $\cos\theta_{\rm T}$ cut because they both use the same kind of information, and tighter $\cos\theta_{\rm T}$ cut means less discriminating power for $\mathcal{F}$. Every time $\cos\theta_{\rm T}$ cut changes, the $\mathcal{F}$ PDF parameters need to be adjusted.

For preliminary selection on Ntuples, we require wide range of $-3 < \mathcal{F} < 4$ (the scale of Figure 3.17 is enlarged to see the detail of the distributions).

3.5.3 $B\overline{B}$ Background

Other major backgrounds for our analyses are from real B events, including the dominant $b \to c$ decays of B and other rare B decays with similar decay topologies.

Usually $b \to c$ decays have negligible effects on charmless B decays, because the products of charmless (quasi-)two-body decays have very high momenta compared with those from charmed decays. But the charmed backgrounds could be a problem if the two charmless mesons from B are not very light, which is the case for $B \to \omega K^*$ and $B \to \omega\rho$ decays. We use generic $B\overline{B}$ MC samples to study the charmed backgrounds for our modes, and find that **peaking** charmed backgrounds are really negligible to all of our modes studied here. We just need to include systematic errors for this type of backgrounds.

Studies using charmless $B\overline{B}$ MC data indicate that cross-feeds from other rare B decays to the PV modes are also negligible, however, these $B\overline{B}$ backgrounds can not be neglected in our VV modes because of heavier masses and broader mass widths of K^* and ρ. For the VV modes, we need to model the $B\overline{B}$ background distributions and include them in our final fits.

First, we run `Q2BApp` jobs using the charmless $B\overline{B}$ MC sample with the same settings as to our signal MC samples, then we apply the same preliminary cuts as on real data or signal MC on the Ntuples from charmless $B\overline{B}$ MC, and we also veto signal events or overestimated JETSET events by scanning the MC truth trees. Only a few events (several hundred – $\sim$2K) in the charmless $B\overline{B}$ Ntuples pass those cuts

for each mode, and we go through the decay trees of those charmless events to identify the dominant charmless backgrounds. Finally, we use exclusive SP4 MC (typical size of 40k–80K events) of these dominant background modes and apply the preliminary selection requirements. Those exclusive MC data provide higher statistics samples to search for backgrounds at a level below 1%, and allow determination of their selection efficiency with greater accuracy than provided by the charmless MC sample. Table 3.8 and 3.9 show the dominant backgrounds for each of the five VV (sub-)modes. The estimated branching ratios are from other measurements or a guess guided by theory when there are no measurements, and we also re-estimate the cross-feeds from modes we are measuring after we unblind.

For each VV mode, we combine all its major $B\overline{B}$ background decays to make a cocktail sample with appropriate proportion of number of events for each of them. The cocktail data are then used to get $B\overline{B}$ background PDFs. Those $B\overline{B}$ background PDFs usually do not have typical shapes common to all the five modes. Unlike continuum backgrounds, distributions of ΔE and $m_{\rm ES}$ do have peaking structures, with shifted ΔE central value and broader widths for ΔE and $m_{\rm ES}$. The reason for this is mainly due to mis-reconstructed real B's. $B\overline{B}$ background can also have the real B daughter resonances in question, especially for ω, because of its narrow width and decay topology. K^*/ρ have much larger widths, so the distributions are much wider and flatter, mostly due to combinatorial and mis-reconstructed contributions. The Fisher for $B\overline{B}$ backgrounds is also fitted with bifurcated Gaussian with the mean of the distribution in between those of signals and continuum backgrounds. Helicity distributions are pretty flat, and we do not expect much difference between real and combinatorial resonance, so we just fit them with one high order polynomial component. We show in Figure 3.18 example distributions of ΔE, $m_{\rm ES}$, two resonance masses, $\mathcal{H}$, and $\mathcal{F}$ for $B\overline{B}$ backgrounds. Due to limited statistics, parameters of $B\overline{B}$ background PDFs have large errors. We include this effect in our systematic studies.

Table 3.8: List of dominant $B\overline{B}$ background modes for the modes $B^+ \to \omega K^{*+}$ and $B^0 \to \omega K^{*0}$. The last two columns of the table give, for each mode, the estimated number of preselected charmless $B\overline{B}$ background events contributing to the real data sample, and the total expected contribution from all relevant modes, before and after unblinding respectively.

Signal mode Bkg. Channel	MC ε [%]	Est. $\mathcal{B}$ [10^{-6}]	Est. presel. [events]	Est. presel. [events]
$\boldsymbol{\omega K^{*+}_{K^0_S\pi^+}}$				
$B^+ \to \eta_{3\pi} K^{*+}_{K^0\pi^+}$	1.2	25.9	1.5	1.5
$B^+ \to \omega\rho^+$	0.02	22.5	0.4	0.2
$B^+ \to \omega K^{*0}_{K^0_S\pi^0}$	1.6	< 23	3.2	0.5
$B^0 \to \eta'_{\rho\gamma} K^0$	0.08	65.2	0.5	0.5
$B^+ \to \rho^0 K^{*+}_{K^0\pi^+}$	0.19	10.6	0.4	0.4
$B^0 \to \omega K^{*0}_{K^+\pi^-}$	0.14	< 23	1.6	0.2
Total			≈ 8	≈ 3
$\boldsymbol{\omega K^{*+}_{K^+\pi^0}}$				
$B^+ \to \omega\rho^+$	0.12	22.5	2.2	1.2
$B^+ \to \eta_{3\pi} K^{*+}_{K^+\pi^0}$	0.45	25.9	0.8	0.8
$B^0 \to \omega K^0$	0.01	5.2	0	0
Total			≈ 3	≈ 2
$\boldsymbol{\omega K^{*0}_{K^+\pi^-}}$				
$B^+ \to \omega K^+$	0.08	5.4	1.5	1.5
$B^0 \to \omega\phi$	2.75	1	1.1	1.1
$B^+ \to \eta'_{\rho\gamma} K^+$	0.014	77.6	0.9	0.9
$B^+ \to \omega\rho^+$	0.036	22.5	0.8	0.4
$B^+ \to \rho^+ K^{*0}_{K^+\pi^-}$	0.14	10.6	1.0	1.0
$B^0 \to \phi K^{*0}_{K^+\pi^-}$	0.20	10.7	1.3	1.3
$B^0 \to \eta_{3\pi} K^{*0}_{K^+\pi^-}$	0.79	17.8	2.3	2.3
$B^+ \to \omega K^{*+}_{K^+\pi^0}$	0.37	10.6	2.2	0.7
$B^+ \to \eta'_{\eta\pi\pi} K^+$	0.011	77.6	0.1	0.1
$B^0 \to \omega\rho^0$	0.39	2.1	0.8	0.2
Total			≈ 12	≈ 10

Table 3.9: List of dominant $B\overline{B}$ background modes for the modes $B^+ \to \omega\rho^+$ and $B^0 \to \omega\rho^0$. The last two columns of the table give, for each mode, the estimated number of preselected charmless $B\overline{B}$ background events contributing to the real data sample, and the total expected contribution from all relevant modes, before and after unblinding respectively.

Signal mode Bkg. Channel	MC ε [%]	Est. $\mathcal{B}$ [10^{-6}]	Est. presel. [events]	Est. presel. [events]
$\boldsymbol{\omega\rho^+}$				
$B^0 \to \rho^+\rho^-$	0.18	26.6	4.1	4.1
$B^+ \to \omega K^{*+}_{K^0_S\pi^+}$	0.10	10.6	0.3	0.1
$B^0 \to \omega\pi^0$	0.48	< 1.2	0.5	0.5
$B^+ \to \omega K^{*0}_{K^0_S\pi^0}$	0.77	< 23	1.6	0.3
Total			≈ 6	≈ 5
$\boldsymbol{\omega\rho^0}$				
$B^+ \to \omega\rho^+$	0.64	22.5	11.4	6.6
$B^0 \to \omega K^{*0}_{K^+\pi^-}$	2.1	< 23	25.6	3.8
$B^0 \to \eta'_{\rho\gamma}K^0$	0.33	65.2	1.9	1.9
$B^+ \to \rho^+\rho^0$	0.17	26.4	3.9	3.9
$B^+ \to \omega\pi^+$	0.24	6.4	1.2	1.2
$B^0 \to \omega K^0$	0.99	5.2	1.4	1.4
$B^+ \to \rho^0 K^{*+}_{K^0\pi^+}$	0.56	10.6	1.2	1.2
$B^0 \to \rho^+\rho^-$	0.014	26.6	0.3	0.3
$B^+ \to \omega K^{*+}_{K^+\pi^0}$	0.16	10.6	0.4	0.1
$B^+ \to X_s\gamma$	0	330	0.5	0.5
$B^0 \to \rho^0\rho^0$	0.24	< 2.1	0.4	0.4
$B^0 \to \eta'_{\rho\gamma}\rho^0$	0.36	4.3	0.4	0.4
Total			≈ 49	≈ 22

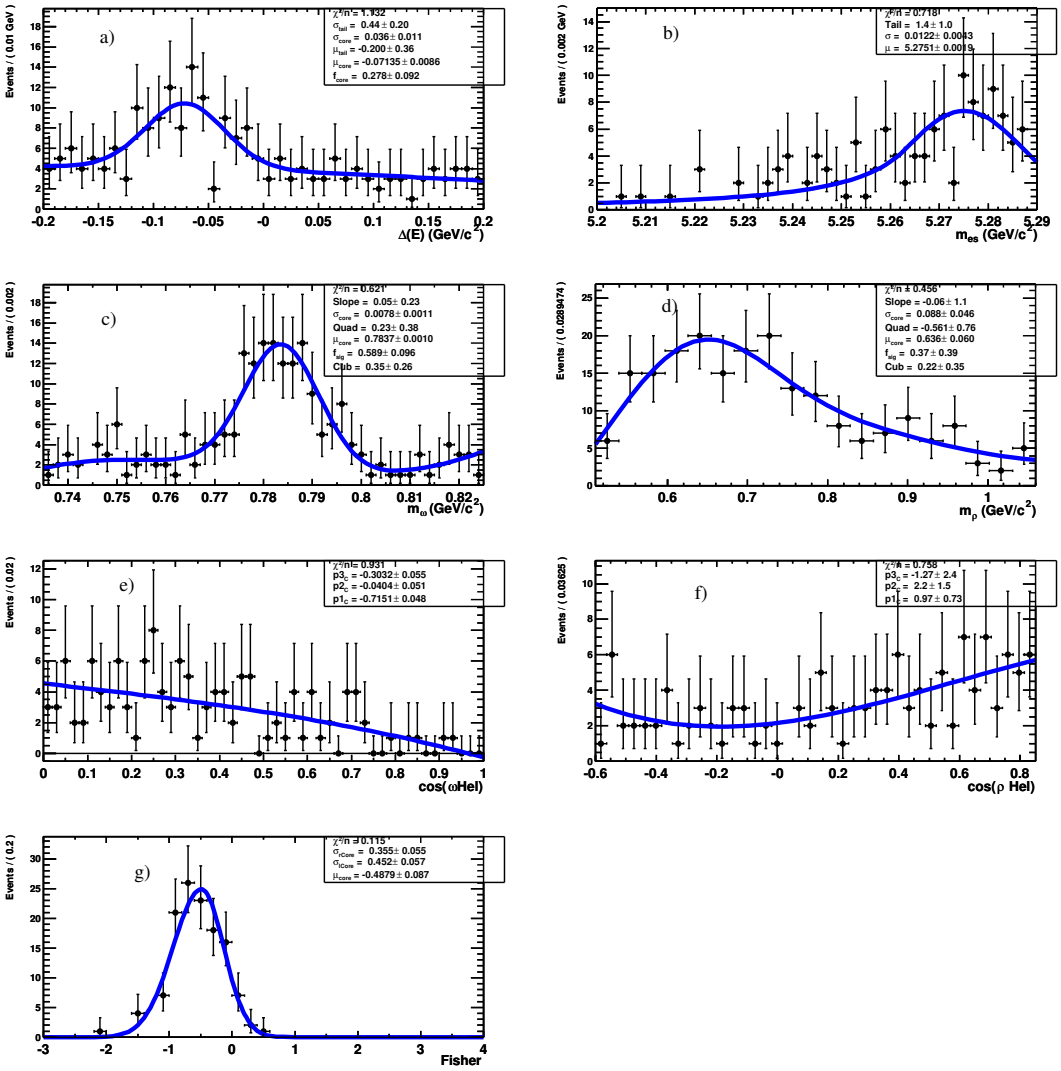

Figure 3.18: $B\overline{B}$ background distributions of a) ΔE, b) $m_{\rm ES}$, c) ω mass, d) ρ mass, e) ω $\mathcal{H}$, f) ρ $\mathcal{H}$, and g) $\mathcal{F}$, for $B \to \omega\rho$ modes using cocktails of exclusive charmless signal MC data.

3.6 Maximum Likelihood Fit

In this section, we will discuss the main method, maximum likelihood [118] (ML) fit, that we use to extract final results. We will also describe several details with respect to the fit not explained in previous sections, and finally we discuss the validation of these methods. For general information on the statistic tools, methods, or terminologies, see for example, Ref. 119, and the Statistics Review of Ref. 12.

From an experimental point of view, the branching fraction of a B decay can be written as

$$\mathcal{B} = \frac{N_{\rm obs}}{\epsilon \times N_{B\overline{B}}}\,, \tag{3.18}$$

where $N_{\rm obs}$ is the ML fit bias corrected (see Sec. 3.6.4.1) number of observed signal events, $N_{B\overline{B}}$ is the total number of $B\overline{B}$ pairs in the sample, and ϵ is the total efficiency of the analysis, i.e., the ratio of $N_{\rm obs}$ to the number of signal events in the sample. For a given sample, we may have already known $N_{B\overline{B}}$, and we can use MC simulation to study the efficiencies of our analyses, which is not too difficult. Our main task is to extract the signal yields, $N_{\rm obs}$.

Two methods are mainly used to get the signal yields: "Cut & Count" method and parameter estimation method based on likelihood function. In "Cut & Count" method, one needs to make much tighter cuts then we have applied in previous sections, and those cuts can be optimized, for example, to maximize the signal-to-background ratio $\frac{N_S^2}{N_S+N_B}$, where N_S and N_B are the numbers of (expected) signal and background events. The signal region for this method is usually much smaller (typical within $\sim 2\sigma$ of the mean values) than we defined (see Sec. 3.5.1) in order to have clean signals. So the efficiency for this method is very low which is not suitable for rare decay studies performed here, and we mainly, if any, use this method as cross check.

To extract signal yields for charmless rare B decays, we primarily use an unbinned, extended multivariate ML fit [120] based on the maximum likelihood method. A number

of preliminary cuts as described in previous sections are applied to select candidates prior to performing the ML fit. The cuts are in general quite loose, especially on the quantities used as input to the ML fit, to allow for high efficiency and to provide sufficient sidebands to characterize the background well. Some events contain more than one signal candidate. On average, we find between 1.13 and 1.27 candidates per event, as detailed in table 3.10. In such situation, our strategy consists of selecting only one of the candidates. The selection is based on a χ^2 constructed from the masses of the resonances involved in the signal decay mode. For example, for mode $\omega K^{*+}_{K^0_S\pi^+}$, the χ^2 is defined by

$$\chi^2(\omega K^{*+}_{K^0_S\pi^+}) = \left(\frac{m_\omega - 0.78257}{0.0082}\right)^2 + \left(\frac{m_{K^*} - 0.892}{0.051}\right)^2 . \tag{3.19}$$

Table 3.10: Average number of candidates per event, as found in real data (on-peak) and in signal MC.

mode	$\omega K^{*+}_{K^0_S\pi^+}$	$\omega K^{*+}_{K^+\pi^0}$	$\omega K^{*0}_{K^+\pi^-}$	$\omega\rho^+$	$\omega\rho^0$
#Data combs/event	1.21	1.22	1.15	1.21	1.15
#MC combs/event (T)	1.27	1.23	1.15	1.20	1.15
#MC combs/event (L)	1.27	1.15	1.14	1.25	1.18
mode	ωK^+		ωK^0	$\omega\pi^+$	
Combs/event	1.13		1.15	1.15	

Suppose, then, we have a total of N events in the data sample passing all the preliminary cuts, and from variant studies, we believe that there are m components (or m hypotheses: signal, continuum background, $B\overline{B}$ background, etc.). As we have shown in previous sections, observables $\mathbf{x}$ of each component have different and definite distributions described by PDFs. Let $\mathcal{P}_j(\mathbf{x})$ be the total PDF for jth component. The $\mathcal{P}_j(\mathbf{x})$ are (usually) the products of PDFs of jth component described in previous sections, where we know those PDFs for different components are determined with various samples of data and Monte Carlo. The PDF parameters got this way are then

usually fixed for the ML fit. Let n_j be the number of events in the sample for jth component (hypothesis), and we know

$$\sum_{j=1}^{m} n_j = N \,. \tag{3.20}$$

The PDF of the total sample, $\mathcal{P}(\mathbf{x})$, can be written as

$$\mathcal{P}(\mathbf{x}) = \sum_{j=1}^{m} n_j \mathcal{P}_j(\mathbf{x}) \,, \tag{3.21}$$

where we omit the overall normalization N, and n_j are the free parameters that we need to estimate. For the sample of N events, the extended likelihood function is

$$\mathcal{L}(\mathbf{x}|n_1 \ldots n_m) = \frac{e^{-\sum n_j}}{N!} \prod_{i=1}^{N} \mathcal{P}(\mathbf{x}_i) \,, \tag{3.22}$$

where the first term takes into account the Poisson fluctuations in the total number of events, and the estimated $n_i \ldots n_m$ are the values maximizing the likelihood function $\mathcal{L}$.

As we have mentioned, we include two components in the ML fit for the three PV modes: signal and continuum background, and three components for all the five VV modes: signal, $B\overline{B}$ background and continuum background. For charged B decays, we also fit the direct CP violation,

$$\mathcal{A}_{ch} = \frac{n^-_{\rm sig} - n^+_{\rm sig}}{n^-_{\rm sig} + n^+_{\rm sig}} \,, \tag{3.23}$$

by having for each hypothesis j two identical components to get positive and negative charged event yields, n^+_j and n^-_j.

The observables used in all the fits are ΔE, $m_{\rm ES}$, $\mathcal{F}$, m_ω, and $\mathcal{H}_\omega$. We do combined fits of ωK^+ and $\omega\pi^+$ and include DIRC pulls $S^{K/\pi}$ with appropriate forms (see Sec. 3.6.1). For VV modes we also include resonance mass $m_{K^*/\rho}$ and helicity $\mathcal{H}_{K^*/\rho}$ of K^*/ρ with proper forms as described previously.

In the next subsections, we will have specific discussions on several topics of our ML fits.

3.6.1 K/π Fitting

We fit ωK^+ and $\omega\pi^+$ modes together in order to eliminate the need for a correction to take account of the cross-feed from one charged mode to the other due to the S cut which allows the tail of the other track hypothesis to enter into the data sample (see Figure 3.4 on page 102).

However, S for K/π are highly correlated, and the same for ΔE. In Figure 3.19, we show the ΔE distributions for K/π hypotheses from $\omega\pi^+$ signal MC sample. The mean of ΔE for K hypothesis in the π sample is centered at about 30 MeV.

The correlations between S^K and S^π, and between ΔE^K and ΔE^π, are through their dependence on track momentum, as we can see from the two dimensional plots of $\delta\Delta E = \Delta E^K - \Delta E^\pi$ vs track lab momentum p and $\delta S = S^\pi - S^K$ vs p in Figure 3.20. The band structure in the δS vs p plot arises from the binning of track's polar angle in the calculation of the θ_c pull distributions. We also show the distributions of $\delta\Delta E$ and δS in Figure 3.21.

So the PDFs with respect to ΔE and S are actually functions of track lab momentum p, $\mathcal{P}^{K/\pi}(m, p, \theta_c)$. We can still write it as three independent PDFs for each hypothesis

$$\mathcal{P}^i(m, p, \theta_c) = \mathcal{P}(\Delta E^i) \cdot \mathcal{P}(S^i) \cdot \mathcal{P}^i(p)\,, \tag{3.24}$$

because ΔE and S are constructed with distributions quite independent of the track momentum. Using the fact that the momentum distribution of the bachelor track is nearly independent of particle type, or event hypothesis, we can write the total PDF for an event, with all other observables taken out, as

$$\begin{aligned}\mathcal{P} = [&n^K_{\rm sig} \cdot \mathcal{P}_{\rm sig}(\Delta E^K) \cdot \mathcal{P}(S^K) + n^\pi_{\rm sig} \cdot \mathcal{P}_{\rm sig}(\Delta E^\pi) \cdot \mathcal{P}(S^\pi) + \\ &n^K_{\rm bkg} \cdot \mathcal{P}_{\rm bkg}(\Delta E^\pi) \cdot \mathcal{P}(S^K) + n^\pi_{\rm bkg} \cdot \mathcal{P}_{\rm bkg}(\Delta E^\pi) \cdot \mathcal{P}(S^\pi)] \times \mathcal{P}(p)\,,\end{aligned} \tag{3.25}$$

where we use ΔE^π for both hypotheses in backgrounds for simplicity. Since the PDF for momentum is outside the overall PDF and has no effects on the yields, $n_j^{K/\pi}$, our fitter

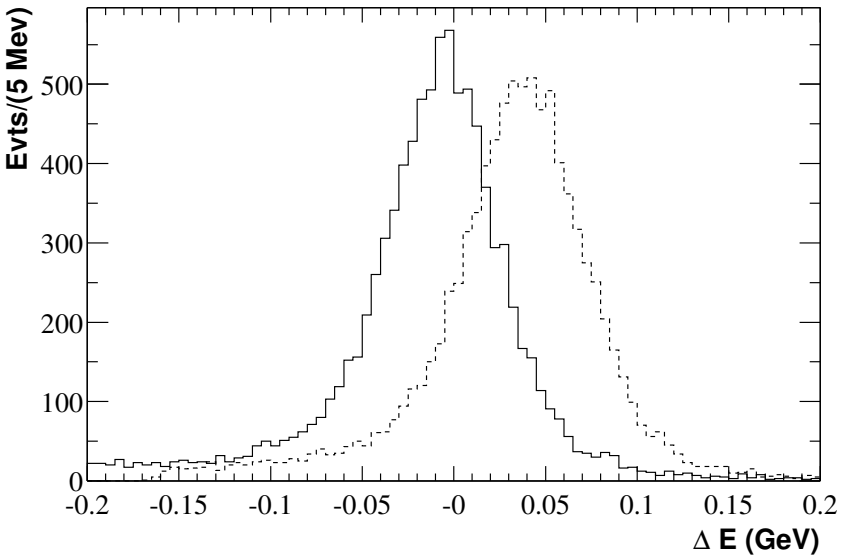

Figure 3.19: ΔE distributions for π (solid line) and K (dashed line) from $\omega\pi^+$ signal MC data. The peak of ΔE for K hypothesis is shifted about 3 MeV.

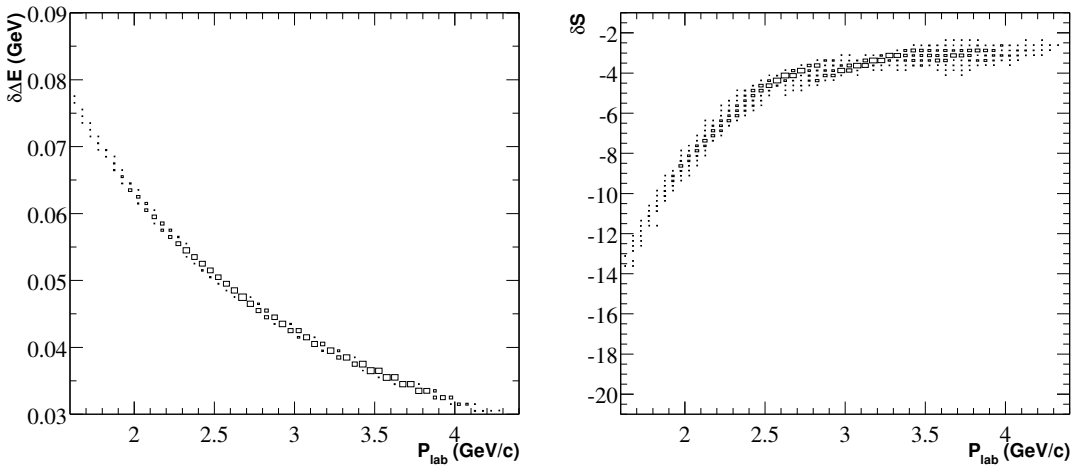

Figure 3.20: Two dimensional plots $\delta\Delta E$ vs $P_{\rm lab}$ (left) and δS vs $P_{\rm lab}$ (right) show the momentum dependence of $\delta\Delta E$ and δS. The plots are from $\omega\pi^+$ signal MC data.

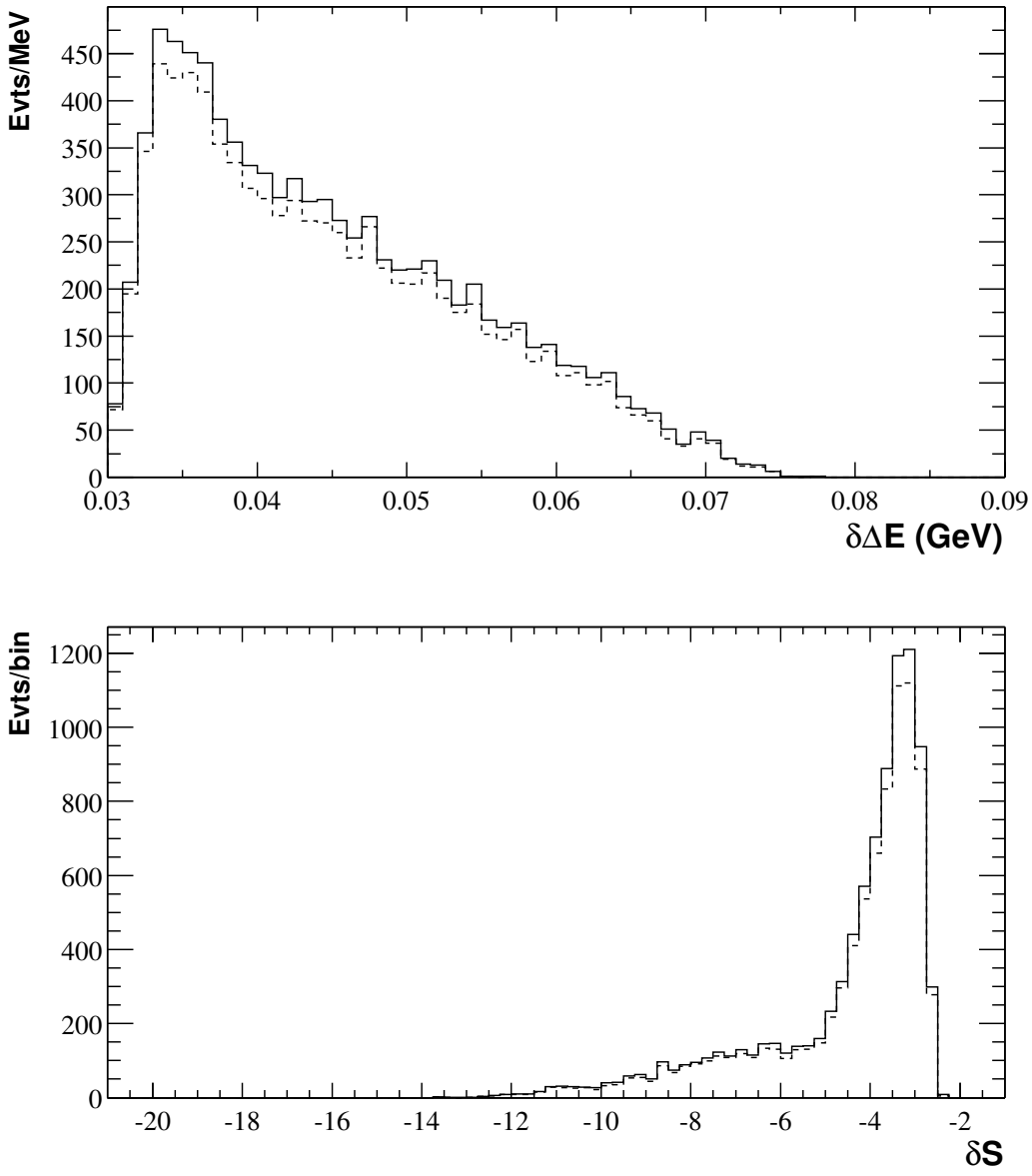

Figure 3.21: Distributions of $\delta\Delta E$ and δS from $\omega\pi^+$ signal MC data. The dashed curves are for subset data with cuts $|\Delta E| < 100\,\mathrm{MeV}$ and $|m_{\mathrm{ES}} - 5.280| < 70\,\mathrm{MeV}/c^2$.

without momentum PDF as in last section is still valid. The problem arises, however, when we try to reproduce the correlations of ($\Delta E^K \Longleftrightarrow \Delta E^\pi$) and ($S^K \Longleftrightarrow S^\pi$) to validate the fitter, since the momentum is not in the final PDFs, and we can not generate correlations through momentum dependence.

We can solve this problem by using the pairs ($\Delta E^\pi,\ \delta\Delta E$) and ($S^\pi,\ \delta S$) instead of ($\Delta E^K,\ \Delta E^\pi$) and ($S^K,\ S^\pi$). The PDF can be rewritten as

$$\begin{aligned}\mathcal{P} =& n^K_{\rm sig}\cdot\mathcal{P}_{\rm sig}(\Delta E^\pi+\delta\Delta E)\cdot\mathcal{P}(S^\pi-\delta S)+n^\pi_{\rm sig}\cdot\mathcal{P}_{\rm sig}(\Delta E^\pi)\cdot\mathcal{P}(S^\pi)+\\ & n^K_{\rm bkg}\cdot\mathcal{P}_{\rm bkg}(\Delta E^\pi)\cdot\mathcal{P}(S^\pi-\delta S)+n^\pi_{\rm bkg}\cdot\mathcal{P}_{\rm bkg}(\Delta E^\pi)\cdot\mathcal{P}(S^\pi)\,.\end{aligned} \tag{3.26}$$

In these operations we distinguish the resolution functions from the separation functions. These two types of functions are quite independent, and the momentum dependence is now only in the separation functions. However, we do not need to model the distributions as shown in Figure 3.20 for separation dependence, because `RooFit` provides a mechanism to generate $\delta\Delta E$ and δS from data. We also illustrate in Figure 3.21 that the distributions of $\delta\Delta E$ and δS for different data regions (signal box, total on-peak region) are quite identical, which justifies the procedure to get the separation functions from data.

We compute the separation variables in preliminary selection stage and require loose cuts to those variables, $0.026 < \delta\Delta E < 0.090$ GeV, and $-21 < \delta S < -1$. We model S^π by a double-Gaussian with both means at 0, and the core Gaussian with area fraction 0.85 and sigma 0.9, the tail Gaussian with sigma 2.0, as we infer from Ref. 107.

3.6.2 f_L Fitting

PDFs of form (3.8) are used in the fitter for VV modes to extract longitudinal polarization fraction f_L, as well as signal yields, $n_{\rm sig}$. To calculate branching fraction $\mathcal{B}$, we need to know the efficiency ϵ in (3.18). Because we have different selection efficiencies

for longitudinal and transverse components, the total efficiency ϵ is a function of f_L:

$$\epsilon = f_L \cdot \epsilon_L + (1 - f_L) \cdot \epsilon_T \,, \tag{3.27}$$

where ϵ_L and ϵ_T are MC efficiencies for longitudinal and transverse components, respectively. So the uncertainty of f_L can transfer to ϵ, and to the branching fraction $\mathcal{B}$, as well as from $n_{\rm sig}$ to $\mathcal{B}$. It is then convenient to fit branching fraction instead of signal yields in the ML fit. For this purpose, we write $n_{\rm sig}$ as a function of ϵ_L, ϵ_T, f_L, $\mathcal{B}$, and $N_{B\overline{B}}$, where f_L and $\mathcal{B}$ are free parameters to fit. We actually have two fit options for VV modes, one is the regular fitter to get signal yields and significance, another one fits directly to get branching fractions.

3.6.3 Floating Continuum Background Parameters

Within the framework of `RooFit` we have the ability to float some of the PDF parameters in the final ML fit. By doing this, continuum background parameters can be determined by making use of the larger statistics available in the full on-peak sample rather than restricting the data to on-peak sidebands. When we initially determine PDFs for our variables, we project onto a specific variable. As a result, the fitter must minimize only a handful of parameters. When we choose to float background parameters in the final ML fit, our fitter must be able to find a minimum in a larger-parameter space. We have tested that our fitter can handle the number of degrees of freedom we use in our final fits (typically $12 \sim 16$).

For the analyses described here, we choose to float the most important parameters in the continuum background, including ARGUS exponent ξ, ΔE coefficients, core parameters of Fisher, combinatorial background fractions and slopes for resonances. We do not, however, float parameters for signal components, but determine them from the signal Monte Carlo (including appropriate corrections as described in previous sections. Additionally, we do not float parameters to which our signal yields are insensitive (such

as tail components of peaking backgrounds). For all parameters floated in our analyses, we initialize their values to those determined from sideband data.

3.6.4 Fit Validation

We build our ML fitter based on several assumptions, and we use this fitter to get our final results. The correctness of our results relies on the correctness of those assumptions and the fitter itself. We must make sure that the analysis is fully validated before we fit to get the results.

We include one or two background components in the fitter and assume others are negligible, which we have to test carefully. We use various data and Monte Carlo samples to check for possible backgrounds. Usually we run our physics analysis job `Q2BApp` on those samples with the same setting as on real or signal MC data and apply the same preliminary selection cuts to the Ntuples of those samples. If the number of events passing the cuts is really small, the background from that particular sample can be neglected safely. Otherwise, we have to include a component in the ML fit for that background, or find a method to suppress it.

The PDF for each component included in the ML fit is usually the product of several PDFs of individual observables. By doing this, we assume that the observables are independent to each other. We choose observables so as to minimize the correlation between them, but these observables are not totally independent. We check the correlation between observables by measuring the correlation coefficients, $r(x, y)$,

$$r(x,y) = \frac{\sum_i (x_i - \overline{x})(y_i - \overline{y})}{\sqrt{\sum_i (x_i - \overline{x})^2 \sum_i (y_i - \overline{y})^2}} \,. \tag{3.28}$$

We find that for all the modes studied here, none of the coefficients is larger than 6%, and by far most are below 1%, justifying our procedure. (Detailed studies on observable correlations are performed for individual modes if particular correlations are expected

for those modes. See Chapter 4 for detailed discussions.) Correlation between ARGUS exponent and Fisher [121] is found common to most of our analyses and `Q2BFit` has been modified to allow fitting for such a correlation [112]. The effects on the final results are found negligible for modes in this work.

We model our signal PDFs mainly from signal MC samples, which could give us parameters slightly different from what they should be in the real data. We use control samples, or if the statistics allow, use our data sample directly to correct any differences. As we have discussed, we have applied ω mass scale and shift corrections, ΔE width scale, $m_{\rm ES}$ mean shift, S shape corrections, etc., to our PDF parameters.

3.6.4.1 Fit Bias

The residual effects due to the correlations in the signal and other imperfection in modeling the PDFs are taken into account in the "ML-fit bias", or the ML fit efficiency, correction.

One of our tests for bias in the fit method is to generate samples of events drawn from the background PDFs into which we embed a known number of events selected randomly from the signal MC sample. We express the fit bias factor as the ratio of (and/or the difference between) the mean yield from the fit to the number of embedded signal events.

3.6.4.2 Goodness-of-Fit Test

One test of the overall fitting procedure is to check the goodness-of-fit [122]. This is defined as how well the χ^2 of the fit to the on-peak data compares with the distribution of fit χ^2 obtained from fit to the data samples generated from the fitter itself. One should expect the measured value to lie with a few sigma of the mean of the generated distributions. The goodness-of-fit test is performed after unblinding.

3.6.5 Signal Significance and Upper Limit

Once we fit the final results, we make the test of signal significance [123], which is the maximum likelihood ratio of the central yield value against the null hypothesis. The ratio is the number of standard deviations of a Gaussian distribution at which point the probability corresponds to that for a null hypothesis to fluctuate to the observed yield. We may claim an observation if the signal significance is greater than 4σ. Otherwise, we calculate the 90% confidence level (CL) upper limit (UL) for the branching fraction, which means a probability of 90% that the real branching fraction is below that limit. We use a procedure described in Sec. 3.7.1 to calculate the ULs with systematics included in the calculation.

3.7 Systematic Errors

The branching fractions measured have systematic as well as statistical uncertainties, including those from the number of $N_{B\overline{B}}$ (Eq. 3.18), ML fits, various efficiencies and production rates.

B Counting Errors

We take the number of produced $B\overline{B}$ pairs in the sample from the luminosity and B counting script [124], which selects inclusive hadronic events in both on- and off-peak data sets and measures the number of $B\overline{B}$ pairs through the increase in the ratio of hadronic events to muon pairs between on- and off-peak data sets due to $\Upsilon(4S)$ production. We assume equal numbers of charged and neutral B's, and determine the error on the number of $B\overline{B}$ events from the script to be 1.1%, which is mainly due to the uncertainty of the MC simulation for the `GoodTracksLoose` candidate list.

ML Fit Errors

We divide systematic errors from ML fit into two categories: the fit bias (or fit efficiency), which is mainly due to observable correlations, as described in Sec. 3.6.4.1, and yield error, which is due to the uncertainties of PDF parameters. We take one-half of the fit bias as systematic errors from the fit bias.

In order to determine the ML fit yield systematic, we would like to float PDF signal parameters in the fit. For modes with a small number of signal events, however, this is not practical. As an alternative, we use control samples, or the on-peak sideband data if statistics allowed, to study how well the MC models the data, and apply appropriate corrections (see Sec. 3.6.4). From these studies, we also determine values by which to vary our signal parameters around these nominal values. We set the variations for signal PDF parameters which have no such studies to their errors from parameter fitting procedures. We then apply these variations, one at a time, to our signal PDFs and re-run the ML fit. We quote the changes in the yields as systematic errors for the parameter uncertainties, and add all these errors quadratically to get the ML fit yield error.

Efficiency Errors

The MC signal efficiency is determined by the ratio of the events used in the fit and the total number of generated MC signal events. To obtain the final efficiency, the MC efficiency has to be corrected for the overestimate of the tracking and neutral efficiencies in the simulation. For the K^0_S efficiency we take the correction determined for the selection we use from Ref. 103. We apply no correction for the K^0_S tracks since the `ChargedTracks` list is used. Finally, the efficiency must be corrected for resonance branching fractions since the channel of interest is forced in signal MC.

We summarize below systematic errors from efficiencies and all other sources.

- Trigger efficiency: The trigger efficiency for multi-hadron events is in excess of 0.9993 [124]. We neglect the systematic error on the tiny inefficiency from this source.

- Track multiplicity: This is for the cut on the minimum number of tracks in the event. We require the reconstruction of at least one track from the other B decay. The signal MC inefficiency for this cut is a few percent. We assign an uncertainty of 1%.

- Track finding/efficiency: The study of absolute tracking efficiency in Ref. 125 provides a systematic error associated with the correction tables for `GoodTracksLoose` tracks of 0.8% per track.

- γ, π^0 finding: The photon efficiency is overestimated in MC [94]. Following the recommendations, we have therefore "smeared" the MC to match the data, and calculate the systematic error per photon by adding in quadrature a fixed contribution of 2.5%.

- K^0_S finding/efficiency: The K^0_S efficiency systematic error due to displaced track origins is conservatively estimated to be 3% [103]. The additional contribution from different effects between `GoodTracksLoose` and `ChargedTracks` was evaluated and found to be a negligible 0.25% [126]. The systematic for finding (prompt) `ChargedTracks` is 1.3% per track [125]; the total K^0_S efficiency systematic including this is 4%.

- Event shape cuts: There are two variables used for event shape cuts, $\cos\theta_{\rm T}$ and $\mathcal{F}$. For $\cos\theta_{\rm T}$, the systematic uncertainty estimate is straightforward, since the expectation is that the distribution of signal MC for this variable should be nearly flat. We take the systematic uncertainty to be one-half of the difference between the observed signal MC efficiency of the $\cos\theta_{\rm T}$ cut used for each analysis and the

expectation of a flat distribution. For $\mathcal{F}$, the systematic uncertainty is included in the ML fit yield error discussed above.

- Particle ID: The PID killing efficiency is determined from the PID tables where data control samples determine efficiencies with an uncertainty of ∼0.1% [95] when integrated over our samples. Thus we take the PID killing systematic error to be negligible. For analyses with a charged kaon, we estimate that the uncertainty of the tight kaon selector (again determined from data) to be 1%.

  As we include the DIRC pull for the prompt charged track in the ML fit for ωh^+, we use the uncertainties on the PID parameterization, as determined from data control samples [107], to vary the PDF in our fit. The resulting change in fit yield is quoted here as the PID systematic.

- $B\overline{B}$ background: $B\overline{B}$ background is included in the fits for VV modes. In principle this accounts for uncertainty in this yield in the statistical error. We quote the $B\overline{B}$ background systematic to be one half the measured change in the signal yield when the number of fit $B\overline{B}$ events is changed by one standard deviation, to allow for uncertainties in the $B\overline{B}$ PDFs.

  For PV modes in this work, we estimate the $B\overline{B}$ background is small and assign ± 1 event as systematic error.

- Polarization fraction f_L: Based on the *BABAR* measurements for $\rho\rho$ and $K^*\rho$ modes [127], we fix the longitudinal polarization fraction f_L to 0.9 for all the VV modes at first, and if we find significant signal yield after unblinding, we will float f_L eventually.

  For the results obtained from fits with fixed f_L we assign the systematic on the yield to be the measured change in branching ratio when f_L is changed by 0.3 ($\simeq 1/\sqrt{12}$).

For the fit with f_L free, we obtain the final branching fraction result directly from ML fit (see Sec. 3.6.2), which gives a statistical error that fully contains the error of branching fraction from f_L.

The dominant systematic on f_L itself when floated, comes from any unmodeled correlations or other effects in the PDFs; we estimate its systematic error based on the observed difference between the fitted means of distributions from pure PDF generated samples and generated background with embedded signal MC samples.

- Charge Asymmetry Systematics: Systematic effects in charge asymmetry measurements with similar kinematics to ωh^+ decays were studied in detail in the $B^+ \to \eta' K^+$ analyses [86], and we assign the same systematic error of 1.1% to the charge asymmetries.

  For the analyses with a K^* or ρ, the charged K or π used for the asymmetry has a much wider momentum spectrum. We assign 2% systematic uncertainty for $\mathcal{A}_{ch}$ that was determined in the study of decay $B \to \phi K^*$ [13].

- MC statistics: Analyses use about 40K events from the 10 series SP4 production. With a typical efficiency of 20%, this gives a relative error of 1.0%. Actual values are given for each mode.

- Branching fractions of daughters: This is simply taken as the uncertainty on the branching fraction from the world averages [12].

3.7.1 Combining Results

We combine branching fractions from different decay sub-modes using their log-likelihood curves to get one branching fraction value [112]. When combining, these curves should be adjusted with the effects of systematic uncertainties, which can be grouped into three types: **additive** systematic uncertainties, which affect the fit yield

and thus the statistical significance of a result, **uncorrelated** systematic uncertainties, which are mode-independent, and generally are a superset of the additive systematic uncertainties, and **correlated** systematic uncertainties, which affect all modes in the same direction. Correlated errors are not applied to individual curves before combining, because they shift all curves in the same direction due to common uncertainties on efficiency and thus have a different effect on the combined log-likelihood curve.

Including a uncorrelated systematic uncertainty σ_{syst} involves convoluting the likelihood with a Gaussian of width σ_{syst}. If the original likelihood curve is Gaussian with width σ_{stat}, this produces a new Gaussian likelihood curve with $\sigma^2 = \sigma^2_{\text{syst}} + \sigma^2_{\text{stat}}$. Equivalently, this adjusts the log-likelihood curve by:

$$\chi^2 = \frac{\chi^2_{\text{stat}}\,\chi^2_{\text{syst}}}{\chi^2_{\text{stat}} + \chi^2_{\text{syst}}}\,, \tag{3.29}$$

where $\chi^2_{\text{stat}} = (x-\mu)^2/\sigma^2_{\text{stat}}$ and similarly for χ^2_{syst}. This has the effect of broadening the log-likelihood curve to account for the systematic uncertainty. Log-likelihood curves corrected by uncorrelated systematic errors are then added together and the new minimum of the combined curve is readjusted to 0. The significance of the combined results is

$$\text{signif}(\sigma) = \sqrt{-2\ln(\mathcal{L}/\mathcal{L}_{\text{max}})}\,, \tag{3.30}$$

evaluated at $n_{\text{sig}} = 0$. To include correlated systematic errors, the curves for individual modes are shifted down one sigma and the mean of the combined curve is found. This is repeated for individual curves shifting up one sigma. The average change of the combined means is the weighted correlated systematic error. And this error is then applied to the original combined curve with uncorrelated systematic errors included to get the final log-likelihood curve including all systematic errors.

The combining procedure is done with a `root` script, `combine.cc`, making use of likelihood scan curves output by `Q2BFit`. Detailed usage of the package can be found in Ref. 128.

Chapter 4

Analysis Results

We present in this chapter our analyses results for charmless two-body rare B decays with ω mesons based on *BABAR* Run 1 and Run 2 data with 88.9×10^6 $B\overline{B}$ pairs, using analysis techniques described in the previous chapter. The results for PV modes: $B^+ \to \omega K^+$, $\omega\pi^+$, and $B^0 \to \omega K^0$, are summarized in Sec. 4.1, and VV results for $B \to \omega K^*$ and $B \to \omega\rho$ are presented in Sec. 4.2. Analysis details for individual modes are also addressed in both sections.

4.1 $B^+ \to \omega K^+$, $\omega\pi^+$ and $B^0 \to \omega K^0$

The observables in the ML fit for $B^0 \to \omega K^0$ mode are: ΔE, $m_{\rm ES}$, $\mathcal{F}$, m_ω, and $\mathcal{H}$. We fit $B^+ \to \omega K^+$ and $\omega\pi^+$ modes simultaneously* with three more observables: $\delta\Delta E$, S, and δS. A set of preliminary selection cuts appropriate for each mode are applied to real and MC data to get final datasets. We include for each mode two PDF components: signal and continuum background. Signal PDFs are got from signal MC data with corrections to take account of the difference between signal and MC data if necessary, and background PDFs are from on-peak sideband data, with major background parameters floated to make use of larger statistics of the full on-peak data in the final fit.

* For historical reason, we first implemented $B^+ \to \omega K^+$ and $\omega\pi^+$ as separate fits [129] and later did K/π combined fitting.

We have investigated potential $B\overline{B}$ background in $B^+ \to \omega K^+$, $\omega\pi^+$ and $B^0 \to \omega K^0$, to validate our procedure of not including a $B\overline{B}$ component in the fit. For each of the three modes, we have applied the full analysis selection to the charmless Monte Carlo sample (luminosity about 3.3× that of the data). In Table 4.1 we list the numbers of events from the sample which pass the preselection cuts after vetoing signal events and events generated by JETSET. We then embed those events into background generated from the PDFs, together with signal events from SP4 signal MC, making the final toy sample[†] the same size as the on-peak data set. We run 500 such toy experiments for each mode and then fit the yield histogram with a Gaussian distribution. The results are shown in Table 4.2. From this study, we find continuum background is negligible (0 ± 1 events for all three modes).

Table 4.1: The number of events passing preliminary selection cuts for PV modes with Charmless B MC data after signal and JetSet events are removed.

Mode	ωK^+	$\omega\pi^+$	ωK^0
# Evts	180	148	43

Table 4.2: Toy study results with charmless $B\overline{B}$ MC sample for PV modes. $N_{\rm embed}$ is the number of charmless $B\overline{B}$ events embedded into the toy sample; $N_{\rm sig}$ is the number of signal events from SP4 signal MC; $N_{\rm tot}$ is the total number of events in each toy sample, which is equal to the size of the on-peak data set; $N_{\rm fit}$ is the mean of the distribution of fitted number of signal events, and $\sigma_{\rm fit}$ is the sigma of the distribution; $N_{\rm fit0}$ is the mean of the distribution of fitted yield from the embedded toy study without $B\overline{B}$ background (see text below), and $\sigma_{\rm fit0}$ is the sigma of the distribution. We use the same notations in other similar tables in this chapter except otherwise specified.

	$N_{\rm embed}$	$N_{\rm sig}$	$N_{\rm tot}$	$N_{\rm fit} \pm \sigma_{\rm fit}$	$N_{\rm fit0} \pm \sigma_{\rm fit0}$
ωK^+	120	87	16729	93.8 ± 11.6	91.7 ± 10.6
$\omega\pi^+$	80	101	30563	107.3 ± 15.6	109.0 ± 13.8
ωK^0	43	27	7560	29.9 ± 6.6	28.1 ± 5.9

[†] We refer to generated sample from ML fitter PDF as toy sample and fit on such toy sample as toy experiment. A pure toy sample is solely generated from the PDF, and an embedded toy sample has a known number of events selected (usually randomly) from other data sources.

We generate both signal and background samples from appropriate set of PDFs then fit these toy samples for pure toy studies. In toy study, we float free parameters as we do for final fit to check if the fit works properly. The "pull" of floated parameter, x, defined as

$$\text{pull} = \frac{x_{\text{fitted}} - x_{\text{init}}}{\sigma_x}\,, \tag{4.1}$$

where x_{fitted} is the fitted value of x in each toy fit, x_{init} is the input value of x in the generator, and σ_x is the fitted error of x, is expected to have normal Gaussian distribution. The pull for background yield is artificially narrow, however, because a fixed number of events was generated, while the extended maximum likelihood fit determines an error that includes the Poisson fluctuations of the sample size.

We summarize pure toy fit results in Table 4.3 for all the fitters, each with 500 toy experiments. The signal yield distributions for combined ωh^+ modes are shown in Figure 4.1, and that for ωK^0 in Figure 4.2.

Table 4.3: Summary of results from pure toy MC studies for PV modes investigated in this work. In each case 500 toy experiments have been used.

Mode		N_{tot}	N_{sig}	$N_{\text{fit}} \pm \sigma_{\text{fit}}$	pull N_{fit} $\mu \pm \sigma$
	ωK^+	16729	87	85.0 ± 14.0	-0.15 ± 0.97
	$\omega \pi^+$	30563	101	97.6 ± 17.5	-0.18 ± 0.95
	ωK^0	9563	33	32.3 ± 8.3	-0.11 ± 0.93
combined	ωK^+	44689	83	83.9 ± 14.1	0.04 ± 1.05
ωh^+	$\omega \pi^+$	44689	101	100 ± 18	-0.04 ± 0.95

We obtain the fit bias factor, as well as further cross checks, by fitting samples of toy background with the expected number of signal MC embedded. Where the expected number of signal events is unknown, we perform toy studies with a number near where we expect signal to be. The results of these studies given in Table 4.4 are for signal

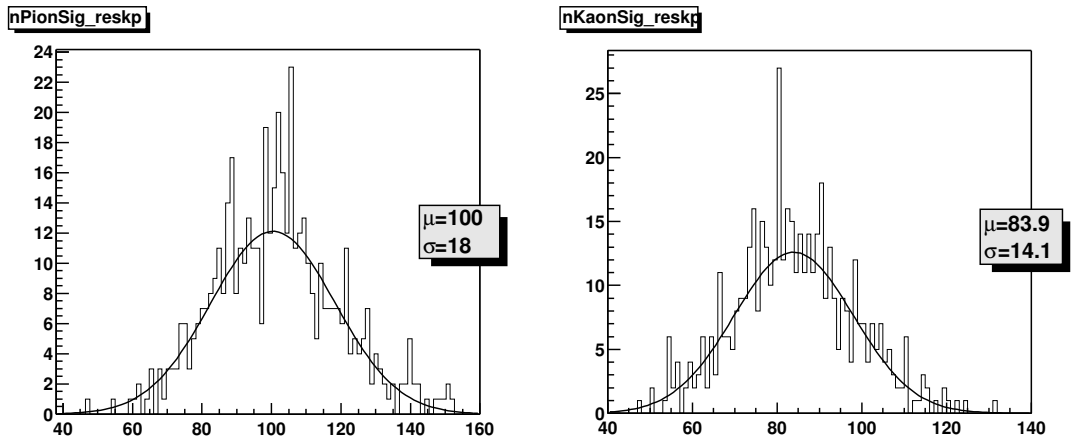

Figure 4.1: Pure toy signal yield distributions for combined $K-\pi$ fitting in $B^+ \to \omega h^+$. Left plot shows $B^+ \to \omega\pi^+$ signal yield; right plot shows $B^+ \to \omega K^+$. A total sample size of 44689 events is used; 101 $B^+ \to \omega\pi^+$ and 83 $B^+ \to \omega K^+$ events are generated.

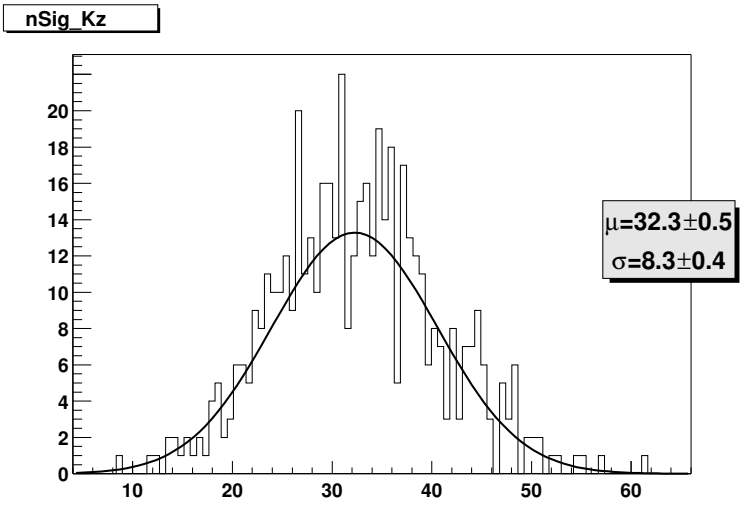

Figure 4.2: Pure toy signal yield distribution for $B^0 \to \omega K^0$. The sample was generated from the PDFs with 33 signal events in 9563 total events.

yields after unblinding. The fit bias here is expressed as the ratio of mean yield from the fit to the number of embedded signal events.

Table 4.4: Summary of results from embedded toy studies for PV modes investigated in this work. In each case 500 toy experiments have been used.

Mode		$N_{\rm tot}$	$N_{\rm sig}$	$N_{\rm fit} \pm \sigma_{\rm fit}$	Bias factor mean$\pm\sigma$
	ωK^+	16729	87	91.7 ± 10.6	1.05 ± 0.12
	$\omega\pi^+$	30563	101	109 ± 13.8	1.08 ± 0.14
	ωK^0	9563	33	34.6 ± 6.2	1.05 ± 0.19
combined	ωK^+	44689	83	91.7 ± 10.7	1.10 ± 0.13
ωh^+	$\omega\pi^+$	44689	101	110 ± 14	1.09 ± 0.14

We show in Table 4.5 the results of the ML fit analyses for off-peak and on-peak data. Shown for each mode are the number of combinations per event (before choosing the best candidate), the number of events to fit, the signal yield, the various efficiencies and product branching fractions, the statistical significance, and the branching fraction. The statistical error on the number of events is taken as the change in the central value when the quantity $-2\ln\mathcal{L}$ changes by one unit. The statistical significance is taken as the square root of the difference between the value of $-2\ln\mathcal{L}$ for zero signal and the value at its minimum. We also give $\mathcal{A}_{ch}$ for the charged modes. The 90% confidence interval of charge asymmetry, obtained from an increase in χ^2 of 2.69, is $[-0.36, 0.19]$ for $B^+ \to \omega K^+$, and $[-0.23, 0.29]$ for $B^+ \to \omega\pi^+$.

In Figure 4.3, we show $m_{\rm ES}$ and ΔE projection plots for $B^+ \to \omega K^+$, $\omega\pi^+$, and $B^0 \to \omega K^0$. To generate each plot, we make cuts on the likelihood ratio in order to optimize the quantity $S^2/(S+B)$, where S represents the probability of an event to be signal, and B the probability that it is background. We find significant signals for all the three PV modes and make the first observation of $B^0 \to \omega K^0$ with statistical significance of 7.5σ.

Table 4.5: ML fit results for $B^+ \to \omega K^+$, $\omega\pi^+$, and $B^0 \to \omega K^0$ from the full Run1+Run2 data set. Charged modes are fit simultaneously.

ML fit quantity	ωK^+	$\omega\pi^+$	ωK^0
Combinations/event	1.12		1.15
Events to fit			
On-resonance	44689		9563
Off-resonance	5142		972
Signal yield			
On-res data	83^{+15}_{-14}	101^{+17}_{-16}	33^{+9}_{-8}
Off-res data	$0. \pm 4.$	$0. \pm 0.02$	$0.0^{+0.9}_{-0.0}$
ML-fit ϵ (%)	110	109	104.2
MC ϵ (%)	20.8	22.1	21.6
Tracking Correction (%)	96.6		96.2
K^0_S Correction (%)	—		96.1
$\prod \mathcal{B}_i$ (%)	89		30.5
Corr. $\epsilon \times \prod \mathcal{B}_i$ (%)	19.6	20.7	6.3
Stat. Signif. (σ)	10.0	9.1	7.5
$\mathcal{B}(\times 10^{-6})$	$4.8 \pm 0.8 \pm 0.4$	$5.5 \pm 0.9 \pm 0.5$	$5.9^{+1.6}_{-1.3} \pm 0.5$
Signal $\mathcal{A}_{ch}$	$-0.09 \pm 0.17 \pm 0.01$	$0.03 \pm 0.16 \pm 0.01$	—
Background $\mathcal{A}_{ch}$	-0.003 ± 0.009	-0.012 ± 0.006	—

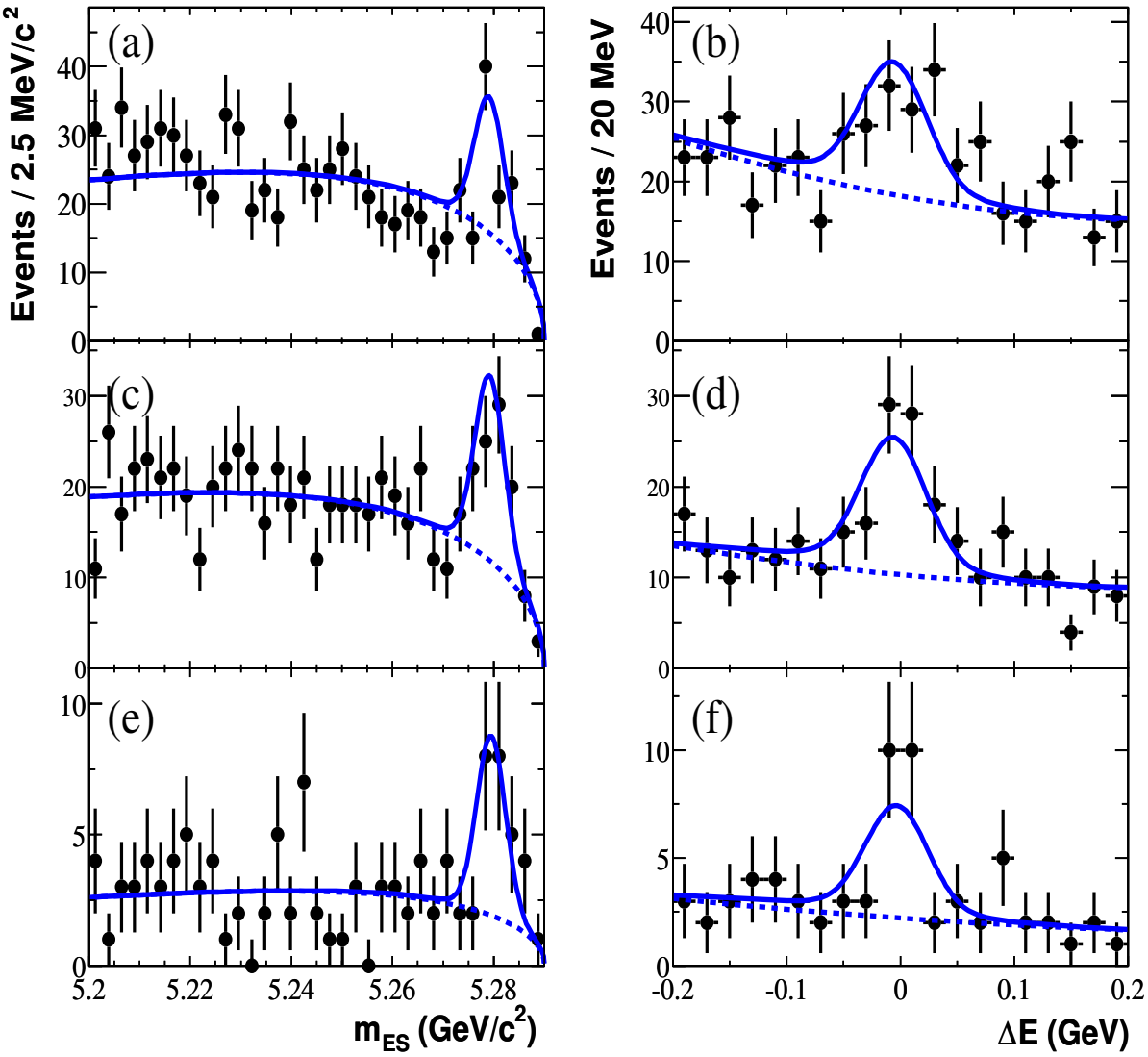

Figure 4.3: Projections of the B candidate $m_{\rm ES}$ and ΔE for $B^+ \to \omega\pi^+$ (a, b), $B^+ \to \omega K^+$ (c, d), and $B^0 \to \omega K^0$ (e, f). Points with errors represent data passing a cut on a likelihood ratio calculated without the quantity that is shown in the plots. The solid curves show the projected fit functions and dashed curves the background functions.

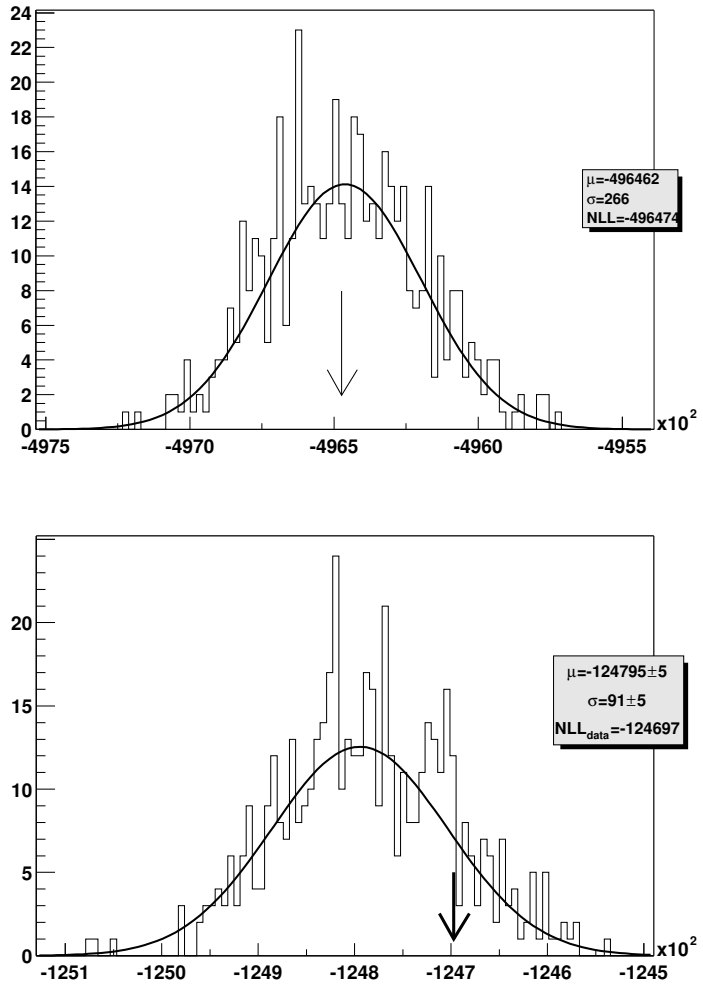

Figure 4.4: Goodness-of-fit plots for $B^+ \to \omega h^+$ (top) and $B^0 \to \omega K^0$ (bottom). The distribution is from 500 pure toy experiments with the number generated signal events equal to the number found in on-peak data. The arrows indicate the $-2\ln\mathcal{L}$ values for on-peak data.

To determine the goodness-of-fit, we run 500 toy MC experiments, generating a sample the size of our on-resonance sample. We generate a number of signal events equal to the number of events found by the fit to on-peak data. The goodness-of-fit plots for $B^+ \to \omega h^+$ and $B^0 \to \omega K^0$ are shown in Figure 4.4, with the arrows indicating the $-2\ln\mathcal{L}$ values for data. The plots show that the $-2\ln\mathcal{L}$ values for data are well within the generated distributions.

Table 4.6 shows the results of our evaluation of the systematic errors for these modes. The fit yield errors are estimated with procedure described in Sec. 3.7, and we list the changes in signal yields when using the different set of ΔE, $m_{\rm ES}$, m_ω, $\mathcal{F}$ and $\mathcal{H}$ parameters in Table 4.7.

Table 4.6: Estimates of systematic errors (in percent) of the $B^+ \to \omega K^+$, $\omega\pi^+$ and $B^0 \to \omega K^0$ branching fractions.

Quantity	ωK^+	$\omega\pi^+$	ωK^0
Fit yield	2.7	3.1	3.2
Fit efficiency/bias	2.7	3.9	2.1
Track multiplicity	1.0	1.0	1.0
Tracking eff/qual	2.4	2.4	3.7
π^0/ γ eff	5.0	5.0	5.0
K^0_S efficiency	—	—	3.0
Number $B\overline{B}$	1.1	1.1	1.1
Branching fractions	1.0	1.0	1.0
MC statistics	1.0	1.0	1.0
$\cos\theta_{\rm T}$	1.0	1.0	1.0
PID	1.4	1.4	1.0
$B\overline{B}$ Background	1.1	1.0	3.0
Total	7.3	8.0	8.8

Table 4.7: Detailed breakdown of variations applied to the signal PDF parameters in order to calculate the ML fit yield systematic for $B^+ \to \omega K^+$, $\omega\pi^+$ and $B^0 \to \omega K^0$. The nominal values and variations around those values were determined from control sample studies for ΔE and $m_{\rm ES}$. Variations for m_ω, $\mathcal{F}$ and $\mathcal{H}$ are the errors from PDF parameter fitting on the signal MC data. The total event systematic is determined by averaging the right and left variations for each parameter then summing those averages in quadrature. Dividing the total event systematic by the signal yield in each channel gives the overall ML fit yield systematic.

		(Fit Yield) - (Nominal Yield)		
Nominal	Variation	ωK^+	$\omega\pi^+$	ωK^0
ΔE offset=0 MeV	+5 MeV	+1.053	+1.407	+0.398
	−5 MeV	−1.640	−1.871	−0.565
ΔE scale=1.05	+0.05	+0.790	+1.607	+0.095
	−0.05	−0.870	−1.750	−0.093
$m_{\rm ES}$ offset=0.7 MeV	+0.2 MeV	−0.619	+0.222	+0.181
	−0.2 MeV	+0.451	+0.004	−0.229
$m_{\rm ES}$ scale=1.00	+0.04	+0.981	+0.840	+0.351
	−0.04	−1.142	−1.017	−0.336
m_ω offset=1.4 MeV	+0.3 MeV	−0.051	−0.089	+0.021
	−0.3 MeV	−0.046	−0.098	+0.005
m_ω scale=1.12	+0.04	−0.003	−0.017	−0.495
	−0.04	−0.018	+0.007	+0.735
$\mathcal{F}$ μ	+1σ	+0.819	+1.250	+0.495
	−1σ	−0.825	−1.248	−0.496
$\mathcal{F}$ σ_L	+1σ	−0.593	−1.047	−0.160
	−1σ	+0.588	+1.034	+0.192
$\mathcal{F}$ σ_R	+1σ	+0.632	+0.905	+0.169
	−1σ	−0.636	−0.908	−0.157
$\mathcal{H}$ P1	+1σ	+0.273	+0.305	+0.108
	−1σ	−0.298	−0.326	−0.119
$\mathcal{H}$ P2	+1σ	+0.019	−0.002	−0.025
	−1σ	−0.028	+0.001	+0.069
Total Events		2.330	3.155	1.048
Total (%) Systematic		2.7%	3.1%	3.2%

4.2 $B \to \omega K^*$ and $B \to \omega\rho$

The observables in the ML fit for $B \to \omega K^*$ and $B \to \omega\rho$ modes are: ΔE, $m_{\rm ES}$, $\mathcal{F}$, m_ω, $m_{K^*/\rho}$, $\mathcal{H}_\omega$ and $\mathcal{H}_{K^*/\rho}$. We construct two-dimensional helicity PDF of $\mathcal{H}_\omega$ and $\mathcal{H}_{K^*/\rho}$ with form as in Eq. (3.8) on page 113 to extract longitudinal polarization fraction f_L of the vector-vector decays. A set of preliminary selection cuts appropriate for each mode are applied to real and MC data to get final datasets. As in PV modes, we include signal and continuum background for each mode with signal PDFs got from signal MC data with necessary corrections for the difference between signal and MC data, and continuum background PDFs from on-peak sideband data, with major background parameters floated to make use of larger statistics of the full on-peak data in the final fit. We find the $B\overline{B}$ background from other charmless rare B decays are not negligible so we also include a $B\overline{B}$ background component in the fit.

Our preliminary studies show that 3, 2, 10, 5 and 22 charmless events are expected in the on-resonance preliminarily selected sample for $\omega K^{*+}_{K^0_S\pi^+}$, $\omega K^{*+}_{K^+\pi^0}$, $\omega K^{*0}_{K^+\pi^-}$, $\omega\rho^+$ and $\omega\rho^0$ respectively. We get $B\overline{B}$ background PDFs from cocktail samples made of major charmless cross-feed decays for each mode listed in Table 3.8 and 3.9 on pages 128–129 with proper weights. Since we float the $B\overline{B}$ yield as well in the ML fit, the cocktail weights only matter in second order, and we include that in the systematic errors of $B\overline{B}$ background.

We have checked that peaking $b \to c$ backgrounds can be safely neglected. For example, we process the generic $B\overline{B}$ MC data for $\omega\rho^+$ mode. About 4K $b \to c$ background events pass the preliminary selection cuts and signal or JETSET event vetoes. We find that the PDFs are similar to those of $q\overline{q}$ background's. We embed 58 signal events with f_L =0.88, and 1200 charmed B background events into the generated continuum background and run 100 such toy experiments. The fitted mean of signal yield is 58.5 ± 1.9, and the fitted $f_L = 0.88 \pm 0.02$, which show negligible signal biases.

Because none of the modes has been observed before, we fix the longitudinal polarization fraction f_L to 0.9 for all of them at first, based on *BABAR* measurements for $\rho\rho$ and $K^*\rho$ [127]. If we find significant signal after unblinding, we will float f_L of those modes eventually.

We summarize pure toy fit results in Table 4.8 for all five modes, and embedded toy study results are shown in Table 4.9.

Table 4.8: Summary of results from pure toy MC studies for all five VV decay channels. The fits have three components (signal, continuum and $B\overline{B}$ backgrounds). In each mode 200 toy experiments have been used.

Mode	$N_{\rm tot}$	$N_{\rm sig}$	$N_{B\overline{B}}$	$N_{\rm fit} \pm \sigma_{\rm fit}$	pull $N_{\rm fit}$ $\mu \pm \sigma$	Bias [ratio]	f_L (fixed)
$\omega K^{*+}_{K^0_S\pi^+}$	11863	12	20	11.3 ± 8.8	-0.08 ± 0.97	0.94	0.9
$\omega K^{*+}_{K^+\pi^0}$	8427	5	20	4.8 ± 7.2	-0.09 ± 1.03	0.95	0.9
$\omega K^{*0}_{K^+\pi^-}$	16625	26	20	27.5 ± 10.4	0.06 ± 0.87	1.06	0.9
$\omega\rho^+$	20145	54	20	54.5 ± 15.4	0.05 ± 1.02	1.01	0.9
$\omega\rho^0$	20769	4	20	3.5 ± 8.6	-0.01 ± 0.83	0.87	0.9

Table 4.9: Summary of embedded toy experiments with embedded SP4 MC signal and charmless $B\overline{B}$ background events. The fits have three components (signal, $B\overline{B}$ background and continuum background). In each mode 200 toy experiments have been used with f_L fixed at 0.9.

Mode	$N_{\rm tot}$	$N_{\rm sig}$	$N_{B\overline{B}}$	$N_{\rm fit}$, $\sigma_{\rm fit}$	Bias [ratio]	Bias [evts]
$\omega K^{*+}_{K^0_S\pi^+}$	11863	12	20	14.9 ± 1.1 , 9.5	1.24 ± 0.09	2.9 ± 1.1
$\omega K^{*+}_{K^+\pi^0}$	8427	5	20	4.9 ± 0.8 , 7.5	0.98 ± 0.16	-0.1 ± 0.8
$\omega K^{*0}_{K^+\pi^-}$	16625	26	20	29.2 ± 1.1 , 10.9	1.12 ± 0.04	3.2 ± 1.1
$\omega\rho^+$	20145	54	20	52.7 ± 2.8 , 17.0	0.98 ± 0.05	-1.3 ± 2.8
$\omega\rho^0$	20769	4	20	3.5 ± 1.0 , 10.3	0.88 ± 0.25	-0.5 ± 1.0

From above toy experiment results, we estimate the sensitivity of on-peak sample measurements. The upper limit estimation assumes that the measured signal yield is zero and the statistical error is given by the average for zero embedded signal events. So if we embed $N_{\rm sig}$ signal events and we get $\sigma_{\rm tot}$ as the sigma of the distribution, the sigma for zero embedded signal events is estimated as $\sigma = \sqrt{\sigma_{\rm tot}^2 - N_{\rm sig}}$. The 90% upper limit estimation is calculated as $1.28\ \sigma/(\epsilon \times N_{B\overline{B}})$. The central value sensitivity is determined for assumed branching ratios of $9{\times}10^{-6}$ for $\omega\rho^+$ and $3.3{\times}10^{-6}$ for the other four modes. The expected results are summarized in table 4.10.

Table 4.10: Expected 90% upper limit (UL) with null observations and statistic significance with assumed branch fractions. The UL is determined using the preliminary selection efficiencies listed in table 4.13 and 4.14. The CLEO results are from Ref. 51.

Mode	σ ($\mathcal{B}=0$)	90% UL [10^{-6}]	CLEO 90% UL [10^{-6}]	$N_{\rm sig}$	$N_{\rm fit} \pm \sigma_{\rm fit}$	signif [σ]
$\omega K^{*+}_{K^0_S\pi^+}$	8.4	4.4	109	10	10.5 ± 9.0	1.2
$\omega K^{*+}_{K^+\pi^0}$	4.5	3.0	129	7	8.3 ± 5.2	1.6
$\omega K^{*0}_{K^+\pi^-}$	11.6	2.1	23	22	25.1 ± 12.5	2.0
$\omega\rho^+$	13.7	4.4	61	50	57.8 ± 15.4	3.8
$\omega\rho^0$	14.8	2.1	11	31	38.3 ± 15.8	2.4

After we unblind the yield-only fits, we find significant signal for $B^+ \to \omega\rho^+$ mode, we then check the full fit with toy studies with f_L floated in the range [0,1] for $B^+ \to \omega\rho^+$ mode before we unblind to get f_L. Table 4.11 summarizes the pure toy study results for different f_L of $\omega\rho^+$ mode. Table 4.12 summarizes the embedded toy study results for different f_L of $\omega\rho^+$ mode.

Table 4.11: Summary of results from pure toy MC studies for $B^+ \to \omega\rho^+$ with floated $f_L \in [0,1]$. For each f_L 200 toy experiments have been used.

Mode $\omega\rho^+$	$N_{\rm sig}$	$N_{\rm fit}$	$\sigma_{\rm fit}$	Bias [ratio]	f_L (in)	f_L (fit)
	54	55.0 ± 3.4	20.9	1.02 ± 0.06	0.5	0.51 ± 0.02
	54	55.8 ± 2.3	19.2	1.03 ± 0.04	0.9	0.85 ± 0.02
	58	60.4 ± 3.1	20.3	1.04 ± 0.05	0.88	0.85 ± 0.02

Table 4.12: Summary of results from embedded toy MC studies for $B^+ \to \omega\rho^+$ with floated $f_L \in [0,1]$. For each f_L 200 toy experiments have been used.

Mode $\omega\rho^+$	$N_{\rm sig}$	$N_{\rm fit}$	$\sigma_{\rm fit}$	Bias [evts]	f_L (in)	f_L (fit)
	54	59.0 ± 3.1	20.8	5.0 ± 3.1	0.5	0.43 ± 0.02
	54	56.4 ± 2.6	22.5	2.4 ± 2.6	0.9	0.83 ± 0.02
	58	62.2 ± 2.8	19.5	4.2 ± 2.8	0.88	0.83 ± 0.02

Figure 4.5 shows the distributions of fitted f_L with input f_L =0.88 from the toy studies. At first we set f_L within the limits [0,1], and we can see from the plots that the distributions are piled up at the physical boundary f_L =1. Rather than treat the difference between the input value of f_L and the mean of the fitted f_L distribution as a bias to be corrected, we judge that the upper (pure toy) and lower (embedded toy) plots in Figure 4.5 are consistent within 0.03, and we assign this 0.03 as a systematic error on f_L. A test fit (see Figure 4.6) later on with f_L free to assume values greater than 1.0 confirms that the true bias is small.

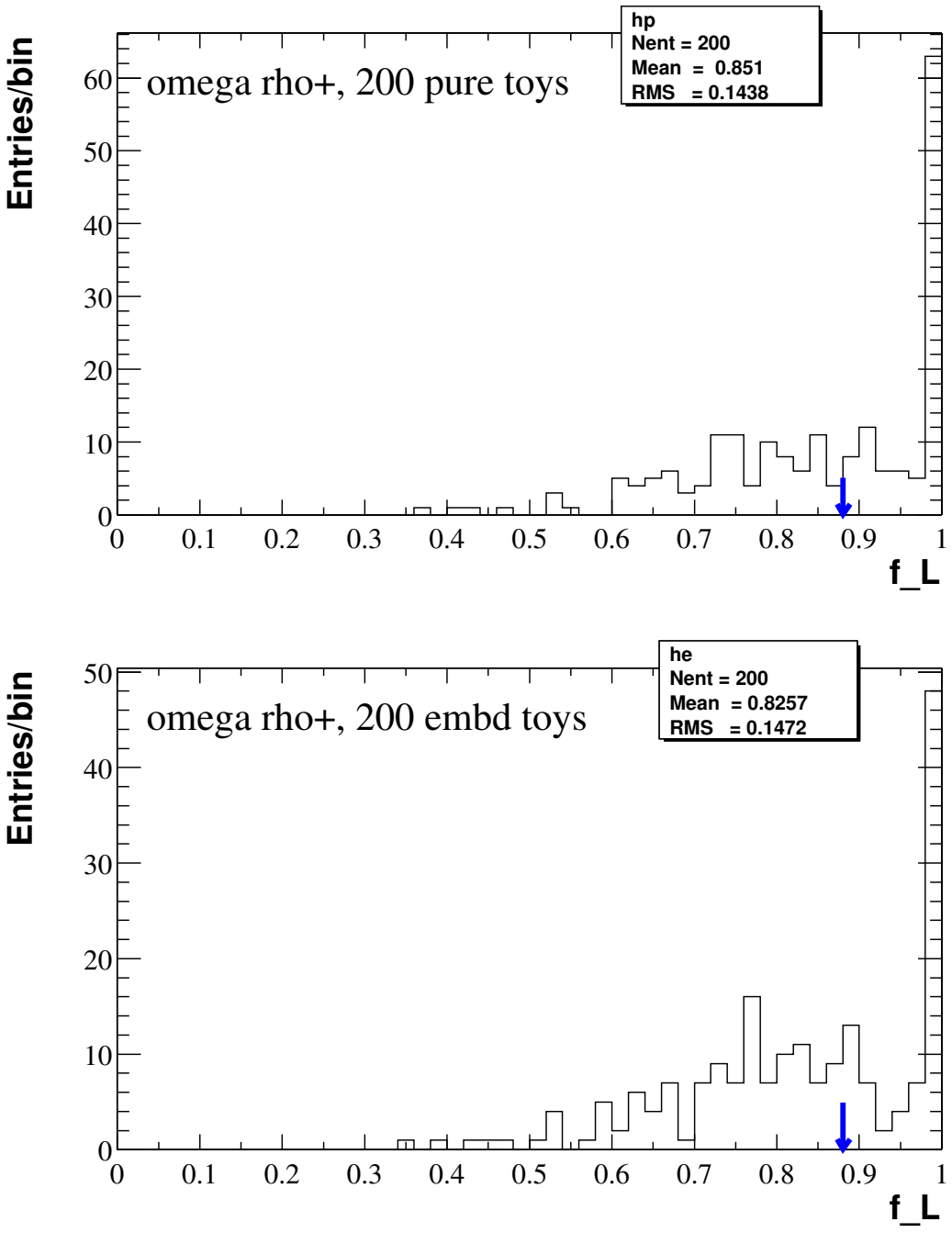

Figure 4.5: Fitted f_L distributions for pure toys (upper) and embedded toys (lower) for $B^+ \to \omega\rho^+$. Arrows at 0.88 indicate the input f_L.

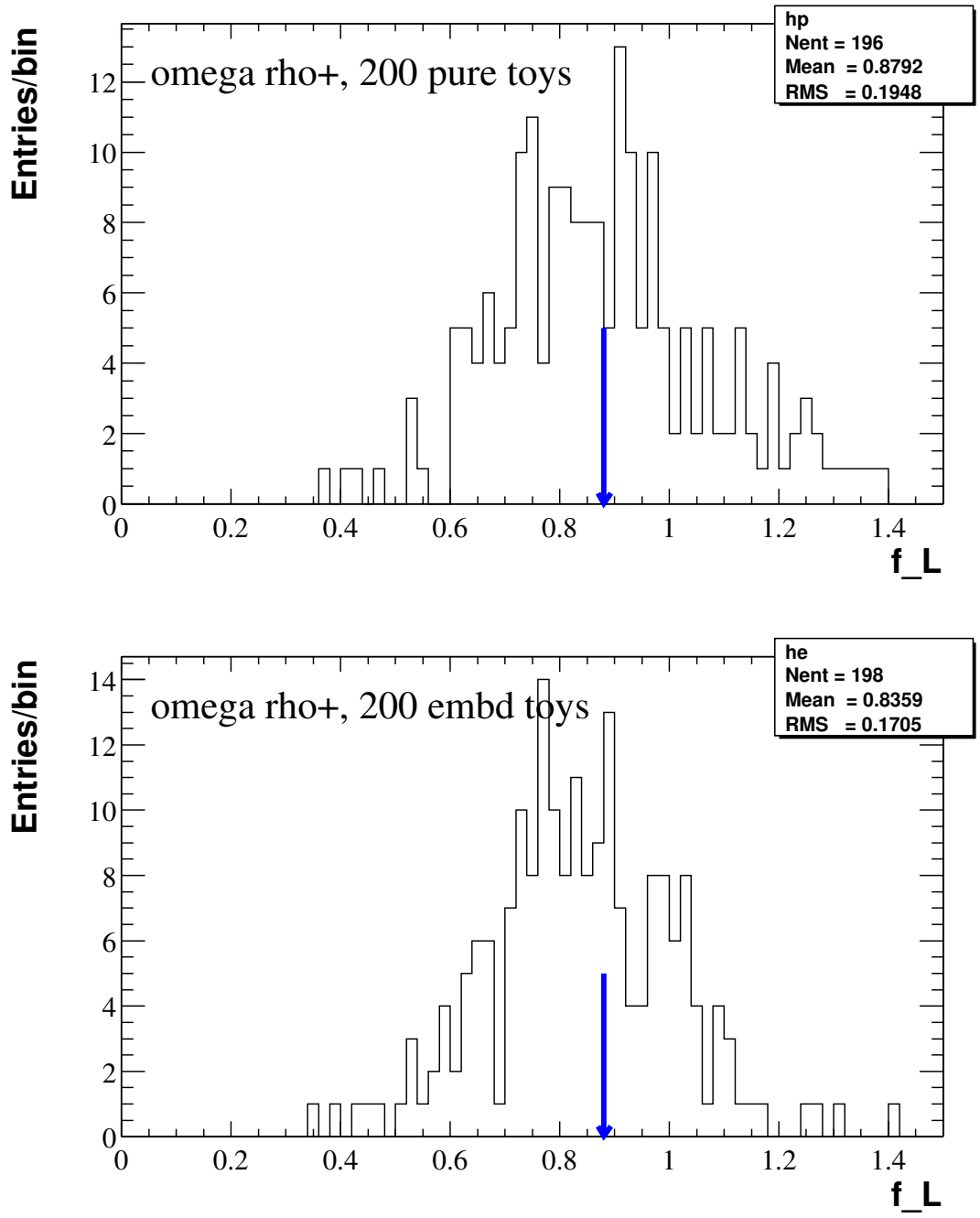

Figure 4.6: Fitted f_L distributions for pure toys (upper) and embedded toys (lower) for $B^+ \to \omega\rho^+$. The distributions are more Gaussian than those in Figure 4.5 as we allow $f_L > 1$. Arrows at 0.88 indicate the input f_L and it shows there is no bias for pure toy and the bias for embedded toy is very close to our estimation, 0.03.

Table 4.13 shows the fit results of the modes $B^+ \to \omega K^{*+}_{K^0_S\pi^+}$, $\omega K^{*+}_{K^+\pi^0}$, and $B^0 \to \omega K^{*0}_{K^+\pi^-}$ for the full Run 1 and Run 2 data set. We combine two decay sub-modes $\omega K^{*+}_{K^0_S\pi^+}$ and $\omega K^{*+}_{K^+\pi^0}$ by summing the curves representing χ^2 and shifting the resulting curve in the ordinate to have its minimum at zero χ^2. The result of this is shown in Figure 4.7. From this curve we obtain the joint likelihood which allows us to extract a 90% CL upper limit, taken to be the branching fraction below which lies 90% of the likelihood integral over the positive branching fraction region.

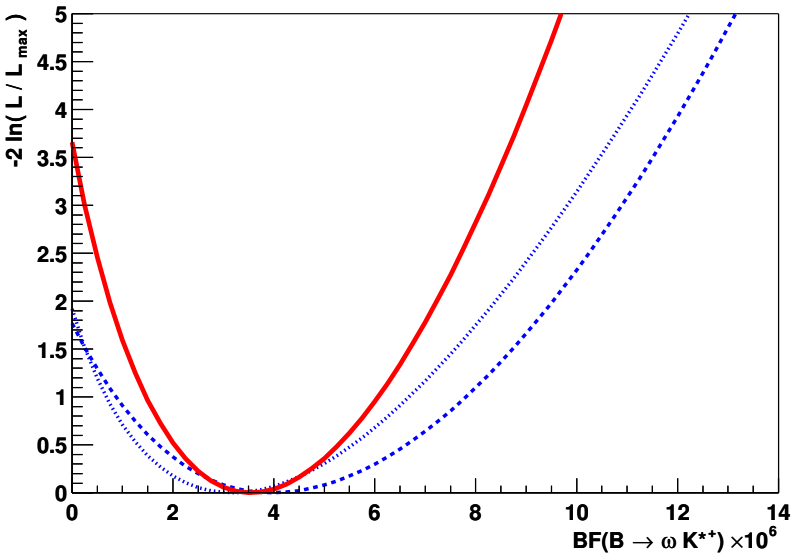

Figure 4.7: Plots of individual and combined $-2\ln\mathcal{L}$ for branching fraction fits; the individual chains are $\omega K^{*+}_{K^0_S\pi^+}$, dashed; $\omega K^{*+}_{K^+\pi^0}$, dotted; and the result of combining both, thick solid.

We show in Table 4.14 the fit results for the modes $B^+ \to \omega\rho^+$ and $B^0 \to \omega\rho^0$ for the full Run 1 and Run 2 data set. For $B^+ \to \omega\rho^+$, we float f_L and the yields of positively and negatively charged ρ so that we can extract the charge asymmetry.

In Figure 4.8, we show $m_{\rm ES}$ and ΔE projection plots for the four VV modes. Contour plots of f_L vs the signal yield and f_L vs branching fraction are shown for

Table 4.13: ML fit values for $B^+ \to \omega K^{*+}_{K^0_S\pi^+}$, $\omega K^{*+}_{K^+\pi^0}$, and $B^0 \to \omega K^{*0}_{K^+\pi^-}$ from the full Run 1 and Run 2 data set.

ML fit quantity	$\omega K^{*+}_{K^0_S\pi^+}$	$\omega K^{*+}_{K^+\pi^0}$	$\omega K^{*0}_{K^+\pi^-}$
$\cos\theta_{\rm T}$ cut	0.8	0.8	0.8
#Data combs/event	1.21	1.22	1.15
#MC combs/event	1.27(T) 1.27(L)	1.23(T) 1.15(L)	1.15 (T) 1.14 (L)
Events to fit			
On-resonance	11863	8427	16625
Off-resonance	1324	957	2116
Signal yield			
On-res data	$11.6^{+8.7}_{-7.2}$	$5.4^{+6.0}_{-4.2}$	$26.1^{+12.1}_{-10.8}$
Off-res data	-4.9 ± 3.8	-3.5 ± 3.9	-9.4 ± 6.5
f_L	0.9 (fixed)	0.9 (fixed)	0.9 (fixed)
90% CL yield UL	29.6	19.7	50.0
Fit $B\overline{B}$ yield (on-res)	$51.8^{+44.1}_{-40.2}$	$4.2^{+24.8}_{-22.0}$	$61.4^{+58.4}_{-53.6}$
ML-fit bias (event)	2.9	-0.1	3.2
MC ϵ (%)	15.0(T) 14.1(L)	9.6(T) 6.64(L)	15.3 (T) 13.6 (L)
MC ϵ (%) corrected with f_L	14.2	6.9	13.8
Tracking Corr. (%)	96.6	96.6	95.4
K^0_S Correction (%)	97.1	—	
$\prod \mathcal{B}_i$ (%)	20.3	29.6	59.2
Corr. $\epsilon \times \prod \mathcal{B}_i$ (%)	2.70	1.98	7.78
Stat. Signif. (σ)	1.4	1.5	2.3
Signif. w. syst. (σ)	1.3	1.4	2.2
$\mathcal{B}(\times 10^{-6})$	$3.9^{+3.7}_{-3.0} \pm 0.9$	$3.1^{+3.4}_{-2.4} \pm 0.9$	$3.4^{+1.8}_{-1.6} \pm 0.4$
UL $\mathcal{B}(\times 10^{-6})$ (incl. syst.)	9.5	8.9	6.0
Combined results			
$\mathcal{B}(\times 10^{-6})$	$3.5^{+2.5}_{-2.0} \pm 0.7$		—
Stat. Signif. (σ)	2.0		—
Signif. w. syst. (σ)	1.9		—
UL $\mathcal{B}(\times 10^{-6})$ (incl. syst.)	7.4		—

Table 4.14: ML fit values for $B^+ \to \omega\rho^+$ and $B^0 \to \omega\rho^0$ from the full Run1+Run2 data set.

ML fit quantity	$\omega\rho^+$	$\omega\rho^0$
$\cos\theta_{\rm T}$ cut	0.65	0.65
#Data combs/event	1.21	1.15
#MC combs/event	1.20 (T) 1.25 (L)	1.15 (T) 1.18 (L)
Events to fit		
On-resonance	20145	20769
Off-resonance	2135	2309
Signal yield		
On-res data	$57.7^{+18.5}_{-16.5}$	$4.3^{+11.0}_{-9.1}$
Off-res data	-13.9 ± 8.2	2.2 ± 4.1
f_L	$0.88^{+0.12}_{-0.15}$	0.9 (fixed)
90% CL yield UL	80.0	22.7
Fit $B\overline{B}$ yield (on-res)	96.4^{+90}_{-86}	98^{+56}_{-53}
ML-fit bias (event)	4.2	-0.5
MC ϵ (%)	9.00 (T) 5.10 (L)	14.1 (T) 10.7 (L)
MC ϵ (%) corrected with f_L	5.57	11.0
Tracking Corr. (%)	96.6	95.4
$\prod \mathcal{B}_i$ (%)	89.1	89.1
Corr. $\epsilon \times \prod \mathcal{B}_i$ (%)	4.79	9.32
Stat. Signif. (σ)	4.8	0.4
Signif. w. syst. (σ)	4.7	0.4
$\mathcal{B}(\times 10^{-6})$	$12.6^{+3.7}_{-3.3} \pm 1.6$	$0.6^{+1.3}_{-1.1} \pm 0.4$
UL $\mathcal{B}(\times 10^{-6})$ (stat.)	—	2.8
UL $\mathcal{B}(\times 10^{-6})$ (incl. syst.)	—	3.3
Signal $\mathcal{A}_{ch}$	$0.05 \pm 0.26 \pm 0.02$	—
Background $\mathcal{A}_{ch}$	-0.01 ± 0.007	—

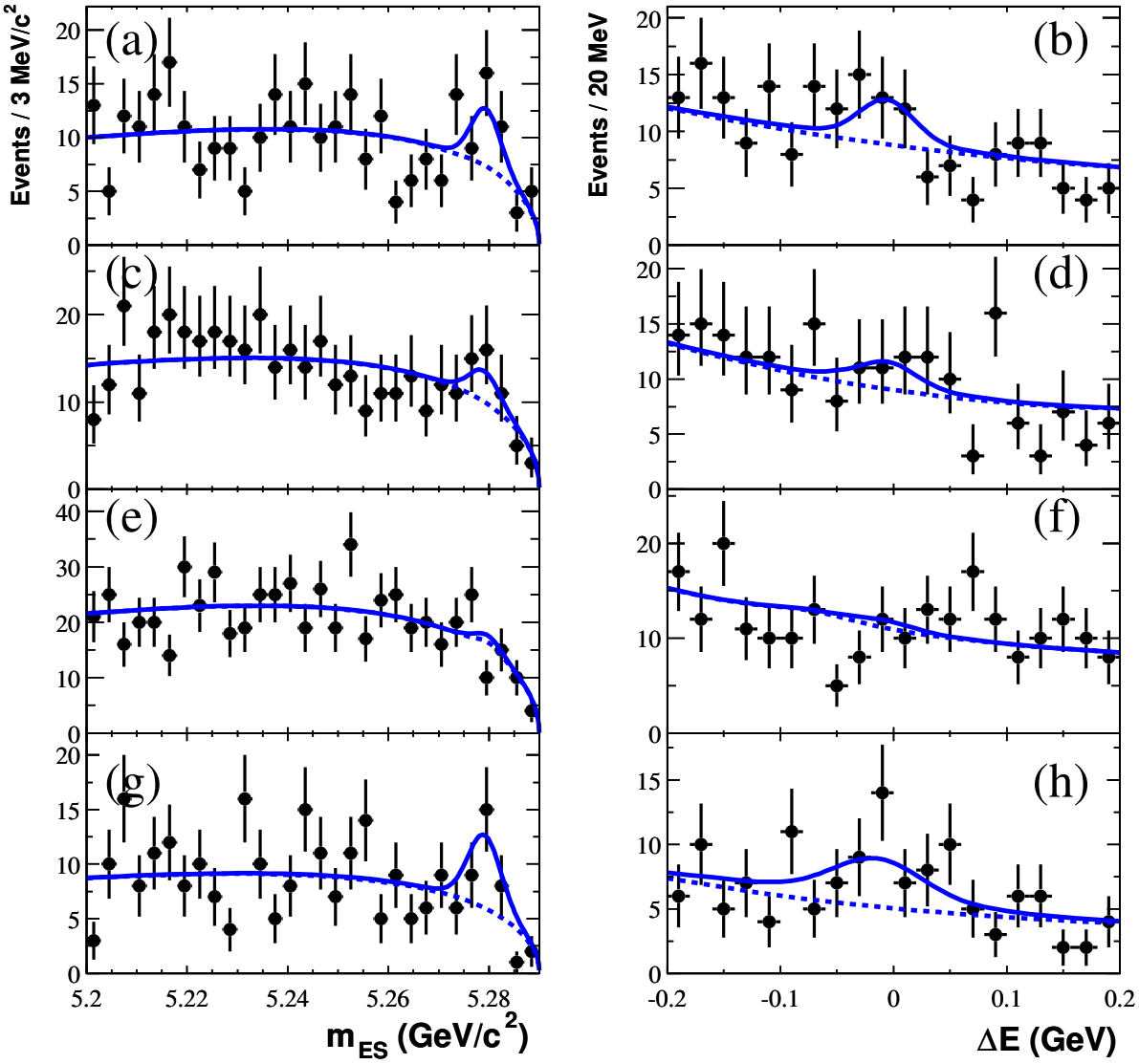

Figure 4.8: Projections of the B candidate $m_{\rm ES}$ and ΔE for $B^0 \to \omega K^{*0}$ (a, b), $B^+ \to \omega K^{*+}$ (c, d), $B^0 \to \omega \rho^0$ (e, f), and $B^+ \to \omega \rho^+$ (g, h). Points with errors represent data passing a cut on a likelihood ratio calculated without the quantity that is shown in the plots. The solid curves show the projected fit functions and dashed curves the background functions.

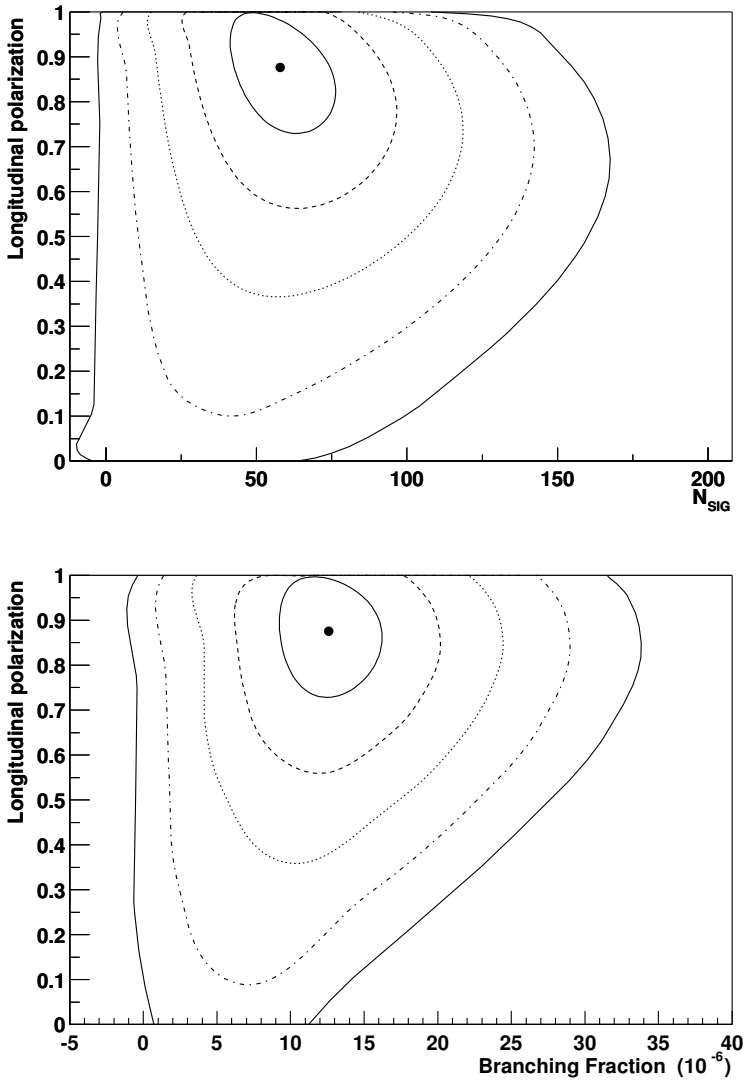

Figure 4.9: Contour plots of (top) f_L vs signal yield and (bottom) f_L vs branching fraction, for $B^+ \to \omega\rho^+$. The solid dot gives the central value; curves give the contours in 1-sigma steps out to 5 sigma.

$B^+ \to \omega\rho^+$ mode in Figure 4.9. The result for the branching fraction comes from a separate fit that takes account of the correlation with f_L of both yield and efficiency. The bottom contour plot in Figure 4.9 demonstrates the reduced correlation in the branching fraction for this fit.

After unblinding, we check for possible correlation between ρ mass and helicity [130] in on-peak data for $B^+ \to \omega\rho^+$ mode. The correlation does exist and actually the correlation coefficient of $\mathcal{H}_\rho$ and m_ρ is about 6% which is the largest for all the correlation coefficients in on-peak data. Figure 4.10 demonstrates the correlation.

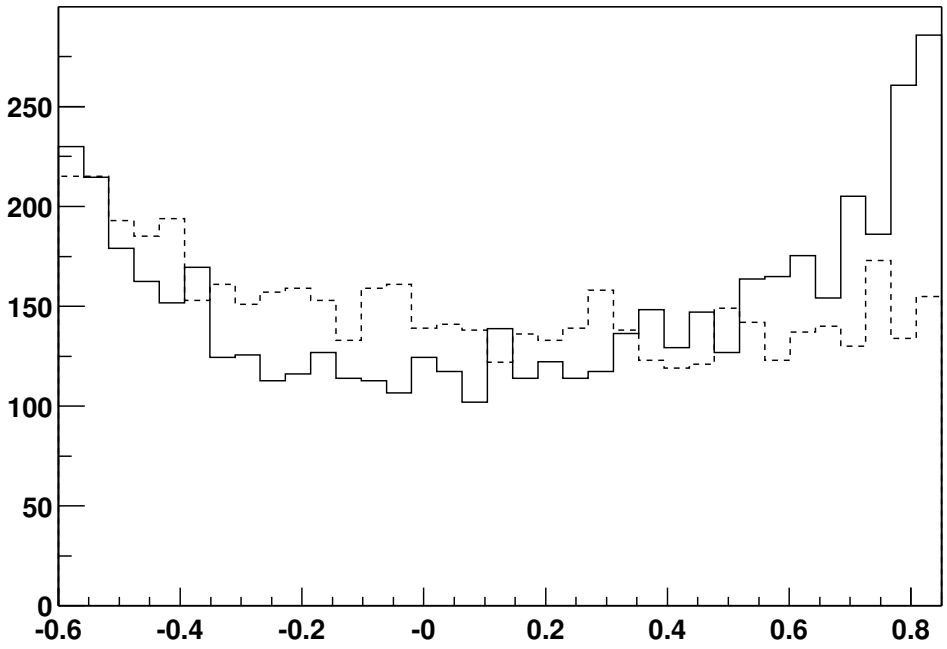

Figure 4.10: $\mathcal{H}_\rho$ distributions for combinatoric background with two ρ mass cuts: $0.9 < m_\rho < 1.07$ (solid), $0.47 < m_\rho < 0.65$ (dashed). The distribution tends to be flat at low mass range and gets more quadratic at high mass range.

We implement this correlation in our ML fitter, `Q2BFit`, by making the coefficient of the quadratic term of that helicity PDF a linear function of ρ mass, i.e.,

$$\mathcal{P}_{\mathcal{H}}^{\rm comb} = 1 + P_1 \cos\theta + (a + b \times m_\rho)\cos^2\theta \,. \tag{4.2}$$

We fit this PDF to on-peak sideband data to find P_1, a and b and then use the PDF in our final fit. We find signal yield changes from 57.7 to 57.4 and f_L from 0.8753 to 0.8748, which is really negligible.

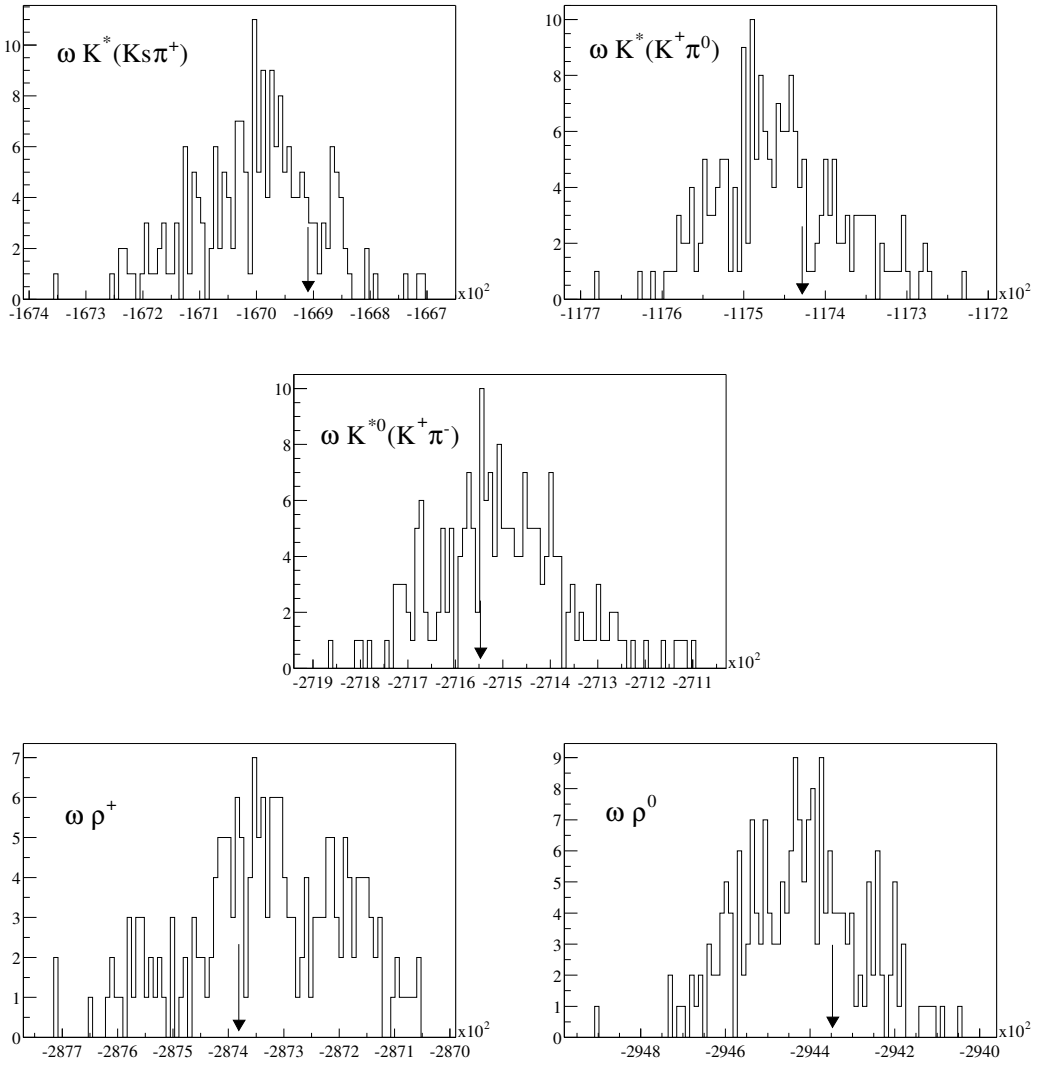

Figure 4.11: Goodness-of-fit plot for $\omega K^{*+}_{K^0_S\pi^+}$ (top left), $\omega K^{*+}_{K^+\pi^0}$ (top right), $\omega K^{*0}_{K^+\pi^-}$ (middle), $\omega\rho^+$ (bottom left), $\omega\rho^0$ (bottom right). The distribution is from 200 pure toy experiments with the number generated signal events equal to the number found in on-peak data. The arrows indicate the $-2\ln\mathcal{L}$ values for on-peak data.

The goodness-of-fit plots for $B \to \omega K^*$ and $B \to \omega\rho$ are shown in Figure 4.11, with the arrows indicating the $-2\ln\mathcal{L}$ values for data. For each fit the result lies well within the expected distribution.

Table 4.15 shows the results of our evaluation of the systematic errors for these modes. The fit yield errors are estimated with procedure described in Sec. 3.7, and we list the changes in signal yields when using the different set of ΔE, $m_{\rm ES}$, m_ω, $m_{K^*/\rho}$, $\mathcal{F}$, $\mathcal{H}_\omega$, and $\mathcal{H}_{K^*/\rho}$ parameters in Table 4.16.

Table 4.15: Estimates of systematic errors of the $B^+ \to \omega K^{*+}_{K^0_S\pi^+}$, $\omega K^{*+}_{K^+\pi^0}$, $B^0 \to \omega K^{*0}_{K^+\pi^-}$, $B^+ \to \omega\rho^+$ and $B^0 \to \omega\rho^0$ branching fractions. 'C' stands for correlated error and 'U' for uncorrelated error (see Sec. 3.7.1).

Quantity	$\omega K^{*+}_{K^0_S\pi^+}$	$\omega K^{*+}_{K^+\pi^0}$	$\omega K^{*0}_{K^+\pi^-}$	$\omega\rho^+$	$\omega\rho^0$
Multiplicative errors (%)					
Track multiplicity (C)	1.0	1.0	1.0	1.0	1.0
Tracking eff/qual (C)	2.4	2.4	3.2	2.4	3.2
π^0/ γ eff (C)	5.1	10.3	5.1	10.3	5.1
K^0_S efficiency (C)	4.0		—		
Number $B\overline{B}$ (C)	1.1	1.1	1.1	1.1	1.1
Branching fractions (U)	0.8	0.8	0.8	0.8	0.8
MC statistics (U)	1.8	2.5	1.9	2.7	2.1
$\cos\theta_{\rm T}$ (C)	1.4	1.4	1.2	1.1	1.4
PID (C)	—	1.0	1.0	—	—
f_L (C)	2.1	6.2	3.6	—	5.5
Total multiplicative (%)	7.8	12.7	7.6	11.1	8.7
Additive errors (events)					
Fit yield (U)	1.2	0.6	2.0	2.1	4.2
Fit bias (U)	1.5	0.1	1.6	2.1	0.3
$B\overline{B}$ Background (U)	1.0	1.3	1.2	1.2	1.4
Total additive (events)	2.1	1.4	2.8	3.2	4.4
Total errors [$\mathcal{B}(\times 10^{-6})$]					
Additive	0.9	0.8	0.4	0.8	0.5
Uncorrelated	0.9	0.8	0.4	0.8	0.5
Correlated	0.3	0.4	0.2	1.4	0.0

Table 4.16: Detailed breakdown of variations applied to the signal PDF parameters in order to calculate the ML fit yield systematic for $B^+ \to \omega K^{*+}_{K^0_S\pi^+}$, $\omega K^{*+}_{K^+\pi^0}$, $B^0 \to \omega K^{*0}_{K^+\pi^-}$, $B^+ \to \omega\rho^+$ and $B^0 \to \omega\rho^0$.

Nominal	Variation	(Fit Yield) - (Nominal Yield)				
		$\omega K^{*+}_{K^0_S\pi^+}$	$\omega K^{*+}_{K^+\pi^0}$	$\omega K^{*0}_{K^+\pi^-}$	$\omega\rho^+$	$\omega\rho^0$
ΔE						
offset=0 MeV	+5 MeV	+0.6	−0.03	−1.7	−0.7	+4.0
	−5 MeV	−1.0	−0.1	+1.3	+0.5	−2.9
scale=1.05	+0.05	−0.2	−0.04	+0.3	+0.5	+1.2
	−0.05	+0.2	−0.04	−0.2	−0.2	+0.1
$m_{\rm ES}$						
offset=0.7 MeV	+0.2 MeV	+0.3	−0.2	−0.2	−0.8	+0.4
	−0.2 MeV	−0.3	+0.1	+0.2	+0.7	+0.9
scale=1.00	+0.04	+0.1	−0.2	+0.5	−0.2	+1.4
	−0.04	−0.1	+0.1	−0.5	+0.2	−0.2
m_ω						
offset=1.1 MeV	+0.3 MeV	+0.1	+0.1	+0.2	−0.2	−0.2
	−0.3 MeV	−0.0	−0.2	−0.1	+0.1	+0.1
scale=1.05	+0.04	−0.1	+0.0	+0.1	−0.0	+0.0
	−0.04	+0.0	−0.1	+0.0	−0.1	−0.1
$m_{K^*/\rho}$						
offset=0 MeV	+1 MeV	−0.1	+0.1	+0.1	−0.1	+0.6
	−1 MeV	−0.1	−0.2	−0.1	−0.1	+0.7
scale=1.0	+0.1	+0.6	+0.2	+0.3	−0.2	+0.5
	−0.1	−0.8	−0.3	−0.2	−0.0	+0.8
$\mathcal{F}$ μ	$+1\sigma$	+0.0	+0.1	+0.8	+1.0	+0.8
	-1σ	−0.0	−0.1	−0.7	−1.0	+0.5
$\mathcal{F}$ σ_L	$+1\sigma$	+0.2	−0.1	−0.2	−0.4	+0.6
	-1σ	−0.2	−0.0	+0.3	+0.4	+0.7
$\mathcal{F}$ σ_R	$+1\sigma$	+0.1	+0.1	+0.3	+0.5	+0.8
	-1σ	−0.1	−0.1	−0.2	−0.5	+0.5
$\mathcal{H}_\omega$	$+1\sigma$	−0.1	−0.2	+0.2	−0.6	+0.7
	-1σ	−0.0	+0.1	−0.1	+0.5	+0.7
$\mathcal{H}_{K^*/\rho}$	$+1\sigma$	−0.1	+0.0	+0.0	−0.5	+0.8
	-1σ	+0.1	−0.1	+0.0	+0.4	+0.4
Total Events		1.2	0.6	2.0	1.9	4.2

We show in Figure 4.12 – 4.15 the sPlots [131] of $m_{\rm ES}$, ΔE, m_ω, m_ρ, $\mathcal{H}_\omega$, $\mathcal{H}_\rho$, and $\mathcal{F}$ for $B^+ \to \omega\rho^+$ mode as cross-check. sPlot is used to project signal or background distributions from a data sample for a variable that is used or not in the original likelihood fit. Unlike the usual likelihood ratio cut projection method, sPlot uses optimally the existing information in the whole data sample for each bin of the projected variable, so as to reduce the uncertainties due to low statistics from cuts. sPlots for an observable are got from sPlot fits with that observable taken out of the fit in the framework of `Q2BFit` based on sPlot `RooFit` implementation [132].

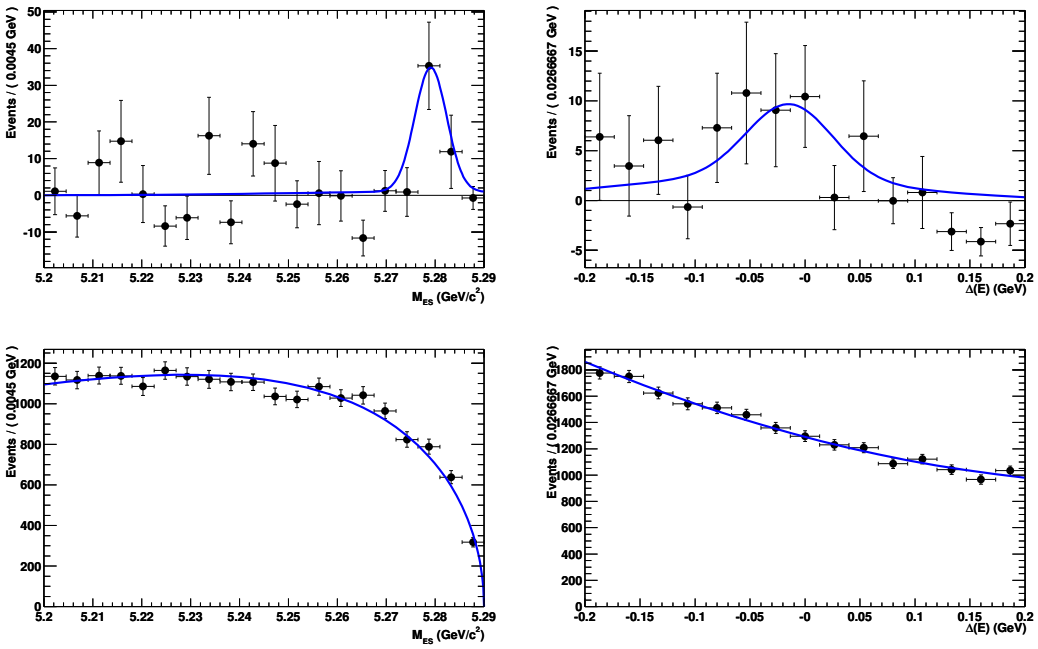

Figure 4.12: $m_{\rm ES}$ (left) and ΔE (right) sPlots for $\omega\rho^+$; signal component (top), continuum background (bottom). Points with errors represent data in the given species. The solid curves show the overlaid PDFs for each component.

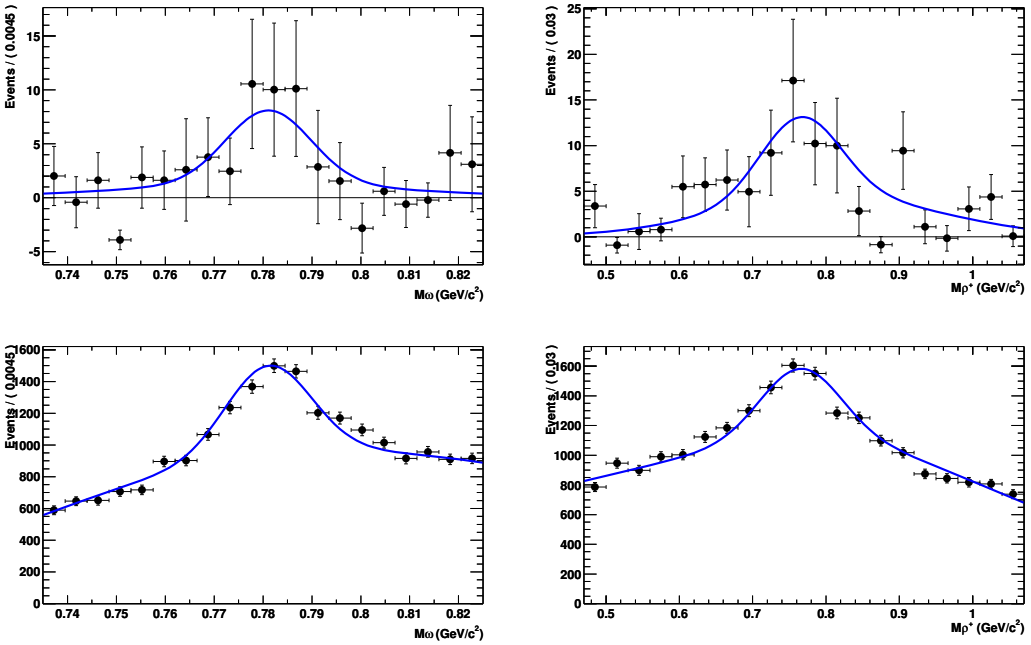

Figure 4.13: M_ω (left) and M_ρ (right) sPlots for $\omega\rho^+$; signal component (top), continuum background (bottom).

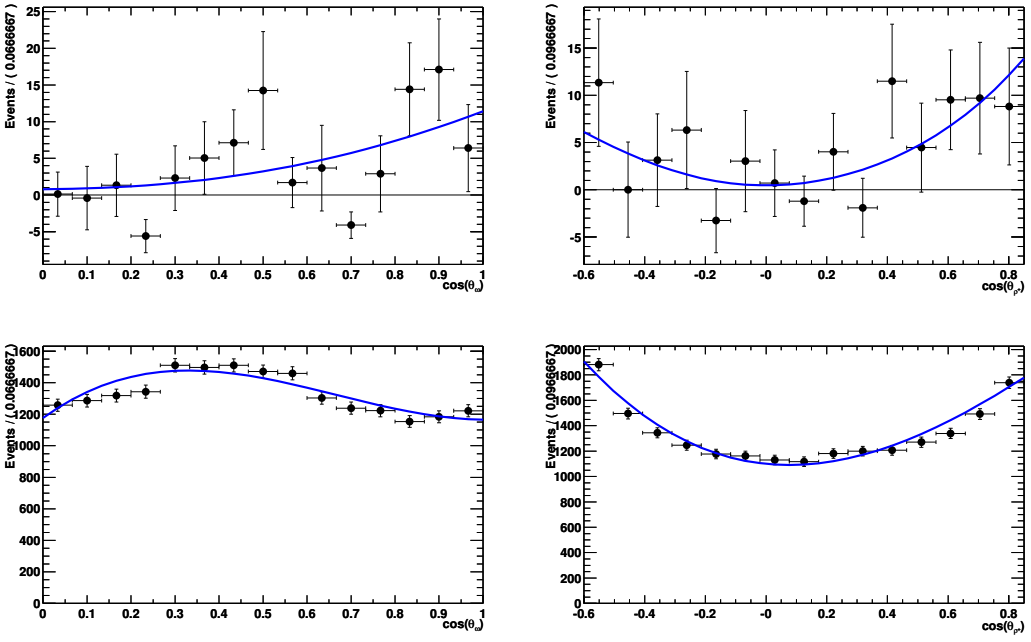

Figure 4.14: $\mathcal{H}_\omega$ (left) and $\mathcal{H}_\rho$ (right) sPlots for $\omega\rho^+$; signal component (top), continuum background (bottom).

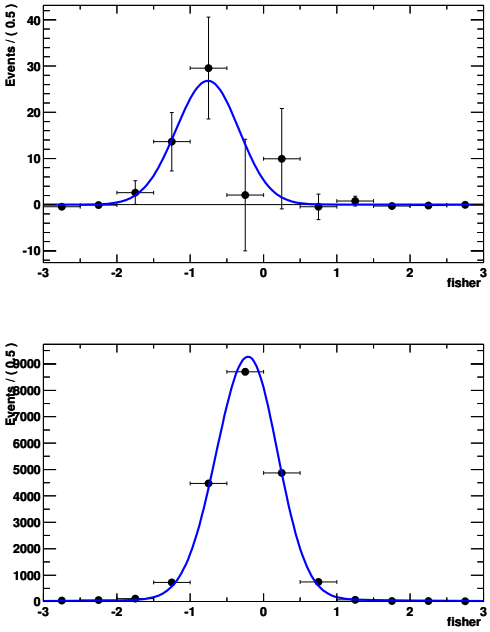

Figure 4.15: $\mathcal{F}$ sPlots for $\omega\rho^+$; signal component (top), continuum background (bottom).

Chapter 5

Conclusions

We have performed blind analyses with 88.9×10^6 $B\overline{B}$ pairs based on *BABAR* Run 1 and Run 2 data for charmless rare B decays with ω mesons, including three pseudoscalar-vector modes, $B^+ \to \omega K^+$, $\omega\pi^+$, and $B^0 \to \omega K^0$, and four vector-vector modes, $B^+ \to \omega K^{*+}$ ($\omega K^{*+}_{K^0_S\pi^+}$, $\omega K^{*+}_{K^+\pi^0}$), $B^0 \to \omega K^{*0}_{K^+\pi^-}$, $B^+ \to \omega\rho^+$ and $B^0 \to \omega\rho^0$.

We find statistically significant signals for all the three PV decays and measure branching fractions. In addition, we measure charge asymmetries for charged decays.

$$\begin{aligned}
\mathcal{B}(B^+ \to \omega K^+) &= (4.8 \pm 0.8 \pm 0.4) \times 10^{-6}\,, \\
\mathcal{B}(B^+ \to \omega \pi^+) &= (5.5 \pm 0.9 \pm 0.5) \times 10^{-6}\,, \\
\mathcal{B}(B^0 \to \omega K^0) &= (5.9^{+1.6}_{-1.3} \pm 0.5) \times 10^{-6}\,, \\
\mathcal{A}_{ch}(B^+ \to \omega K^+) &= -0.09 \pm 0.17 \pm 0.01\,, \\
\mathcal{A}_{ch}(B^+ \to \omega \pi^+) &= 0.03 \pm 0.16 \pm 0.01\,.
\end{aligned}$$

We have made the first observation of $B^0 \to \omega K^0$, and these results are published in *Physical Review Letters* [133]. These results are in good agreement with theoretical expectations as in Table 1.7 on page 38 and are consistent with, but more precise than, previous measurements [52, 53, 134]. The reports [51, 53] of a branching fraction for $B^+ \to \omega K^+ \gtrsim 10 \times 10^{-6}$ are now definitively ruled out. The final state ωK^0 is a CP eigenstate. With future large data samples it will be possible to measure time-dependent CP asymmetry. Recent results from *BABAR* [21] and Belle [22] show 4.2σ and 3.2σ direct CP violation effects in the decays of $B^0 \to K^+\pi^-$ and $B^0 \to \pi^+\pi^-$, respectively. Belle indicates a possible non-zero $\mathcal{A}_{ch}$ for $B^+ \to \omega\pi^+$ mode [135]. All

these rare modes have relatively low branching fractions, and direct *CP* violations from weak phase differences among different decay amplitudes can be enhanced through FSI (see Sec. 1.5.2.1 on page 22). Theoretical calculations show that direct *CP* violation effects could be sizable for $B^+ \to \omega\pi^+$ [136]. It is then interesting to study these *PV* modes again using the much larger sample now available at *BABAR*.

We have made more precise measurements of the four VV modes. We observe $B^+ \to \omega\rho^+$ for the first time (4.7σ) and measure the longitudinal polarization fraction f_L and charge asymmetry $\mathcal{A}_{ch}$ for this mode. We also determine much tighter 90% CL upper limits than previous searches for the other modes.

$$
\begin{aligned}
\mathcal{B}(B^0 \to \omega K^{*0}) &= (3.4^{+1.8}_{-1.6} \pm 0.4) \times 10^{-6} \quad (< 6.0 \times 10^{-6})\,, \\
\mathcal{B}(B^+ \to \omega K^{*+}) &= (3.5^{+2.5}_{-2.0} \pm 0.7) \times 10^{-6} \quad (< 7.4 \times 10^{-6})\,, \\
\mathcal{B}(B^0 \to \omega \rho^0) &= (0.6^{+1.3}_{-1.1} \pm 0.4) \times 10^{-6} \quad (< 3.3 \times 10^{-6})\,, \\
\mathcal{B}(B^+ \to \omega \rho^+) &= (12.6^{+3.7}_{-3.3} \pm 1.6) \times 10^{-6}\,, \\
f_L(B^+ \to \omega \rho^+) &= 0.88^{+0.12}_{-0.15} \pm 0.03\,, \\
\mathcal{A}_{ch}(B^+ \to \omega \rho^+) &= 0.05 \pm 0.26 \pm 0.02\,.
\end{aligned}
$$

As for the $\rho\rho$ modes [127,137,138], we find that $B^+ \to \omega\rho^+$ is dominated by longitudinal spin alignment, and it has relatively large decay rate (compared to $\pi\pi$) with tree diagram. The branching fraction for $B^+ \to \omega\rho^+$ is about half the value found for both $\rho^+\rho^0$ and $\rho^+\rho^-$. The measurement of $B^0 \to \omega\rho^0$, together with that of $\rho^0\rho^0$, sets tight constraints on the penguin pollution. These branching fraction measurements are in general agreement within errors with the theoretical estimates (see Table 1.7 on page 38). Both *BABAR* [127,139] and Belle [140] have observed surprisingly large transverse components of $B \to \phi K^*$, in disagreement with the expected $1/m_b^2$ suppression [141]. Recent theoretical explanations [142] suggest that similar phenomena may occur in $B \to \omega K^*$, and it may have a different *CP* violation pattern for the transverse component. These modes may become observable with the sensitivity of the current *BABAR* data sample.

Bibliography

[1] J. J. Thomson, Philosophical Magazine **44**, 293 (1897).

[2] T.D. Lee and C.N. Yang, Phys. Rev. **104**, 254 (1956).

[3] C.S. Wu, E. Ambler, R. Hayward, D. Hoppes, and R. Hudson, Phys. Rev. **105**, 1413 (1957).

[4] M. Goldhaber, L. Grodzins, and A. Sunyar, Phys. Rev. **109**, 1015 (1958).

[5] J. H. Christenson, J. W. Cronin, V. L. Fitch, and R. Turlay, Phys. Rev. Lett. **13**, 138 (1964).

[6] A. D. Sakharov, ZhETF Pis. Red. **5**, 32 (1967); JETP Lett. **5**, 24 (1967).

[7] W. Pauli, Phys. Rev. **58**, 716 (1940).

[8] S. L. Glashow, Nucl. Phys. **22**, 579 (1961); S. Weinberg, Phys. Rev. Lett. **19**, 1264 (1967); A. Salam, *Elementary Particle Theory,* (Stockholm: Almquist and Wiksells, 1967).

[9] D. H. Perkins, *Introduction to High Energy Physics,* (Cambridge University Press, 2000).

[10] *BABAR* Collaboration, edited by P. F. Harrison and H. R. Quinn, *The BABAR Physics Book,* SLAC-R-504 (1998).

[11] G. Kramer, W. F. Palmer, Phys. Rev. D **45**, 193 (1992).

[12] S. Eidelman *et al.*, *Review of Particle Physics,* Phys. Lett. B **592**, 1 (2004). `http://pdg.lbl.gov.`

[13] A. V. Gritsan, *BABAR* (internal) Analysis Document #498, (2003).

[14] M. Kobayashi and T. Maskawa, Prog. Th. Phys. **49**, 652 (1973).

[15] N. Cabibbo, Phys. Rev. Lett. **10**, 531 (1963).

[16] L.L. Chau and W.Y. Keung, Phys. Rev. Lett. **53**, 1802 (1984).

[17] L. Wolfenstein, Phys. Rev. Lett. **51**, 1945 (1983).

[18] NA48 Collaboration, J. R. Batley *et al.*, Phys. Lett. B **544**, 97 (2002).

[19] KTeV Collaboration, A. Alavi-Harati *et al.*, Phys. Rev. D **67**, 012005 (2003).

[20] *BABAR* Collaboration, B. Aubert *et al.*, Phys. Rev. Lett. **89**, 281802 (2002).

[21] *BABAR* Collaboration, B. Aubert *et al.*, hep-ex/0407057, (2004).

[22] Belle Collaboration, K. Abe *et al.*, Phys. Rev. Lett. **93**, 021601 (2004). hep-ex/0401029

[23] ARGUS Collaboration, H. Albrecht *et al.*, Phys. Lett. B **192**, 245 (1987).

[24] UA1 Collaboration, C. Albajar *et al.*, Phys. Lett. B **186**, 247 (1987).

[25] M. Bander, S. Silverman and A. Soni, Phys. Rev. Lett. **43**, 242 (1979).

[26] A. Ali, G. Kramer, and C.D. Lü, Phys. Rev. D **59**, 014005 (1999). hep-ph/9805403

[27] A. B. Carter and A. I. Sanda, Phys. Rev. Lett. **45**, 952 (1980); Phys. Rev. D **23**, 1567 (1981).

[28] I. I. Bigi and A. I. Sanda, Nucl. Phys. B **193**, 85 (1981); Nucl. Phys. B **281**, 41 (1987).

[29] I. Dunietz and J. Rosner, Phys. Rev. D **34**, 1404 (1986).

[30] Ya. I. Azimov, N. G. Uraltsev and V. A. Khoze, Sov. J. Nucl. Phys. **45**, 878 (1987).

[31] I. I. Bigi *et al.*, *CP Violation,* ed. C. Jarlskog, World Scientific (1992).

[32] M. K. Gaillard and B. W. Lee, Phys. Rev. Lett. **33**, 108 (1974);
G. Altarelli and L. Maiani, Phys. Lett. B **52**, 351 (1974);
J. Ellis, M. K. Gaillard, and D. V. Nanopoulos, Nucl. Phys. B **100**, 313 (1975);
A. I. Vainshtein, V. I. Zakharov, and M. A. Shifman, ZhETF Pis. Red. **22**, 123 (1975); JETP Lett. **22**, 55 (1975).

[33] R. Fleischer, Z. Phys. C **62**, 81 (1994);
N. G. Deshpande and X.-G. He, Phys. Lett. B **336**, 471 (1994).

[34] A. Ali, G. Kramer, and C.D. Lü, Phys. Rev. D **58**, 094009 (1998). hep-ph/9804363

[35] M. Gronau, O. F. Hernández, D. London, J.L. Rosner, Phys. Rev. D **50**, 4529 (1994).

[36] M. Gronau, J. L. Rosner, Phys. Rev. D **53**, 2516 (1996).

[37] R. Fleischer, Int. J. Mod. Phys. **A12**, 2459 (1997). hep-ph/9612446

[38] K. G. Wilson, Phys. Rev. **179**, 1499 (1969).

[39] W.-S. Hou and K.-C. Yang, Phys. Rev. D **61**, 073014 (2000). hep-ph/9908202

[40] Y.H. Chen *et al.*, Phys. Rev. D **60**, 094014 (1999). hep-ph/9903453

[41] H.-Y. Chang and K.-C. Yang, Phys. Lett. B **511**, 40 (2001). hep-ph/0104090

[42] A. Abada *et al.*, (APE Collaboration), Phys. Lett. B **365**, 275 (1996); J. M. Flynn *et al.*, (UKQCD Collaboration), Nucl. Phys. B **461**, 327 (1996); L. Del Debbio *et al.*, (UKQCD Collaboration), Phys. Lett. B **416**, 392 (1998).

[43] A. Ali, V. M. Braun, H. Simma, Z. Phys. C **63**, 437 (1994), hep-ph/9401277; P. Ball and V. M. Braun, Phys. Rev. D **55**, 5561 (1997), hep-ph/9701238.

[44] M. Neubert and B. Stech, in *Heavy Flavors*, 2nd ed. (World Scientific, Singapore, 1998).

[45] R. Aleksan *et al.*, Phys. Rev. D **67**, 094019 (2003). hep-ph/0301165

[46] L.-L. Chau *et al.*, Phys. Rev. D **43**, 2176 (1991).

[47] A. Deandrea, N. Di Bartolomeo, R. Gatto, and G. Nardulli, Phys. Lett. B **318**, 549 (1993), hep-ph/9308210; A. Deandrea, N. Di Bartolomeo, R. Gatto, F. Feruglio, and G. Nardulli, Phys. Lett. B **320**, 170 (1994), hep-ph/9310326.

[48] G. Kramer, W. F. Palmer, and H. Simma, Nucl. Phys. B **428**, 77 (1994). hep-ph/9402227

[49] G. Kramer, W. F. Palmer, H. Simma, Z. Phys. C **66**, 429 (1995). hep-ph/9410406

[50] D. Du and L. Guo, Z. Phys. C **75**, 9 (1997). hep-ph/9510259

[51] CLEO Collaboration, T. Bergfeld *et al.*, "Observation of $B^+ \to \omega K^+$ and Search for Related B Decays Modes," Phys. Rev. Lett. **81**, 272 (1998). hep-ex/9803018

[52] CLEO Collaboration, C. P. Jessop *et al.*, "Study of Charmless Hadronic B Meson Decays to Pseudoscalar-Vector Final States," Phys. Rev. Lett. **85**, 2881 (2000). hep-ex/0006008

[53] Belle collaboration, K. Abe *et al.*, "Observation of $B^\pm \to \omega K^\pm$ Decay," Phys. Rev. Lett. **89**, 191801 (2002). hep-ex/0207019

[54] J. D. Bjorken, Nucl. Phys. B Proc. Suppl. **11**, 325 (1989).

[55] "PEP-II: An Asymmetric B Factory. Conceptual Design Report," SLAC-R-418, (1993).

[56] *BABAR* Collaboration, D. Boutigny, *et al.*, "*BABAR* Technical Design Report," SLAC-R-457, (1995).

[57] *BABAR* Collaboration, B. Aubert *et al.*, "The *BABAR* Detector," Nucl. Instr. Meth. A **479**, 1 (2002). hep-ex/0105044

[58] P. Oddone, in *Proceedings of the UCLA Workshop: Linear Collider $B\overline{B}$ Factory Conceptual Design,* p.243, edited by D. Stork, (World Scientific, 1987).

[59] M. Sullivan, "B Factory Interaction Region Design," SLAC-PUB-7563, *Proceedings of the IEEE Particle Accelerator Conference (PAC97),* Vancouver, BC, Canada (1997).

[60] J. Seeman *et al.*, "Results and plans of the PEP-II B-factory," SLAC-PUB-10547, *Presented at 9th European Particle Accelerator Conference (EPAC 2004)*, Lucerne, Switzerland, 5-9 Jul 2004.

[61] P. Billoir, Nucl. Instr. and Methods **225**, 352 (1984).

[62] D. Barbieri *et al.*, Nuo. Cim. **A112**, 113 (1999).

[63] B. N. Ratcliff, SLAC-PUB-5946 (1992); B. N. Ratcliff, SLAC-PUB-6047 (1993); P. Coyle *et al.*, Nucl. Instr. Meth. A **343**, 292 (1994), (SLAC-PUB-6371).

[64] A. Drescher *et al.*, Nucl. Instr. Meth. A **237**, 464 (1985).

[65] L. Lista and F. Fabozzi, "Muon Identification in the *BABAR* Experiment," *BABAR* (internal) Analysis Document #60, (2000).

[66] "The VxWorks realtime operating system and Tornado Development interface," Wind River Systems, Inc., Alameda, CA, USA. http://www.windriver.com/

[67] P. F. Harrison, "Blind analysis," J. Phys. **G28**, 2679 (2002).

[68] B. Stroustrup, *The C++ Programming Language,* (Addison-Wesley Pub Co, 2000).

[69] "The *BABAR* Application Framework," http://www.slac.stanford.edu/BFROOT/www/doc/workbook/framework1/framework1.html

[70] J. K. Ousterhout, *Tcl and the Tk Toolkit,* (Addison-Wesley Professional, 1994); P. Raines, *Tcl/Tk Pocket Reference,* (O'Reilly & Associates, 1998); http://www.tcl.tk.

[71] "GenFwkInt," http://www.slac.stanford.edu/BFROOT/www/Physics/Tools/generators/GenFwkInt/GenFwkInt.html

[72] D. J. Lange, "The EvtGen particle decay simulation package," Nucl. Instr. Meth. A **462**, 152 (2001). http://www.slac.stanford.edu/~lange/EvtGen/

[73] T. Sjöstrand, "PYTHIA 5.7 and JETSET 7.4 Physics and Manual," CERN-TH-7112-93-REV (1995). hep-ph/9508391

[74] "BgsApp–Detector Geometry, Particle Tracking and Hit Scoring," http://www.slac.stanford.edu/BFROOT/www/Computing/Offline/Simulation/web/simcodes/bgsapp/bgsapp_main.html

[75] S. Agostinelli *et al.*, "Geant4—a simulation toolkit," Nucl. Instr. Meth. A **506**, 250 (2003). SLAC-PUB-9350. http://wwwasd.web.cern.ch/wwwasd/geant4/

[76] Sh. Rahatlou, "Moose: *BABAR* Simulation Application," http://www.slac.stanford.edu/BFROOT/www/Computing/Documentation/CM2/intro/030_run_executables/Moose.html

[77] B. Jacobsen, "Beta: A package for analysis access to reconstructed data," http://www.slac.stanford.edu/BFROOT/www/Computing/Offline/Beta/Beta.html

[78] J. Back, "The BetaTools and BetaCoreTools Packages," http://www.slac.stanford.edu/BFROOT/www/Physics/Tools/BetaTools/BetaTools.html

[79] W. C. van Hoek, "Quasi2Body Ntuple," http://www.slac.stanford.edu/~mirna/internal/new_ntuple_quasi2body.html

[80] "CompositionTools User's Guide," http://www.slac.stanford.edu/BFROOT/www/Physics/Tools/Vertex/CompGuide/index.html

[81] R. Brun, O. Couet, N. Cremel-Somon, and P. Zanarini, "PAW, Physics Analysis Workstation User's Guide," CERN-Q-121, (1999). http://wwwasd.web.cern.ch/wwwasd/paw/

[82] R. Brun, F. Rademakers *et al.*, "The ROOT Users Guide, V4.08," http://root.cern.ch.

[83] M. Goto, "The CINT C/C++ interpreter," http://root.cern.ch/root/Cint.html

[84] W. Verkerke and D. Kirkby, "The RooFit Toolkit for Data Modeling," http://roofit.sourceforge.net.

[85] W. C. van Hoek, http://www.slac.stanford.edu/~mirna/internal/Q2BFit_time.html

[86] F. Blanc *et al.*, *BABAR* (internal) Analysis Document #490, (2004).

[87] Per Cederqvist *et al.*, "Version Management with CVS," http://www.gnu.org/software/cvs/

[88] L. Dalesio *et al.*, "The Experimental Physics and Industrial Control System Architecture: past, present and future," Nucl. Instr. Meth. A **352**, 179 (1994).

[89] A. S. Johnson, "Java analysis studio," SLAC-PUB-7963, Presented at *International Conference on Computing in High-Energy Physics, (CHEP 98)*, Chicago, IL, (1998). http://jas.freehep.org/

[90] H. Schildt, *Java 2: The Complete Reference, fifth ed.*, (McGraw-Hill Osborne Media, 2002); http://java.sun.com.

[91] A. Ballaminut *et al.*, "WIRED - World Wide Web Interactive Remote Event Display," SLAC-REPRINT-2000-033, Prepared for *International Conference on Computing in High-Energy Physics and Nuclear Physics (CHEP 2000)*, Padova, Italy, (2000). http://www.slac.stanford.edu/BFROOT/www/Computing/Graphics/Wired/index.html

[92] "*BABAR* Database Summaries," http://www.slac.stanford.edu/BFROOT/www/doc/workbook/nanomicro/nanomicro.html

[93] "The Kanga Home Page," http://www.slac.stanford.edu/BFROOT/www/Computing/Offline/Kanga/index.html

[94] "Systematic corrections for the neutrals," http://www.slac.stanford.edu/BFROOT/www/Physics/Tools/BetaTools/MicroNeutralKilling-RUN2.html

[95] F. Yumiceva, "PID Killing and Tables," http://www.slac.stanford.edu/BFROOT/www/Physics/Tools/Pid/PidKilling/PidKilling.html

[96] R. Sinkus and T. Voss, Nucl. Instr. Meth. A **391**, 360 (1997).

[97] "Proton Selectors Performance," http://www.slac.stanford.edu/BFROOT/www/Physics/Tools/Pid/Protons/performance.html

[98] A. Höcker, "A Maximum Likelihood Method for DIRC Particle Identification," *BABAR* (internal) Analysis Document #23, (2000).

[99] G. Mancinelli and S. Spanier, "Kaon Selection at *BABAR*," *BABAR* (internal) Analysis Document #116, (2001).

[100] G. Mancinelli and S. Yellin, "An Event Likelihood Algorithm for DIRC-Based Particle Identification," *BABAR* (internal) Analysis Document #165, (2003).

[101] Pi0 lists (before release 12), http://www.slac.stanford.edu/BFROOT/www/Physics/Analysis/AWG/Neutrals/doc/pi0lists-beforerelease12.html

[102] M. Bona, R. Faccini, and M. Langer, "Studies on $K^0_S \to \pi^+\pi^-$ reconstruction," *BABAR* (internal) Analysis Document #19, (2000).

[103] A. V. Telnov and A. V. Gritsan, "$K^0_S \to \pi^+\pi^-$ Reconstruction Efficiency in *BABAR*: Release-10 Data vs. SP4 Monte Carlo," *BABAR* (internal) Analysis Document #677, (2003).

[104] "The Vertexing User's Guide," http://www.slac.stanford.edu/BFROOT/www/Physics/Tools/Vertex/VtxGuide/index.html

[105] F. Blanc *et al.*, "Exclusive Charmless Two-Body B decays to ω mesons in Run 1 and Run 2 Data," *BABAR* (internal) Analysis Document #528, (2003).

[106] F. Blanc *et al.*, "Exclusive Charmless Two-Body B decays to ωK^* and $\omega\rho$ in Run 1 and Run 2 Data," *BABAR* (internal) Analysis Document #641, (2004).

[107] M. Bona *et al.*, "Measurement of Branching Fractions and *CP*-Violating Asymmetries in $B \to h^+h'^-$ Decays," *BABAR* (internal) Analysis Document #446, (2002). Supporting document to Ref. 20.

[108] F. Blanc *et al.*, "Exclusive Charmless Two-Body B Decays to ηh^+, $\eta' h^+$, and ωh^+," *BABAR* (internal) Analysis Document #642, (2003).

[109] J. Smith, A. Soffer, and R. Waldi, "Recommendation for Exclusive B Reconstruction Analysis Variables," *BABAR* Analysis Note #497, (1999).

[110] ARGUS Collaboration, H. Albrecht *et al.*, Z. Phys. C **48**, 543 (1990).

[111] F. Blanc *et al.*, "Exclusive Charmless Two-Body B decays to η, η' and ω mesons in 1999-2001 Data," *BABAR* (internal) Analysis Document #390, (2002).

[112] F. Blanc *et al.*, "Exclusive Charmless Two-Body B Decays to η and η' Mesons," *BABAR* (internal) Analysis Document #521, (2004).

[113] S. Brandt *et al.*, Phys. Lett. **12**, 57 (1964);
E. Fahri, Phys. Rev. Lett. **39**, 1587 (1977).

[114] R. A. Fisher, Ann. Eugenics **7**, 179 (1936).

[115] CLEO Collaboration, D. M. Asner *et al.*, Phys. Rev. D **53**, 1039 (1996). hep-ex/9508004

[116] A. Höcker *et al.*, "Search for $B^0 \to a_0^{\pm}(980)\pi^{\mp}$", *BABAR* (internal) Analysis Document #141, (2001); *BABAR* Collaboration, B. Aubert *et al.*, SLAC-PUB-8930, (*BABAR*-CONF-01-07), (2001). hep-ex/0107075

[117] A. Bevan *et al.*, "A Search for the decay $B^0 \to \pi^0\pi^0$," *BABAR* (internal) Analysis Document #432, (2002); *BABAR* Collaboration, B. Aubert *et al.*, Phys. Rev. Lett. **91**, 021801 (2003). hep-ex/0303028

[118] J. W. Harris and H. Stocker, "Maximum Likelihood Method," in *Handbook of Mathematics and Computational Science,* p.824, (Springer-Verlag 1998).

[119] P.G. Hoel, *Introduction to Mathematical Statistics, fifth ed.,* (Wiley Text Books, 1984).

[120] P. Bloom *et al.*, "Maximum likelihood fit analyses of quasi-two-body charmless B decay modes," *BABAR* (internal) Analysis Document #117, (2001);
P. Bloom *et al.*, "'Charmless B meson decays with ω or η' mesons," *BABAR* (internal) Analysis Document #178, (2001).

[121] A. V. Gritsan, Y. Groysman, and L-M. Mir, *BABAR* (internal) Analysis Document #604, (2003). Supporting document to Ref. 137.

[122] G. W. Snedecor and W. G. Cochran, *Statistical Methods, 8th ed.,* (Iowa State University Press, 1989).

[123] P. K. Sinervo, "Signal significance in particle physics," in *the proceedings of Conference on Advanced Statistical Techniques in Particle Physics,* Durham, England, (2002). hep-ex/0208005

[124] C. Hearty, "Measurement of the Number of $\Upsilon(4S)$ Mesons Produced in Run 1 (B Counting)," *BABAR* (internal) Analysis Document #134, (2001).

[125] M. Bona *et al.*, "Report of the Tracking Efficiency Task Force for 2001," *BABAR* (internal) Analysis Document #324, (2002).

[126] A. V. Telnov and A. V. Gritsan, "Branching Fractions in $B \to \phi h$ and Search for Direct *CP* Violation in $B^{\pm} \to \phi K^{\pm}$," *BABAR* (internal) Analysis Document #406, (2002); *BABAR* Collaboration, B. Aubert *et al.*, Phys. Rev. D **69**, 011102 (2004). hep-ex/0309025

[127] *BABAR* Collaboration, B. Aubert *et al.*, Phys. Rev. Lett. **91**, 171802 (2003). hep-ex/0307026

[128] S. J. Bailey, "Combining Likelihood Curves," http://www.slac.stanford.edu/~bailey/combine/ (2004).

[129] *BABAR* Collaboration, B. Aubert *et al.*, "Observation of B Meson Decays to $\omega\pi^+$, ωK^+, and ωK^0," SLAC-PUB-9693, (*BABAR*-CONF-03-010), (2003). hep-ex/0303040

[130] L.-M. Mir, A. V. Gritsan, and A. Breon, "Search for the decay $B \to \rho^0\rho^0$," *BABAR* (internal) Analysis Document #821, (2004).

[131] M. Pivk and F. R. Le Diberder, "sPlots: a statistical tool to unfold data distributions," LAL-04-07, (2004). physics/0402083

[132] N. Danielson, "Making sPlots in RooFit with RhhSPlot," http://www.slac.stanford.edu/BFROOT/www/Physics/Analysis/AWG/chrmls_hadronic/TwoBody/RooFithh/splots/splots.html
`Q2BSPlot` in `Q2BFit` is based on `RhhSPlot`.

[133] *BABAR* Collaboration, B. Aubert *et al.*, "Observation of $B^0 \to \omega K^0$, $B^+ \to \eta\pi^+$, and $B^+ \to \eta K^+$ and Study of Related Decays," Phys. Rev. Lett. **92**, 061801 (2004). hep-ex/0311016

[134] *BABAR* Collaboration, B. Aubert *et al.*, "Measurements of the Branching Fractions of Exclusive Charmless B Meson Decays with η' or ω Mesons," Phys. Rev. Lett. **87**, 221802 (2001). hep-ex/0108017

[135] Belle Collaboration, C.H. Wang *et al.*, "Measurement of the Branching Fractions for $B \to \omega K$ and $B \to \omega\pi$," Phys. Rev. D **70**, 012001 (2004). hep-ex/0403033

[136] S. Barshay, G. Kreyerhoff, and L. M. Sehgal, "Direct *CP* Violation in $B^\mp \to \pi^\mp\omega$, $\pi^\mp\rho^0$, $\pi^0\rho^\mp$, and in $\overline{B}^0(B^0) \to \pi^\mp\rho^\pm$ With an Enhanced Branching Ratio for $\pi^0\rho^0$," Phys. Lett. B **595**, 318 (2004). hep-ph/0405012

[137] *BABAR* Collaboration, B. Aubert *et al.*, "Observation of the Decay $B^0 \to \rho^+\rho^-$ and Measurement of the Branching Fraction and Polarization," Phys. Rev. D **69**, 031102 (2004). hep-ex/0311017

[138] Belle Collaboration, J. Zhang *et al.*, "Observation of $B^+ \to \rho^+\rho^0$," Phys. Rev. Lett. **91**, 221801 (2003). hep-ex/0306007

[139] *BABAR* Collaboration, B. Aubert *et al.*, "Measurement of the $B^0 \to \phi K^{*0}$ Decay Amplitudes," SLAC-PUB-10564, (2004). hep-ex/0408017

[140] Belle Collaboration, K.-F. Chen *et al.*, "Measurement of Branching Fractions and Polarization in $B \to \phi K^{(*)}$ Decays," Phys. Rev. Lett. **91**, 201801 (2003). hep-ex/0307014

[141] A. L. Kagan, "Polarization in $B \to VV$ Decays," UCTP-102-04, (2004). hep-ph/0405134

[142] W.-S. Hou and M. Nagashima, "Resolving the $B \to \phi K^*$ Polarization Anomaly," hep-ph/0408007